THEORETICAL AND NUMERICAL ANALYSIS OF VISCOUS-INVISCID INTERACTION

2007

Ramesh Yapalparvi

School of Mathematics

Contents

Word count 22140

List of Figures

9

Abstract

In this thesis some fundamental fluid dynamics phenomena are studied based on the asymptotic analysis of the Navier-Stokes equations at large values of the Reynolds number ($Re \to \infty$). In the first part of the thesis, a numerical method comprising of a finite difference representation of the derivatives with respect to the x-coordinate measured along the body surface and Chebychev collocation along the normal y coordinate is discussed; this method has been used in the paper by Korolev *et al.* (2002). We extend this technique to study,

- Jet like boundary-layers encountering corners, humps and indents.

- Liquid layers encountering convex corners, humps and indents.

- Supersonic flows past humps, indents.

The second part of the thesis deals with understanding the phenomena of boundary-layer separation over moving walls in supersonic flow. The problem is investigated numerically. Assuming that the wall speed u_w is an order $Re^{-\frac{1}{8}}$ quantity, the interaction process may be described by the equations arising from the *triple-deck theory*. We obtain the numerical results for the wall moving either in the downstream or in the upstream direction. The numerical results, indicate that the Moore, Rott & Sears criterion for separation is satisfied for a downstream moving wall but is not applicable for an upstream moving wall for supersonic flows. We also show that the pressure calculated analytically for $u_w \gg Re^{-\frac{1}{8}}$, agrees with our numerical calculations.

Declaration

No portion of the work referred to in this thesis has been submitted in support of an application for another degree or qualification of this or any other university or other institution of learning.

Copyright

Acknowledgements

I wish to credit this achievement to all the people who have been a towering influence on my life much before and after I undertook my PhD research too. My PhD supervisor was Prof. Anatoly I Ruban. I am extremely grateful to him for allowing me to undertake this research. Prof. Ruban encouraged me to think about different aspects of my research and awakened my thoughts to completely new multi-directional and complex distributed environs. His directions helped me to learn a lot from my mistakes and exorcised my fear of treading on the unknown. I thank Prof. Ruban for all this and much more for which mere words fail to provide justice for his Herculean effort in guiding me. I would also like to take this opportunity to express my indebtedness to my co-supervisor Prof. J. S. B Gajjar. His regular advice and insights gave a new vision for my research. He has always provided me with heartwarming support all through my stay at Manchester.

I would like to thank my examiners Dr J. W. Elliott and Prof P. W. Duck for helping me to improve the quality of presentation in this thesis.

The research reported in this thesis was funded by the Faculty Scholarship of the Department of Mathematics, University of Manchester. I am forever indebted to the Department of Mathematics and the University for granting me with the scholarship which instilled a sense of pride and courage in me to strive to achieve my very best. I would like to thank Dr Chris Paul and Mr. Paul Greenwood in helping me with computing facilities and also for the innumerable wonderful discussions that are etched in memory for ever.

My parents, Nirmala and Mohan have been a constant source of strength, encouragement and happiness. They have always provided me with unconditional love and

moral support. Thank you dear mom and dad, I could not have asked for more from both of you. My sister and her husband, Sudha and Praveen have been encouraging me to push beyond my own ability and they have been a pillar of strength.

My dearest friends Aravind (Aru), Chandan (Gowda), Jayaprathap (JP), Prashant (KP) and Sushrutha (Sush) have stood by me through thick and thin. Though the guys are living around the world they have been with me from many years and all through my PhD providing all the emotional security and support. Thank you boys, you all have made my day under the sun. I would like to thank my friend Shreyas for his support, encouragement and useful conversation during the last phase of my research.

Finally, I would like to thank Dr Chris Paul once again for having proof read my thesis. This thesis would not have been made possible without his help.

Chapter 1

Introduction

1.1   Flow Separation

One of the most interesting aspects of fluid flows is the phenomenon of separation with increasing values of the Reynolds number. Of particular interest is the aerodynamic situation, where a rigid body is placed in a uniform stream. The Reynolds number is the dimensionless ratio of inertial to viscous forces. High Reynolds number flows correspond to relatively fast flows of fluids with relatively small viscosity. In general we observe that, above a critical value of the Reynolds number i.e $Re > Re_c$, at some point on the body surface, the fluid gets detached from the surface of the body. This creates a region of relatively slower re-circulating flow, downstream of the separation point S, see Figure 1.1. Thus, for example many "common" gases and liquids, such as air and water, have very small viscosity so that, their flows are characterised by high Reynolds numbers. This is the reason why most of the liquid and gas flows encountered in nature and in engineering applications involve separation.
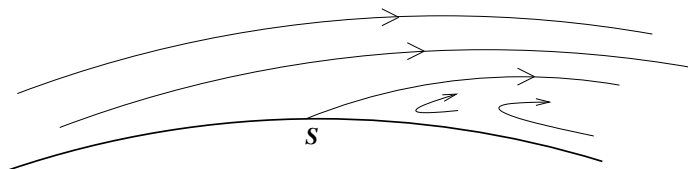
Figure 1.1: Diagram showing separation point and flow reversal.

To achieve a high Reynolds number flow that does not involve separation requires careful attention. For example, if an aerofoil is placed in a uniform subsonic stream, then the design and shape of it is important. Here the term subsonic refers to dimensionless Mach number (ratio of speed of free stream to speed of sound) is less than unity. Such an aerofoil should have a streamlined shape, its cross section has a parabolic-shaped leading-edge and terminating in a cusped shape trailing edge. Moreover the ratio of its maximum thickness- to-chord length should be small, and it should be aligned, or at a small angle of attack, to the oncoming stream. The angle of attack should tend to zero as the Reynolds number approaches infinity. However, at sufficient high Reynolds numbers the flow eventually separates and its effect on the global flow field may often be local, so called small-scale separation, with only a small region of separated flow. As the Reynolds number is further increased it results in more global disruption to the flow field, consisting of a large separation region.

Separation causes drastic effects in the operating characteristic of aircraft wings, helicopter blades and turbine blades, leading to a degradation of performance. Separation is accompanied by a loss of lift, an increase in the drag force, pulsations in the pressure and, may result in the onset of flutter and buffeting.

In case of bluff bodies such as circular cylinders, for very low values of Re, say, $0 < Re < 4$, the flow is attached and symmetrical. For values of Reynolds number, say, $4 < Re < 40$, the flow becomes separated on the back of the cylinder, forming two distinct, stable reversed flow eddies. A photograph of this type is shown in Figure 1.2, where $Re = 26$. As the value of Reynolds number is increased, say, $Re > 40$, the flow behind the cylinder becomes unstable and looses its symmetry and never returns to its attached form.

Figure 1.2: Visualisation of the cylinder flow by Taneda; $Re = 26$.

For simplicity, we often consider, both theoretically and numerically the idealised problem of obtaining attached flow past a two-dimensional aerofoil. This approximates the above experimental situation, provided the aspect ratio, the ratio of wing span to chord length, is large, so that three-dimensional effects due to the wing tips are negligible. The numerical results of such a streamlined aerofoil confirms the experimental findings. The surface pressure experiences a pressure drop as we move away from the stagnation point, which is located in the vicinity of the leading edge of the aerofoil. The pressure increases as we move towards the trailing edge. The geometry of the aerofoil is crucial which determines where exactly the separation occurs.

For such streamlined aerofoils, it is found that, in absence of separation and away from the immediate vicinity of the rigid body, the flow is approximated well by the solution corresponding to attached ideal flow. Ideal flow is incompressible, irrotational and inviscid. Given that inviscid flow necessarily yields a tangential slip velocity over the aerofoil, it is understandable that there is some discrepancy near to the body. Theoretical techniques like perturbation methods have been extensively used for obtaining the attached ideal solution for a thin aerofoil in closed form.

Once again considering flow past a circular cylinder, numerical simulations indicate large scale separation for moderate values of Reynolds number. Consequently only the flow over a forward part of the cylinder, away from the cylinder wall and

reversed flow, has any sort of agreement with the well know attached analytic inviscid solution. The numerical simulation agrees quite well with the theoretical family of separating inviscid flows up to the point of separation and away from the cylinder with the theoretical family of separating inviscid flows, the so-called Kirchoff (1869) family has a tangential separating streamline. Recently numerical solutions at relatively high values of Reynolds number have shown agreement with inviscid Prandtl-Batchelor model flows for closed wakes consisting of non-zero uniform vorticity.

1.2 Boundary-layer theory

Boundary-layer theory has provided a framework for investigating many aspects of fluid flow at high Reynolds numbers. Prandtl (1904) was the first person to provide crucial insight into the separation phenomenon. Prandtl observed that despite "common" gas and liquids experience having very low viscosity, viscous effects did play a major role in the separation phenomenon. He argued that high Reynolds number flow around a rigid body may be treated as inviscid everywhere except in a very thin region adjacent to the body surface, the so-called boundary layer. Within this region, which has a thickness of $O(Re^{-1/2})$, viscosity plays a major role in order to reduce the tangential velocity u reduced from the slip-velocity predicted by the inviscid theory to almost zero at the surface.

The boundary layer is governed by a parabolic, non-linear, viscous subset of the full elliptical governing Navier-Stokes equations, the so-called boundary layer equations. The solutions of these equations yields a corresponding normal velocity, of $O(Re^{-1/2})$, at the edge of the boundary layer. This generally implies that normal velocity at the boundary-layer edge is small, thereby suggesting that the influence of the boundary layer on the outer inviscid flow is small. Classical Prandtl boundary-layer theory is based on a hierarchal approach where the outer inviscid flow is calculated by first ignoring the presence of the boundary-layer and then analysing the boundary-layer by perturbing about the leading-order inviscid solution. Blasius (1908) provided

the analytical solution for the finite flat plate which led to a viscous contribution to the drag force in line with everyday experience.

Although classical boundary-layer theory is based on the premise that the effect of viscous layer on the outer flow is negligible, it yields insight into separation phenomenon. It has been shown, by means of direct numerical integration of the boundary layer equations or analytical Falkner-Skan similarity solutions, that the inviscid pressure distribution played a major role in understanding the behaviour of the boundary layer. The flow remains attached if the pressure gradient is favourable i.e, the pressure decreases downstream. However, under an adverse pressure gradient, i.e. the pressure increases downstream, the boundary-layer tends to separate from the body, that is the skin friction, defined by

$$\tau_w(x^*) = \mu \frac{\partial u}{\partial y} \mid_{y=0} \tag{1.1}$$

vanishes at the point $x^* = x_S$, that is $\tau_w(x_S) = 0$, with the point $x^* = x_S$ identified as separation point. Note that in (1.1) μ is the fluid viscosity, $y = 0$ corresponds to the body surface and u is the x-component of the velocity, where x measures distances along the body surface. The fluid particles near the wall have low kinetic energy and are sensitive to streamwise pressure variations. Even a small increase in pressure may cause the fluid particles near the wall to reverse direction of flow forming a recirculating region characteristic of a separation phenomenon.

Although numerical calculations of the parabolic boundary-layer equations were initially unable to penetrate through the regions of separated flow, subsequently using so-called interactive methods suggested that the skin friction τ_w turns negative, a layer of reversed flow ($u < 0$) emerges near the wall, giving rise to a region of recirculation which, originates from point x_s, in line with the experimental observations.
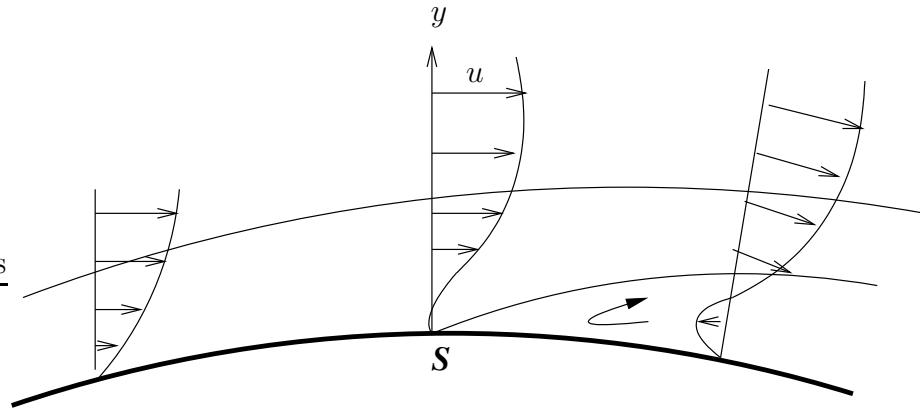
Figure 1.3: Boundary-layer separation.

Landau & Lifshitz (1944) showed that the solution to the boundary layer equations is singular at the separation point. They demonstrated that the skin friction produced by the boundary layer on the body decreases as separation is approached proportional to the square root $\tau_w \propto \sqrt{s}$ of the distance s, where $s = x_s - x$ from the separation point, where the separation point S is shown in the Figure 1.3. The velocity component normal to the body grows inversely to $\sqrt{s}$. This singularity, the so-called Goldstein singularity was further confirmed and elucidated by Goldstein (1948). Goldstein demonstrated that the solution of the boundary-layer equations cannot be continued downstream of the separation point. He also confirmed the structure of the singularity predicted by Landau & Lifshitz (1944) by means of rigorous mathematical analysis of the flow in close proximity to the zero skin friction point.

1.3   Shock/wave boundary-layer interaction

A shock wave can be defined as a mechanical wave of large amplitude, propagating at supersonic velocity ($M_\infty > 1$), across which pressure, density, velocity, temperature, and any related properties change in a nearly discontinuous manner. Shock waves can arise from steady supersonic flow over bodies, bomb blasts, or any other form of intense explosion.

Theoretically, from an inviscid point of view, shock waves are treated as a curve of

discontinuity. The discrete jumps in flow properties then satisfy certain integral (conservation) properties of the governing equations, which results in Rankine-Huginot relations. However the shock wave can, in much the same way as boundary-layers, be regarded as a thin region, typically on the order of 10^{-5} cm, in which viscosity cannot be neglected, viscosity allowing for a smoothly change in the fluid properties. Shock waves in supersonic flow may be classified as normal or oblique according to whether the orientation of the surface of abrupt change is perpendicular or at an angle to the direction of flow. The classical example is of a normal shock which is perpendicular to the direction of flow, provoked by motion of a piston in a shock tube. In order to be consistent with gain in entropy remains constant across the wave, the flow ahead of the shock must be locally supersonic and that behind the shock subsonic. The associated rise in the pressure and density leads to the situation being called compressive.

Another important aspect of fluid dynamics is the effect of interaction of shock wave with the boundary layer over a rigid wall. This typically occurs in supersonic and transonic flows (mixed region $M_\infty < 1$ and $M_\infty > 1$). Examples include flows through supersonic engine inlets, near wing/body junctures, in turbines and compressors, and over transonic aerofoils.

Consider a streamlined aerofoil placed in a fast, but still subsonic, stream. The value of free stream Mach number at which the flow somewhere on the surface first reaches $M_\infty = 1$ is defined as as the critical Mach number. Above a critical value of subsonic Mach number, the flow can become locally supersonic and shows pockets of supersonic flow over both the middle or forward portion of the top surface of the aerofoil, terminated by weak shock waves behind which the flow becomes subsonic again, see Figure 1.4. As the free-stream Mach number is increased, a similar transonic region will develop on the lower surface.
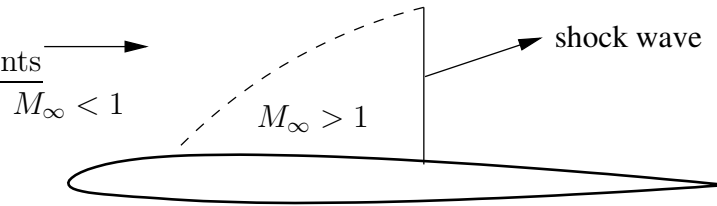
Figure 1.4: Diagram showing a normal shockwave on an aerofoil..

The effects of a shock wave impinging on the boundary layer on a rigid wall has been studied extensively by many experimentalists during the forties and fifties. If the presence of the boundary layer could be ignored, the intersection of a shock wave with a solid boundary would imply a discontinuity in surface pressure and perhaps an irregular reflection. Ackeret *et al.* (1947) were the first to study these effects in their study of transonic flow past aerofoils. Subsequent studies have been done by many experimentalists, such as Liepmann (1946), Chapman *et al.* (1958), Hakkinen *et al.* (1959). Based on the inviscid theory, it is expected that the supersonic regime is terminated by a shock wave, or even change continuously into a subsonic regime. Instead a complicated pattern of shock waves was observed, particularly when the boundary layer was laminar, in which a characteristic feature of shock was was their lambda (λ) structure. The reason for this appears to be due to the fact that the boundary layer has become detached at the foot of the main (primary) shock, boundary-layer separation having occurred far upstream from the point of impingement of the primary shock. The second arm of the λ structure is due to a secondary shock forming near the separation as shown in Figure 1.5. One would also expect a strong separation at the foot of a shock because the sharp pressure rise is transmitted through the boundary layer to the wall where it acts on slowly moving fluid.
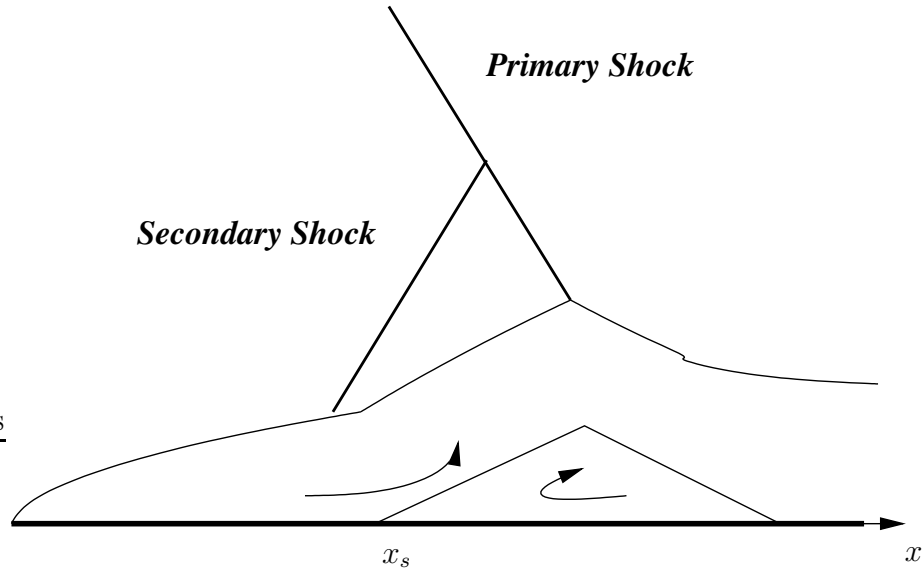
Figure 1.5: Schematic representation of the separation provoked by impinging shock, and formation of the shock λ structure.

Similar results were observed in a more simplified and controlled set-up. For example, consider a flat plate to be placed in a supersonic flow parallel to the free stream velocity as shown in Figure 1.6. An oblique shock wave is produced in the flow by an obstacle placed, say an wedge, situated above the plate. This shock impinges upon the boundary layer on the plate surface at point A, and the focus of attention was on the behaviour of perturbations induced in the flow through the interaction between the shock wave and the boundary layer.
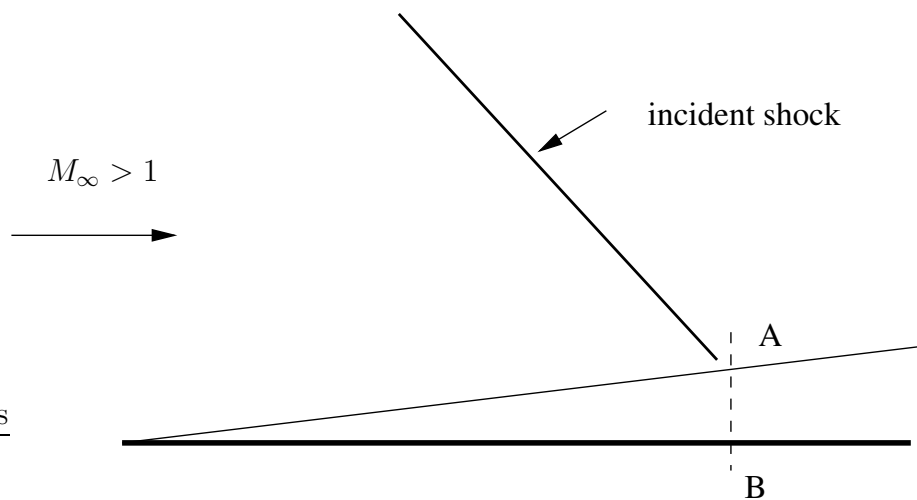
Figure 1.6: Shock-wave interaction with a boundary layer.

Experimental findings of Liepmann (1946) showed that, unless the incident shock was weak, the flow separated from the plate surface some distance upstream of the incident shock. It was also established that the boundary layer was perturbed well ahead of the separation point, and the distance over which the pressure perturbations were able to propagate upstream of the separation point through the boundary layer was significantly larger than the boundary-layer thickness. Any rise in pressure in the boundary layer prior to separation causes the streamlines at the bottom of the inviscid region to deviate away from the wall giving rise to a secondary shock. Together with primary shock they form a λ structure. The separation point moves upstream with further increase in shock strength, the distance from the foot of the primary shock being roughly proportional to the pressure rise across the shock. The separation generates compressive waves which coalesce to form a secondary shock. Downstream of separation the boundary layer detaches from the wall as a free shear layer, and a region of stagnant or slowly eddying fluid is set up below it often referred to as dead water region. The main (primary) shock the impinges on the free shear layer, which reflects it as an expansion fan and simultaneously turned back to the wall where it reattaches, generating another shock wave.

It has been observed that the flow properties near separation are independent of the incident shock and that after separation the wall pressure continues to rise forming a "plateau", typically when the pressure rise at separation has increased twofolds. Further rise in pressure takes place near reattachment.

The above description refers to purely laminar flows. However, the flow becomes turbulent due to the onset of instability of the boundary layer, even without the presence of shock. The instabilities are further aggravated by adverse pressure gradients and free shear layers.

1.4   Upstream influence

The effect of the shock wave is to cause compressive disturbances to the flat plate boundary-layer flow, since it induces a rise in surface pressure. Compressive disturbances are also induced by surface geometries. Chapman *et al.* (1958) studied variety of situations where separation was induced by surface geometries such as steps and corners, where separation occurred invariably upstream of the disturbance.

Two questions, of fundamental theoretical importance immediately strikes. First, how do disturbances propagate upstream through an unseparated boundary layer?. Second, what is the mechanism by which the boundary layer separates when the main shock is strong enough to provoke separation ahead of it, and which is locally independent of it?. The upstream influence observed in experiments were perplexing at the time since the theory of inviscid supersonic flow does not allow disturbances to propagate upstream, since the governing Euler equations are hyperbolic. This suggests that the inviscid flow should remain unperturbed everywhere in front of the incident shock. On the other hand, since the boundary-layer equations are parabolic and Prandtl's hierarchal strategy requires us to solve the equations with the outer solution which is unperturbed in front of the point where the shock impinges upon the boundary layer. It is also found that the boundary layer is also incapable of conducting any perturbations upstream of shock impinging point. However it was noted that the streamwise length scales were small and the associated inviscid velocity gradients at the foot of the shock were large, possibly invalidating boundary-layer theory. In addition when separation was present, the reversed flow beneath the shear layer could transmit disturbances upstream, however this dead-air mechanism does not apply upstream of separation. Finally between the supersonic main stream and the wall is a subsonic regime, the governing equations of which are elliptic, which could permit some upstream propagation.

Chapman *et al.* (1958) in their experiments set up a cycle in which the growth of the boundary layer produced an adverse pressure gradient which, in turn, promoted

further growth in the boundary layer. Using this argument they were able to esti-mate the pressure rise to separation, accounting for both Reynolds number and Mach number dependence.

Historically, the theoretical explanation of the phenomenon initially followed in-viscid point of view, since it was assumed that disturbances in the boundary layer, due to an interaction with a weak shock, are controlled by the inviscid equations of motion, on the grounds that they occur so quickly that viscous forces are negligible. The first step towards a theoretical explanation was given by Howarth (1948). He assumed that changes took place so rapidly that viscosity was of secondary impor-tance in the phenomenon. However, Lighthill (1950), showed that purely inviscid theory was inadequate. Stewartson (1951) considered the case of a large adverse pressure gradient acting over a short distance and showed that an inner viscous sub-layer develops close to the wall could separate while the main part of the boundary layer remains unchanged. Crocco & Lees (1952) showed that when an inviscid outer stream is coupled to the displacement upstream of separation, upstream propagation of disturbances is possible. Later Lighthill (1953) developed a theory of the interac-tion between a weak shock and a boundary layer. He introduced an inner boundary layer to his earlier study and produced a coherent self-consistent theory. Although unable to account for separation, Lighthill also showed how a spontaneous reaction with a possibility of separation could occur within the boundary layer. The theoret-ical work of Lighthill (1953) formed the basis of the supersonic *triple-deck* theory of Stewartson & Williams (1969) and Neiland (1969) which included nonlinear effects and provided a theoretical explanation for the upstream influence, as well as for self-induced separation of a boundary layer in supersonic flow. In this theory, upstream influence extends over a streamwise distance of $O(Re^{-\frac{3}{8}})$ which, although small, is asymptotically large compared with the boundary-layer thickness.

Subsequently triple-deck theory has been applied to many seemingly diverse prob-lems throughout the subsonic, supersonic and hypersonic flow regimes. Comprehen-sive descriptions of triple-deck problems appear in the reviews of Neiland (1974), Nei-land (1981), Stewartson (1974), Stewartson (1981), Messiter (1979), Messiter (1983),

Adamson & Messiter (1980), Smith (1982), Sychev *et al.* (1998) and Sobey (2000).

1.5   Triple Deck theory

Let us consider a two-dimensional flow past a compression ramp constructed from two flat plates AO and OB as shown in Figure 1.7. We shall assume that AO is aligned with the oncoming flow, and OB makes an angle θ with AO. Let us denote the velocity, density, viscosity and pressure in the unperturbed free stream by U_∞, ρ_∞, μ_∞ and p_∞, respectively. Let L be the distance from the leading edge A to the corner O.
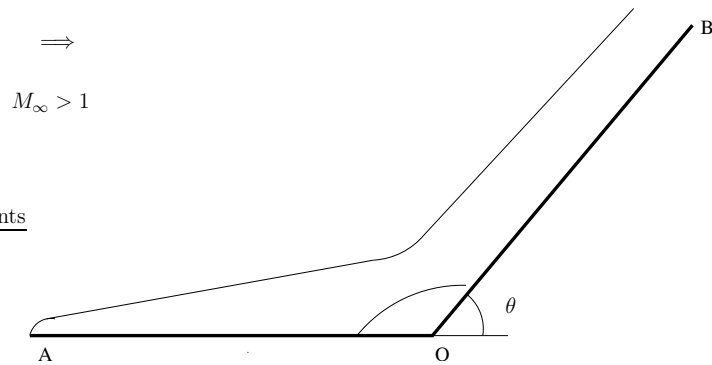
Figure 1.7: Supersonic flow over compression ramp.

The Mach number in the free stream is given by the formula

$$M_\infty = \frac{U_\infty}{a_\infty}, \qquad a_\infty = \sqrt{\gamma \frac{p_\infty}{\rho_\infty}}$$

where a_∞ is the speed of sound and γ is the specific heats ratio. We shall assume that the oncoming flow is supersonic, i.e. M_∞ is an order one quantity greater than unity. We shall further assume that the compression ramp angle is small and

$$\theta = Re^{-1/4}\theta_0,$$

where θ_0 is an order one quantity, and that the Reynolds number

$$Re = \frac{\rho_\infty U_\infty L}{\mu_\infty}$$

is large.
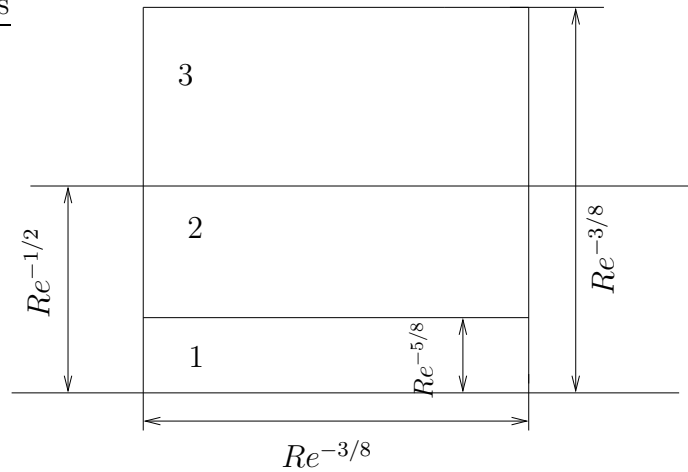
Figure 1.8: Triple deck structure

Detailed study of the interaction process for the corner flow was given by Stewartson (1974) and Neiland (1971b) based on the asymptotic analysis of Navier-Stokes equations at high Reynolds number. It was established that the interaction region has a three tiered structure that occurs in the vicinity of the separation point. This so-called triple deck structure is shown in the Figure 1.8. The streamwise extent of the interaction region is of order $O(Re^{-3/8})$ and is composed of

- a near-wall viscous sublayer of thickness $O(Re^{-5/8})$ (region 1 in Figure 1.8);

- a middle layer of thickness $O(Re^{-1/2})$, corresponding to the upstream boundary layer (region 2 in Figure 1.8);

- an upper layer of thickness $O(Re^{-3/8})$, occupying the portion of the external flow above the boundary layer (region 3 in Figure 1.8).

The interaction process can be described as follows. The velocity in the viscous sublayer is of order $O(Re^{-1/8})$ compared to the free-stream value and the motion is relatively slow. Because of the slow motion, this region is highly sensitive to pressure changes and even a small pressure increase of order $O(Re^{-1/4})$ is sufficient to cause significant deceleration of fluid particles there by resulting in flow reversal which is characteristic of separated flows. This also leads to a thickening of flow filaments

and the streamlines, being displaced from the wall, change their shape. The flow also separates when the scaled ramp angle $\theta_0 = Re^{1/4}\theta$ reaches a critical value.

The middle layer whose thickness is $O(Re^{-1/2})$, represents the continuation of the conventional boundary layer into the interaction region. The velocity is $O(1)$ and due to high speed, the flow is inviscid, but rotational and is less sensitive to pressure changes. Thus the streamlines in region 2 are parallel to each other and carry the deformation produced by the displacement effect of the viscous sublayer.

Finally, the potential flow (inviscid and irrotational) in region 3 serves to 'convert' the perturbations in the streamlines into pressure changes that are then transmitted to the viscous sublayer through the main part of the boundary layer. Due to the passive role of region 2, this type of interaction is called viscous-inviscid interaction.

Let $*$ denote the dimensional form form so that $(x^*, y^*) = L(\hat{x}, \hat{y})$ denote the dimensional distances with corresponding velocity components $(u^*, v^*) = U_\infty(U, V)$ and the pressure $p^* = p_\infty + \rho U_\infty^2 P$.

In the main deck, the solution is sought in the following form

$$U = U_B(Y) + Re^{-\frac{1}{8}} A(X) U_B'(Y) + \ldots, V = -Re^{-\frac{1}{8}} A'(X) U_B(Y) + \ldots, P = Re^{-\frac{1}{4}} P(X) + \ldots$$
$$(1.2)$$

where $X = Re^{\frac{1}{8}}\hat{x}$, $Y = Re^{\frac{1}{2}}\hat{y}$. The solution in the potential flow region yields the result $P(X) = -\beta A'(X)$ where $\beta = \sqrt{M_\infty^2 - 1}$.

The viscous sublayer i.e region 1 has a thickness of $Re^{-\frac{5}{8}}$, where $\bar{y} = Re^{\frac{1}{8}} = Re^{\frac{5}{8}}\hat{y}$. Asymptotic solution of the Navier-Stokes equations in the viscous sublayer (region 1 in Figure 1.8) can be written in the form obtained by Stewartson 1970; Neiland 1971b.

$$U = Re^{-\frac{1}{8}}\hat{u}(X, \bar{y}), V = Re^{-\frac{3}{8}}\bar{v}(X, \bar{y}), P = Re^{-\frac{1}{4}}\hat{p}(X). \qquad (1.3)$$

.Then the boundary-layer equations can be given by which directly shows the forcing, namely

$$\hat{u} = \bar{v} = 0 \quad \text{at} \quad \bar{y} = \hat{f}(X), \qquad (1.4)$$

$$\hat{u} \sim \lambda(\bar{y} + \hat{A}(X)) \quad \text{as} \quad \bar{y} \to \infty. \tag{1.5}$$

where $\lambda = U'_B(0)$, where the wall deformation is given by $y^* = f^*$, where $f^* = LRe^{-\frac{5}{8}}\hat{f}(X)$. Introducing Prandtl transformation

$$\hat{v} = \bar{v} - \hat{f}_X\hat{u}, \quad \tilde{y} = \bar{y} - \hat{f}(X)$$

which gives

$$\hat{u} = \bar{v} = 0 \quad \text{at} \quad \tilde{y} = 0, \tag{1.6}$$

$$\hat{u} \sim \lambda(\tilde{y} + \hat{A}(X) + f(X)) \quad \text{as} \quad \tilde{y} \to \infty. \tag{1.7}$$

.

Finally we can give the scalings as

$$\hat{x} = LRe^{-3/8}\frac{\mu_0^{-1/4}\rho_0^{-1/2}}{\lambda^{5/4}\beta^{3/4}}x, \qquad \hat{y} = LRe^{-5/8}\frac{\mu_0^{1/4}\rho_0^{-1/2}}{\lambda^{3/4}\beta^{1/4}}(y + f(x))$$

$$\hat{u} = U_\infty Re^{-1/8}\frac{\mu_0^{1/4}\rho_0^{-1/2}}{\lambda^{-1/4}\beta^{1/4}}u, \qquad \hat{v} = U_\infty Re^{-3/8}\frac{\mu_0^{3/4}\rho_0^{-1/2}}{\lambda^{-3/4}\beta^{-1/4}}\left(v + u\frac{\partial f}{\partial x}\right)$$

$$\hat{p} = p_\infty + \rho_\infty U_\infty^2 Re^{-1/4}\frac{\mu_0^{1/2}\rho_0^{-1/2}}{\lambda^{-1/2}\beta^{1/2}}p, \qquad \tau_w^* = \mu_\infty\frac{U_\infty}{L}Re^{\frac{1}{2}}\lambda\tau(x). \tag{1.8}$$

which will eliminate the order one parameters and replaces the above conditions by

$$u = v = 0 \quad \text{at} \quad y = 0, \tag{1.9}$$

$$u \sim y + A(X) + f(X) \quad \text{as} \quad y \to \infty. \tag{1.10}$$

where $\mu_0 = \frac{\mu^*}{\mu_\infty}|_{y=0}$, $\rho_0 = \frac{\rho^*}{\rho_\infty}|_{y=0}$ and $\lambda = U'_B(0)$ are suitably non-dimensionalised viscosity, density and skin friction on the wall directly ahead of the triple-deck region, and the constant β being defined as $\beta = \sqrt{M_\infty^2 - 1}$. The transformations used in (1.8) can be used in rescaling of the variables characteristic in the method of matched asymptotic expansions. They also allow the interaction problem to be rewritten in a similar form involving only one controlling parameter

$$\alpha = \frac{\theta_0}{\mu_0^{1/2}\lambda^{1/2}\beta^{1/2}}$$

using an affine transformation. Finally the transformations also involve Prandtl's transposition, which effectively introduces a new curvilinear coordinate system with x measured along the body contour and y in the normal direction. The body contour is defined in these variables by a function $f(x)$ which for the compression ramp can be written as

$$f(x) = \alpha H(x). \tag{1.11}$$

Substituting (1.8) into the Navier-Stokes equations and allowing $Re \to \infty$ results in the boundary layer equations

$$u\frac{\partial u}{\partial x} + v\frac{\partial u}{\partial y} = -\frac{dp}{dx} + \frac{\partial^2 u}{\partial y^2}, \qquad \frac{\partial u}{\partial x} + \frac{\partial v}{\partial y} = 0. \tag{1.12}$$

These equations have to be solved using the no-slip condition on the body surface

$$u = v = 0 \quad \text{at} \quad y = 0, \tag{1.13}$$

and the matching conditions with the "near wall part" of the velocity profile in the boundary layer upstream of interaction region satisfying

$$u = y \quad \text{at} \quad x \to -\infty \tag{1.14}$$

and in the middle layer (region 2 in the Figure 1.8) satisfying

$$u \to y + A(x) + f(x) + \cdots \quad \text{as} \quad y \to \infty. \tag{1.15}$$

The function $A(x)$ in (1.15) determines the shape of the streamlines in the main part of the boundary layer and is thus called as displacement function. Using (1.15) in the second equation of (1.12) it may be easily deduced that at the outer edge of the viscous sublayer $v/u = -dA/dx$. The slope of the streamlines at the 'bottom' of the upper tier is given by $\vartheta = -dA/dx + df/dx$, since the deformation of the streamlines produced by the viscous sublayer remains unaffected across the middle layer.

The response of the inviscid flow outside the boundary layer to the displacement of the boundary layer can be analysed using the Navier-Stokes equations. This analysis leads to the derivation of the so called 'interaction law' that relates the induced

pressure p to the displacement function A. In the case of supersonic flow it is given by Ackeret's formula

$$p = -\frac{dA}{dx}. \tag{1.16}$$

In order to analyse upstream influence, an additional boundary condition specifying the state of the flow downstream of the interaction region is required. We shall assume that

$$(p, A') \rightarrow (\alpha, -\alpha) \quad \text{as} \quad x \rightarrow +\infty. \tag{1.17}$$

This condition completes the formulation of the interaction problem (1.12)-(1.17) and makes its solution unique.

1.6 Overview

In this thesis we discuss some fundamental fluid dynamics phenomena based on the *triple-deck* theory at high Reynolds number ($Re \rightarrow \infty$). In Chapter 2, we discuss the numerical method used to solve the interactive boundary-layer equations for various interaction laws, for example, supersonic flow over a moving wall, humps and indents, Wall-Jets flow past corners, humps and indents, and liquid layer flows over convex corners, humps and indents. The numerical method has been used in the paper by Korolev *et al.* (2002). In Chapters 3 and 4, we describe in detail the problem formulation and the numerical results. The results obtained are compared with previous results of Merkin & Smith (1982), Merkin (1983) and Gajjar (1987). In Chapter 5, we discuss boundary-layer separation over moving walls. Numerical results are obtained and the criterion for separation over moving walls in supersonic flows is discussed.

Chapter 2

Numerical method

2.1 Introduction

The set of viscous-inviscid interaction equations, were once, quite unconventional. Before the theoretical work of Neiland (1969), Stewartson & Williams (1969), no proper numerical method existed for solving these equations and even the simple incipient separation problems presented difficulties. Many physical situations that lead to an interaction between the boundary layer and the external inviscid flow have the same mathematical formulation as the Prandtl boundary layer equations governing flow in the viscous near-wall region with no slip conditions holding on the body surface. The remaining boundary condition depends on the interaction model being used. If the displacement effect is known, then the surface pressure distribution within the interaction region can be given using the corresponding interaction laws. For example when the external flow is supersonic $(p = -A')$, subsonic $\left(p = \frac{1}{\pi} \int_{-\infty}^{\infty} \frac{A'(\zeta)}{x-\zeta} \right)$, wall jets $(p = -A'')$, liquid layers $(p = -A'' - \sigma A)$ and at the hypersonic limit $(p = \pm A)$. However neither the pressure distribution nor the displacement thickness are known in advance. In order to find the pressure distribution and displacement thickness it is necessary to solve the Prandtl boundary layer equation with the appropriate interaction law. Catherall & Mangler (1966) were the first to provide numerical solutions using the inverse method in the separated regions. Werle & Vatsa (1974) developed a time-relaxation method for supersonic boundary-layer separation. Later Williams

(1975) provided the numerical results for self-induced separation. Subsequent numerical solutions for flows past corners were published by Rizzetta *et al.* (1978) and Ruban (1978).

Many numerical techniques have been developed to solve the interaction problem for example, marching and inverse methods, iteration methods, time relaxation methods, semi-inverse methods, quasi-simultaneous methods, spectral methods, direct methods and Semi-Direct methods. Detailed descriptions of these numerical techniques are given in Chapter 7 of Sychev *et al.* (1998). In this Chapter, a numerical technique using finite differences in the streamwise direction combined with Chebychev collocation in the normal direction is discussed.

2.2   Description of numerical technique

The interactive boundary layer equations are given by

$$\frac{\partial\psi}{\partial y}\frac{\partial^2\psi}{\partial y\partial x} - \frac{\partial\psi}{\partial x}\frac{\partial^2\psi}{\partial y^2} = -\frac{dp}{dx} + \frac{\partial^3\psi}{\partial y^3}, \tag{2.1}$$

subject to

$$\psi = \frac{\partial\psi}{\partial y} = 0 \quad \text{on} \quad y = 0, \tag{2.2}$$

$$\psi \sim \frac{1}{2}\big(y + A(x) + f(x)\big)^2 + p(x) \quad \text{as} \quad y \to \infty, \tag{2.3}$$

together with some local pressure-displacement law

$$p = \mathcal{L}(A). \tag{2.4}$$

where $\mathcal{L}$ is some linear local differential operator. Let us define $\psi_{j,k} = \psi(x_j, y_k)$ where $1 \le j \le M$, $0 \le k \le N$ and the vector function $\underline{\Psi}_j = (\psi_{j,0}, \psi_{j,1}, \ldots, \psi_{j,N})^T$. We shall assume a uniform grid along the x-direction over the finite domain $x_1 \le x \le x_M$ with an uniform grid spacing $\Delta x = x_j - x_{j-1}$ is used. In the y-direction Chebychev collocation is used, using function values at the collocation points. The finite domain $0 < y < \infty$ is linearly mapped into $-1 < z < 1$, so that $y_k = y(z_k) = \frac{1}{2}y_\infty(1 + z_k)$, where $z_k = -\cos(k\pi/N)$ and at each x-gridpoint the corresponding

Chebychev collocation equations satisfying the interactive boundary layer equations and boundary conditions are solved. The derivative of $\psi_{j,k}$ in the y-direction is given by

$$\frac{\partial^n \psi_{j,k}}{\partial y^n}\left(x_j, y(z_k)\right) = \sum_{s=0}^{N} D^n_{k,s} \psi_{j,s} \quad \Rightarrow \quad \frac{\partial^n}{\partial y^n}\underline{\Psi}_j = \mathbf{D}^n \underline{\Psi}_j$$

where $D_{k,s}$ are the elements of the Chebychev differentiation matrix $\mathbf{D}$. Thus in matrix form the derivative values may be computed as the matrix vector product

$$\begin{pmatrix} \frac{\partial \psi_{j,0}}{\partial y} \\ \frac{\partial \psi_{j,1}}{\partial y} \\ \vdots \\ \frac{\partial \psi_{j,N}}{\partial y} \end{pmatrix} = \mathbf{D} \begin{pmatrix} \psi_{j,0} \\ \psi_{j,1} \\ \vdots \\ \psi_{j,N} \end{pmatrix}, \tag{2.5}$$

the second and third derivatives are as,

$$\begin{pmatrix} \frac{\partial^2 \psi_{j,0}}{\partial^2 y} \\ \frac{\partial^2 \psi_{j,1}}{\partial^2 y} \\ \vdots \\ \frac{\partial^2 \psi_{j,N}}{\partial^2 y} \end{pmatrix} = \mathbf{D}^{(2)} \begin{pmatrix} \psi_{j,0} \\ \psi_{j,1} \\ \vdots \\ \psi_{j,N} \end{pmatrix} \tag{2.6}$$

and

$$\begin{pmatrix} \frac{\partial^3 \psi_{j,0}}{\partial^3 y} \\ \frac{\partial^3 \psi_{j,1}}{\partial^3 y} \\ \vdots \\ \frac{\partial^3 \psi_{j,N}}{\partial^3 y} \end{pmatrix} = \mathbf{D}^{(3)} \begin{pmatrix} \psi_{j,0} \\ \psi_{j,1} \\ \vdots \\ \psi_{j,N} \end{pmatrix} \tag{2.7}$$

The elements of the derivative matrix for the first derivative are given by $D_{k,s} = D_N(k,s)$ where

$$D_N(k,s) = \frac{c_s(-1)^{k+s}}{c_k(z_k - z_s)}; \quad 0 \le s, k \le N, \quad s \ne k,$$

$$D_N(k,k) = \frac{z_s}{2(1 - z_k^2)}; \quad 1 \le s \le N - 1,$$

$$D_N(0,0) = -D_N(N,N) = \frac{2N^2 + 1}{6},$$

$c_0 = c_N = 2$ $c_k = 1$ when $1 \le k \le N - 1$. The elements of the second and third derivative differentiation matrices are given in Canuto *et al.* (1988). A Matlab

code for generating higher-order derivatives of the Chebychev differentiation matrix is given in the book by Trefethen (2000).

Taking either a three-point second-order backward difference operator or a three-point second-order forward difference for $\frac{\partial u}{\partial x}$

$$\frac{\partial^2 \psi}{\partial y \partial x}(x_j, y_k) = \frac{e_{j,k}}{2\Delta x}\left[(D\psi)_{j-2,k} - 4(D\psi)_{j-1,k} + 3(D\psi)_{j,k}\right]$$
$$-\frac{(1 - e_{j,k})}{2\Delta x}\left[(D\psi)_{j+2,k} - 4(D\psi)_{j+1,k} + 3(D\psi)_{j,k}\right]$$

where $e_{j,k}$ is a switching function defined by

$$e_{j,k} = \begin{cases} 1 & \text{if } D\psi_{j,k} > \epsilon \\ \frac{1}{2\epsilon}(\epsilon + D\psi_{j,k}) & \text{if } -\epsilon < D\psi_{j,k} < \epsilon \\ 0 & \text{if } (D\psi_{j,k} < -\epsilon) \end{cases}$$

where typically $\epsilon = 10^{-2}$ is used. Thus $(\psi_{yx})_{j,k}$ may be expressed as

$$\frac{\partial^2 \psi}{\partial y \partial x}(x_j, y_k) = \alpha_{j,k}(D\psi)_{j-2,k} + \beta_{j,k}(D\psi)_{j-1,k} + \gamma_{j,k}(D\psi)_{j,k} + \delta_{j,k}(D\psi)_{j+1,k} + \sigma_{j,k}(D\psi)_{j+2,k}$$

where

$$\alpha_{j,k} = \frac{e_{j,k}}{2\Delta x}, \qquad\qquad \beta_{j,k} = -\frac{2e_{j,k}}{\Delta x},$$
$$\gamma_{j,k} = e_{j,k}\frac{3}{2\Delta x} - (1 - e_{j,k})\frac{3}{2\Delta x}$$
$$\delta_{j,k} = (1 - e_{j,k})\frac{2}{\Delta x}, \qquad\qquad \sigma_{j,k} = -(1 - e_{j,k})\frac{1}{2\Delta x}.$$

We employ a three-point second-order backward difference for v in general and a three-point second-order central difference in regions of secondary separation, then

$$\frac{\partial \psi}{\partial x}(x_j, y_k) = \frac{1}{2\Delta x}\left[\psi_{j-2,k} - 4\psi_{j-1,k} + 3\psi_{j,k}\right]$$

for $j < j_b$ and $j > j_b$, whereas for $j_b \leq j_b \leq j_e$

$$\frac{\partial \psi}{\partial x}(x_j, y_k) = \frac{1}{2\Delta x}\left[\psi_{j+1,k} - \psi_{j-1,k}\right]$$

That is

$$\frac{\partial \psi}{\partial x}(x_j, y_k) = \bar{\alpha}_{j,k}\psi_{j-2,k} + \bar{\beta}_{j,k}\psi_{j-1,k} + \bar{\gamma}_{j,k}\psi_{j,k} + \bar{\delta}_{j,k}\psi_{j+1,k} + \bar{\sigma}_{j,k}\psi_{j+2,k}$$

where

$$\bar{\alpha}_{j,k} = \frac{1}{2\Delta x}, \quad \bar{\beta}_{j,k} = -\frac{2}{\Delta x},$$
$$\bar{\gamma}_{j,k} = \frac{3}{2\Delta x}, \quad \bar{\delta}_{j,k} = \bar{\sigma}_{j,k} = 0$$

for $j < j_b$ and $j > j_b$, whereas for $j_b \leq j_b \leq j_e$

$$\bar{\alpha}_{j,k} = \bar{\sigma}_{j,k} = 0, \quad \bar{\beta}_{j,k} = -\frac{1}{2\Delta x}$$

$$\bar{\gamma}_{j,k} = 0, \qquad \bar{\delta}_{j,k} = \frac{1}{2\Delta x}$$

The values $j = j_s$ and $j = j_e$, denote the x-locations of the start and end of the region of secondary separation. The pressure-displacement relation i.e, the interaction law $\frac{dp}{dx}$ that when discretized can be written in the following form

$$\left(\frac{dp}{dx}\right)_j = \varepsilon_1 A_{j-2} + \varepsilon_2 A_{j-1} + \varepsilon_3 A_j + \varepsilon_4 A_{j+1} + \varepsilon_5 A_{j+2}$$

We give a few examples for different pressure-displacement laws

$$A'(x_j) = \frac{1}{2\Delta x}(A_{j+1} - A_{j-1}) + O(\Delta x^2 A'''(x_j)) \tag{2.8}$$

$$A''(x_j) = \frac{1}{\Delta x^2}\left(A_{j+1} - 2A_j + A_{j-1}\right) + O(\Delta x^2 A^{iv}(x_j)) \tag{2.9}$$

$$A'''(x_j) = \frac{1}{2\Delta X^3}(A_{j+2} - 2A_{j+1} + A_{j-1} - A_{j-2}) + O(\Delta x^2 A^{iv}(x_j)) \tag{2.10}$$

For computational convenience we have used the following discretization in Chapter 3

$$A'''(x_j) = \frac{1}{\Delta x^3}\left(A_{j+1} - 3A_j + 3A_{j-1} - A_{j-2}\right) + O(\Delta x A^{iv}(x_j)). \tag{2.11}$$

Thus we have the equation (2.1)

$$(\mathbf{D}\psi)_{j,k}\left[\alpha_{j,k}(D\psi)_{j-2,k} + \beta_{j,k}(D\psi)_{j-1,k} + \gamma_{j,k}(D\psi)_{j,k} + \delta_{j,k}(D\psi)_{j+1,k} + \sigma_{j,k}(D\psi)_{j+2,k}\right]$$

$$-(\mathbf{D}^2\psi)_{j,k}\left[\bar{\alpha}_{j,k}\psi_{j-2,k} + \bar{\beta}_{j,k}\psi_{j-1,k} + \bar{\gamma}_{j,k}\psi_{j,k} + \bar{\delta}_{j,k}\psi_{j+1,k} + \bar{\sigma}_{j,k}\psi_{j+2,k}\right]$$

$$= -\left[\varepsilon_1 A_{j-1} + \varepsilon_2 A_{j-1} + \varepsilon_3 A_j + \varepsilon_4 A_{j+1} + \varepsilon_5 A_{j+2}\right] + (\mathbf{D}^3\psi)_{j,k}.$$

The above equation was enforced at the collocation points z_k for $1 < k < N - 1$. Introducing $\bar{A}_j = A(x_j) - \alpha f_0(x_j)$, the following boundary conditions were also imposed

$$\psi_{j,0} = 0, \quad (\mathbf{D}\psi)_{j,0} = 0, \quad (\mathbf{D}\psi)_{j,N} = y_\infty + A(x_j) = y_\infty + \bar{A}_j, \quad (\mathbf{D}^2\psi)_{j,N} = 1.$$

The above discretisation gives $(N + 2)$ equations for the $(N + 2)$ unknowns $\psi_{j,k}$ and A_j at each x grid point for $1 < j \leq M$. For the first two locations $j = 0, 1$ the

unperturbed solution was used, and in all computations the value of x_j for $j = M$ corresponds to being in the reattachment point region.

The nonlinear system of equations was solved by first introducing a Newton-Raphson linearisation with $\psi_{j,k} = \hat{\psi}_{j,k} + \Delta\psi_{j,k}, \quad A_j = \hat{A}_j + \Delta A_j$, and then solving a linear system for the corrections $\Delta\psi_{j,k}, \quad \Delta A_j$. The linear equations for the corrections $\Delta\psi_{j,k}$ and ΔA_j are

$$
\left[(\mathbf{D}\hat{\psi})_{j,k}\alpha_{j,k} \sum_{s=1}^{N} \mathbf{D}_{k,s}\Delta\psi_{j-2,s} - (\mathbf{D}^2\hat{\psi})_{j,k}\bar{\alpha}_{j,k}\Delta\psi_{j-2,k} \right]
$$

$$
+ \left[(\mathbf{D}\hat{\psi})_{j,k}\beta_{j,k} \sum_{s=1}^{N} \mathbf{D}_{k,s}\Delta\psi_{j-1,s} - (\mathbf{D}^2\hat{\psi})_{j,k}\bar{\beta}_{j,k}\Delta\psi_{j-1,k} \right]
$$

$$
+ \left[(\mathbf{D}\hat{\psi})_{j,k}\delta_{j,k} \sum_{s=1}^{N} \mathbf{D}_{k,s}\Delta\psi_{j,s} - (\mathbf{D}^2\hat{\psi})_{j,k}\bar{\delta}_{j,k}\Delta\psi_{j-2,k} \right]
$$

$$
+ \left[\alpha_{j,k}(D\hat{\psi})_{j-2,k} + \beta_{j,k}(D\hat{\psi})_{j-1,k} \right.
$$

$$
\left. + \gamma_{j,k}(D\hat{\psi})_{j,k} + \delta_{j,k}(D\hat{\psi})_{j+1,k} + \sigma_{j,k}(D\hat{\psi})_{j+2,k} \right] \sum_{s=1}^{N} \mathbf{D}_{k,s}\Delta\psi_{j,s}
$$

$$
- \left[\bar{\alpha}_{j,k}\hat{\psi}_{j-2,k} + \bar{\beta}_{j,k}\hat{\psi}_{j-1,k} + \bar{\gamma}_{j,k}\hat{\psi}_{j,k} + \bar{\delta}_{j,k}\hat{\psi}_{j+1,k} + \bar{\sigma}_{j,k}\hat{\psi}_{j+2,k} \right] \sum_{s=1}^{N} \mathbf{D}_{k,s}^2\Delta\psi_{j,s}
$$

$$
+ \left[(\mathbf{D}\hat{\psi})_{j,k}\delta_{j,k} \sum_{s=1}^{N} \mathbf{D}_{k,s}\Delta\psi_{j+1,s} - (\mathbf{D}^2\hat{\psi})_{j,k}\bar{\delta}_{j,k}\Delta\psi_{j+1,k} \right]
$$

$$
+ \left[(\mathbf{D}\hat{\psi})_{j,k}\sigma_{j,k} \sum_{s=1}^{N} \mathbf{D}_{k,s}\Delta\psi_{j+2,s} - (\mathbf{D}^2\hat{\psi})_{j,k}\bar{\sigma}_{j,k}\Delta\psi_{j+2,k} \right]
$$

$$
+ \left[\varepsilon_1\Delta A_{j-2} + \varepsilon_2\Delta A_{j-1} + \varepsilon_3\Delta A_j + \varepsilon_4\Delta A_{j+1} + \varepsilon_5\Delta A_{j+2} \right] - (\mathbf{D}^3\Delta\psi)_{j,k}
$$

$$
= - \left[\varepsilon_1\hat{A}_{j-2} + \varepsilon_2\hat{A}_{j-1} + \varepsilon_3\hat{A}_j + \varepsilon_4\hat{A}_{j+1} + \varepsilon_5\hat{A}_{j+2} \right] + (\mathbf{D}^3\Delta\psi)_{j,k}
$$

$$
- (\mathbf{D}\hat{\psi})_{j,k} \left[\alpha_{j,k}(D\hat{\psi})_{j-2,k} + \beta_{j,k}(D\hat{\psi})_{j-1,k} \right.
$$

$$
\left. + \gamma_{j,k}(D\hat{\psi})_{j,k} + \delta_{j,k}(D\hat{\psi})_{j+1,k} + \sigma_{j,k}(D\hat{\psi})_{j+2,k} \right]
$$

$$
+ (\mathbf{D}^2\hat{\psi})_{j,k} \left[\bar{\alpha}_{j,k}\hat{\psi}_{j-2,k} + \bar{\beta}_{j,k}\hat{\psi}_{j-1,k} + \bar{\gamma}_{j,k}\hat{\psi}_{j,k} + \bar{\delta}_{j,k}\hat{\psi}_{j+1,k} + \bar{\sigma}_{j,k}\hat{\psi}_{j+2,k} \right]
$$

which can be written in the form

$$
\sum_{s=0}^{N} F_{k,s}^{(j)}\Delta\psi_{j-2,s} + A_{k,s}^{(j)}\Delta\psi_{j-1,s} + B_{k,s}^{(j)}\Delta\psi_{j,s} + C_{k,s}^{(j)}\Delta\psi_{j+1,s} + E_{k,s}^{(j)}\Delta\psi_{j+2,s}
$$

$$
\left[\varepsilon_1\Delta A_{j-2} + \varepsilon_2\Delta A_{j-1} + \varepsilon_3\Delta A_j + \varepsilon_4\Delta A_{j+1} + \varepsilon_5\Delta A_{j+2} \right] = \hat{R}_k^{(j)}.
$$

In a matrix form

$$\mathbf{F}^{(j)}\Delta\underline{\Psi}_{j-2} + \mathbf{A}^{(j)}\Delta\underline{\Psi}_{j-1} + \mathbf{B}^{(j)}\Delta\underline{\Psi}_j + \mathbf{C}^{(j)}\Delta\underline{\Psi}_{j+1} + \mathbf{E}^{(j)}\Delta\underline{\Psi}_{j+2}$$

$$+\left[\varepsilon_1\Delta A_{j-2} + \varepsilon_2\Delta A_{j-1} + \varepsilon_3\Delta A_j + \varepsilon_4\Delta A_{j+1} + \varepsilon_5\Delta A_{j+2}\right]\underline{I} = \underline{R}^{(j)}$$

where $\underline{I}$ is the vector $\underline{I} = [1, 1, \cdots 1]^T$, $\Delta\underline{\Psi} = [\Delta\psi_{j,k}, \Delta A_j]$. Now suppose we take that

$$\underline{\gamma}_j = \left[\psi_{j,0}, \psi_{j,1}, \ldots, \psi_{j,N}, A_j\right]^T$$

The hatted quantities represent an approximate solution. The form of the above equations leads to a block pentadiagonal system of equations that can be written as

$$\mathbf{F_p}\underline{\gamma}_{j-2} + \mathbf{A_p}\underline{\gamma}_{j-1} + \mathbf{B_p}\underline{\gamma}_j + \mathbf{C_p}\underline{\gamma}_{j+1} + \mathbf{E_p}\underline{\gamma}_{j+2} = \underline{\mathbf{R}}_{j,k} \qquad (2.12)$$

where, for example

$$\mathbf{F_p^{(j)}} = \begin{bmatrix} F_{1,1} & F_{1,2} & \cdots & F_{1,N} & \varepsilon_1 \\ F_{2,1} & F_{2,2} & \cdots & F_{2,N} & \varepsilon_1 \\ \vdots & \vdots & \vdots & \vdots & \vdots \\ F_{N,1} & F_{N,2} & \cdots & F_{N,N} & \varepsilon_1 \end{bmatrix}$$

and

$$\mathbf{E_p^{(j)}} = \begin{bmatrix} E_{1,1} & E_{1,2} & \cdots & E_{1,N} & \varepsilon_5 \\ E_{2,1} & E_{2,2} & \cdots & E_{2,N} & \varepsilon_5 \\ \vdots & \vdots & \vdots & \vdots & \vdots \\ E_{N,1} & E_{N,2} & \cdots & E_{N,N} & \varepsilon_5 \end{bmatrix}$$

and is solved using a direct method developed by Gajjar, see also Korolev $et\ al.$ (2002) which basically involves Gaussian elimination. Typically 8-10 Newton iterations are sufficient to obtain the complete solution to an accuracy of 10^{-6}. We used this numerical technique to study

- Jet-like boundary layers encountering corners, humps and indentations,

- Liquid layer flows over convex corners, humps and indentations, and

- Supersonic flows past corners, humps and indentations.

These problems along with the numerical results and the structure of the matrices are provided in subsequent chapters.

Chapter 3

Double deck structure revisited

3.1 Introduction

One of the most important applications of viscous-inviscid interaction theory is the analysis of the flow separation observed in near-wall jets and thin films. The need to investigate the structure of a jet flow near its point of separation from a wall arises in many diverse situations. For example in rotating fluids, flow in pipes/channels, oscillatory motions, and free convection boundary-layers, as well as wall jets near corners and other wall discontinuity conditions. The interaction might be as a result of self-induced separation, a corner point or a trailing edge.

The first attempt to study this sort of behaviour was made by Smith & Duck (1977). They showed that jet flow can develop free interactions which has a double-deck structure in which the unknown induced pressure is due to the centrifugal forces acting across the jet. They also showed that during interaction the fluid near the wall forms a viscous sublayer, driven along by the induced local pressure gradient, whereas the majority of the boundary layer reacts in an inviscid displaced fashion. Upstream of the separation the sublayer pressure increases slightly causing a decrease in the skin friction, and the sublayer expands. The associated movement of fluid in the inviscid region then induces a pressure drop across the jet but, because the pressure at the edge of the jet does not change, the transverse pressure gradient reinforces the pressure increase of the wall. They concluded that separation, followed by a sizeable

eddy of reversed flow, takes place over a streamwise length scale of $O(Re^{-\frac{3}{7}})$ distance along the wall.

Later Merkin & Smith (1982) applied this theory to free convection boundary layers near the corners of a body contour and at the trailing edge of a flat plate. They found that the corner problem has some similarities with supersonic flow near a convex corner, as discussed by Stewartson (1974), though the pressure displacement relation is different. They concluded that, for concave corners with sufficiently large angles there will be a reversed-flow region centred on the corner, and that for the convex corners the flow will separate downstream of the corner.

In this chapter we shall consider the behaviour of a jet-like boundary layer when it encounters a small hump or indentation. The problem studied is identical to that considered by Merkin (1983). The humps and indentations considered are of the form $\hat{y} = Re^{-\frac{9}{14}}\hat{h}\exp(-\hat{k}^2 X^2)$, where $\hat{x} = Re^{-\frac{3}{8}}X$. Here $\hat{h}$ and $\hat{k}$ are constants corresponding to the height and spread of the hump or indentation respectively in the lower deck scalings. For small transverse humps and indentations i.e. $|h| \ll 1$ and $k = O(1)$, Merkin (1983) obtained both analytical solutions for small humps i.e $|h| \ll 1$, and numerical results for moderate humps and indentations, with $h = O(1)$. He concluded that for a sufficiently large value of h separation always occurs, with the reversed flow eddy situated on the lee side of the humps ($h > 0$) and located symmetrically about the centre of any indentation ($x = 0$). He also concluded that for larger values, a Goldstein-Stewartson type of singularity appears near the separation point for long humps ($k \ll 1$). Merkin also observed that by increasing k, separation was observed at smaller values of $|h|$.

Recently Gajjar (1987) has studied liquid layer flow over a convex corner at high Reynolds number ($Re \to \infty$). Gajjar also required a double-deck structure, similar to that for the wall-jet case, to describe the flow interaction. Gajjar (1987) found that the computed results and the fluid dynamics functions, including skin friction and pressure far downstream did not return to their undisturbed values far downstream ($x \to \infty$). Instead the viscous wall-layer continued to get thinner with the fluid moving much faster. The "interaction law" is a combination of a special case of that

occurs in the hypersonic flow theory of Brown *et al.* (1975) and the "jet law" of Smith & Duck (1977). In this chapter, we also investigate liquid layer flows over humps and indents. This double-deck structure follows closely the usual triple-deck ideas for local boundary-layer interactions.

3.2 Wall-Jet flow past concave and convex corners

3.2.1 Problem formulation

Consider a jet-like boundary-layer, or wall-jet, flowing past a corner. The corner is formed by means of two flat plates AO and OB as shown in the Figure 3.1 where OB makes a small angle $\theta \propto Re^{-\frac{3}{14}}\alpha$ with O$\hat{x}$, and $\alpha = O(1)$.
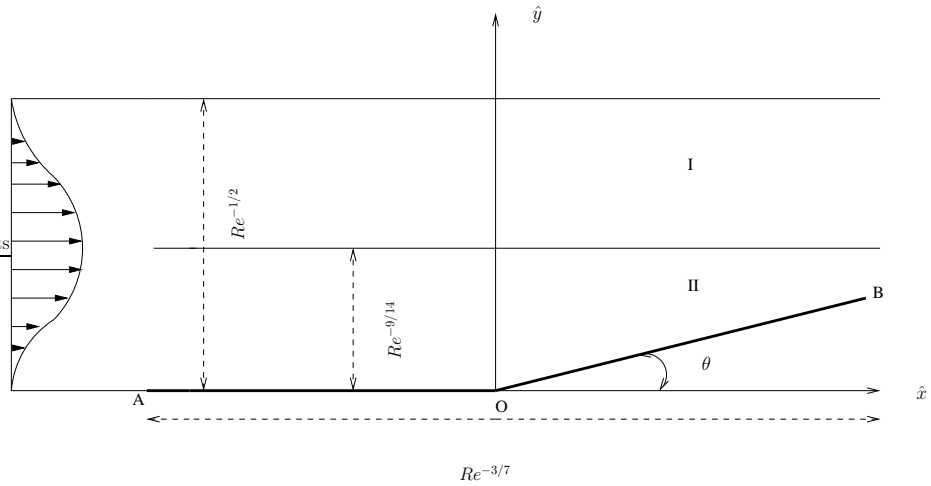
Figure 3.1: Double deck structure.

The flow is assumed to be steady, laminar, incompressible and two-dimensional. The interaction has a double-deck structure, Region I and Region II, as shown in the figure. The streamwise extent is estimated to be about $O(Re^{-\frac{3}{7}})$ and has a thickness of $O(Re^{-\frac{1}{2}})$. The presence of the jet-like profile upstream implies

$$U \to U_B(Y) + O(Re^{-\frac{3}{7}}), \quad \text{as} \quad X \to -\infty, \quad V \to O(Re^{-\frac{1}{2}}), \quad P \to O(Re^{-1}),$$

with $X = Re^{\frac{3}{7}}\hat{x}$, and $Y = Re^{\frac{1}{2}}\hat{y}$ defining the boundary layer coordinate. Here $U_B(Y)$ is the oncoming boundary-layer profile with the properties $U_B(Y) \sim \lambda Y + O(Y^2)$ as

$Y \to 0$ and $U_B(Y) \to 0$ as $Y \to \infty$, where $\lambda = U'_B(0) > 0$. Outside the boundary layer, the upstream velocities are of $O(Re^{-\frac{1}{2}})$ and pressure of $O(Re^{-1})$, so that motion is inviscid and relatively slow.

In region I, $Y = O(1)$, the form of velocities and pressure are given as

$$U \to U_B(Y) + Re^{-\frac{1}{7}}u_1(X,Y), \quad V = Re^{-\frac{3}{14}}v_1(X,Y), \quad P = Re^{-\frac{2}{7}}p_1(X,Y),$$

with relative errors $O(Re^{-\frac{2}{7}})$. The small disturbances are inviscid and the stream-wise pressure gradient is negligible compared to transverse pressure gradient. The solutions are given by

$$u_1 = \hat{A}(X)U'_B(Y), \quad v_1 = -\hat{A}'(X)U_B(Y), \quad \frac{\partial p_1}{\partial Y} = -U_B(Y)\frac{\partial v_1}{\partial X}, \qquad (3.1)$$

where $\hat{A}$ is an unknown function of X, with $\hat{A}(-\infty) = 0$. The viscous sublayer region II has a thickness of $Re^{-\frac{9}{14}}$, where $\bar{y} = Re^{\frac{9}{14}}\hat{y}$. The solutions to the first order are sought in the following form

$$U = Re^{-\frac{1}{7}}\hat{u}(X,\bar{y}), \quad V = Re^{-\frac{5}{14}}\hat{v}(X,\bar{y}), \quad P = Re^{-\frac{2}{7}}\hat{p}(X). \qquad (3.2)$$

Substituting in the Navier-Stokes equations, the continuity and transverse momentum equation are given by

$$\frac{\partial \hat{u}}{\partial X} + \frac{\partial \hat{v}}{\partial \bar{y}} = 0, \quad \hat{u}\frac{\partial \hat{u}}{\partial X} + \hat{v}\frac{\partial \hat{u}}{\partial \bar{y}} = -\frac{\partial \hat{p}}{\partial X} + \frac{\partial^2 \hat{u}}{\partial \bar{y}^2}, \qquad (3.3)$$

with the following boundary conditions

$$\hat{u} = \hat{v} = 0 \quad \text{at} \quad \bar{y} = \hat{f}(X), \quad \hat{u} \sim \lambda\bar{y} + \hat{A}(\hat{x}) \quad \text{as} \quad \bar{y} \to \infty, \qquad (3.4)$$

$$\hat{u} \sim \lambda\bar{y}, \quad \hat{v} \to 0, \quad \hat{p} \to 0 \quad \text{as} \quad X \to -\infty. \qquad (3.5)$$

The above conditions reflect the no-slip condition at the wall, the matching with inviscid region I and the upstream conditions. The relation between $\hat{p}$ and $\hat{A}$ is found by integrating (3.1) to find p_1 and is given by

$$p_1 = \hat{p}(X) + \hat{A}''(X)\int_0^Y U_B^2(Y)dY, \qquad (3.6)$$

the value of $p_1(X,0)$ ensures continuity of pressure between regions I and II. The velocities induced just outside the boundary layer are expected to be of $O(Re^{-\frac{1}{7}})$

since u_1, $v_1 \to 0$ as $Y \to \infty$. From the Bernoulli's equation, the pressure must of $O(Re^{-\frac{2}{7}})$. Therefore we need $p_1(X, \infty)$ to be zero. From (3.6), we have

$$\frac{d^2\hat{A}}{dX^2} = -\gamma \hat{p}(X),$$
(3.7)

where $\gamma^{-1} = \int_0^\infty U_B^2(Y)dY$ is known as a positive constant.

Equations (3.3), (3.4) and (3.7) completes the formulation of the free interaction problem. By means of normalisation and also taking Prandtl transformation, the factors λ, γ are removed from the fundamental problem given by equations (3.3), (3.4), (3.7)

$$(\hat{u}, \hat{v}, \hat{p}, \hat{A}, X, \bar{y}) = \left(\gamma^{-\frac{1}{7}}\lambda^{\frac{3}{7}}u, \gamma^{\frac{1}{7}}\lambda^{\frac{4}{7}}v, \gamma^{-\frac{2}{7}}\lambda^{\frac{6}{7}}p, \gamma^{-\frac{1}{7}}\lambda^{-\frac{4}{7}}A, \gamma^{-\frac{3}{7}}\lambda^{-\frac{5}{7}}x, \gamma^{-\frac{1}{7}}\lambda^{-\frac{4}{7}}y\right).$$

We also need to redefine θ. We know that $\theta = Re^{-\frac{3}{14}}\theta_0$. Scaling out parameters leads to redefining of θ_0 as $\theta_0 = \alpha\lambda^{\frac{1}{7}}\gamma^{\frac{2}{7}}$ where $\lambda = U_B'(0)$. The detailed description is given in paper by Smith & Duck (1977). This leads to boundary-layer equations given by (1.12)-(1.15). An additional boundary condition can be considered as well

$$\frac{\partial^2 \psi}{\partial y^2} = 1 \quad \text{at} \quad y = \infty,$$
(3.8)

and the interaction law

$$p = -\frac{d^2 A}{dx^2}.$$
(3.9)

$$p \to 0, A \sim -\alpha X \quad \text{as} \quad X \to +\infty$$
(3.10)

3.2.2 Numerical results

The pressure-displacement relation is given by equation (3.9). For computational convinience, the $\frac{dp}{dx}$ term is approximated by a four point finite-difference formula in order to incorporate the third-order derivative of $A'''(x_j)$ as in (2.11). The matrix equation has the same form as (2.12). The elements of the matrices are given in Appendix B. We use the same numerical method as discussed in Chapter 2 with an uniform grid . Finite values of $x_{-\infty} = -40$, $x_\infty = 40$ were used in order to truncate the domain along the streamwise direction. A step size of $\Delta x = 0.01$ (i.e. 8001 points) was used in the streamwise direction. It was found from numerical experiments that

64 points were sufficient to resolve the flow features in the y-direction. Numerical calculations for both concave and convex corners have been obtained and the results compared with those of Merkin & Smith (1982). For computational convenience and to avoid special treatment of the corner region, the corner was rounded slightly so that $\frac{d^2 f}{dx^2}$ was a smooth function everywhere. In the present study, the surface was defined by

$$f(x) = \frac{1}{2}\alpha\left[x + \sqrt{x^2 + r^2}\right], \tag{3.11}$$

where α is the scaled angle. Here r is called the rounding parameter, and as $r \to 0$ the surface collapses to the sharp corner. All subsequent results are given for $r = 0.5$.

PSfrag replacements
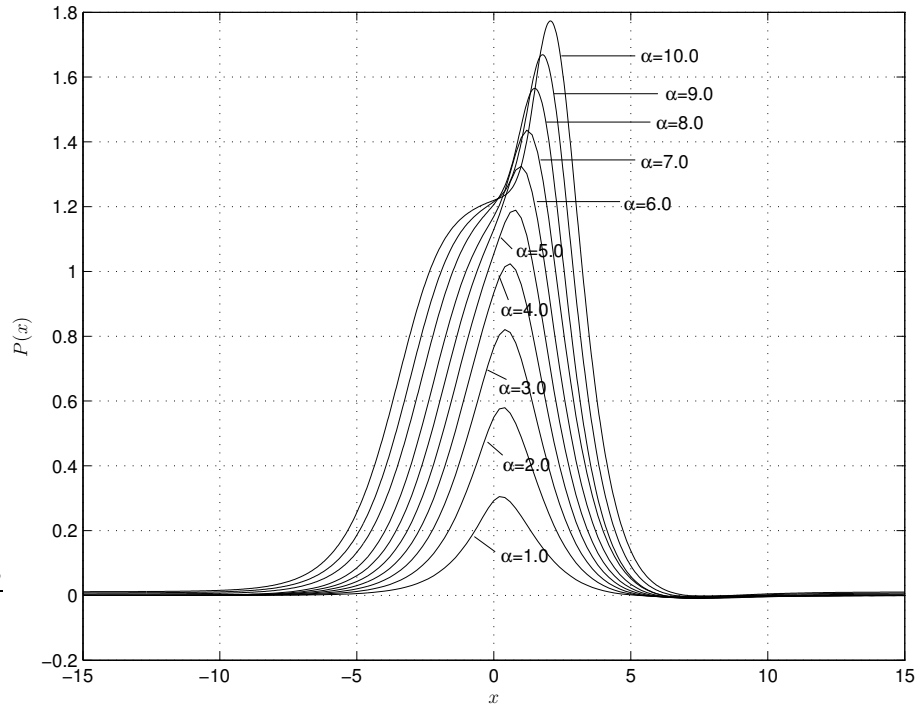
Figure 3.2: Pressure distributions for various angles with concave corners.
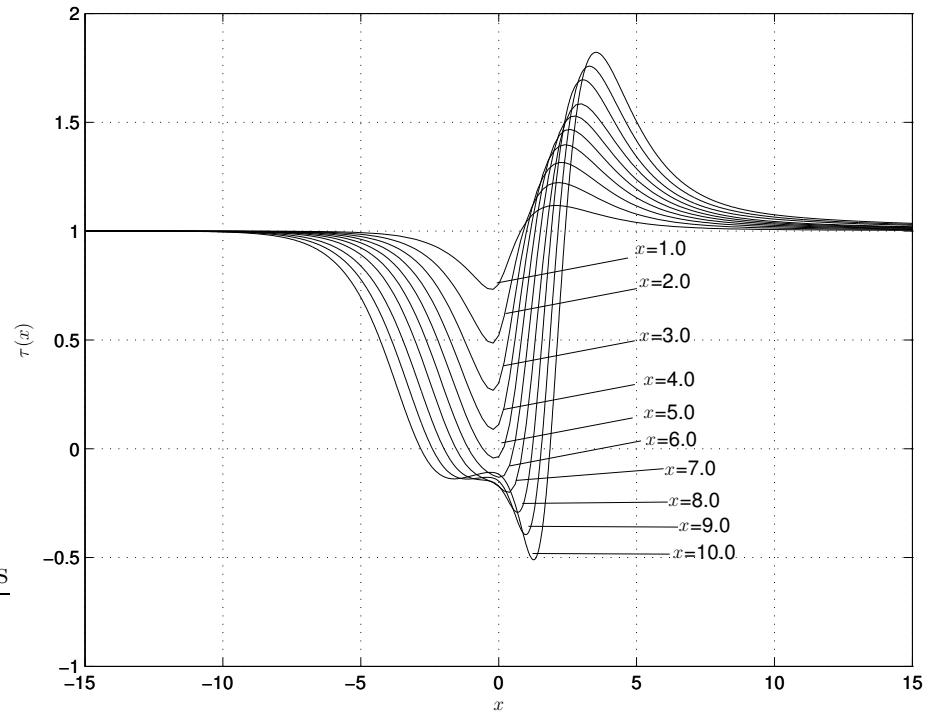
Figure 3.3: Skin friction distributions for various angles with concave corners.
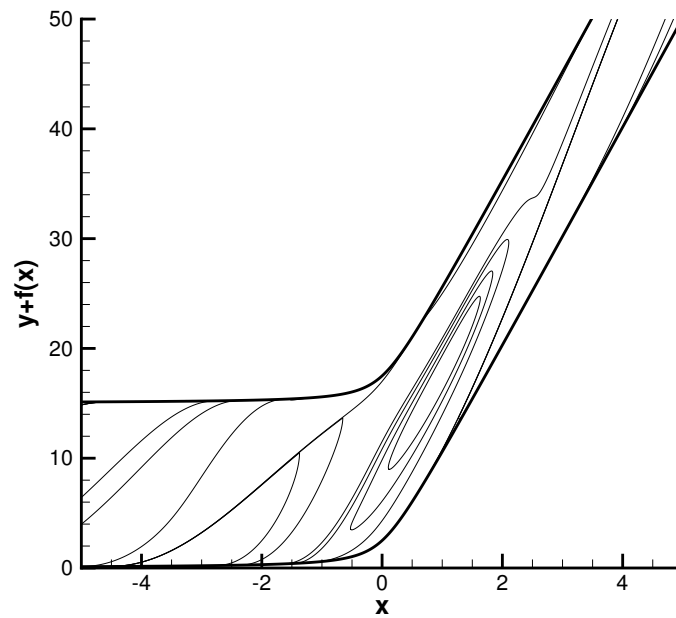
Figure 3.4: Streamline pattern showing reversed flow for $\alpha = 6.0$ for concave corners.

From the numerical solution, we have the following results for the case of concave corners. Far upstream of the corner point the flow is unperturbed with skin friction $\tau = 1$ as required by the boundary condition (3.8) and the pressure satisfying $p = 0$. With increasing α the flow becomes increasingly less attached as the corner is approached with the skin friction falling to a decreasing minimum, τ_{min}, which is located in the vicinity of the corner. The flow is increasingly more attached downstream of the corner, as α increases with the skin friction rising to an increasing maximum, τ_{max}, before falling back to its far-downstream unperturbed level . The skin friction ($\tau > 0$) remains positive for $\alpha < 4.5$, and then the separation region is formed where skin friction ($\tau < 0$) is negative approximately at $\alpha = 4.5$ which is significantly higher than the value, namely $\alpha = 3.5$, obtained by Merkin & Smith (1982). The extent of the separation region, where $\tau < 0$, increases somewhat with increasing α, with position of separation point moving upstream and position of reattachment moving downstream. With increasing α, the pressure rises to a maximum and is located in the vicinity of the corner, before falling back to zero.

For moderate angles, $6.0 \leq \alpha \leq 10.0$, the pressure develops a "plateau", that is the pressure rises to a constant value, whose value seems independent of α. Smith & Duck (1977) observe the value of pressure "plateau" to be 0.6750, whereas Merkin & Smith (1982) observe it to be around 1.6. We see that the value at which the pressure attains a "plateau" is 1.2. After this plateau the pressure rises to a maximum, whose value increases with α. The plateau pressure is associated with a slow reversed flow bubble, where the skin friction has a small, but negative constant value, which also seems to be independent of α. Subsequently the skin friction drops to a minimum value i.e τ_{min} before sharply rising to its maximum value so that reattachment occurs in the vicinity of the pressure maximum. All these results are shown in Figures 3.2, 3.3, 3.4. One can observe fully reversed flow at $\alpha = 6.0$ consisting of fluid rotating slowly in a clockwise direction.
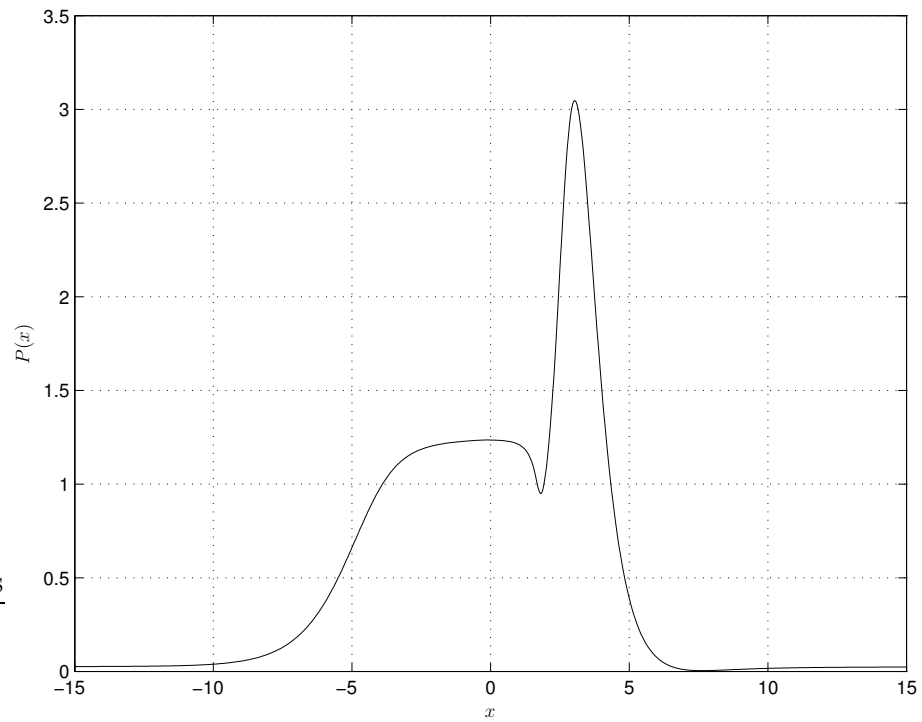
Figure 3.5: Pressure distribution for $\alpha = 14.0$ for concave corners.
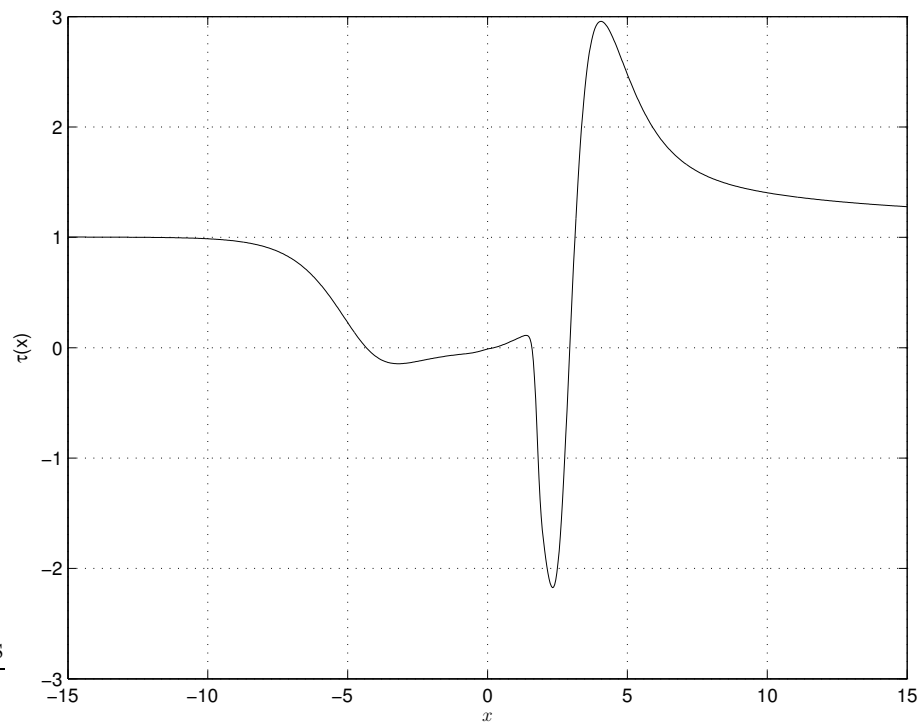
Figure 3.6: Skin friction distribution for $\alpha = 14.0$ for concave corners.

PSfrag replacements
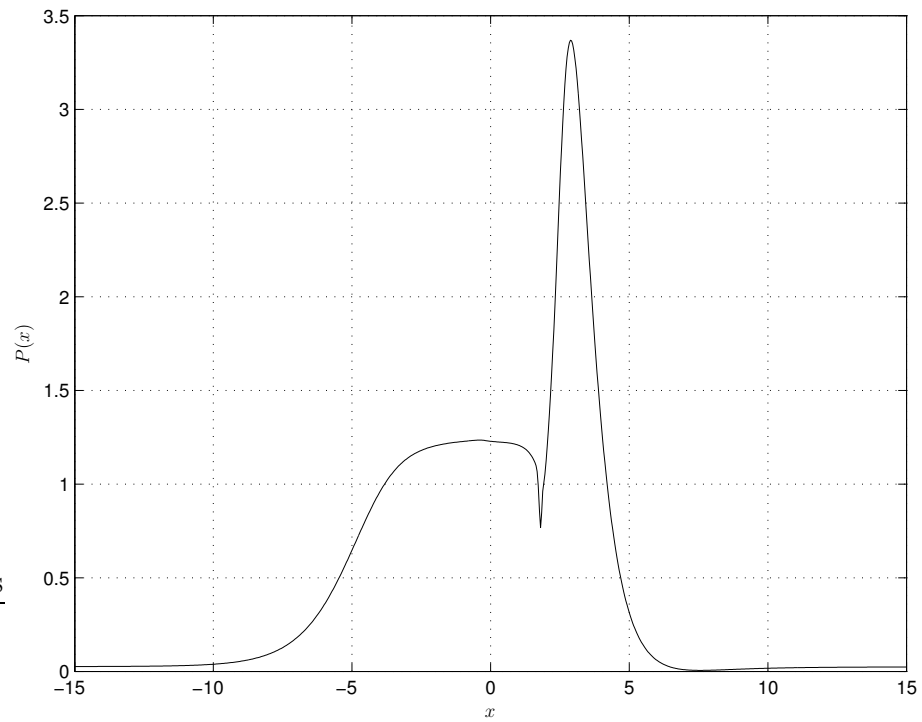
Figure 3.7: Pressure distribution for $\alpha = 15.0$ for concave corners.

PSfrag replacements
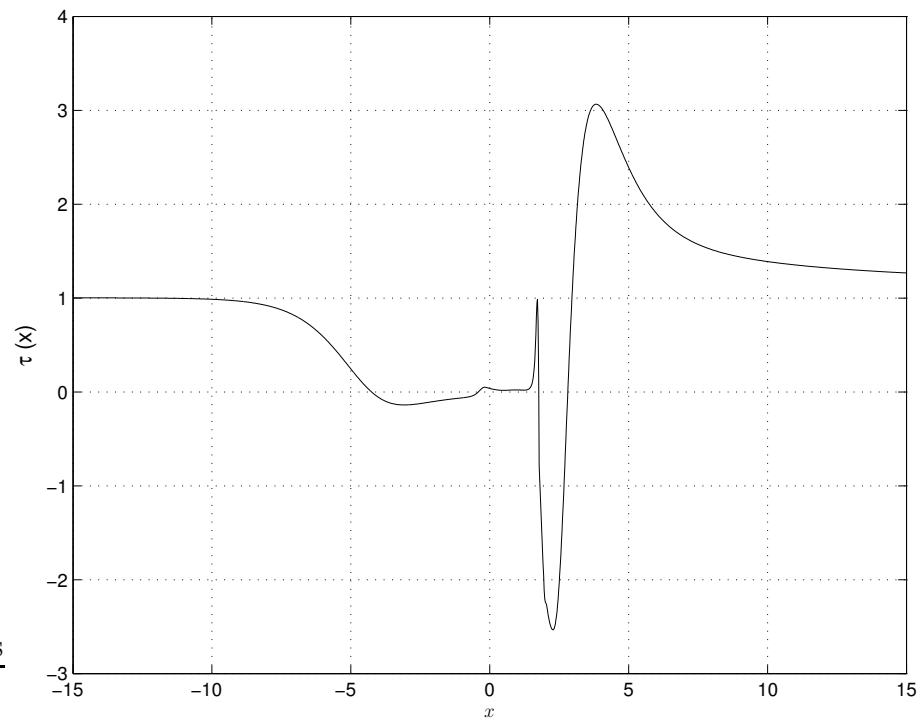
Figure 3.8: Skin friction distribution for $\alpha = 15.0$ concave corners.

For higher angles of α, $10 \leq \alpha \leq 15.0$ new flow features are observed as seen in the results for $\alpha = 14.0$ and $\alpha = 15.0$; see Figures 3.5-3.8. The pressure starts to increase causing flow deceleration in the boundary-layer. The skin friction decreases crossing zero at the separation point, it then reaches a minimum before slowly increasing again. While the skin friction remains negative, the fluid near the wall moves slowly in the opposite direction to the rest of the flow and the pressure distribution develops a "plateau" which can be clearly seen in Figures 3.5 and 3.7. An angle of $\alpha = 14.0$ is sufficient for secondary separation to be seen within the primary separation region, with a small region of positive skin friction, see Figure 3.6. Downstream of the corner the flow returns to its unperturbed state as required by the boundary condition (3.8). The streamline pattern for $\alpha = 15.0$ is shown in Figure 3.9. We can see that the flow separates at $x = -4.25$ and forms the primary separation region. One can observe the formation of a separation bubble within this primary separation region which reattaches at $x = -0.4$ and separates at $x = 1.75$. The primary separation bubble reattaches at $x = 2.8$. In addition we also observe the formation of a large eddy and a small separation bubble within the primary separation region.

We encountered problems with the convergence of the numerical method as the angle was increased, indicating a possibility of singularity. The solutions remain smooth. The lack of convergence is due to the rapid fragmentation of the separation region, with additional eddies forming one inside the another. Our numerical method did not develop any oscillations in the regions of secondary separation for larger α as mentioned in Korolev *et al.* (2002). This may be due to the difference in pressure-displacement law. We also performed calculations with different values of y_{max}. The minimum value of Δy was kept constant. The results are displayed in Figures 3.10 and **??**. They clearly show that restricting the outer boundary to $y_{max} = 15$ results in "overshooting" of the minimal skin friction. We observed that for $y_{max} = 50$ there was no dependence of the numerical results on the size of the computational domain. In Merkin & Smith (1982) calculations, they restricted the outer boundary to $y_{max} = 14$. Our calculations suggest that no reliable results can be obtained using

a value of $y_{max} = 14$ for an angle more than $\alpha = 10$. As a result $y_{max} = 50$ was chosen for our calculations.
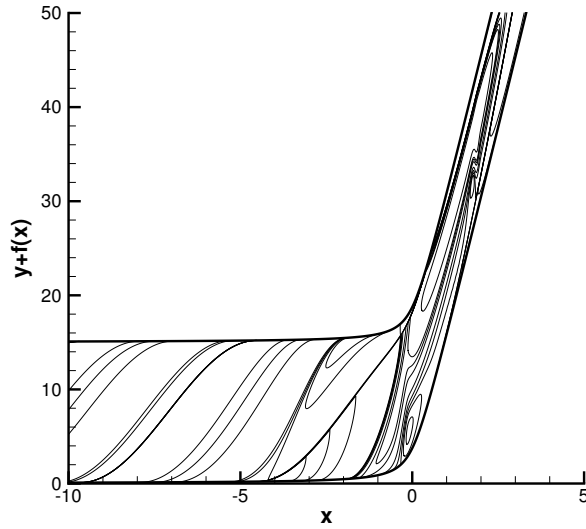
Figure 3.9: Stream line distribution for $\alpha = 15.0$.

PSfrag replacements
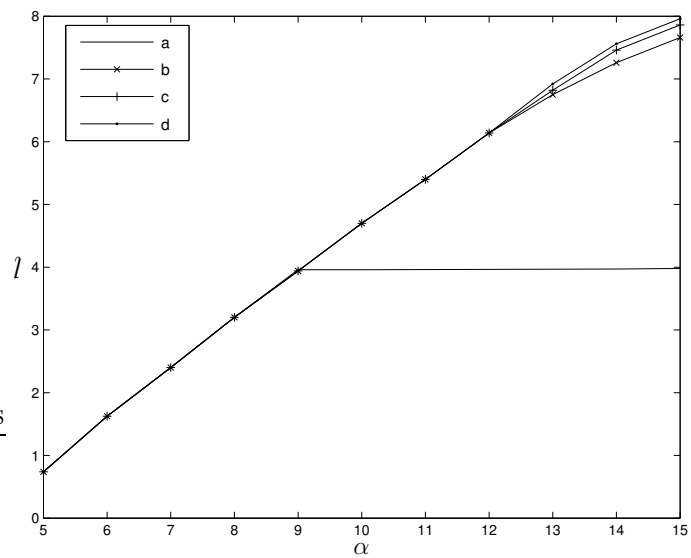
Figure 3.10: Influence of the size of the computational domain on the solution for length l of the separation region (a) $y_{max} = 15$, (b) $y_{max} = 40$,(c) $y_{max} = 50$, (d) $y_{max} = 75$.

PSfrag replacements
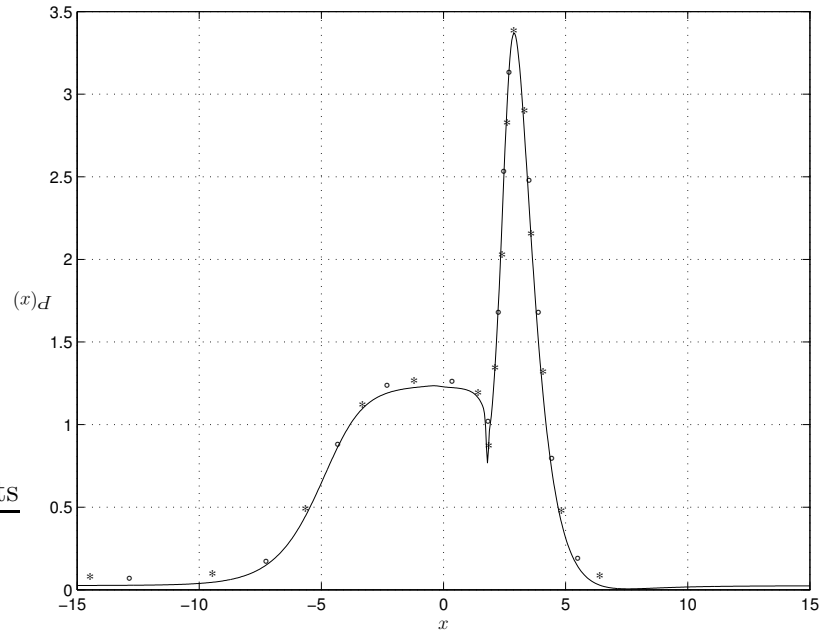
Figure 3.11: Pressure distributions for various sizes of the uniform grid for $\alpha = 15.0$:$'$ $-'(8001 \times 64),' \circ'(1601 \times 70),' *'(1201 \times 90)$.

PSfrag replacements
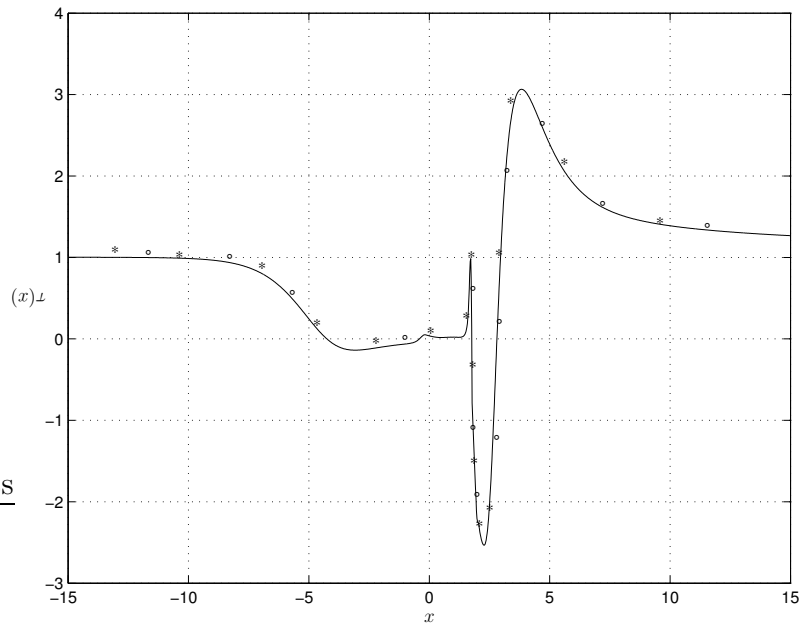
Figure 3.12: Skin friction distributions for various size of the uniform grid for $\alpha = 15.0$:$' -'(8001 \times 64),' \circ'(1601 \times 70),' *'(1201 \times 90)$.

The assessment of the impact of using different size grids on the numerical solution was performed using grid sizes of 8001×64, 1601×70 and 1201×90. The pressure and shear plots for these grids are shown in Figures 3.11 and 3.12. The Figures suggest that our results are independent of the grids we have used.

For convex corners, the pressure decreases (see Figure 3.13) and the shear (see Figure 3.14) increases very rapidly towards the corner. After the corner the pressure rises to a small positive maximum before falling to its undisturbed state, whilst shear rapidly falls to a negative minimum followed by a rather slow rise to its undisturbed value far downstream. Further decrease in α ensures increase in maximum and minimum values in both pressure and skin friction. For a large enough value of α there is a reversed flow region downstream of the corner. Starting with $\alpha = -6.10$ there is a reversed flow region downstream of the corner. For lower values of α, the skin friction appears to plateau out at its negative minimum before rising to its undisturbed state. This effects in reattachment point moving downstream, and the reversed flow eddy has fluid moving faster than the concave case. For $\alpha = -7.0$ the size of the region of reversed flow has increased and the separation point has moved closer to the corner. Looking at the streamline pattern, Figure 3.15, we observe that the flow separates downstream of the corner at $x = 0.8$ and reattaches at $x = 5.2$. We had problems with the convergence as the angle was lowered. For concave case we observe that the skin friction return to its undisturbed state much slower than for convex case.

PSfrag replacements
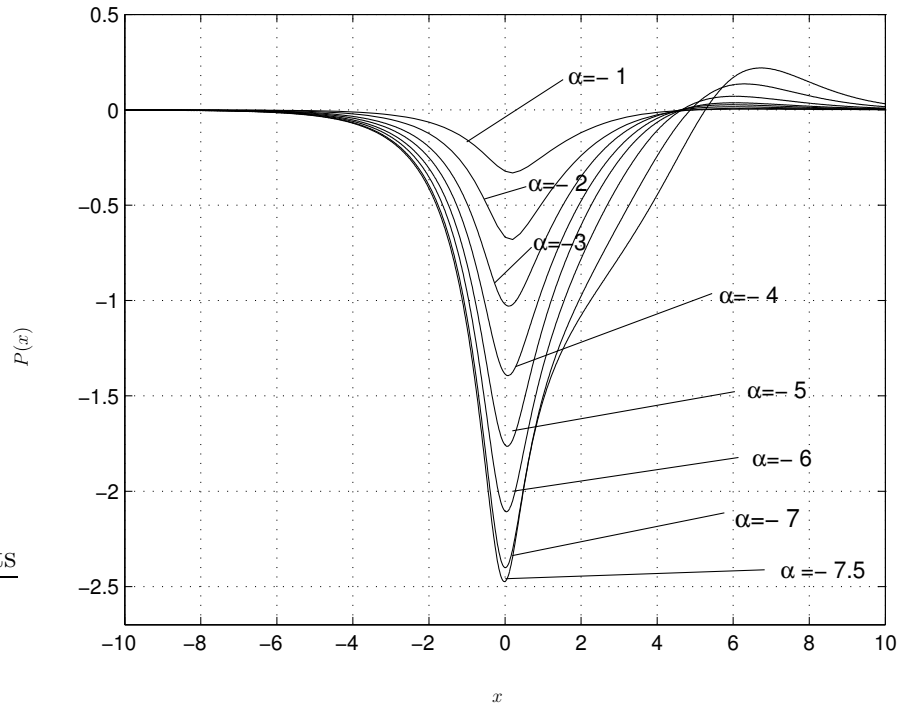
Figure 3.13: Pressure distributions for various angles with convex corners.

PSfrag replacements
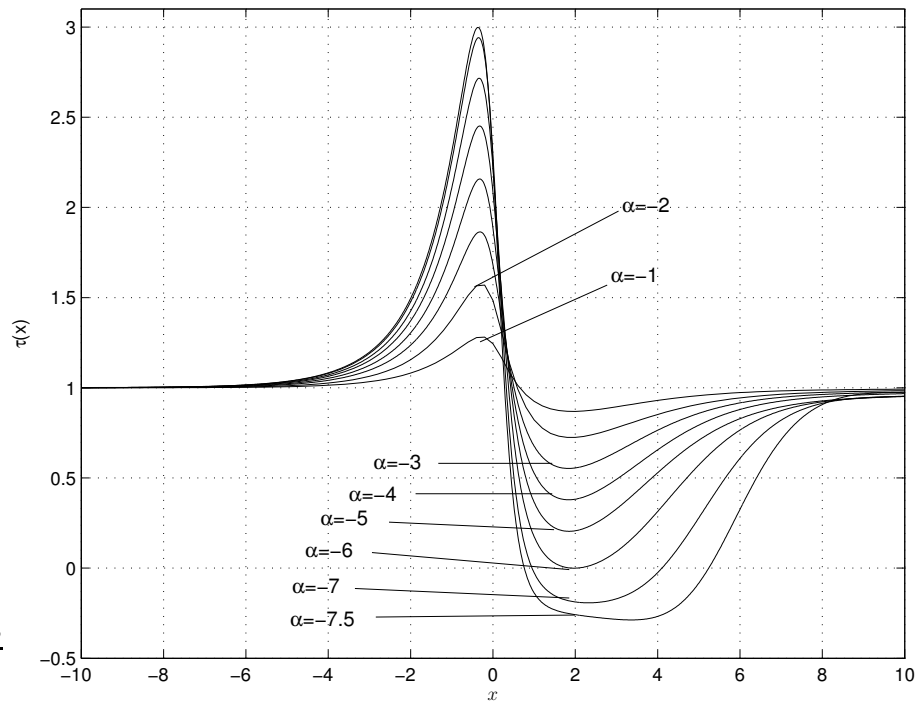
Figure 3.14: Skin friction distributions for various angles with convex corners.
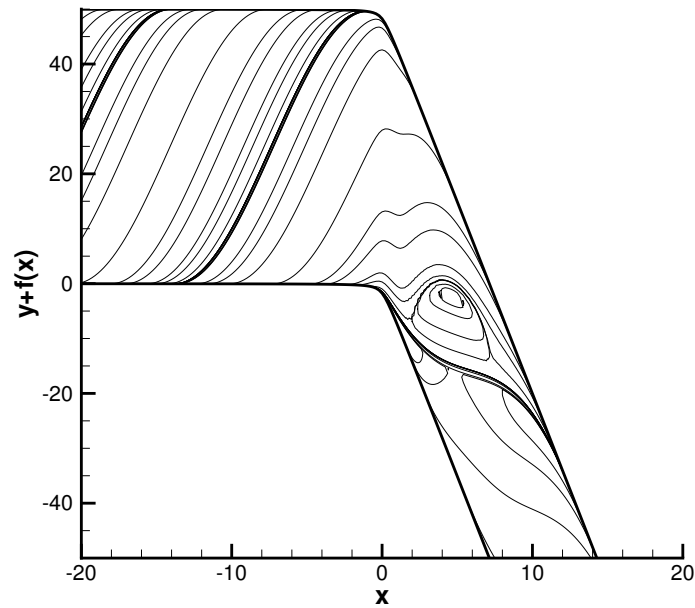
Figure 3.15: Stream line pattern showing reversed flow for convex corner with $\alpha = -7.0$.

3.3 Wall-Jet flow past humps and indentations

3.3.1 Problem formulation

Consider a wall-jet past a hump or distortion, where the hump is shown in Figure 3.16. The shape of the hump/indent is the same as the one used by Merkin (1983) and is given by

$$\bar{y} = hF(x; k) \quad \text{where} \quad F(x; k) = \exp(-k^2 x^2). \tag{3.12}$$
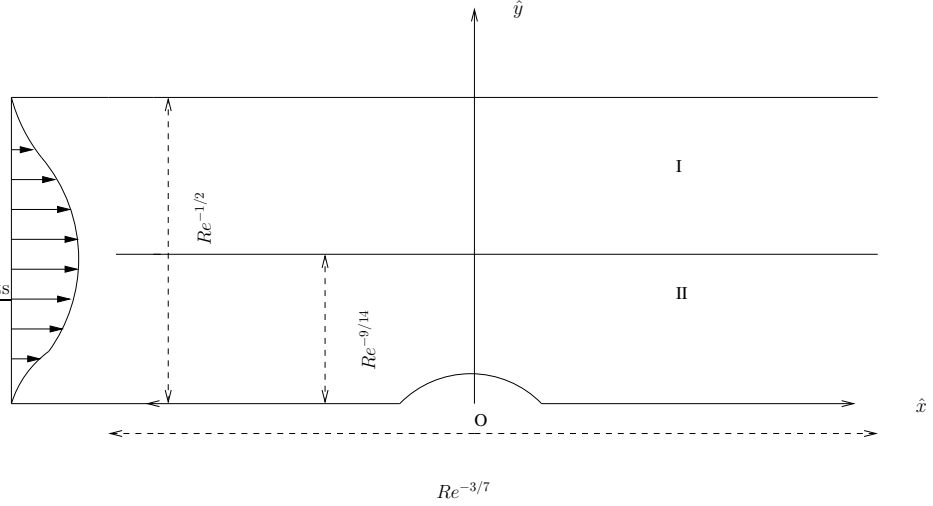
Figure 3.16: Double deck structure showing flow past a hump.

The shape of a hump is concave-convex-concave and an indentation is convex-concave-convex. For positive h equation (3.12) represents a hump; if h is negative then we have an indentation. The near-wall jet past the hump/indentation is given by the double deck theory. The interaction has a double-deck structure, as shown in Figure 3.16. The dimensions of the hump or indentation have been chosen to ensure that it lies within the wall-layer of the wall-jet double-deck structure considered. Region I is the main part of the boundary-layer that has a thickness of $O(Re^{-\frac{1}{2}})$. Region II is the viscous sub-layer that has a thickness of $O(Re^{-\frac{9}{14}})$. The streamwise extent of the structure is estimated to be $O(Re^{-\frac{3}{7}})$. The flow properties are governed by the fluid motion in region II. Without employing the Prandtl transformation the no-slip condition is

$$u = \bar{v} = 0 \quad \text{as} \quad \bar{\psi} = \bar{\psi}_y = 0 \quad \text{on} \quad \bar{y} = hf(k, x),$$

where $u = \bar{\psi}_y$, $\bar{v} = -\bar{\psi}_x = 0$ and we have used transformation similar to (1.8) to scale out the $O(1)$ flow parameters. To employ the Prandtl transformation we put

$$y = \bar{y} - hf(k, x) \quad \text{and} \quad v = \bar{v} - hf_x u.$$

The equations governing the fluid flow are equations (1.12)-(1.15) but they have to be solved using the boundary condition

$$p \to 0, A \to 0 \quad \text{as} \quad X \to \infty, \tag{3.13}$$

and the interaction law (3.9).

3.3.2   Numerical results for humps

In this section we discuss the numerical results obtained for for humps only, that is
for $h > 0$ in (3.12). We shall consider both moderate, $h = O(1)$ and large humps,
$h \gg 1$. We shall also assess the effect of hump width, as opposed to hump height
by considering different values of k, namely $k = 0.5, 1.0, 2.0$. We use the numer-
ical method described in Chapter 2. Computations were performed on a uniform
grid with 1601 points in the x direction and 64 points in the y direction for stream
function. The streamwise domain was truncated at $x_{-\infty} = -40.0$ and $x_\infty = 40.0$.
The computational domain along the y direction was chosen to be from $y = 0$ to
$y_{max} = 50$.

We start with the case of a relatively long hump. The pressure distribution and
skin friction for $k = 0.5$ and various values of h are shown in Figures 3.17 and 3.18.
There is a critical value $h = h_c$ at which separation first occurs, there being a reversed
flow separation eddy present downstream of the hump peak for all $h > h_c$. Merkin
(1983) observed that separation occurs for a value of h between $h = 5$ and $h = 6$,
and interpolated his results to get $h \approx 5.75$ as the value of h where the incipient
separation occurs.

From our calculations, we observe that the incipient separation occurs for a much
lower value $h \approx 5.02$. As in the case of concave corner, as h increases a pressure
plateau forms in conjunction with a fairly weak reverse flow bubble. This is followed
by a rise to a pressure maximum, in conjunction with a skin-friction minimum and
reattachment of the flow. Although here the plateau level is negative and follows the
pressure minimum near the hump peak at $x = 0$. We observe reattachment approxi-
matelt at $x \approx 7.0$.

Merkin (1983) also suggested that at large values of h, in addition to the recircu-
lation region behind a hump, there would also be a recirculation region ahead of the
hump and extrapolating his results he suggested that this would occur for $h \approx 16.8$.

We observed a separation region ahead of the hump at $h \approx 14.96$. The pressure, skin friction and streamline pattern for $h = 15.95$ are shown in Figures 3.19, 3.20 and 3.21 respectively. Looking at the pressure distribution Figure 3.19 there is a flattening of pressure in the separation region followed by a sharp decrease which appears to be associated with an initial separation and a small embedded region of forward flow respectively. We also have a sharp increase in pressure near the reattachment. These features, including the small counter-rotating eddy can be seen in the stream line pattern in Figure 3.21. The flow separates at $x = -2.55$ and reattaches at $x = -1.95$ ahead of the hump. We observe that downstream of the hump the flow separates at $x = 0.3$ and reattaches at $x = 10.0$. Within this region of separated flow we observe a secondary separation bubble which separates at $x = 7.9$ and reattaches at $x = 8.05$.

We had problems with the convergence of the numerical method for the value $h > 15.95$. This may be due to the appearance of a Goldstein-Stewartson type singularity mentioned in Merkin (1983).
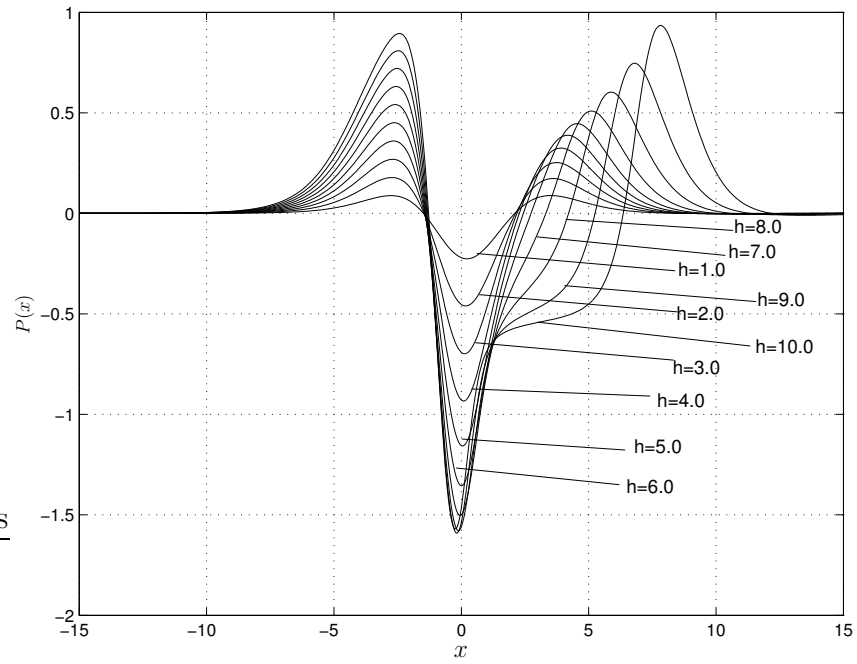
Figure 3.17: Pressure distributions for $k = 0.5$ for various values of h.
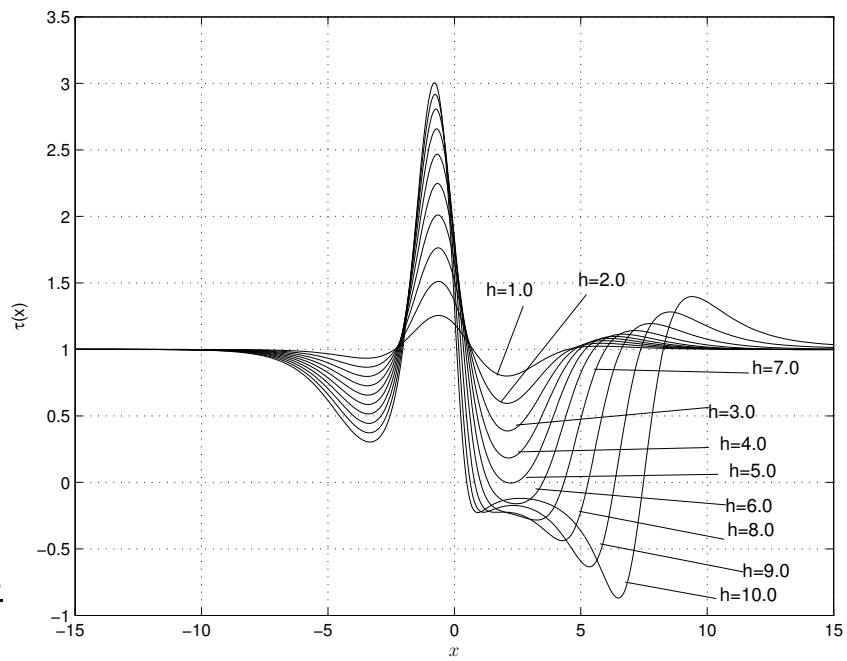
Figure 3.18: Skin friction distributions for $k = 0.5$ for various values of h.

PSfrag replacements
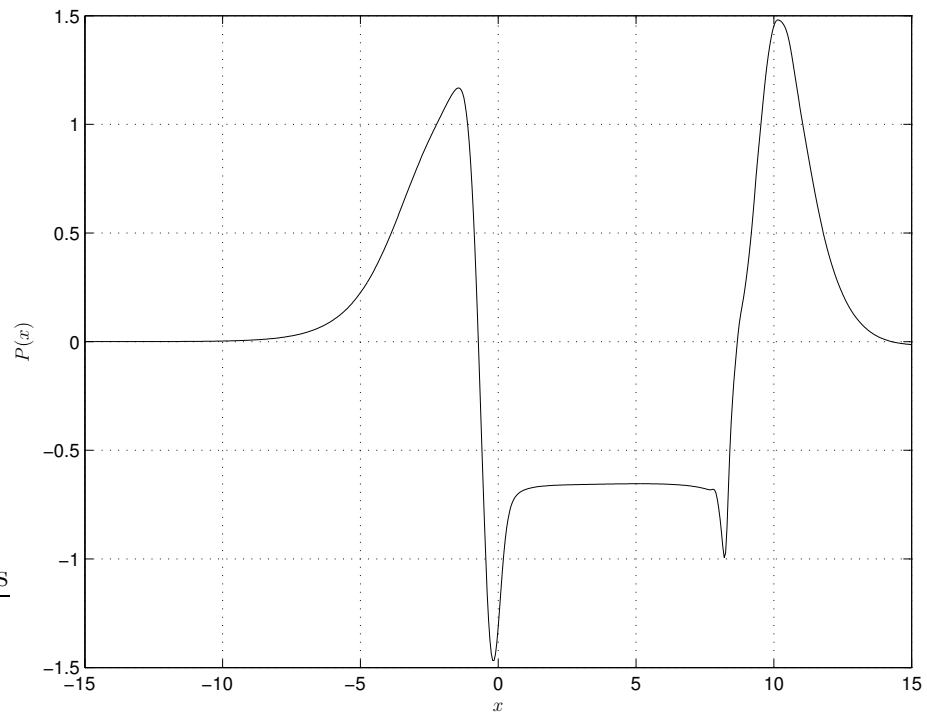
Figure 3.19: Pressure distribution for $k = 0.5$ at $h = 15.95$.

PSfrag replacements
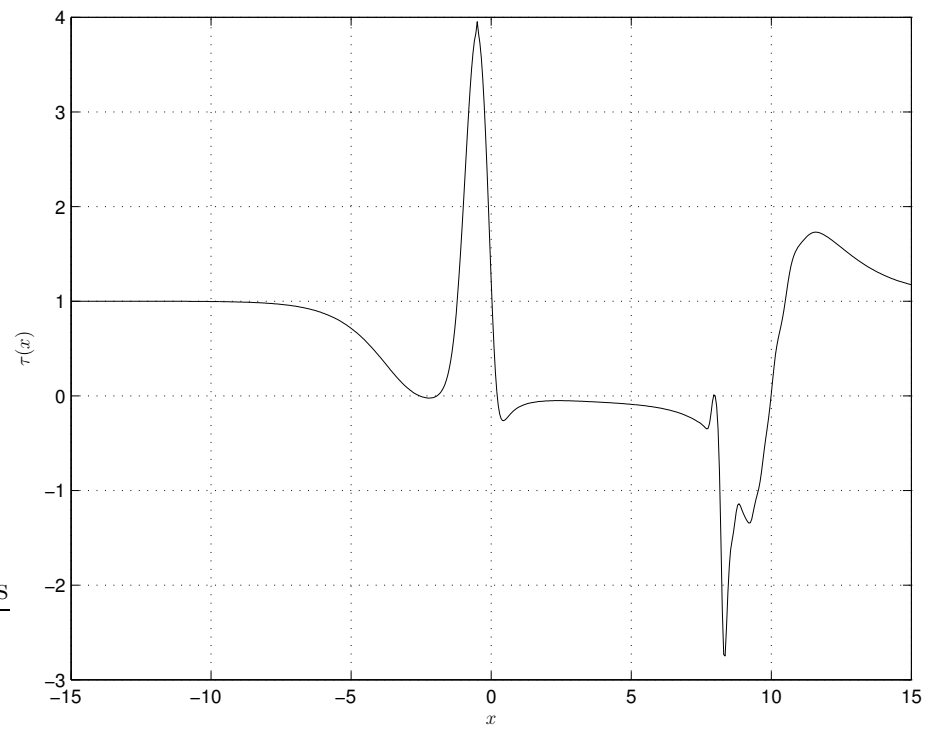
Figure 3.20: Skin friction distribution for $k = 0.5$ at $h = 15.95$.
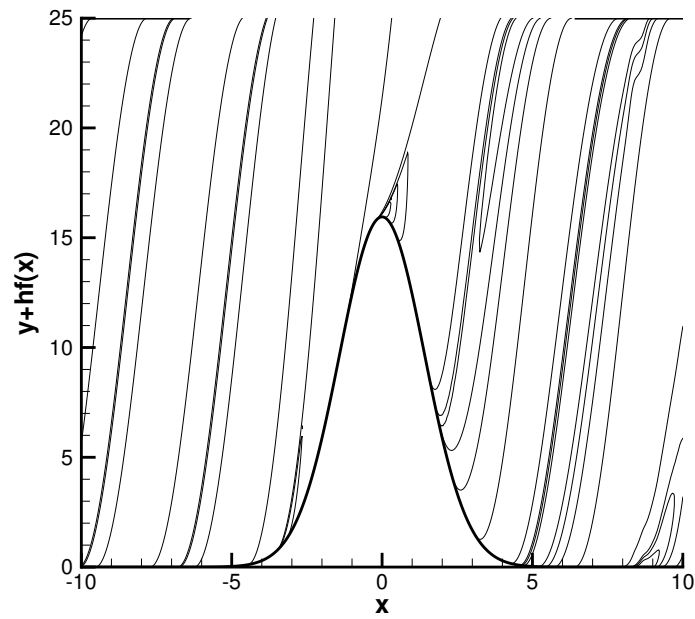
Figure 3.21: Stream line pattern for $k = 0.5$ at $h = 15.95$.

PSfrag replacements
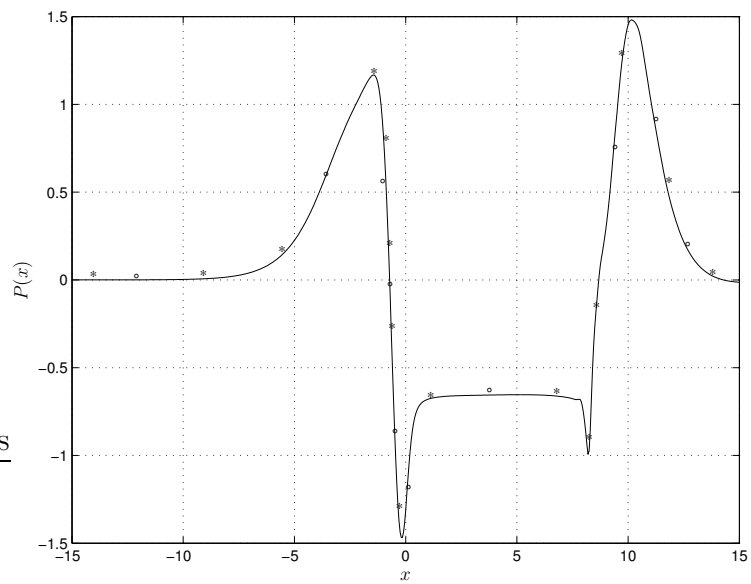
Figure 3.22: Pressure distributions for various sizes of uniform grid with $h = 15.95$, $k = 0.5$: '-' (8001×64), 'o' (1601×70), '*' (1201×90).

PSfrag replacements
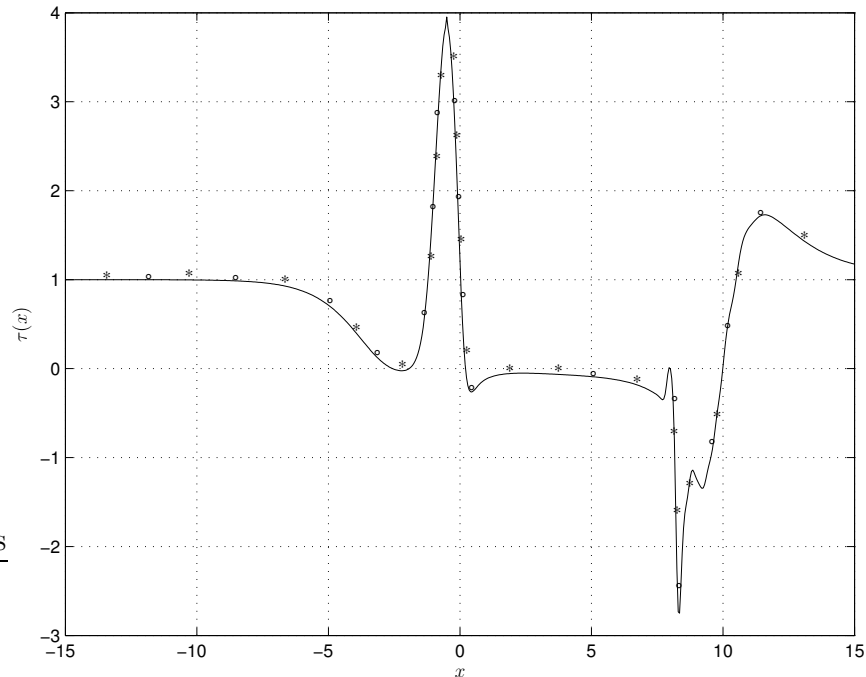
Figure 3.23: Skin friction for various sizes of uniform grid with $h = 9.0$, $k = 0.5$: '-' (8001×64), 'o' (1601×70), '*' (1201×90).

The independence of the accuracy of our numerical solutions for a sufficiently large number of grid points is demonstrated in Figures 3.22 and 3.23 which show the pressure and wall shear distributions calculated on three different grids for $h = 15.95$ and $k = 0.5$.

In order to investigate the effect of the hump width we also calculated the flow for $k = 1.0$. The pressure and skin friction distributions are shown in Figures 3.24 and 3.25. Qualitatively the results are much the same as for the larger values of k, except, as mentioned by Merkin (1983), that this more sudden forcing causes the effects to be obtained at a smaller values of hump height h. The separation behind the hump occurs at $h = 2.62$. At higher values of h, say $h = 7.85$, one can observe a separation region ahead of the hump. Figures 3.26, 3.27, 3.28 show the pressure and skin friction distributions and the streamlines for $h = 10.25$. At this value of h we observe a flattening of the pressure profile in the separation region behind the hump and a sharp increase in the pressure profile near the reattachment. Looking

at the streamline pattern, the flow ahead of the hump separates at $x = -2.44$ and reattaches at $x = -1.3$. Downstream of the hump, the flow separates at $x = 0.1$ and reattaches at $x = 9.0$. The secondary separation region extends from $x = 7.0$ to $x = 7.35$. The streamline pattern is plotted in Figure 3.28 in curvilinear coordinates, not in Cartesian coordinates, which explains the depression near $x = 0$.

PSfrag replacements
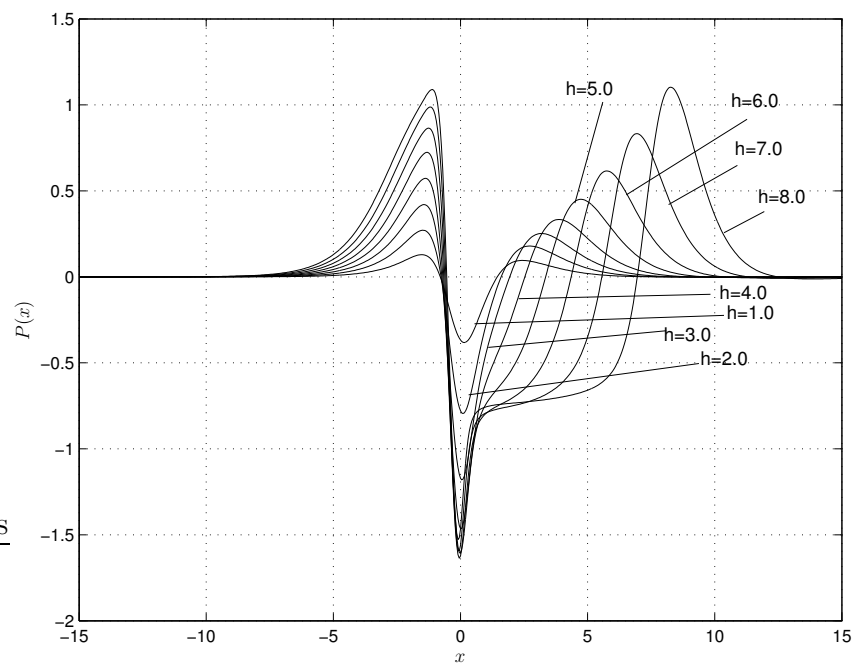
Figure 3.24: Pressure distributions for $k = 1.0$ and various values of h.
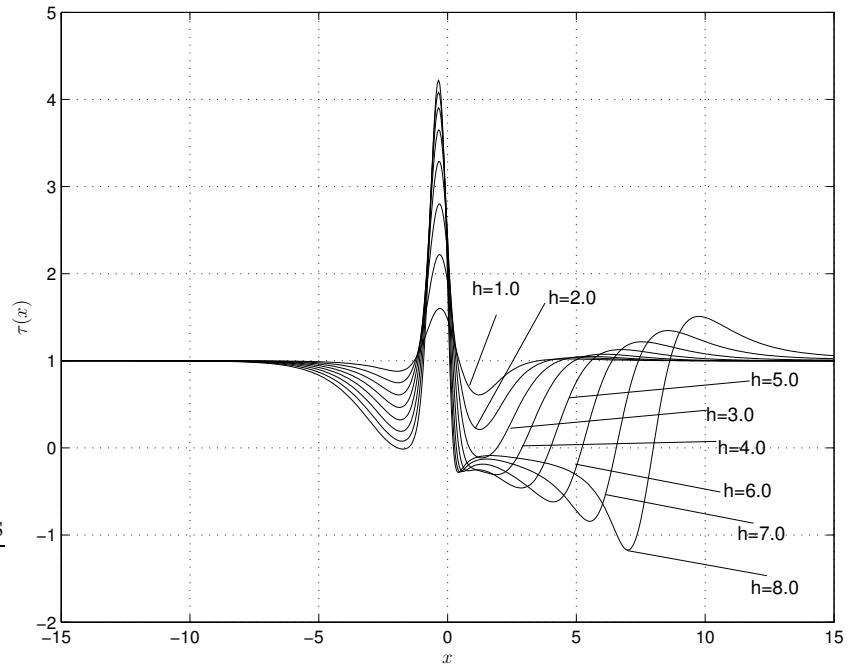
Figure 3.25: Skin friction distributions for $k = 1.0$ and various values of h.
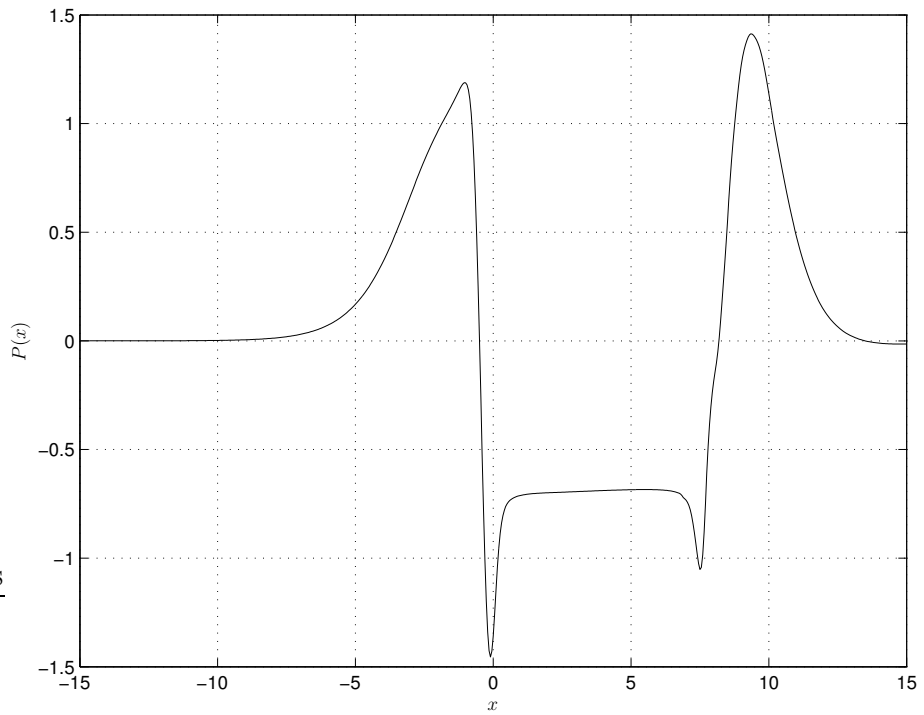
Figure 3.26: Pressure distribution for $k = 1.0$ and $h = 10.25$.

PSfrag replacements
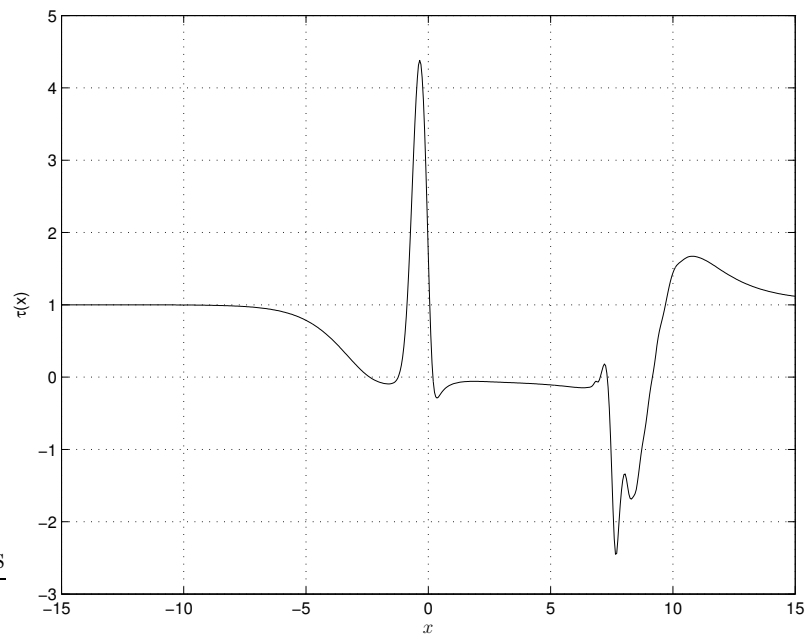
Figure 3.27: Skin friction distribution for $k = 1.0$ and $h = 10.25$.
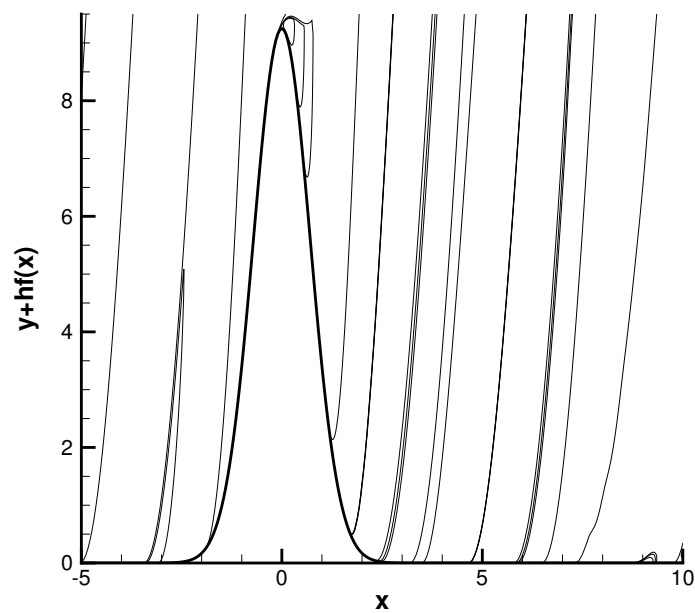
Figure 3.28: Streamline pattern for $k = 1.0$ and $h = 10.25$.

PSfrag replacements
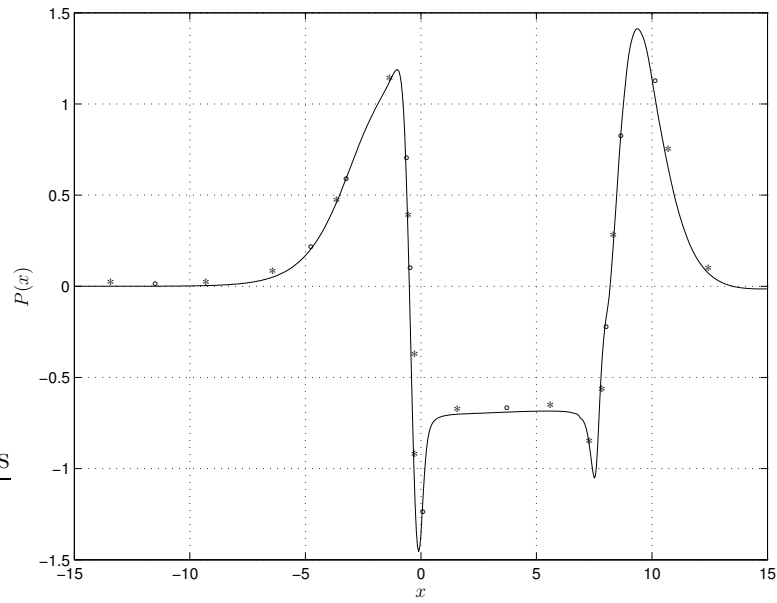
Figure 3.29: Pressure distributions for various size of uniform grid for $h = 10.25$, $k = 1.0$: '-' (8001×64), '∘' (1601×70), '∗' (1201×90).

PSfrag replacements
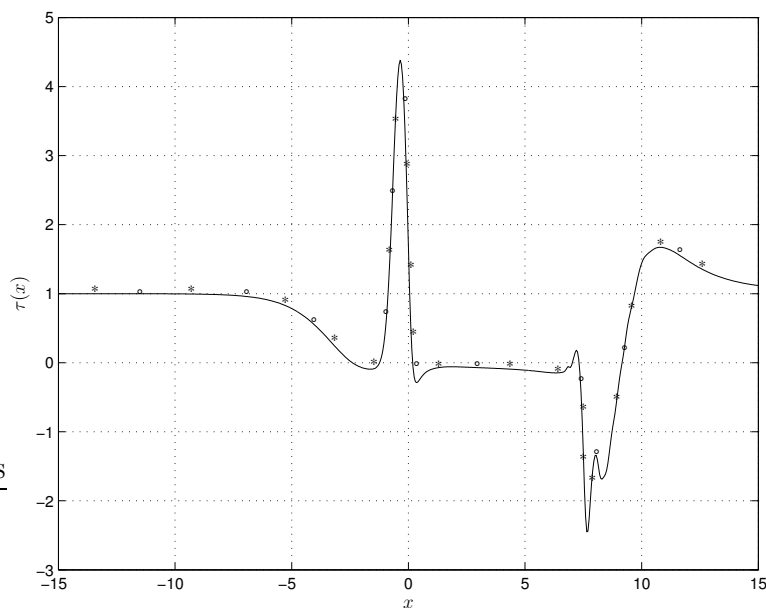
Figure 3.30: Skin friction for various size of uniform grid for $h = 10.25$, $k = 1.0$: '-' (8001×64), '∘' (1601×70), '∗' (1201×90).

The accuracy of our calculated results has been verified by solving the equations using a range of different grids. The effect of different size grids on the solution for

$h = 10.25$, $k = 1.0$ is shown in Figures 3.29 and 3.30. As may be observed, the graphs
are almost indistinguishable in the interval $x \in [-15, 15]$.

Increasing the width parameter k corresponds to shrinking the hump width in the
x-direction. Figures 3.31, 3.32 show the pressure and skin friction distributions for
various values of h with $k = 2.0$. Qualitatively the results are much the same as for
two previous larger values of k. We observe that the flow now separates for a value
$h = 1.78$ behind the hump. Fig 3.33 shows the streamline pattern. As mentioned by
Merkin (1983), for larger values of k separation occurs at lower values of h. Later
the separation occurs at $h = 5.4$ upstream of the hump. Figure 3.33 shows the
streamline pattern for $h = 8.0$. We can observe that the flow separates at $x = -1.65$
and reattaches at $x = -0.55$ ahead of the hump and then separates again at $x = 0.1$
and reattaches at $x = 8.15$ behind the hump. Figures 3.34 and 3.35 show the values
of h at which the separation first occurs and the values beyond which the solutions
do not converge for values of k.

PSfrag replacements
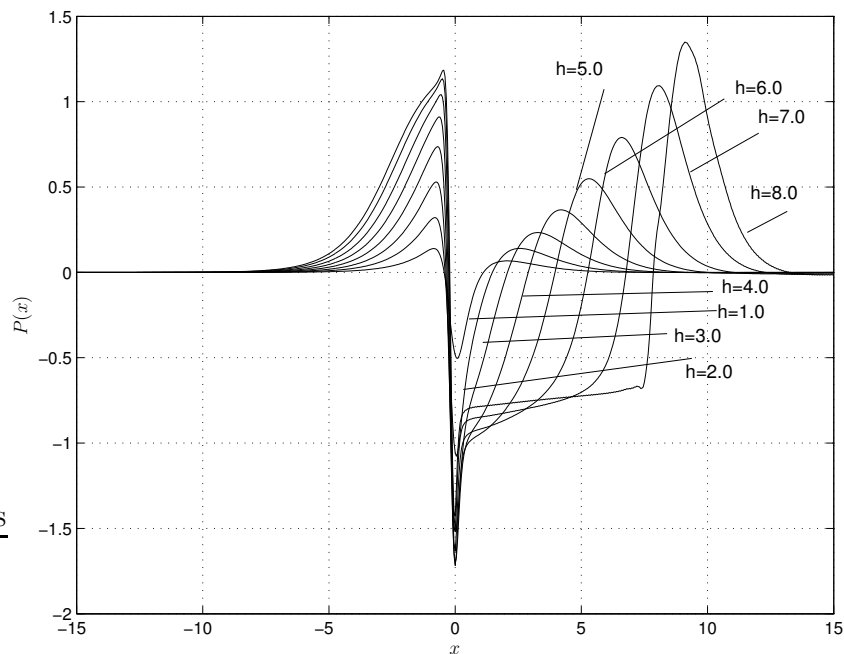
Figure 3.31: Pressure distributions for $k = 2.0$ and various values of h.
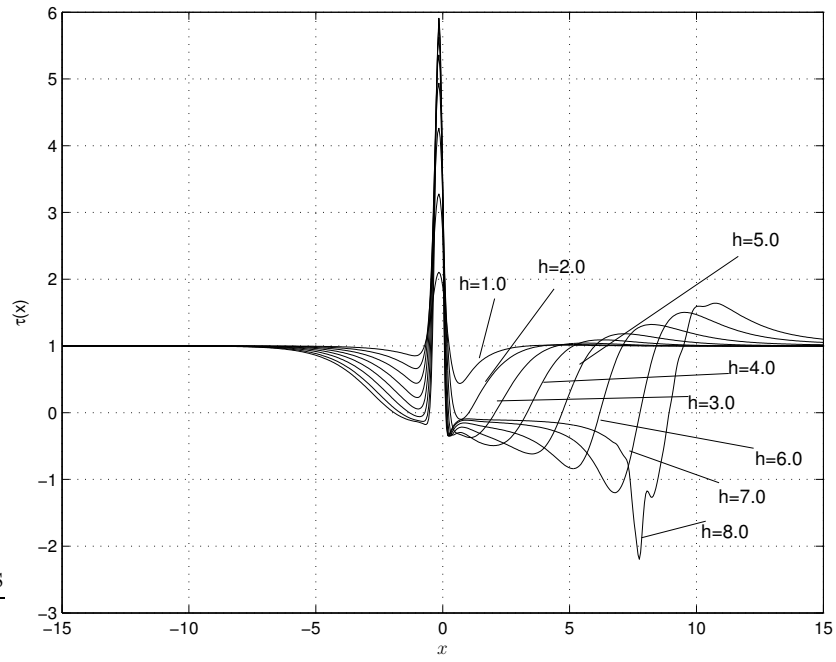
Figure 3.32: Skin friction distributions for $k = 2.0$ and various values of h.
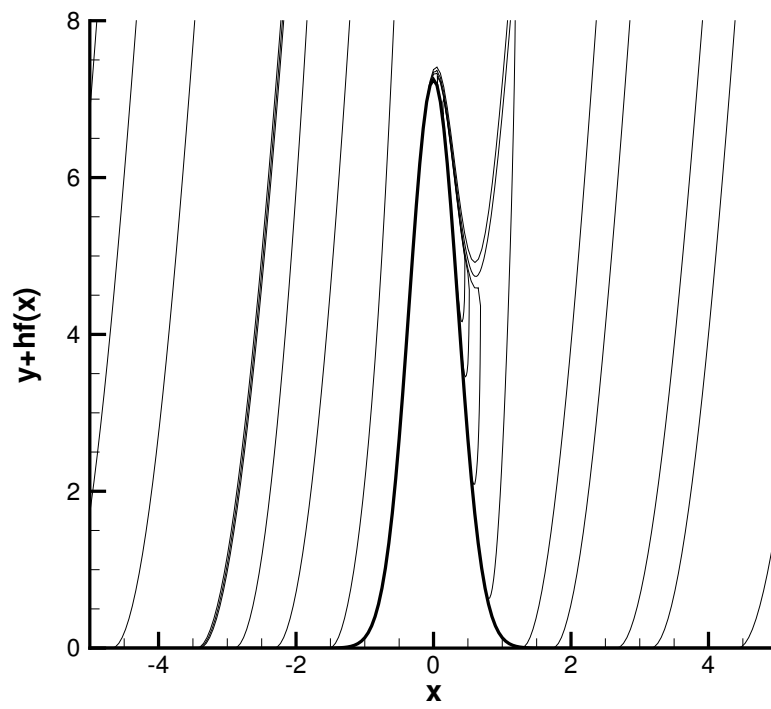
Figure 3.33: Streamline pattern for $k = 2.0$ and $h = 8.0$.
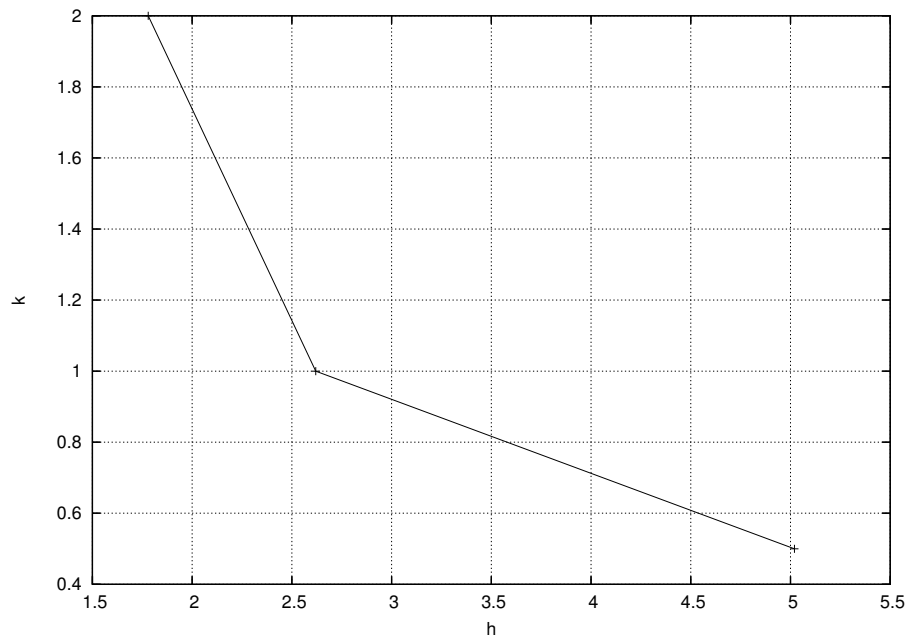
Figure 3.34: Figure showing the values of h at which separation first occurs for various values of k.
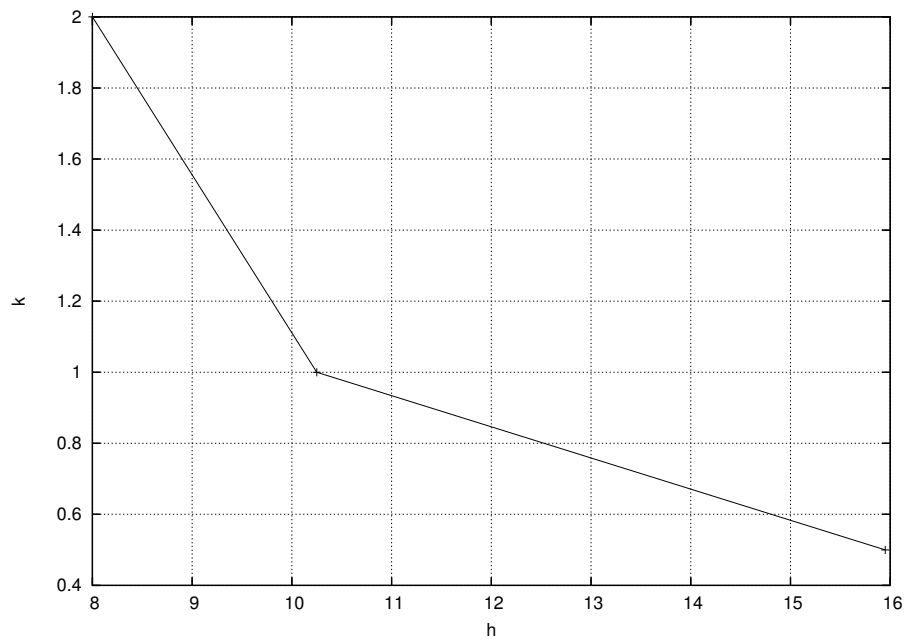
Figure 3.35: Figure showing the values of h beyod which the solutions do not converge for various values of k.

3.3.3 Numerical results for near-wall jet past indentations

In this section, we will show numerical results for a jet-like boundary-layer approaching an indentation, that is for $h < 0$ in (3.12). We shall consider both moderate, $h = O(1)$ and large indents $|h| \gg 1$. As in the case of humps, we assess the effects of the indentation width by considering different values of k.

The pressure and skin friction distributions for $k = 0.5$ and various values of $h < 0$ are shown in Figures 3.36, 3.37. Once again we find that separation first occurs at a critical value of h, namely $h = h_c$. Merkin (1983) estimated that $h_c = -5.57$.

According to our calculations separation occurs for $h \approx -4.52$. We also observe that there is a tendency for the pressure distribution curves to flatten out in the separated region as value of $|h|$ increases, and that there is a sharp increase in both in p and τ near reattachment. At a large negative value of h for example $h = -13.25$ as shown in Figures 3.38-3.39, we observe a "plateau" in the pressure distribution over the separation region, slightly downstream of the pressure distribution plateau the pressure drops and then increases sharply forming a kink, followed by a sharp decrease in pressure before finally increasing to its downstream value. For $h = -13.25$ one can observe a secondary separation that is evident from the skin friction plot which has a small region of positive skin friction as shown in Figure 3.39. The streamlines are shown in Figure 3.40. The flow separates at $x = -2.5$ and reattaches at $x = 2.0$ forming the primary separation region. The secondary separation region that can be observed within the primary separation region extends from $x = 1.14$ to $x = 1.21$. We observe that in contrast to the case of humps, where there are regions of reversed flow, ahead and behind the hump peak, for indents there is a single major separated region symmetrically located with respect to the indentation.
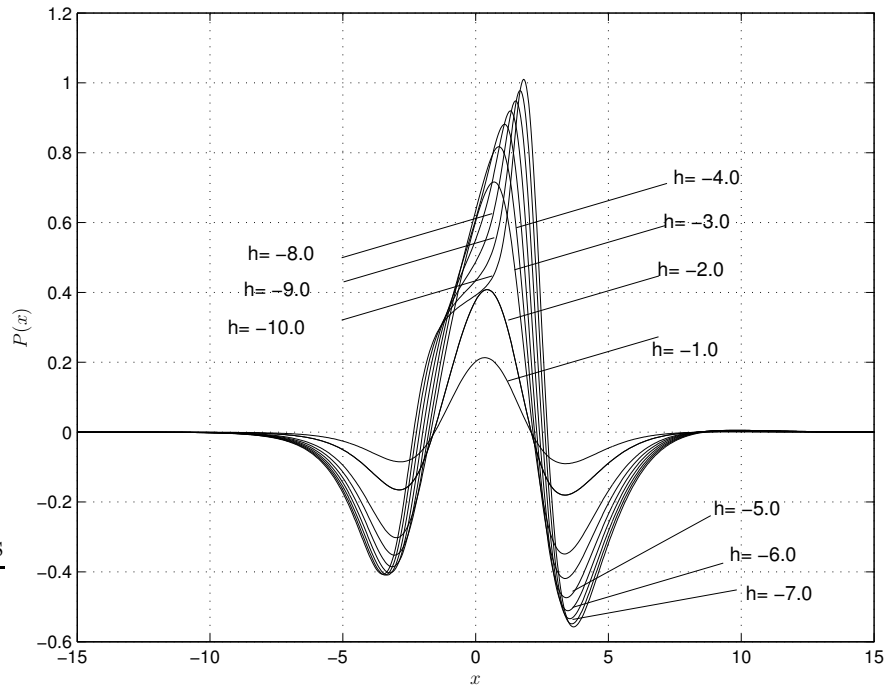
Figure 3.36: Pressure distributions for $k = 0.5$ and various values of h.
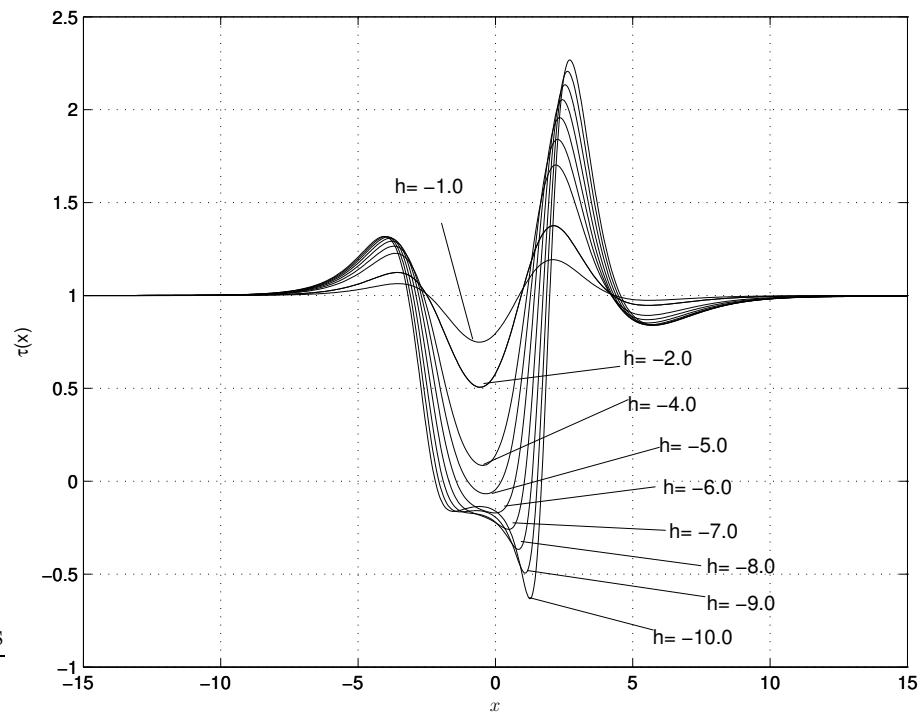
Figure 3.37: Skin friction distributions for $k = 0.5$ and various values of h.

PSfrag replacements
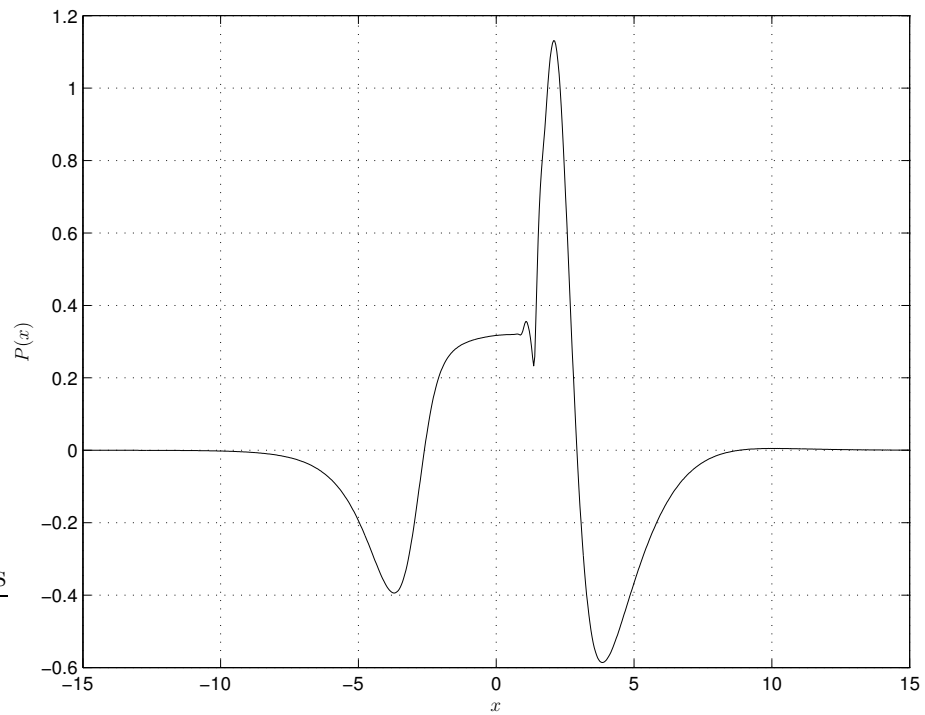
Figure 3.38: Pressure distribution for $k = 0.5$ and $h = -13.25$.

PSfrag replacements
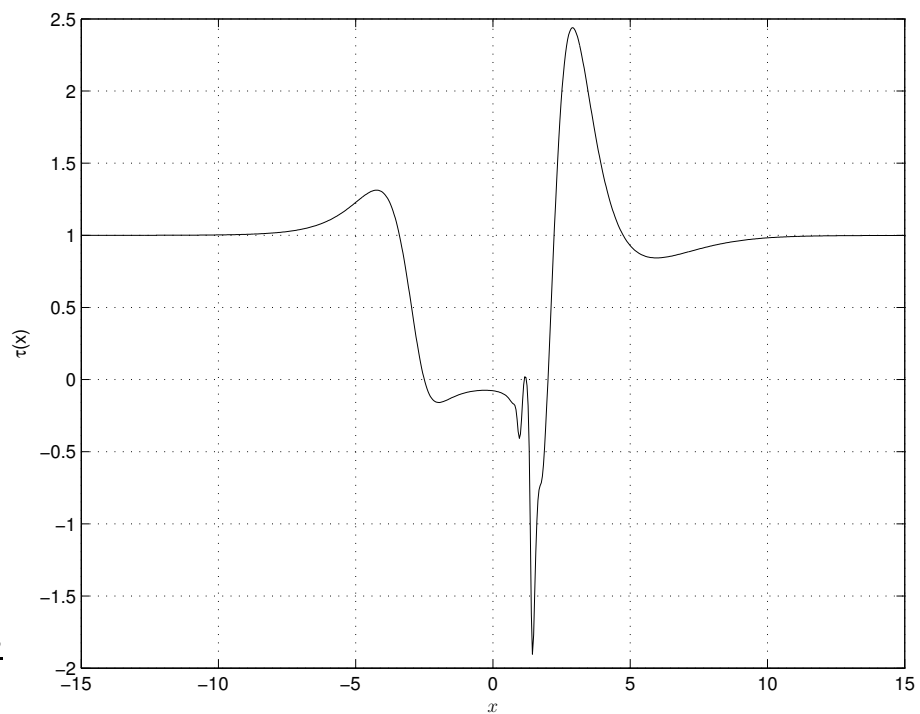
Figure 3.39: Skin friction distribution for $k = 0.5$ and $h = -13.25$.
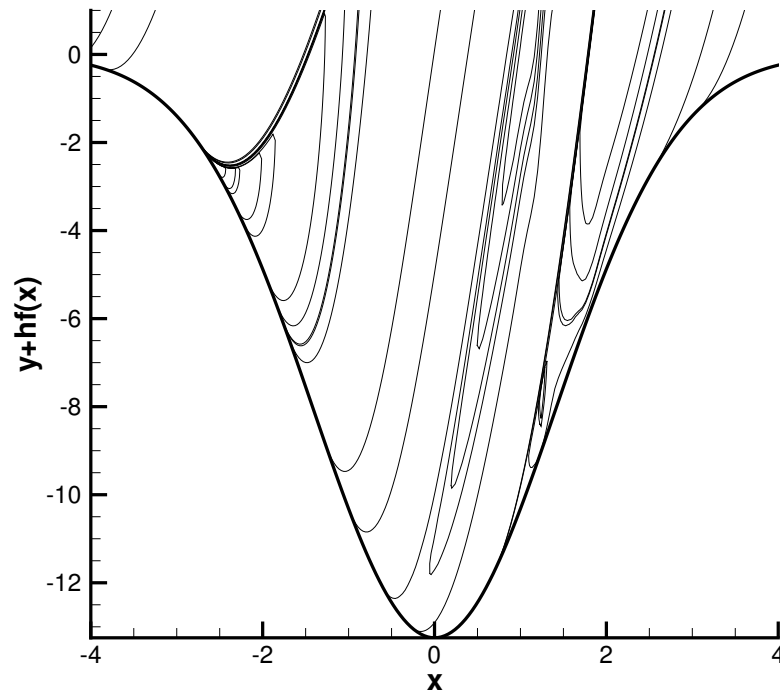
Figure 3.40: Streamline pattern for $k = 0.5$ and $h = -13.25$.

In order to investigate the effect of the indent width parameter k we performed calculations for $k = 1.0$ and $k = 2.0$. The pressure and skin friction distributions for $k = 1.0$, $\quad$ 2.0 for various values of h are shown in Figures 3.41 - 3.45. Again the results appear similar to those for $k = 0.5$, albeit on a more condensed scale, and new flow effects occur at a smaller values of the indentation depth $|h|$. For $k = 1.0$ the flow separates at $h = -2.34$ and for $k = 2.0$ the flow separates at $h = -1.86$. Looking at the stream line plots in Figures 3.43 and 3.46, we observe that the flow separates at $x = -0.7$ and reattaches at $x = 0.3$ for $k = 1.0$ and $h = -3.0$ and the separation region extends from $x = -0.5$ to $x = 0.4$ for $k = 2.0$ and $h = -3.0$. We observe that the separated region is centred on the indent. As the value of k increases the incipient separation occurs at smaller values of h which is consistent with the values mentioned above.
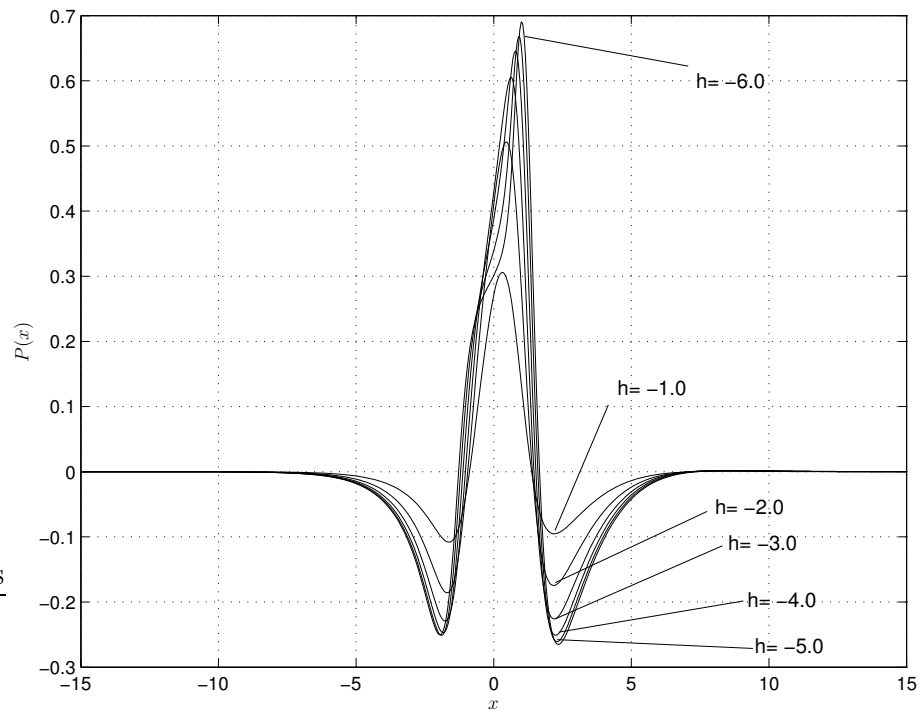
Figure 3.41: Pressure distributions for $k = 1.0$ and various values of h.
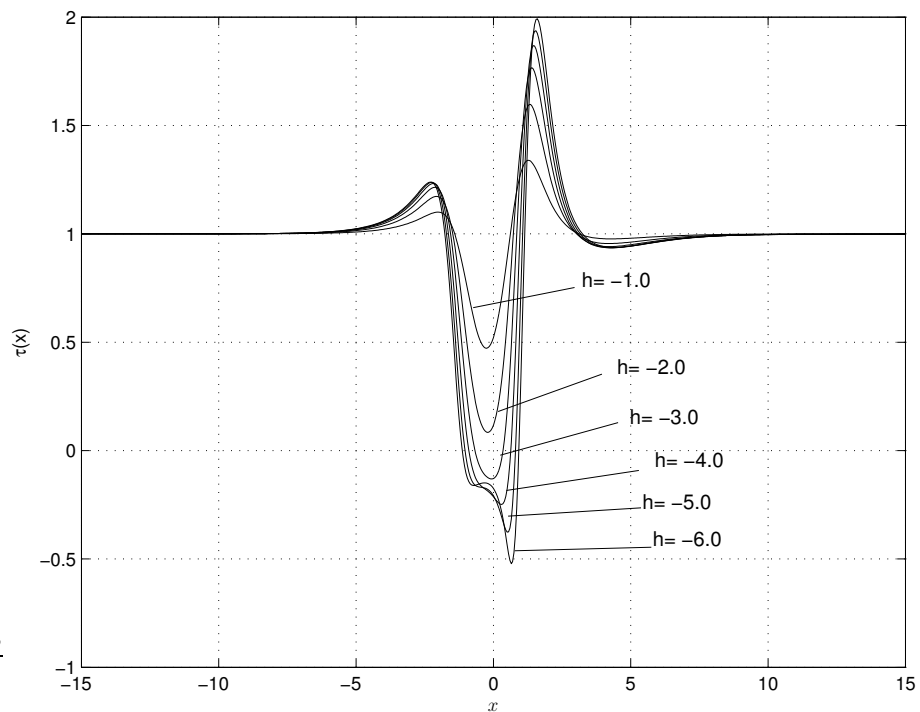
Figure 3.42: Skin friction distributions for $k = 1.0$ and various values of h.
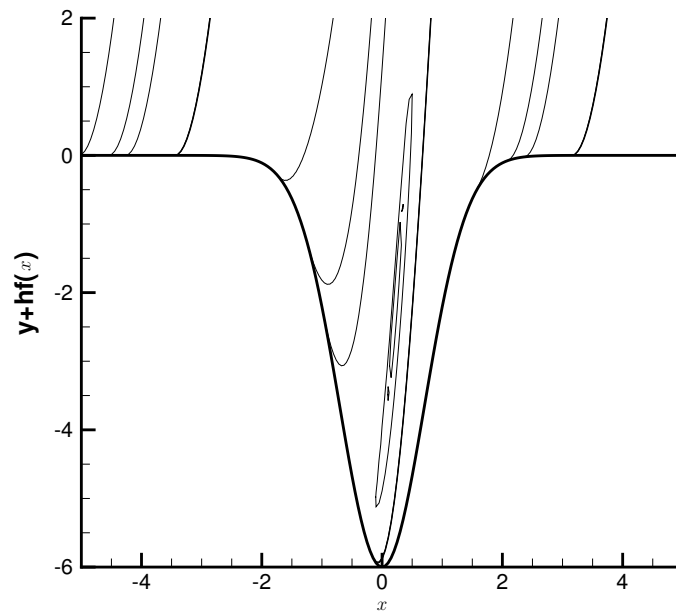
Figure 3.43: Stream line pattern for $k = 1.0$ and $h = -6.0$.
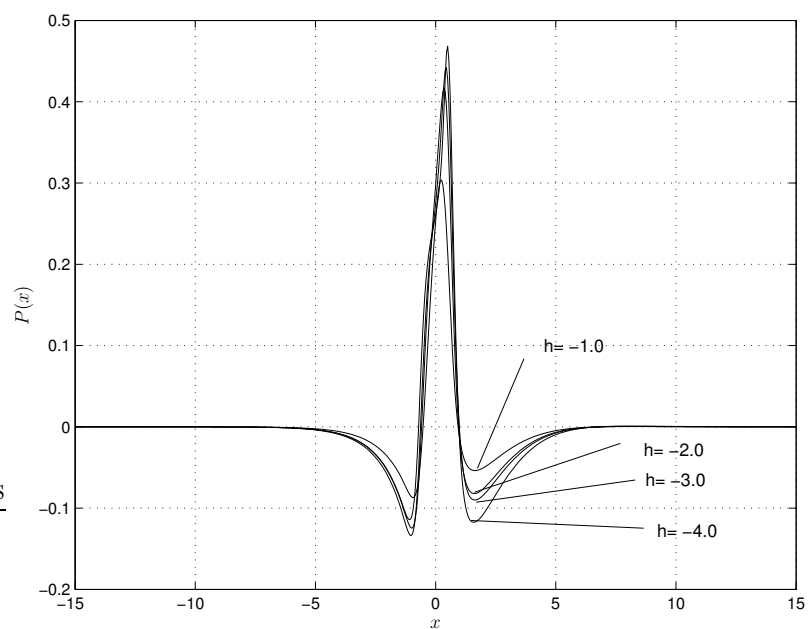
Figure 3.44: Pressure distributions for $k = 2.0$ and various values of h.
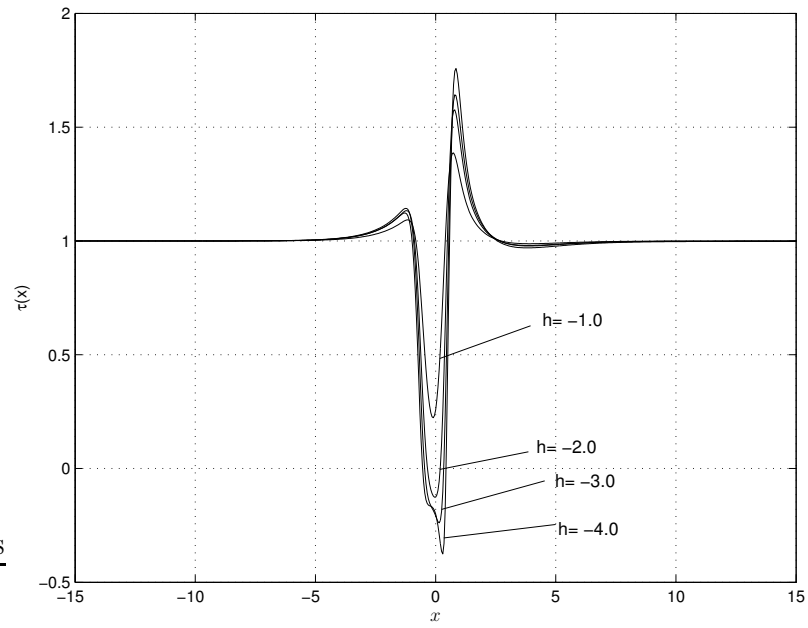
Figure 3.45: Skin friction distributions for $k = 2.0$ and various values of h.
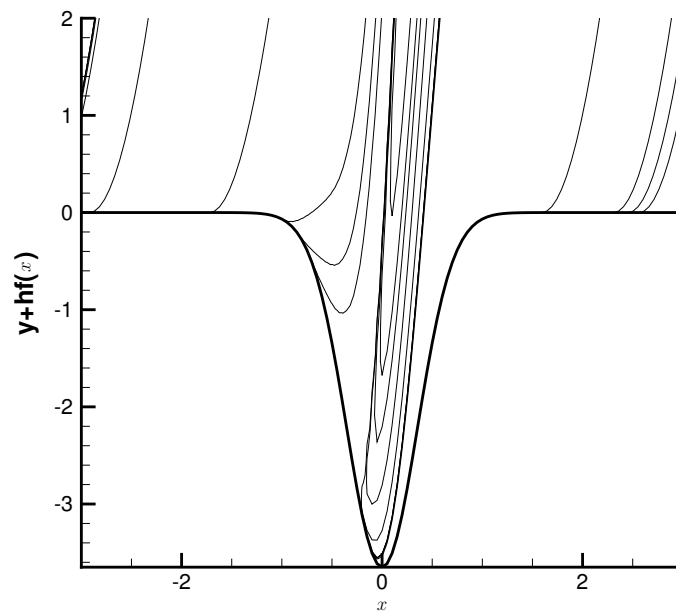
Figure 3.46: Stream line patterns for $k = 2.0$ and $h = -4.0$.

3.4   Liquid layer flows over convex corner

In this section we discuss liquid layer flows over convex corners at high Reynolds numbers ($Re \to \infty$). We consider the case in which the oncoming profile is fully-developed. The Reynolds number is assumed to be large, and the motion is assumed to be steady, laminar and two-dimensional. We concentrate on the flow of a liquid layer down an inclined plane which has angles β and $\beta + \theta$ to the horizontal, upstream and downstream respectively, as shown in the Figure 3.47. In contrast to the wall-jet, here we take $\theta = Re^{-\frac{3}{7}}\alpha$, where $\alpha = O(1)$, to ensure that the corner stays within the lower viscous region II. The angle β must be $O(Re^{-\frac{5}{7}})$ strictly. If the plane is nearly horizontal with $\beta \ll Re^{-\frac{5}{7}}$, then for the leading order the hypersonic laws apply with pressure proportional to the local boundary layer displacement. If $\beta \gg Re^{-\frac{5}{7}}$ then the jet law of Smith & Duck (1977) holds. We are concerned with the convex corner problem where α is of $O(Re^{-\frac{3}{7}})$

The same double decked structure for the flow which was earlier used to explain the behaviour of the near-wall jet encountering corners, humps and indents is proposed. In the present case, gravitational forces are considered. The upstream form is dominated by surface tension-streamline curvature term (A_{xx}) and the downstream form by the gravitation term (A). The displaced free surface is equal to the local boundary layer displacement ($-A$). The interaction law is a combination of a special case of that occurring in the hypersonic flow theory of Brown *et al.* (1975) and the "jet law" of Smith & Duck (1977).

3.4.1   Problem formulation

We note that the dimensionless incompressible Navier-Stokes equations are of the form and body force is considered

$$(\underline{u}.\underline{\nabla})\underline{u} = -\underline{\nabla}p + \frac{1}{F}\sin\beta\Big[1, -\frac{1}{\tan\beta}\Big] + \frac{1}{Re}\nabla^2\underline{u} \qquad (3.14)$$

where $\underline{u} = U(\bar{u}, \bar{v})$ is a velocity vector, F is the dimensionless Froude number. For half-Poiseuille flow we must take

$$F = \frac{U^2}{gL} = Re\sin\beta = \frac{UL}{\nu}\sin\beta \Rightarrow U = \frac{gL^2}{\nu}\sin\beta$$

or for a general developed case we must have supercritical flow, since we require

$$\frac{Re\sin\beta}{F} = O(1) \quad\text{or}\quad F = \frac{U^2}{gL} \sim Re\sin\beta \sim Re^{\frac{2}{7}} \quad\text{for}\quad \beta = O(Re^{-\frac{5}{7}})$$

A detailed description of the problem formulation is given in the paper by Gajjar (1987). Taking the Prandtl transformation, and the forcing term is given by $f = \alpha F(x; r)$ for wedge, or $f = hF(x; k)$ for hump/indentation. The equations governing the flow are the boundary-layer equations given by (1.12)-(1.15) except for the pressure-displacement law which is given by

$$p = -A'' - \sigma A. \tag{3.15}$$

where $\sigma \propto \left(\beta Re^{\frac{5}{7}}\right)^{-1}$ is inversely proportional to the angle of inclination of the plane.

An additional boundary condition describing the downstream state is given by,

$$p \rightarrow = -\sigma\alpha x, \quad A' \rightarrow \alpha \quad\text{as}\quad x \rightarrow \infty, \tag{3.16}$$

. In contrast to the earlier wedge investigations, here the sense of α is opposite to that considered previously and in contrast to both the supersonic and wall-jet flows the pressure grows without bound far downstream, which ensures a far different asymptotic form for skin friction give by

$$\tau \sim c^2(\alpha\sigma)^{\frac{3}{4}}x^{\frac{1}{4}}$$

According to Bowles & Smith (1992), the pressure-displacement law can also written as

$$p = -A + \gamma A''\text{where} \quad \gamma \propto \frac{F^7}{R^2}\left(K\frac{T}{F} - 1\right)$$

where T is the surface tension. When surface tension effects dominate those of streamline curvature we have $\gamma > 0$, and possible upstream capillary waves, but he situation still holds good for relatively weak surface tension. Notice that for $|\gamma| \ll 1$ corresponds to $|\sigma| \gg 1$.
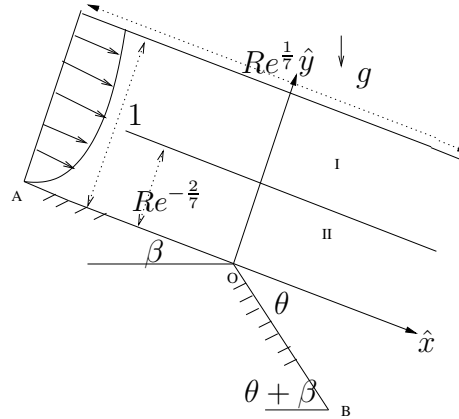
Figure 3.47: Sketch of basic geometry.

3.4.2   Numerical results

In this section we present some numerical results and compare them with the results of Gajjar (1987). We perform numerical computations for different values of σ. The computations are performed for a slightly smoothed body shape, $f(x) = \frac{1}{2}\alpha\left[x + \sqrt{x^2 + r^2}\right]$, where α is defined as the scaled angle. Here r is called the rounding parameter, and as $r \to 0$ the surface collapses to a sharp corner. The numerical modelling of the flow is made easier by using this smoothed body shape. In particular, the smoothed body shape avoids requiring special treatment of the corner region where a concentration of the mesh points would otherwise be needed. For all subsequent calculations, the smoothing parameter was taken to be $r = 0.5$.

Gajjar (1987) uses three different numerical procedures to solve the equations (1.12)-(1.15) and (3.15) ; two using shooting techniques and the third is based on global iteration. He encountered severe difficulty in implementing the downstream boundary condition (3.16) with the shooting techniques. All three numerical techniques had problems with the convergence as the angle was increased. Gajjar also used a smooth corner to avoid oscillations in his solution, effectively taking $f(x) = \alpha x H(x)\tanh(x^2)$ and observed that the separation obtained for $\sigma = 0.1$ is at $\alpha \sim -3.3$, and for $\sigma = 1.0$ he hints that the separation may occur at $\alpha = -15$. Gajjar (1987) only considered cases $\sigma = 0.1$ and $\sigma = 1.0$. The numerical method

used is the same as in Chapter 2. The pressure-displacement relation is given by equation (3.15).

The $\frac{dp}{dx}$ term is approximated by a four point finite-difference formula estimating the third-order derivative $A'''(x_j)$ and a forward difference formula estimating $A'(x_j)$

$$-\frac{dp}{dx} = \frac{A_{j+1} - 3A_j + 3A_{j-1} - A_{j-2}}{\Delta x^3} + \sigma\frac{A_{j+1} - A_j}{\Delta x} + O(\Delta x). \qquad (3.17)$$

This discretized equation leads to the same matrix form as (2.12). The elements of the matrices are given in Appendix B. For $\sigma = 0.0$, the problem reduces to the one discussed in §3.2. Calculations were performed on a uniform grid with 3201 points in the streamwise direction and 64 polynomials representing the stream function in the y direction. Finite values of $x_{-\infty} = -40$ and $x_\infty = 40$ were used to truncate the computational domain in the streamwise direction. A value of $y_{max} = 50$ was chosen to truncate the computational domain along the y direction. With this numerical technique we did not encounter any problems with the downstream boundary condition (3.16). Typically only 7 or 8 Newton iterations were needed for the iterations to converge.

Results for $\sigma = 0.1$

Upstream and in the vicinity of the corner the results for $|\alpha| \ll 1$ are similar to Figures 3.13 and 3.14, namely a free interaction in which the pressure drops and skin friction increases which can be seen in the pressure and skin friction distributions, see Figures 3.48, 3.49. We observe that the incipient separation occurs at $\alpha = -13.4$. The pressure and skin friction distribution for the separated flow are shown in Figures 3.50 and 3.51 for $\alpha = -14.0$. The streamline pattern of the separated flow is shown in Figure 3.52. The flow separates downstream of the corner at $x = 0.8$ and reattaches at $x = 2.4$. From Figures 3.48-3.49 we see that both pressure and skin friction do not return to their undisturbed state, the same as in Gajjar (1987). The interaction is expressed concisely by the pressure-displacement laws together with equations (1.12) - (1.15), (3.15) and (3.16). The results show that for fully developed flows, while the leading order displacement of the free surface is the same as for the boundary layer displacement, the surface pressure which drives the boundary layer is made up of

(1) the induced hydrostatic pressure due to displacement of the free surface, and (2) the induced pressure due to vertical acceleration of the fluid. For the convex corner this latter component (2) (A'') is important closest to the corner, whereas the other component (1) (A) is responsible for the adjustment to the new downstream state.
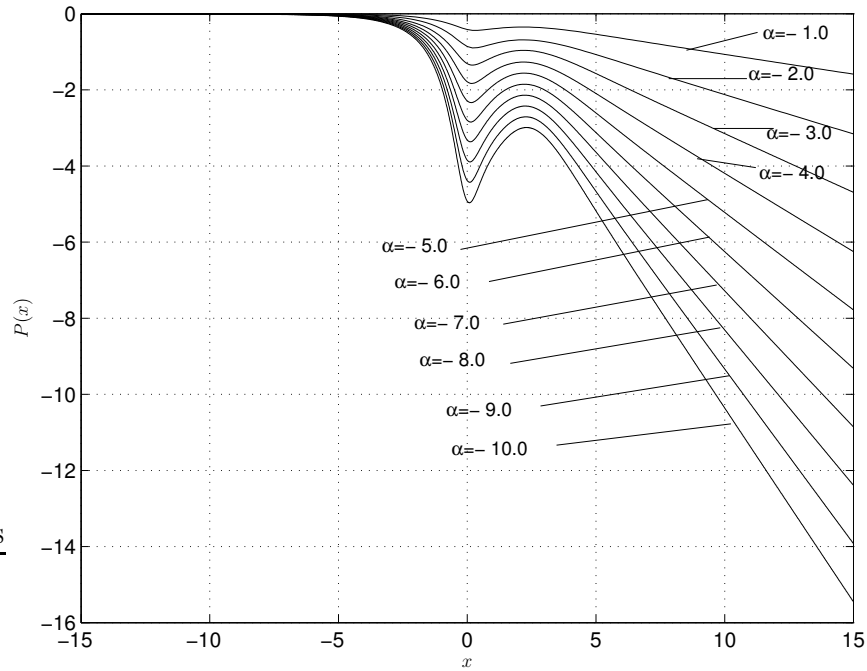
Figure 3.48: Pressure distributions for various angles of α and $\sigma = 0.1$.

PSfrag replacements
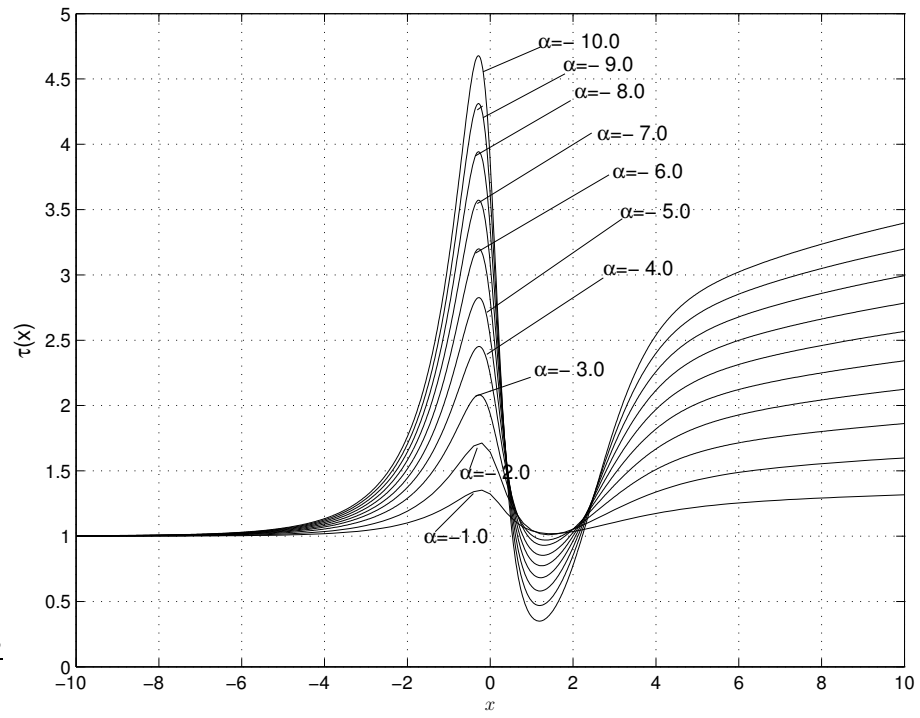
Figure 3.49: Skin friction distributions for various angles of α and $\sigma = 0.1$.
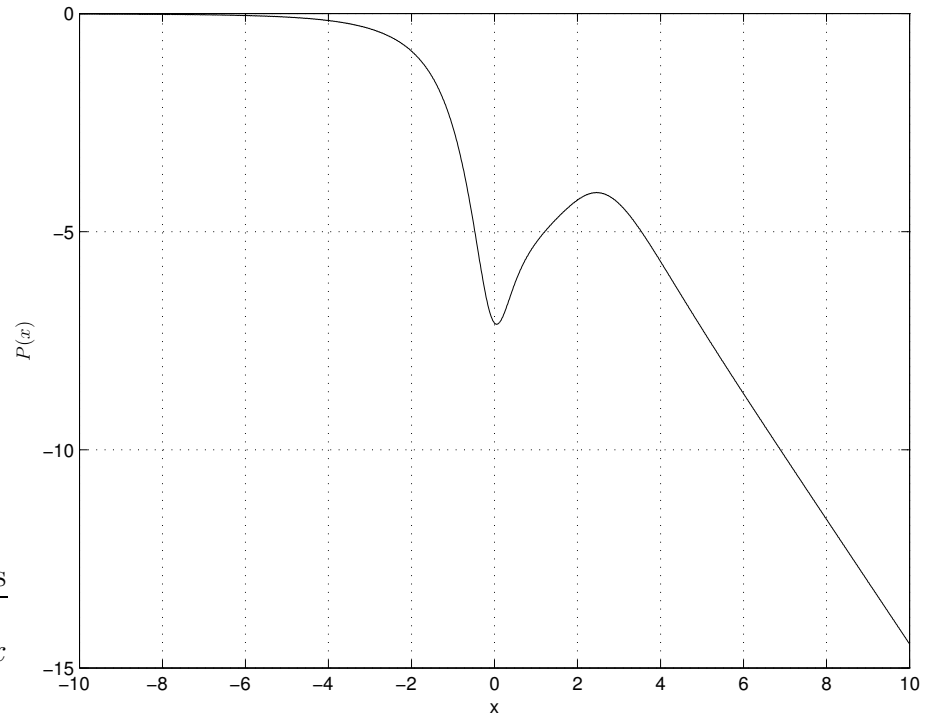
Figure 3.50: Pressure distribution for separated flow for $\sigma = 0.1$, $\alpha = -14.0$.

PSfrag replacements
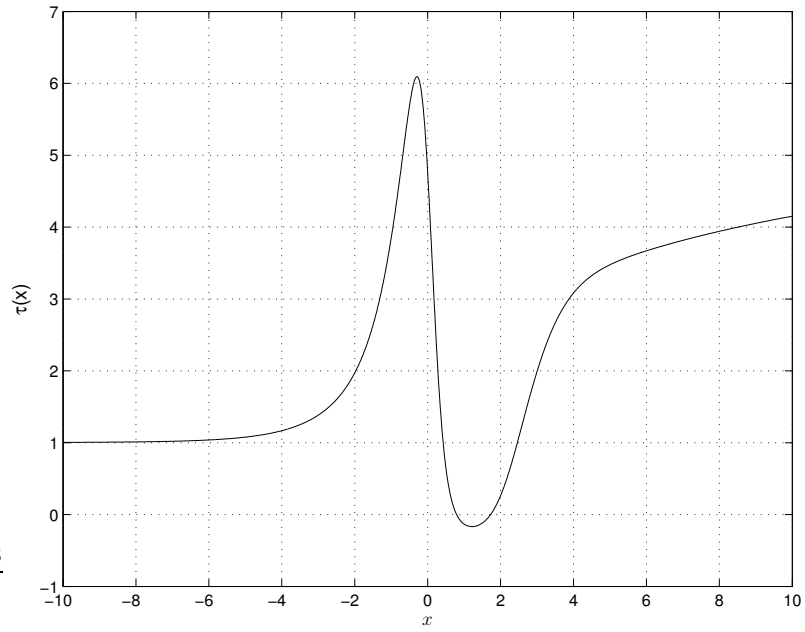
Figure 3.51: Skin friction distribution for separated flow for $\sigma = 0.1$, $\alpha = -14.0$.
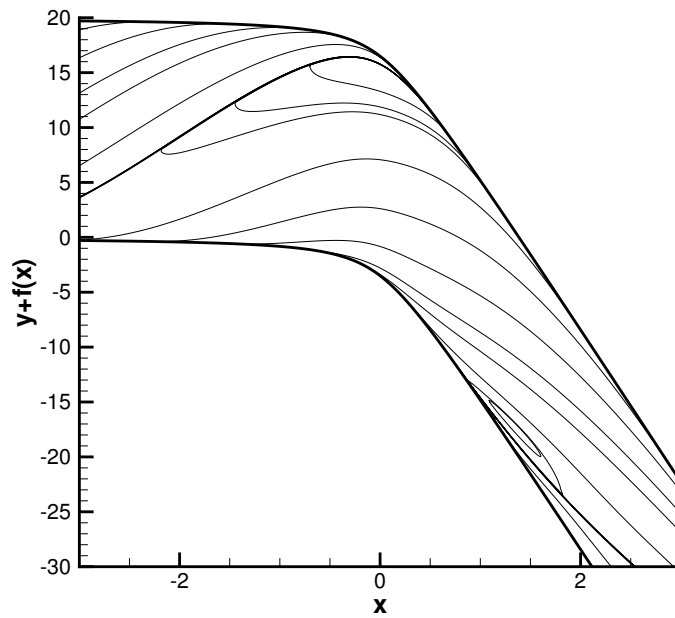
Figure 3.52: Streamline patterns showing separation region for $\sigma = 0.1$, $\alpha = -14.0$.

Results for $\sigma = 1.0$

The pressure and skin friction distributions for $\sigma = 1.0$ are in Figures 3.53 and

3.54. We can see that the pressure decreases slightly in the vicinity of the corner and downstream of the corner it increases linearly. The skin friction figure shows a maximum in the vicinity of the corner, decreases slightly downstream of it and finally increases far downstream of the corner. The pressure and skin friction distributions for $\alpha = -20$ are shown in Figures 3.54 and 3.55. Gajjar in his paper hints that for $\sigma = 1.0$, separation may occur at $\alpha = -15$. Our numerical results suggests that there is no separation even as far as $\alpha = -20$. Even up as far as $\alpha = -30$ we did not observe any separation. The pressure distribution also suggests that there is no longer any local pressure minimum or maximum, but only a favourable pressure gradient, suggesting no separation

PSfrag replacements
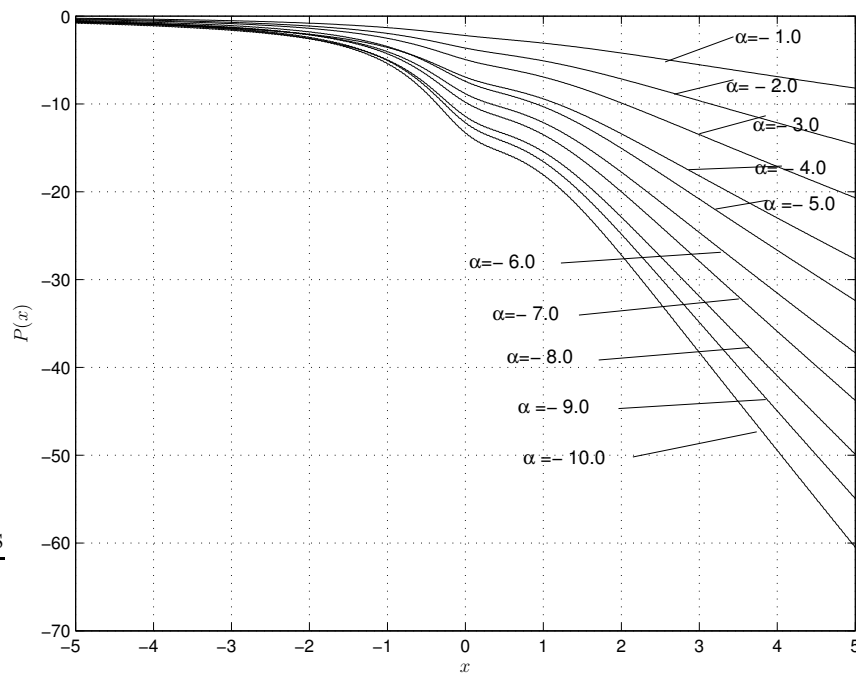
Figure 3.53: Pressure distributions for various angles of α and $\sigma = 1$.
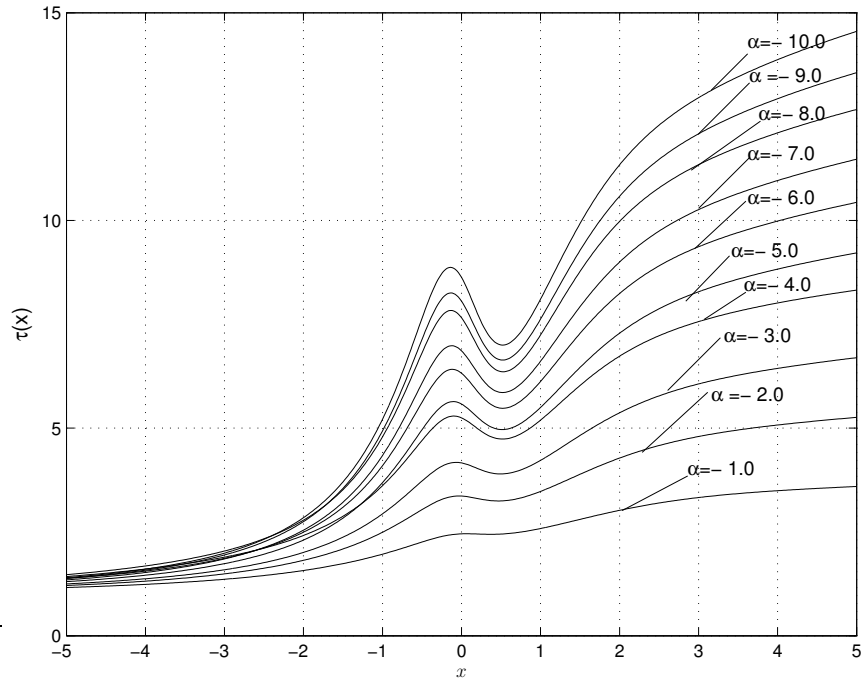
Figure 3.54: Skin friction distributions for various angles of α and $\sigma = 1$.
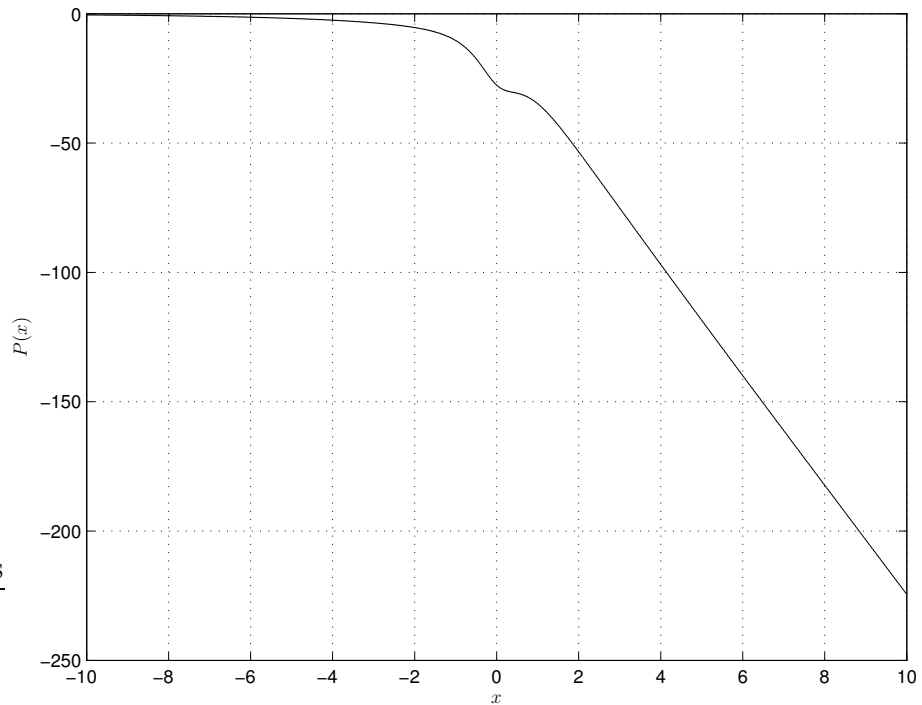
Figure 3.55: Pressure distribution for $\alpha = -20.0$ and $\sigma = 1$.

PSfrag replacements
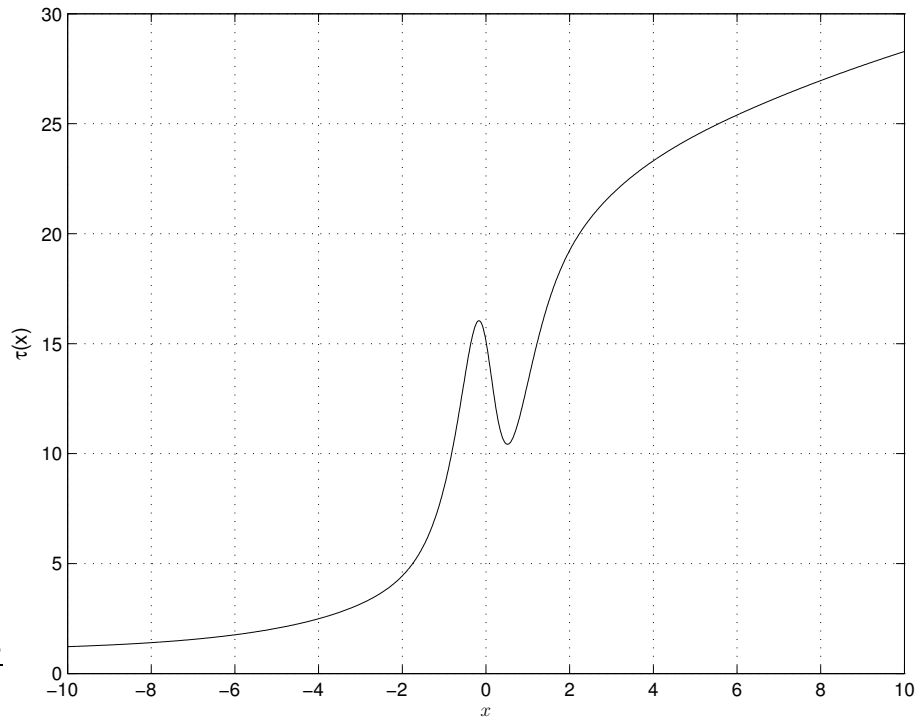
Figure 3.56: Skin friction distribution for $\alpha = -20.0$ and $\sigma = 1$.

Results for $\sigma = 2.0$

For $\sigma = 2.0$, the pressure and skin friction distributions are shown in Figures 3.57 and 3.58. As one can observe, the pressure decreases linearly except for a slight drop in the vicinity of the corner. The shear increases linearly until there is a slight drop just downstream of the corner and then finally increases far downstream. We did not have any problems with the convergence of our numerical method as the value of σ was increased. The domain along the streamwise direction which was truncated previously at $x_{-\infty} = -40$ and $x_\infty = 40$ produced oscillations in the results. For this reason, larger computational domains were tried and we found that with $x_{-\infty} = -80$ and $x_\infty = 80$ the calculations did not produce any oscillations in the results, and therefore the calculations were performed with $x \in [-80, 80]$.
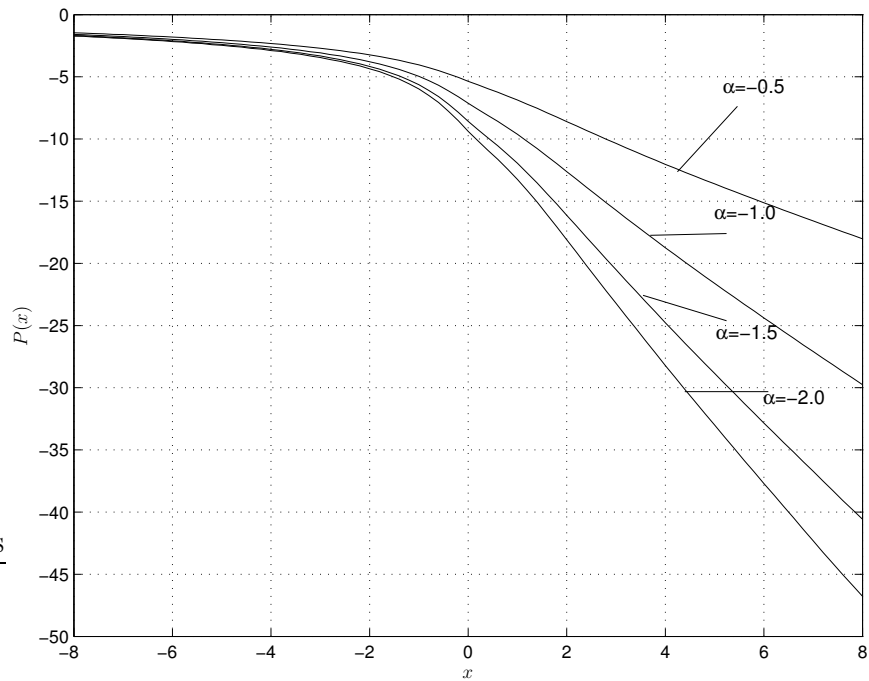
Figure 3.57: Pressure distributions for various angles of α and $\sigma = 2$.
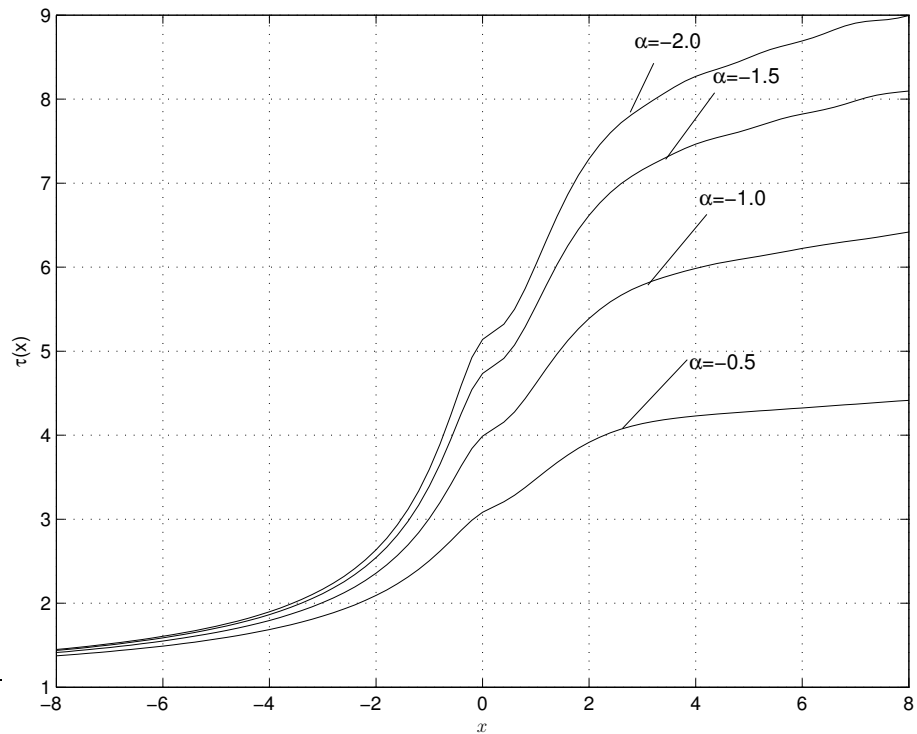
Figure 3.58: Skin friction distributions for various angles of α and $\sigma = 2$.

PSfrag replacements
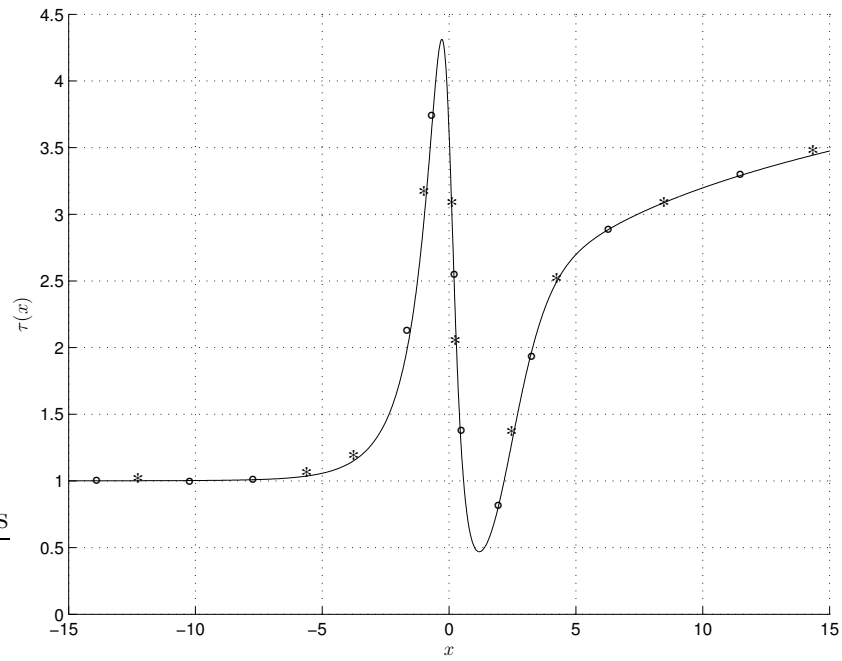
Figure 3.59: Skin friction distributions for various grids with $\sigma = 0.1$, $\alpha = -9.0$: '-' (3201×64), 'o' (1601×70), '$*$' (1201×90).

PSfrag replacements
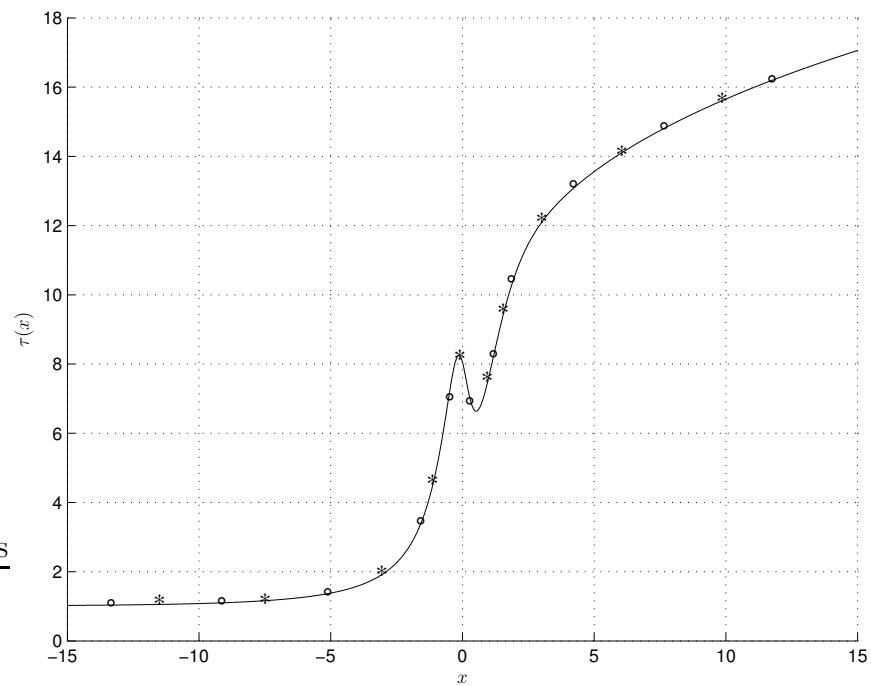
Figure 3.60: Skin friction distributions for various grids with $\sigma = 1.0$, $\alpha = -9.0$: '-' (3201×64), 'o' (1601×70), '$*$' (1201×90).

PSfrag replacements
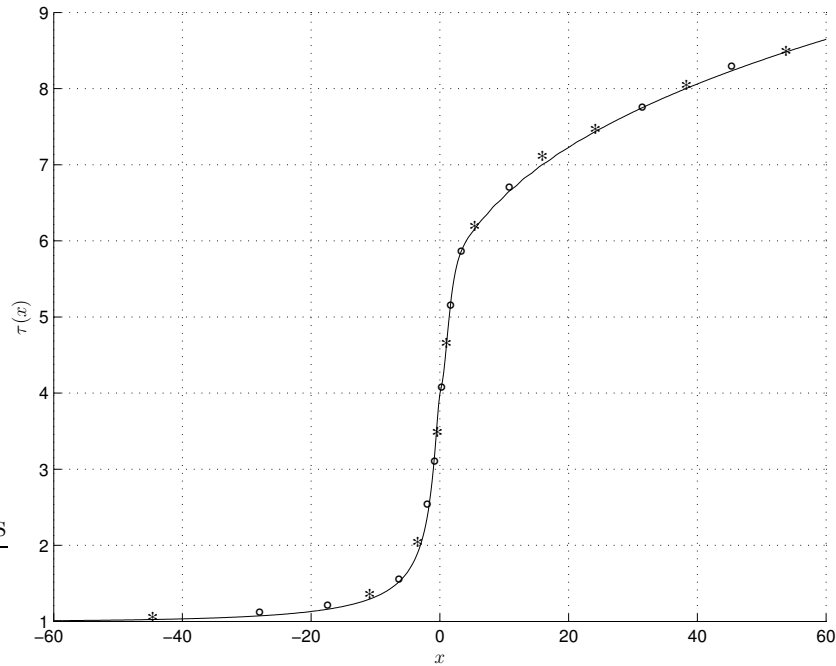
Figure 3.61: Skin friction distributions for various grids with $\sigma = 2.0$, $\alpha = -1.0$: '-' (3201×64), 'o' (1601×70), '*' (1201×90).

Calculations were performed to assess the dependency of the computed result on the grid size, the results of which appear in Figures 3.59, 3.60, 3.61 for $\sigma = 0.1, 1.0, 2.0$. As one can observe the results are visually indistinguishable. The results were also checked by changing the size of the domain along the streamwise direction, see Figure 3.62. Again the results are indistinguishable.

PSfrag replacements
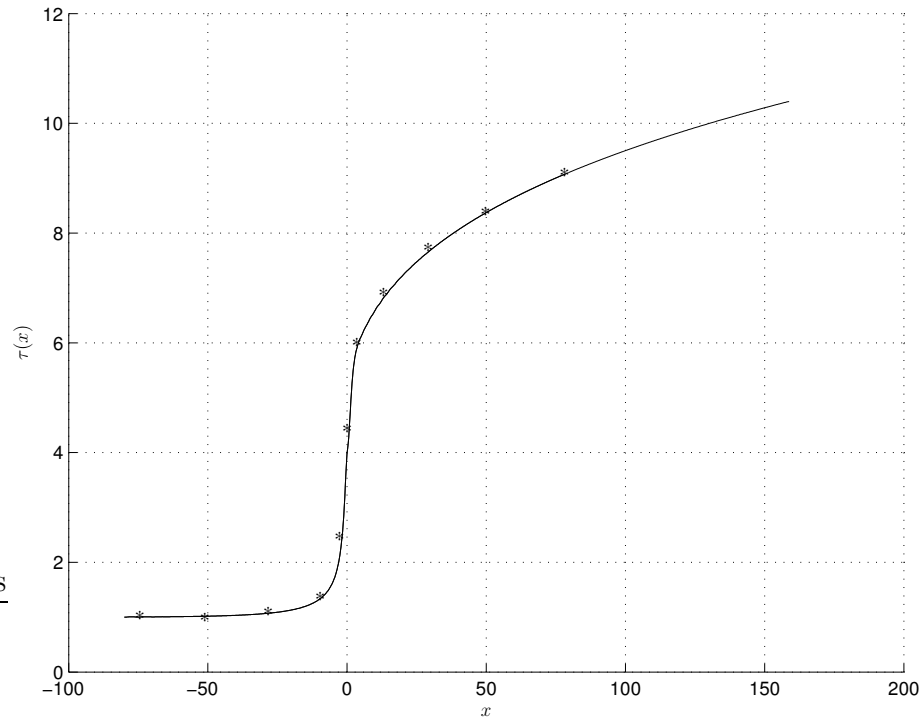
Figure 3.62: Skin friction distributions for various grids with $\sigma = 2.0$, $\alpha = -1.0$: '-' $x \in [-80, 80]$, '*' $x \in [-80, 160]$.

Figures 3.63 and 3.64 show the pressure and skin friction distributions for various values of σ at $\alpha = -2.0$. As the value of σ is increased the pressure falls linearly and skin friction increases linearly. Unlike the wall-jet problem of Chapter 3 the asymptotic form of (3.16) ensures that both pressure and skin friction do not return to their undisturbed state far downstream.
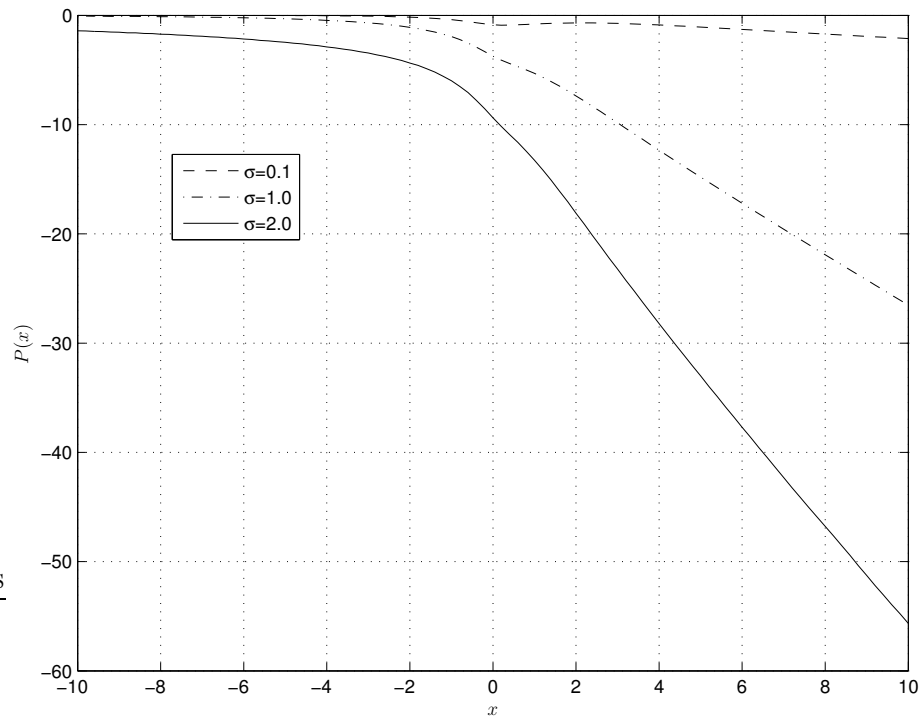
Figure 3.63: Pressure distributions for various values of σ with $\alpha = -2.0$.
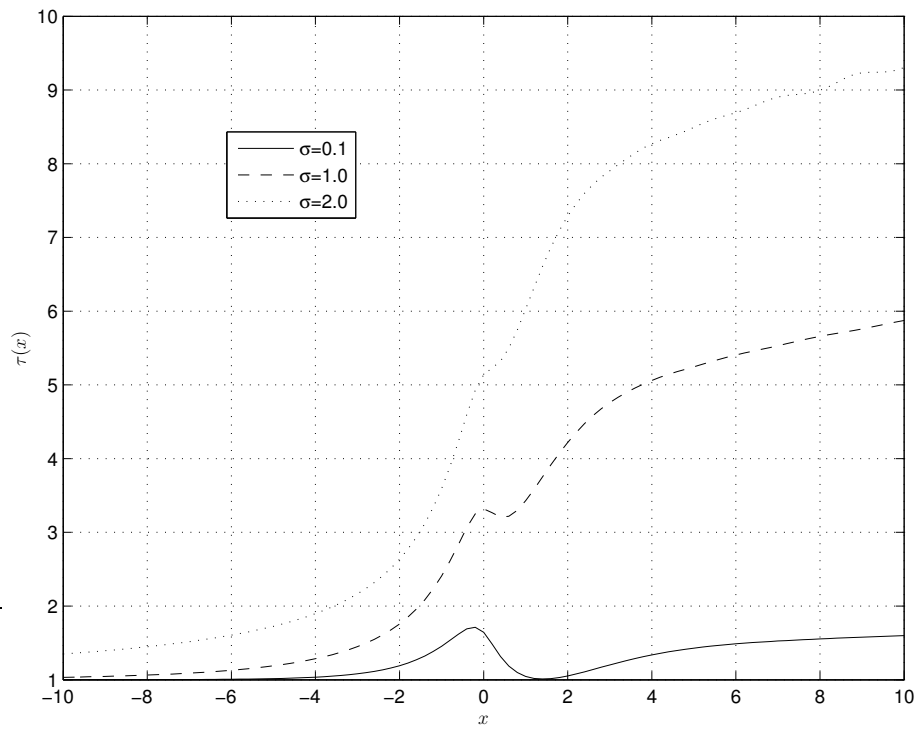
Figure 3.64: Skin friction distributions for various values of σ with $\alpha = -2.0$.

3.5   Liquid layer flow over humps and indentations

The boundary shape was chosen to be $f = h \exp(-k^2 x^2)$ for a range of values of σ, h and k ($h > 0$). The computational domain along the streamwise direction that was truncated previously at $x_{-\infty} = -40$ and $x_{\infty} = 40$ produced oscillations in the results. Calculations were performed using various domain values in the streamwise direction and it was found that for $x_{-\infty} = -100$ and $x_{\infty} = 100$ there were no oscillations in the results. 8001 points were used in the streamwise direction and 64 polynomials represented the stream function in the y-direction. The same numerical technique discussed in Chapter 2 was used. The governing equations and problem formulation are exactly the same as for the jet-like boundary layer approaching humps and indentations except for the pressure-displacement law.

Results for $\sigma = 0.5$

For $\sigma = 0.5$, we observe that for $k = 1.0$, the flow first separates at $h = 4.3$ ahead of the hump and at $h = 4.6$ behind the hump. Looking at the pressure plot in Figure 3.65, we observe that there is a rise in the pressure in front of the hump followed by a decrease in the vicinity of the centre of the hump ($x = 0$), and then the pressure increases downstream of the hump ($x > 0$), followed by a decrease in pressure before reaching its original condition ($p = 0$). The shear stress shown in Figure 3.66 first decreases in front of the hump and then increases in the vicinity of centre of the hump ($x = 0$). Behind the hump the shear stress first decreases, then reaches a maximum before finally returning to its original value ($\tau = 1$).

We increased the hump width parameter k in order to investigate the effect of the jump width on the fluid flow. We performed calculations with $k = 2.0$ and observed that separation occurs at $h = 1.9$ behind the hump and at $h = 4.0$ ahead of the hump. The pressure distribution curves tend to flatten in the separation region behind the hump as the value of h is increased. The shear profile shows the same behaviour as that for $k = 1.0$. We observe that separation is induced at smaller values of h as the value of k is increased.
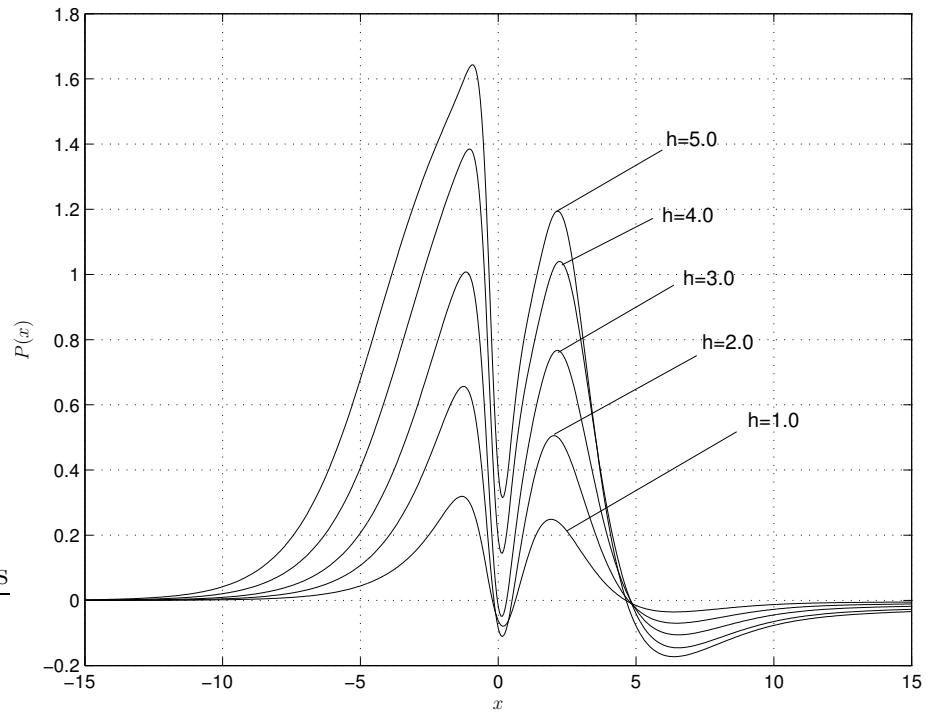
Figure 3.65: Pressure distributions for various values of h with $k = 1.0$, $\sigma = 0.5$.
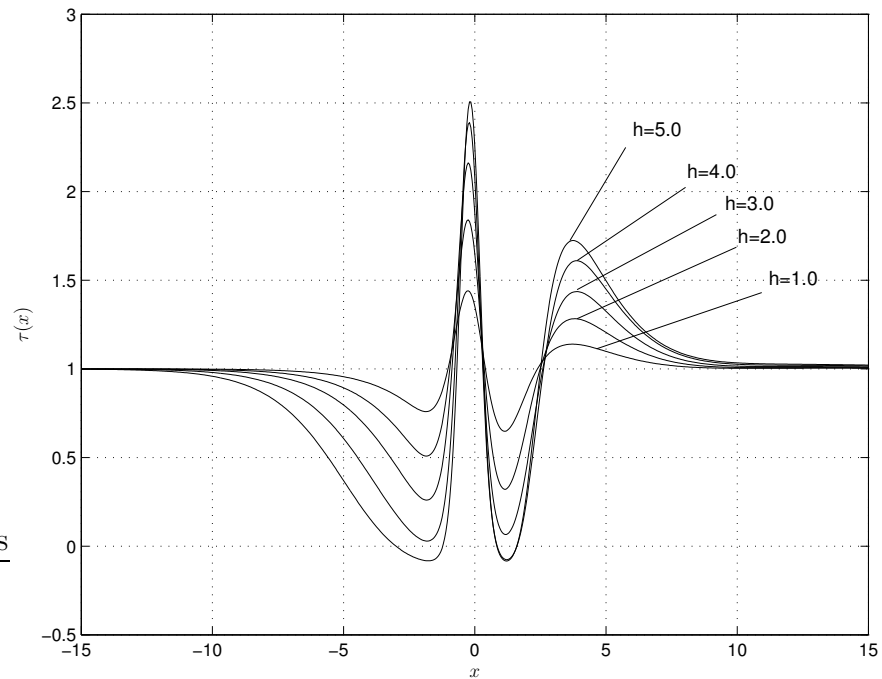
Figure 3.66: Skin friction distributions for various values of h with $k = 1.0$, $\sigma = 0.5$.

PSfrag replacements
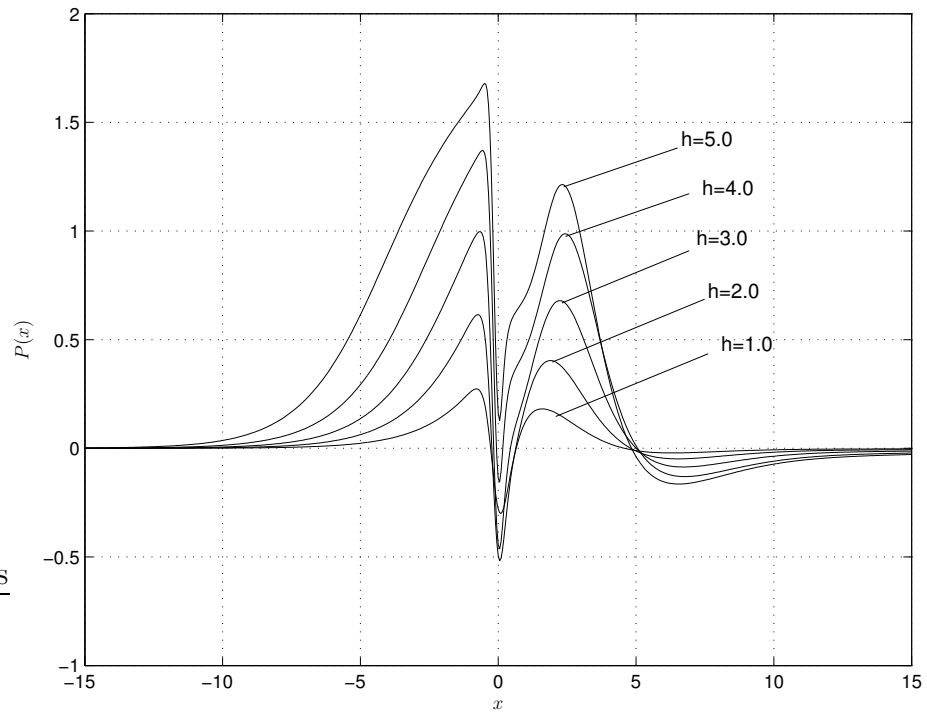
Figure 3.67: Pressure distributions for various values of h with $k = 2.0$, $\sigma = 0.5$.

PSfrag replacements
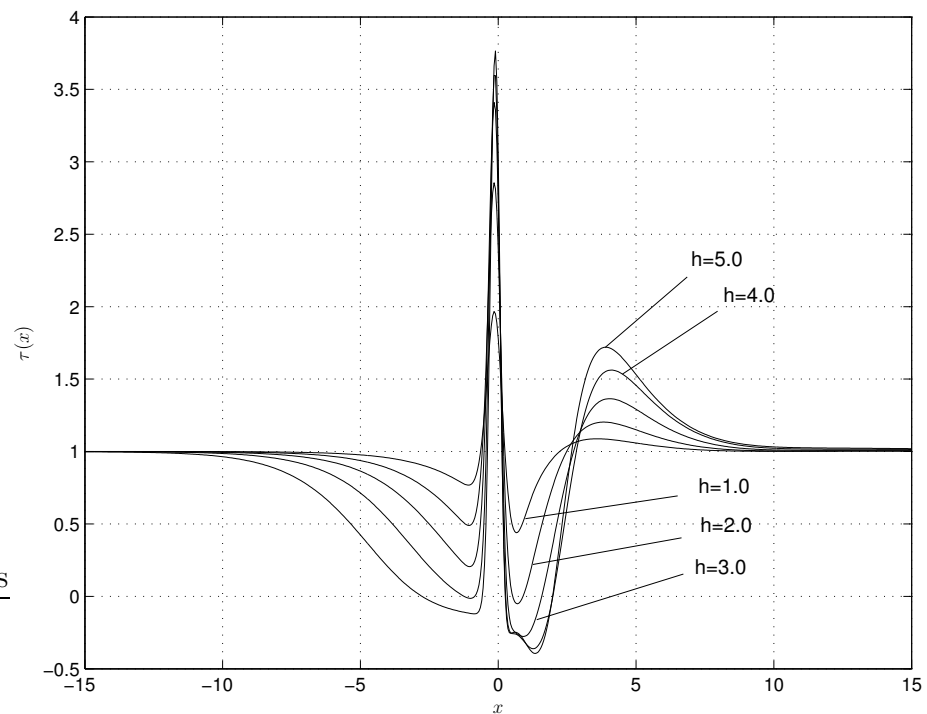
Figure 3.68: Skin friction distributions for various values of h with $k = 2.0$, $\sigma = 0.5$.

Results for $\sigma = 1.0$

In this section we present numerical results for $\sigma = 1.0$ with k and h varying. For $k = 1.0$, the flow separates at $h = 5.85$ ahead of the hump and at $h = 10.0$ behind the hump. Looking at the pressure profile in Figure 3.69, we see that there is a sharp decrease in pressure along the centre of the hump ($x = 0$) at higher values of h. From the shear profile shown in Figure 3.70, there is a sharp increase in the shear along the centre of the hump ($x = 0$) that decreases sharply immediately downstream of the centre of the hump ($x > 0$) where the flow undergoes separation. The pressure and shear plots for $h = 10.0$ are shown in Figures 3.71 and 3.72. We observe that ahead of the obstacle, we see free interaction with $p > 0$ together with the hydraulic jump, see Gajjar & Smith (1983).

For $k = 2.0$, the flow separates at $h = 2.85$ behind the hump and at $h = 5.7$ ahead of the hump. The pressure increases ahead of the hump and decreases sharply at the exact centre of the hump ($x = 0$) displaying apparent discontinuous behaviour, see Figure 3.74. The shear stress shown in Figure 3.75 decreases ahead of the hump ($x < 0$), increases sharply at the centre of the hump ($x = 0$), decreases sharply slightly downstream of the centre of the hump ($x > 0$) and once again increases before reaching its initial state ($\tau = 1.0$). For $k = 1.0$, the flow separates at $x = -51.0$ and reattaches at $x = -10$ ahead of the hump, and then separates at $x = 1.0$ and reattaches at $x = 1.5$ behind the hump as shown in Figure 3.73.

Finally, for $k = 2.0$ and $h = 6.0$ the streamline pattern shown in Figure 3.76 suggests that the flow separates at $x = -11.0$ and reattaches at $x = -1.0$ behind the hump. The flow ahead of the hump undergoes separation at $x = 0.5$ and reattaches at $x = 1.5$. We observe that from the streamline pattern the separation region behind the hump is much shorter than the separation region ahead of the hump.
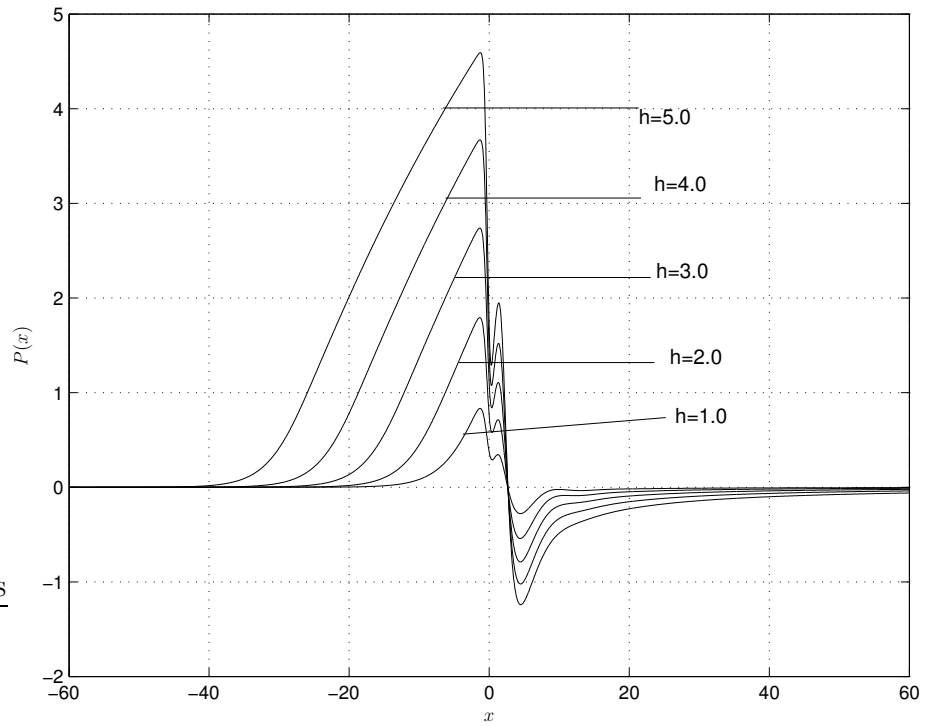
Figure 3.69: Pressure distributions for various values of h with $k = 1.0$, $\sigma = 1.0$.
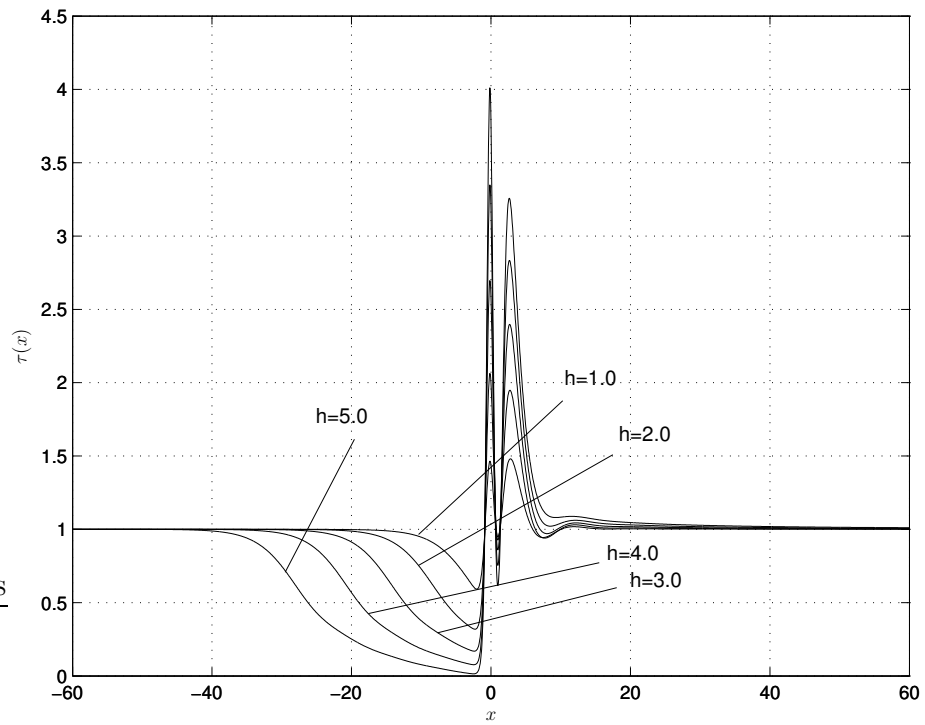
Figure 3.70: Skin friction distributions for various values of h with $k = 1.0$, $\sigma = 1.0$.
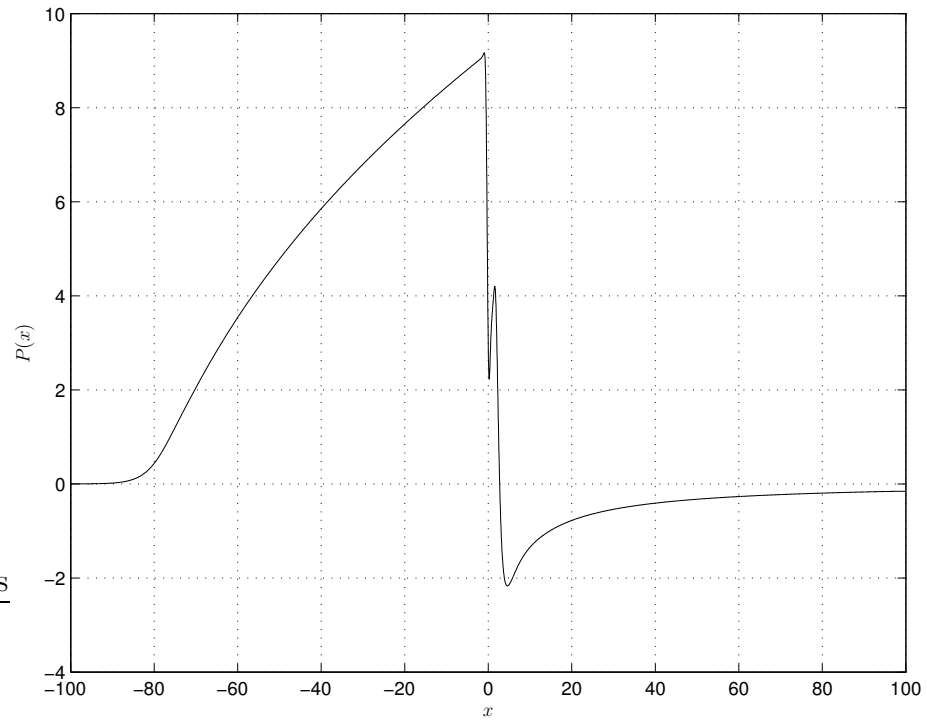
Figure 3.71: Pressure distribution for $h = 10$ with $k = 1.0$, $\sigma = 1.0$.
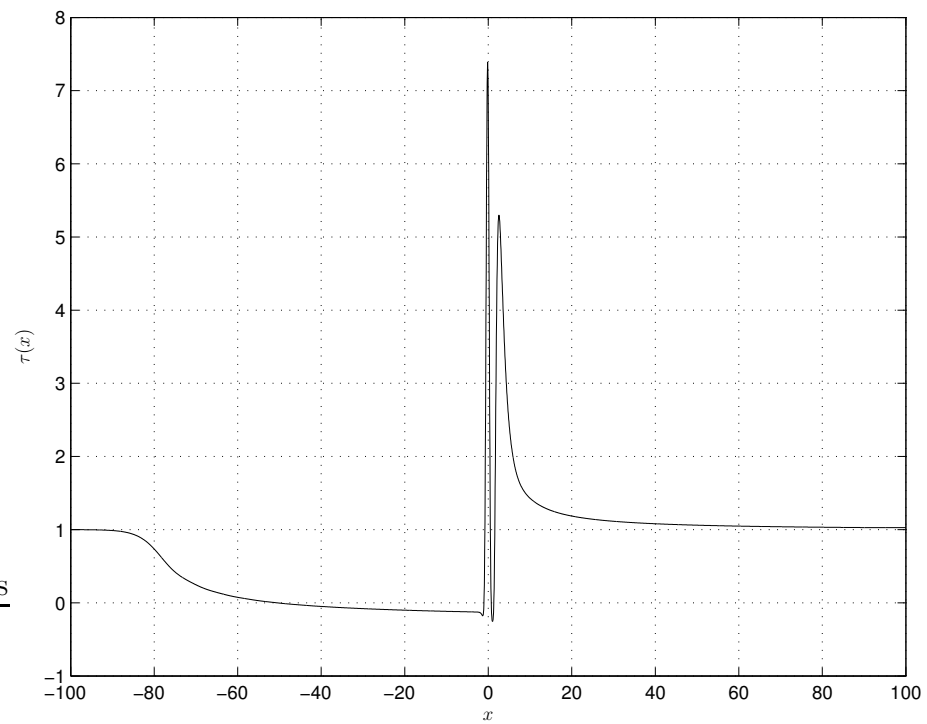
Figure 3.72: Skin friction distribution for $h = 10$ with $k = 1.0$, $\sigma = 1.0$.
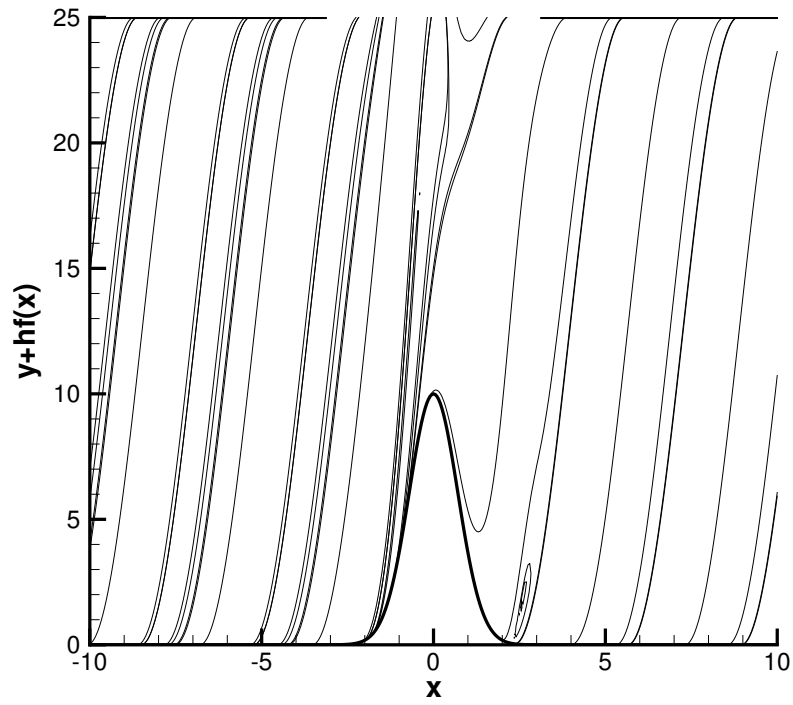
Figure 3.73: Streamline pattern for $h = 10.0$ with $k = 1.0$, $\sigma = 1.0$.

PSfrag replacements
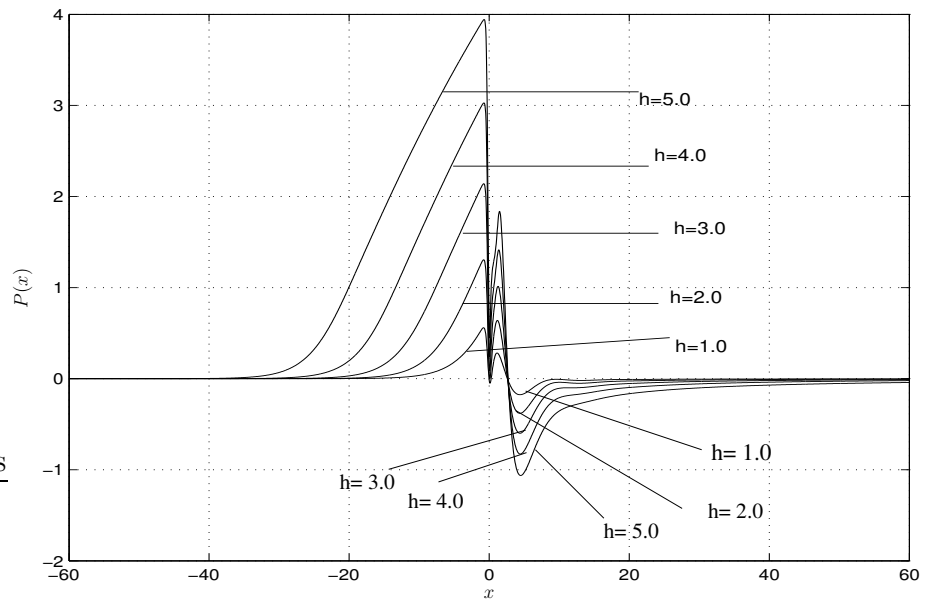
Figure 3.74: Pressure distributions for various values of h with $k = 2.0$, $\sigma = 1.0$.
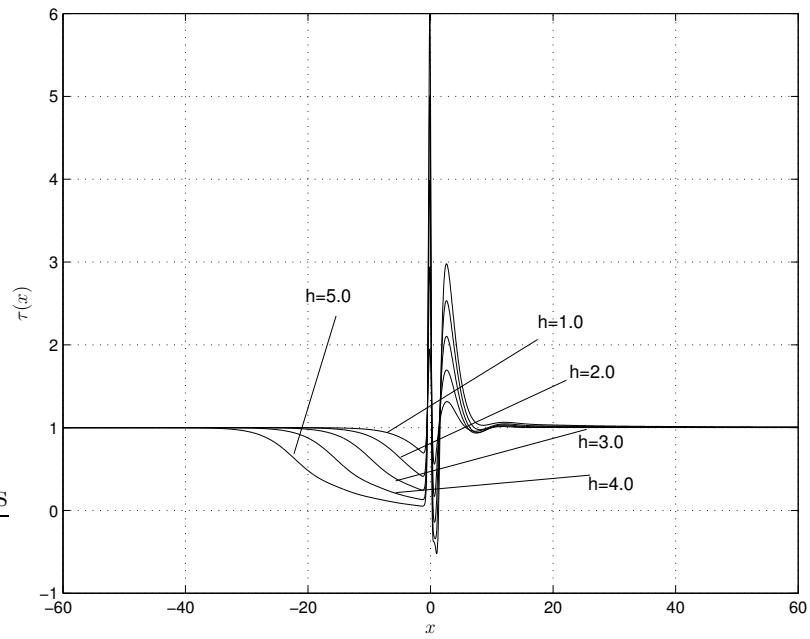
Figure 3.75: Skin friction distributions for various values of h with $k = 2.0$, $\sigma = 1.0$.
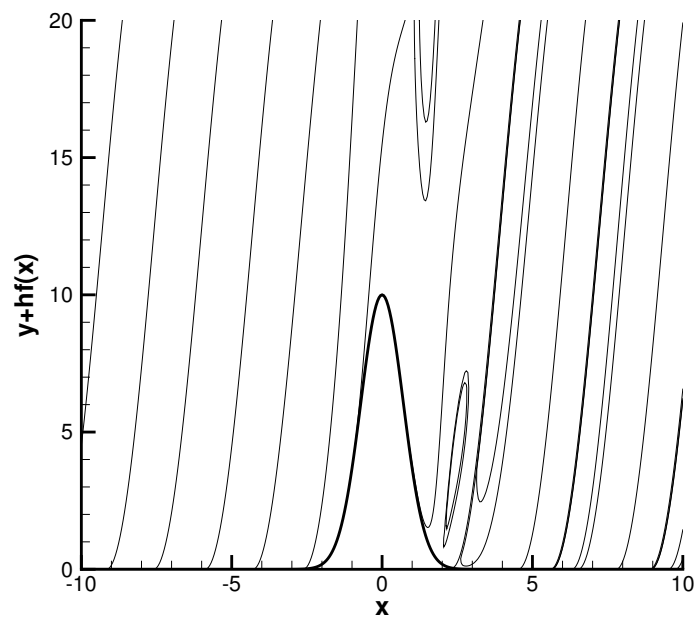
Figure 3.76: Streamline pattern for $h = 6.0$ with $k = 2.0$, $\sigma = 1.0$.

Results for $\sigma = 2.0$

In this section we present numerical results for $\sigma = 2.0$ with k and h varying. Looking at the pressure distributions, see Figure 3.77, the pressure increases linearly from its initial value $(p(x) = 0)$ ahead of the hump, decreases sharply at the centre of the hump $(x = 0)$ displaying apparent discontinuous behaviour and finally increasing exhibiting a oscillatory behaviour behind the hump before reaching its initial value. The shear decreases from its initial value and increases at $x = 0$, then decreases again before slightly increasing downstream of $x = 0$. Downstream of the centre of the hump $(x > 0)$, the flow is oscillatory as shown in Figure 3.78. Figures 3.79 and 3.80 show the behaviour of pressure and shear for $h = 10.0$. We observe that at larger values of h there is no oscillatory behaviour downstream of centre of the hump. The flow separates at $h = 7.0$. A step size of $\Delta x = 0.001$ was used around the centre of the hump to see whether the oscillations occurred at lower values of h for both $k = 1.0$ and $k = 2.0$. Our numerical result showed that the oscillations still occurred.

For $k = 2.0$, the pressure increases linearly from its initial value ahead of the hump, decreases sharply at the centre of the hump $(x = 0)$ and then finally increases to its initial value, see Figure 3.81. The pressure exhibits oscillatory behaviour behind the hump. The shear stress decreases from its initial value before increasing sharply at the centre of the hump $(x = 0)$. It then decreases slightly behind the hump exhibiting oscillatory behaviour before reaching its initial value $(\tau = 1)$ as shown in Figure 3.82. The flow separates at $h = 4.0$. The streamline plot shown in Figure 3.85 indicates that the flow separates at $x = 0.15$ and reattaches at $x = 0.4$ behind the hump.

From the computed results for $\sigma = 2.0$ we observe short-scale waves which decay downstream both in the pressure and skin friction distributions. This sort of behaviour was observed by Gajjar (1987) and Bowles & Smith (1992).
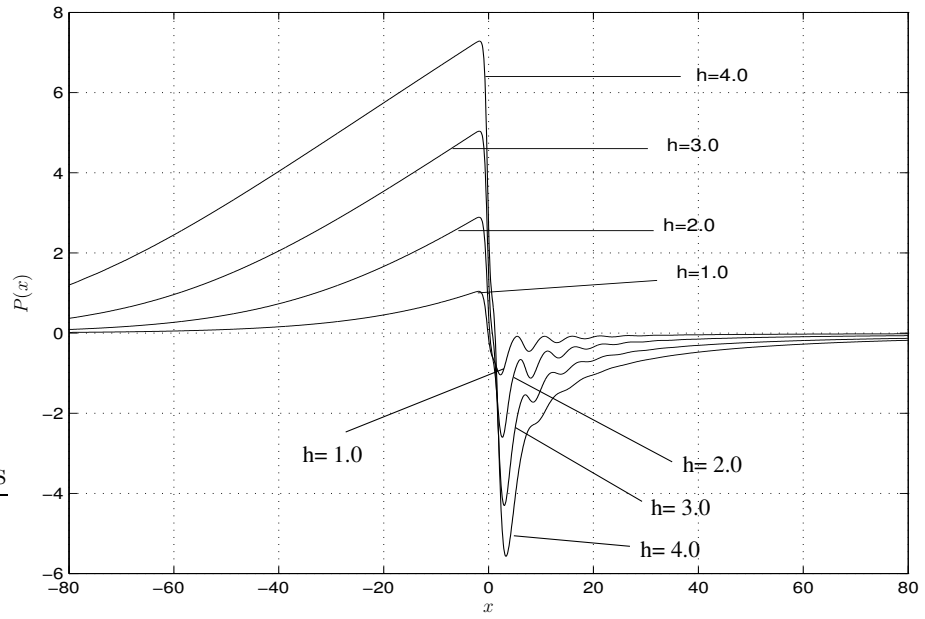
Figure 3.77: Pressure distributions for various values of h with $k = 1.0$, $\sigma = 2.0$.
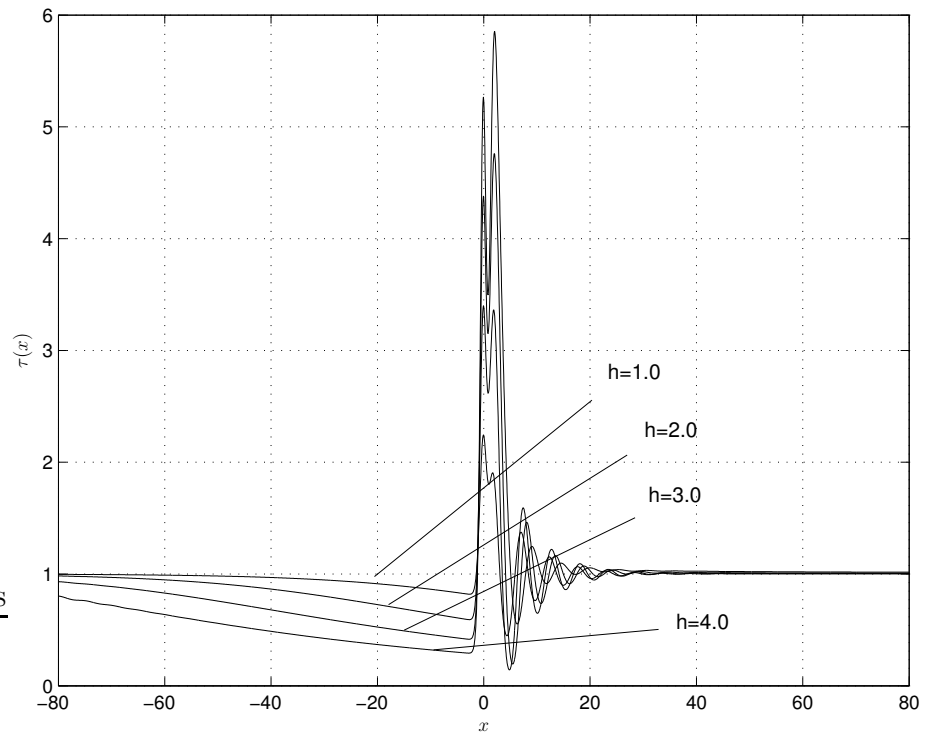
Figure 3.78: Skin friction distributions for various values of h with $k = 1.0$, $\sigma = 2.0$.
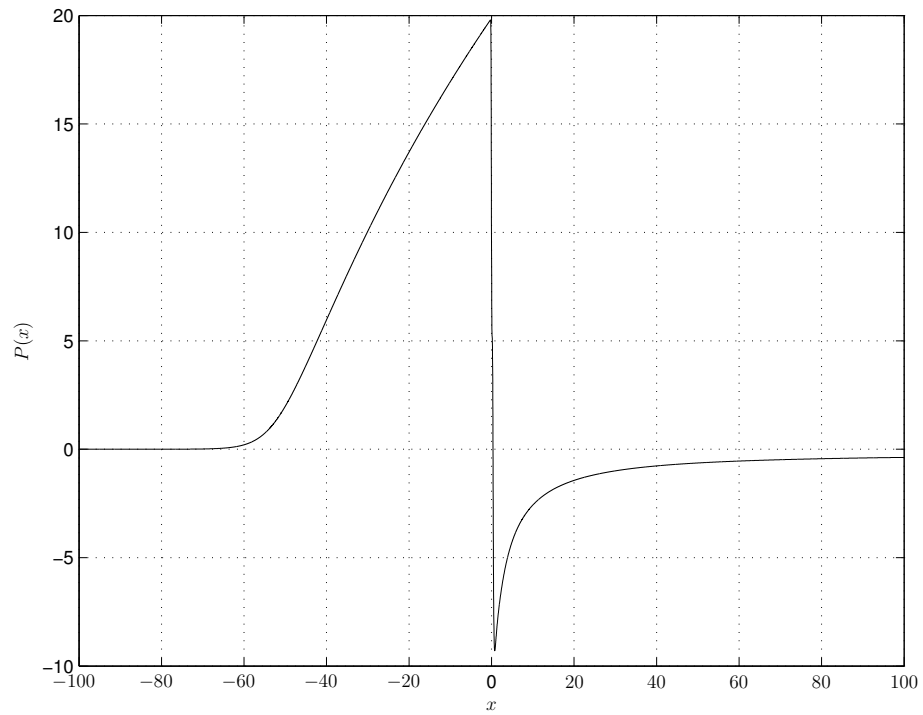
Figure 3.79: Pressure distribution for $h = 10$ with $k = 1.0$, $\sigma = 2.0$.
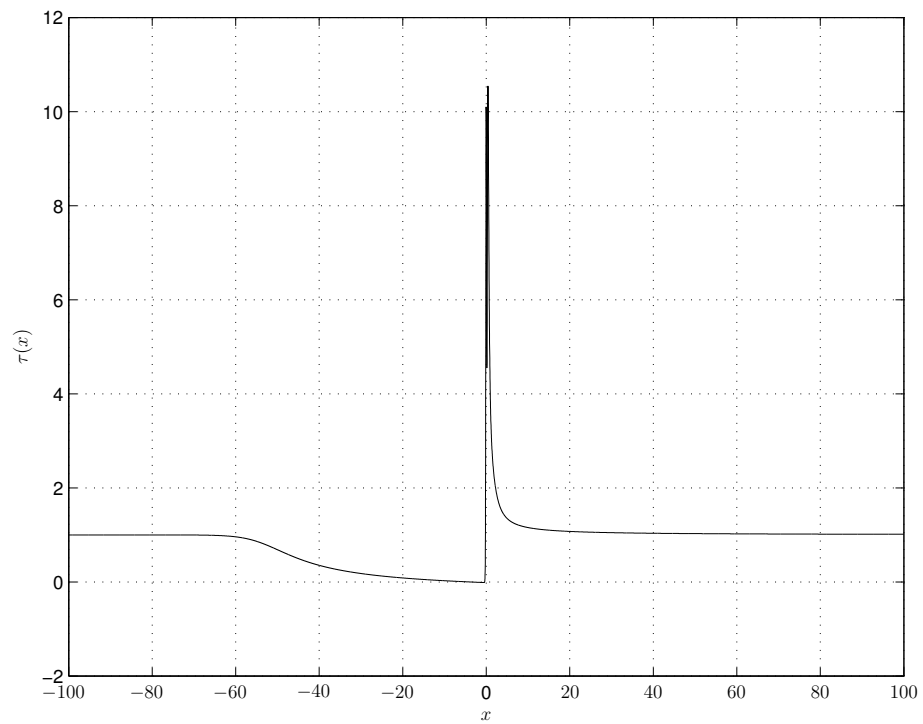
Figure 3.80: Skin friction distribution for $h = 10$ with $k = 1.0$, $\sigma = 2.0$.
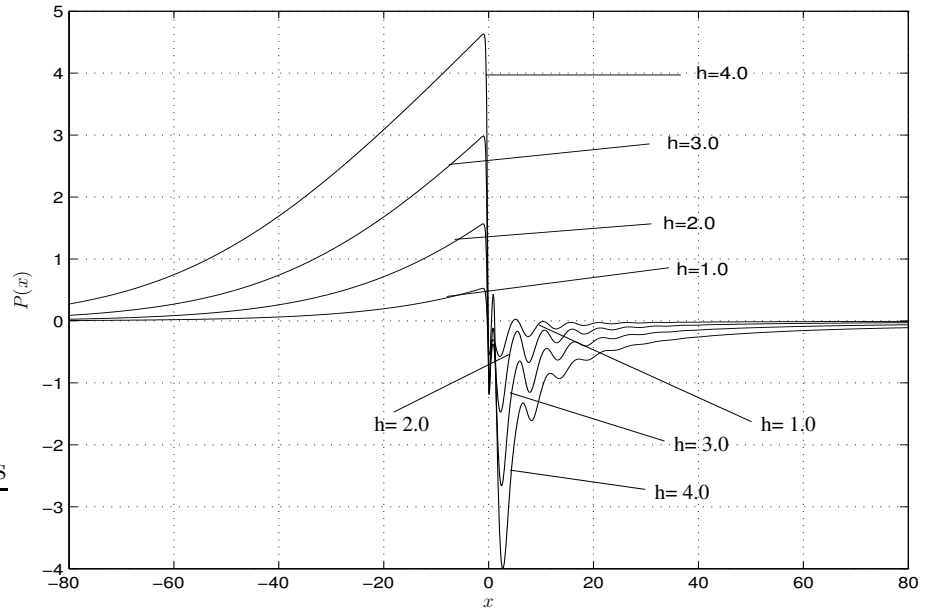
Figure 3.81: Pressure distributions for various values of h with $k = 2.0$, $\sigma = 2.0$.
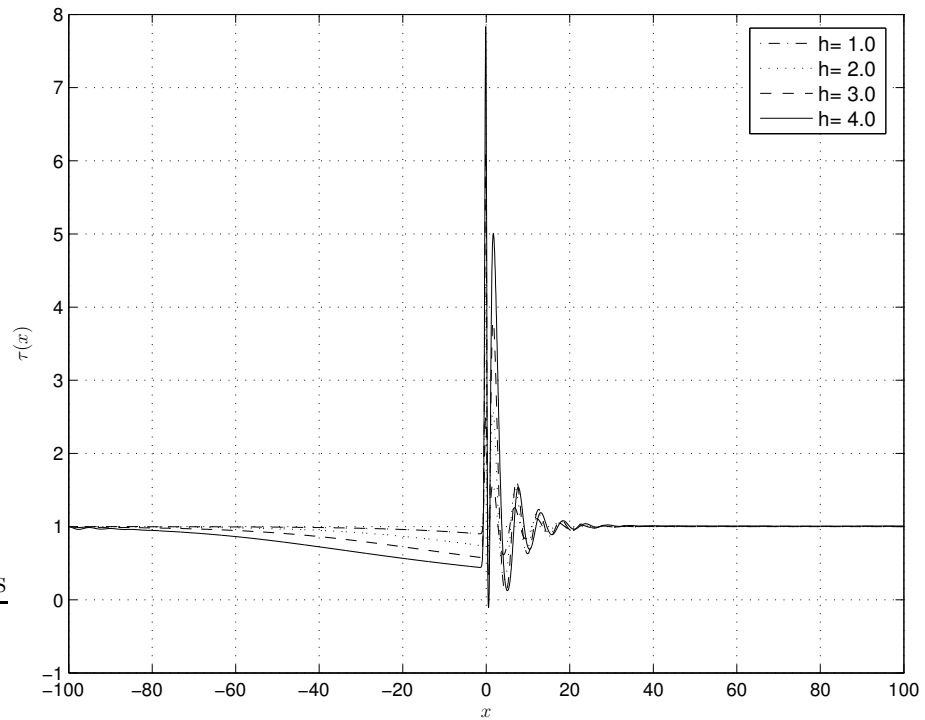
Figure 3.82: Skin friction distributions for various values of h with $k = 2.0$, $\sigma = 2.0$.
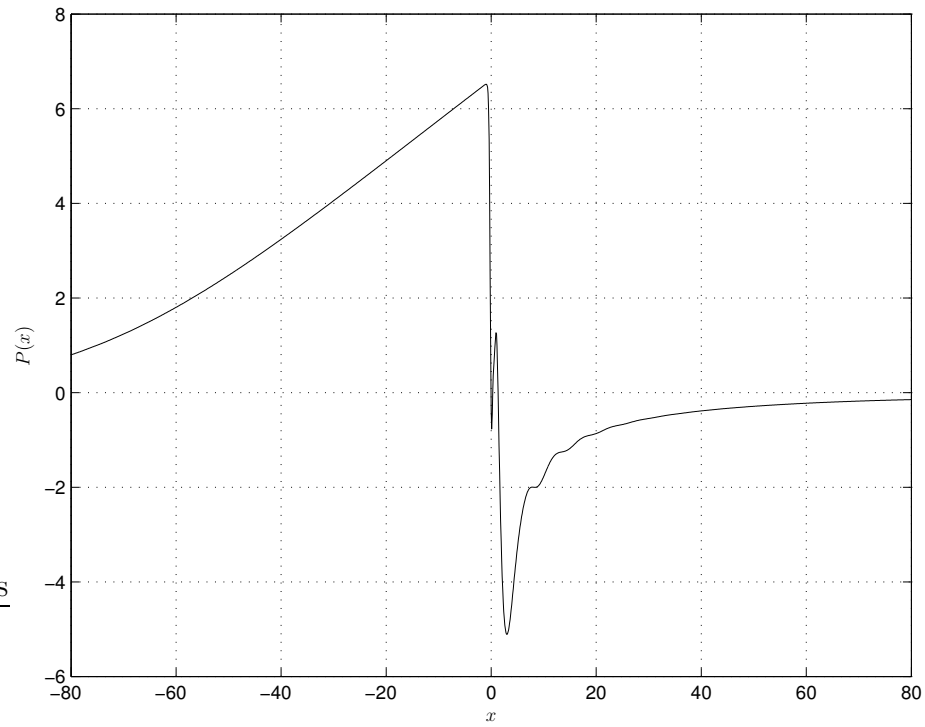
Figure 3.83: Pressure distribution for $h = 5.0$ with $k = 2.0$, $\sigma = 2.0$.
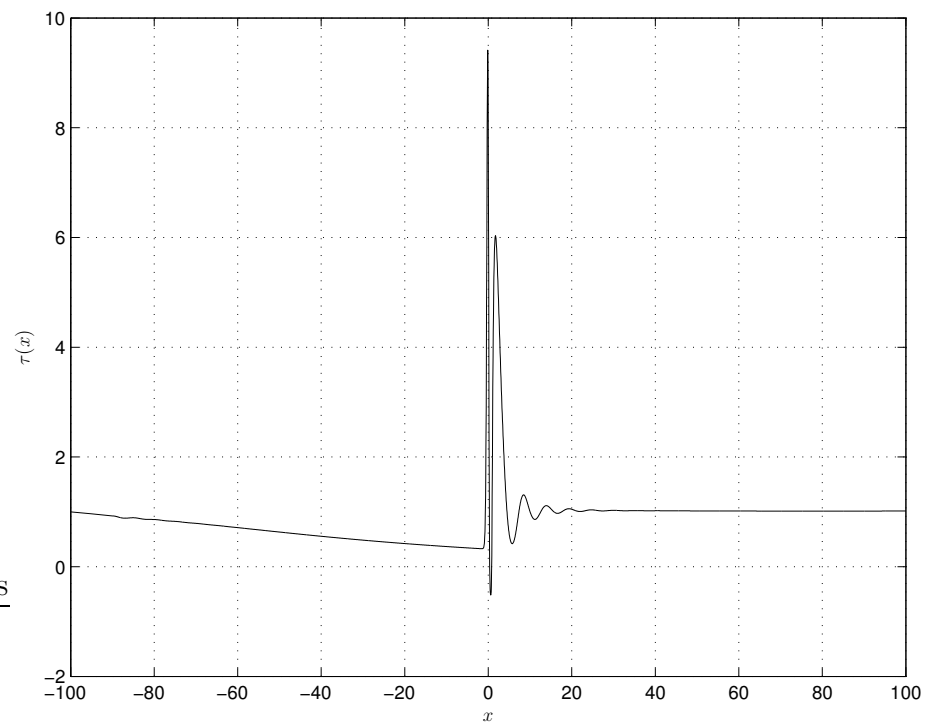
Figure 3.84: Skin friction distribution for $h = 5.0$ with $k = 2.0$, $\sigma = 2.0$.
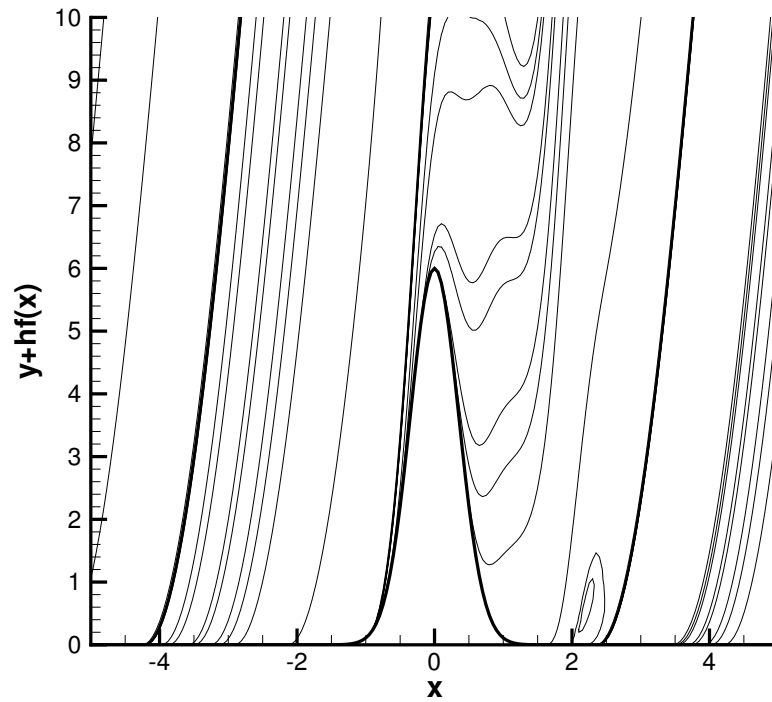
Figure 3.85: Streamline pattern for $h = 5.0$ with $k = 2.0$, $\sigma = 2.0$.

In order to assess the impact of the grid size on the numerical solution several tests were performed using various grid sizes the results of which appear in Figures 3.86 and 3.87. We can see that the results are visually indistinguishable and thus for sufficiently small grids the computed results are independent of the grid size.
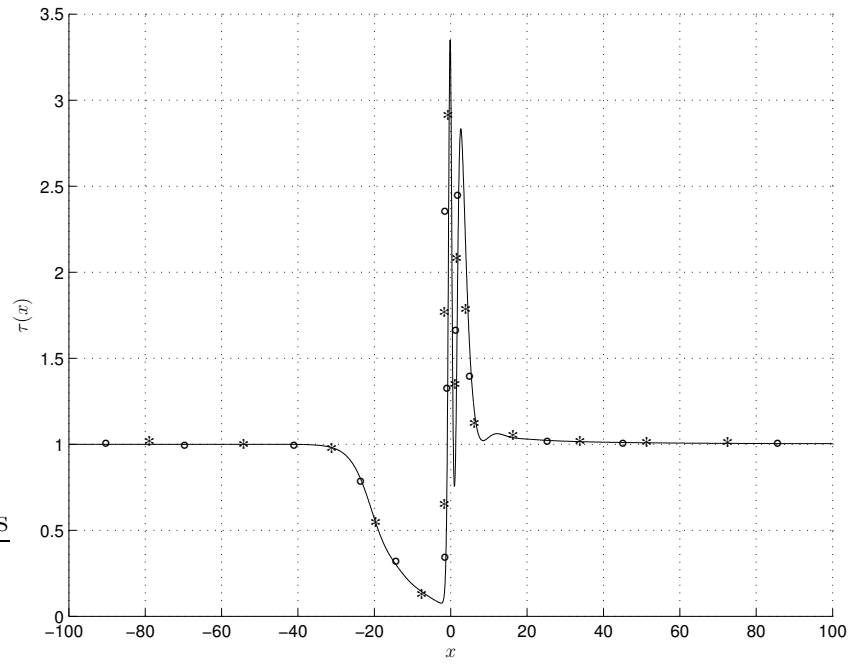
Figure 3.86: Skin friction distributions for various grids with $\sigma = 1.0$, $k = 1.0$, $h = 5.0$: '-' (8001×64), 'o' (4001×70), '*' (6001×90).
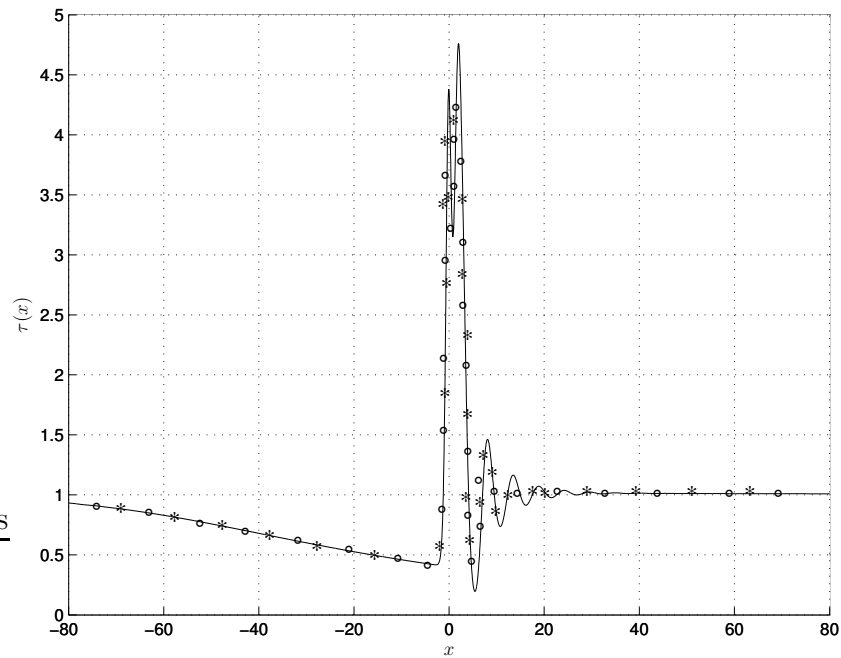
Figure 3.87: Skin friction distributions for various grids with $\sigma = 2.0$, $k = 1.0$, $h = 3.0$: '-' (8001×64), 'o' (4001×70), '*' (6001×90).

The pressure and skin friction distributions are shown in Figures 3.88 and 3.89 for various values of σ with $h = 4.0$ and $k = 1.0$. We observe that as the value of σ is increased, the appearance of short-scale waves which decay downstream increases.

PSfrag replacements
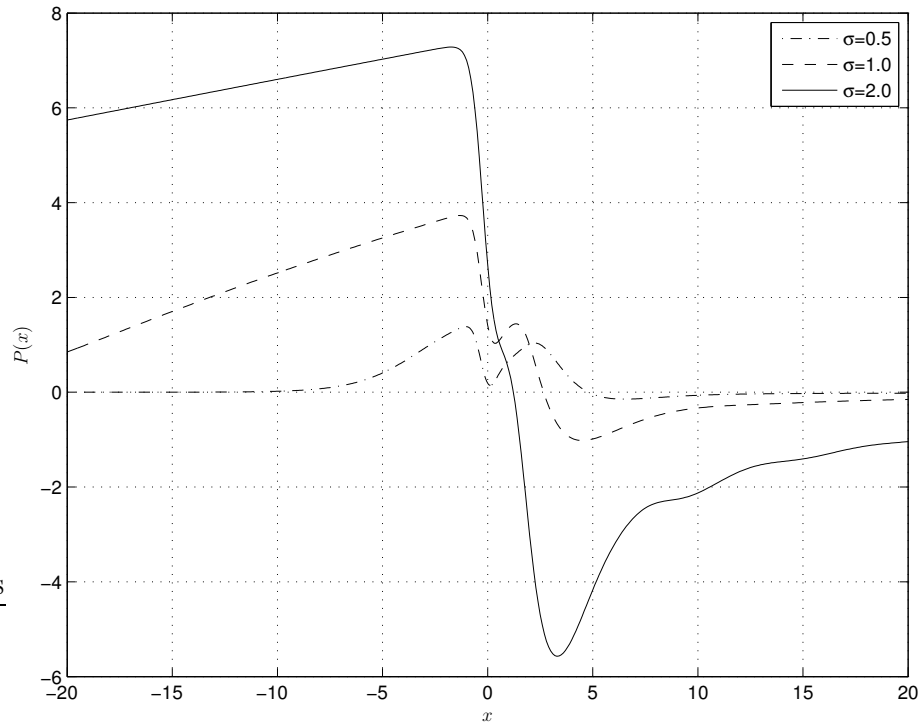
Figure 3.88: Pressure distributions for various values of σ for $h = 4.0$, $k = 1.0$.
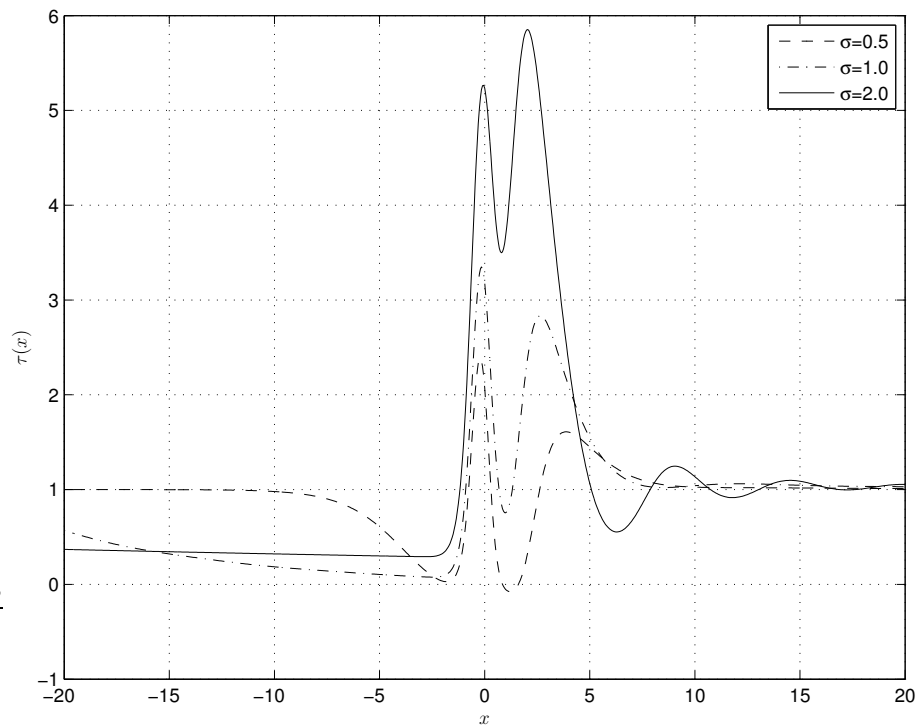
Figure 3.89: Skin friction distributions for various values of σ for $h = 4.0$, $k = 1.0$.

3.5.1   Flow over indentations

In this section we discuss the numerical results for a liquid layer flow over indentations. The shape of the indent is chosen to be $f = h\exp(-k^2x^2)$ for a range of values of h and k ($h < 0$). The computations were performed with $x_{-\infty} = -100$ and $x_\infty = 100$ with a uniform grid. 8001 points were used in the streamwise direction and 64 polynomials in the y direction.

Results for $\sigma = 0.5$

For $k = 1.0$, the pressure decreases from its initial value ahead of the indent and increases in the vicinity of the centre of the indent ($x = 0$) as shown in Figure 3.90. The pressure decreases behind the indent and finally increases to its initial value. The flow undergoes separation at $h = -2.7$ which can be observed by looking at the

shear plot, see Figure 3.91. The shear stress increases from its initial value ahead of the indent, decreases at the centre of the indent ($x = 0$), increases slightly behind the indent, decreases once again behind the indent and finally increases to its initial value ($\tau = 1.0$). The separation region is centred on the indent. At $h = -7.0$, we observe that the pressure tends to flatten out in the separated region and increase sharply near the reattachment as shown in Figure 3.92.

Next we increased the width of the indent which corresponds to shrinking the indent along the x-direction. For $k = 2.0$ the pressure and shear distributions are shown in Figures 3.94 and 3.95. The pressure and shear exhibit the same behaviour as for the case when $k = 1.0$. From the shear plot we can see that the flow separates at $h = -1.8$. As observed previously induced separation occurs at a smaller value of h as the value of k is increased.

PSfrag replacements
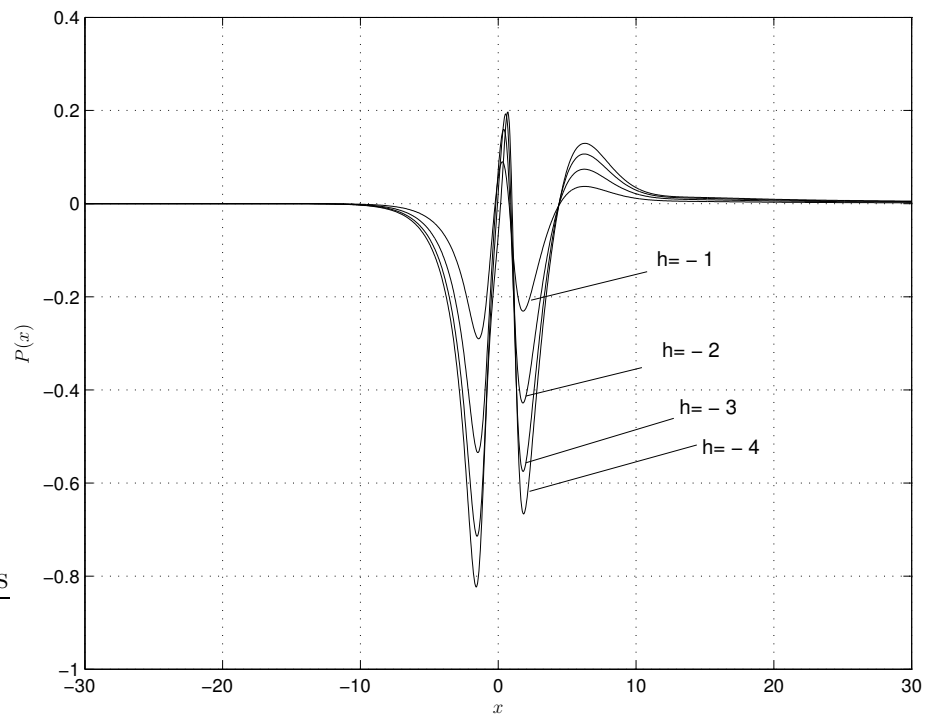
Figure 3.90: Pressure distributions for various values of h with $k = 1.0$, $\sigma = 0.5$.
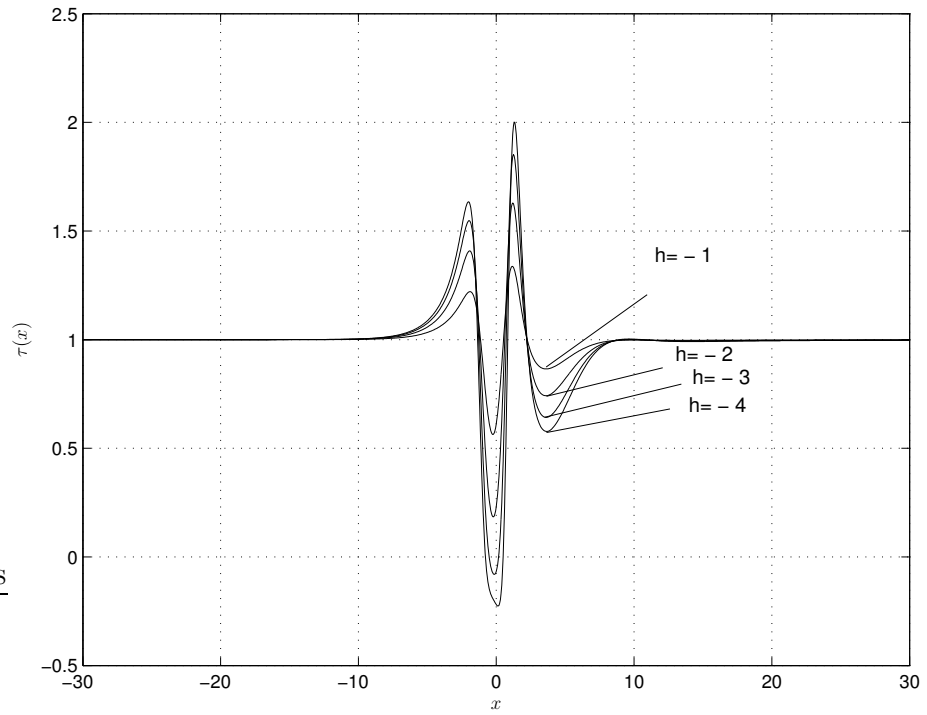
Figure 3.91: Skin friction distributions for various values of h with $k = 1.0, \sigma = 0.5$.
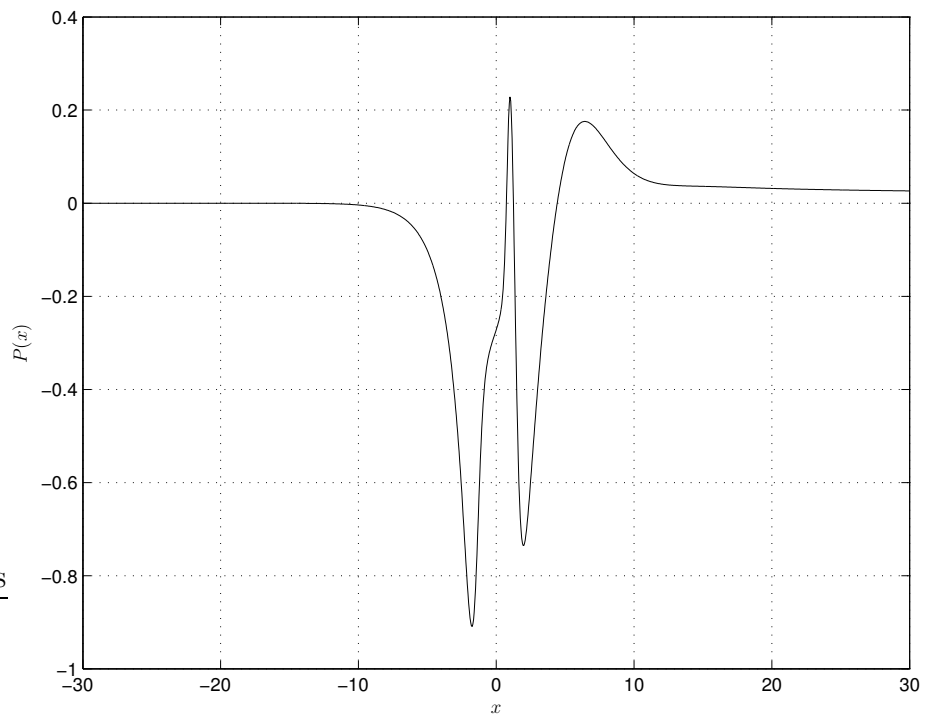
Figure 3.92: Pressure distribution for $h = 7.0$ with $k = 1.0, \sigma = 0.5$.
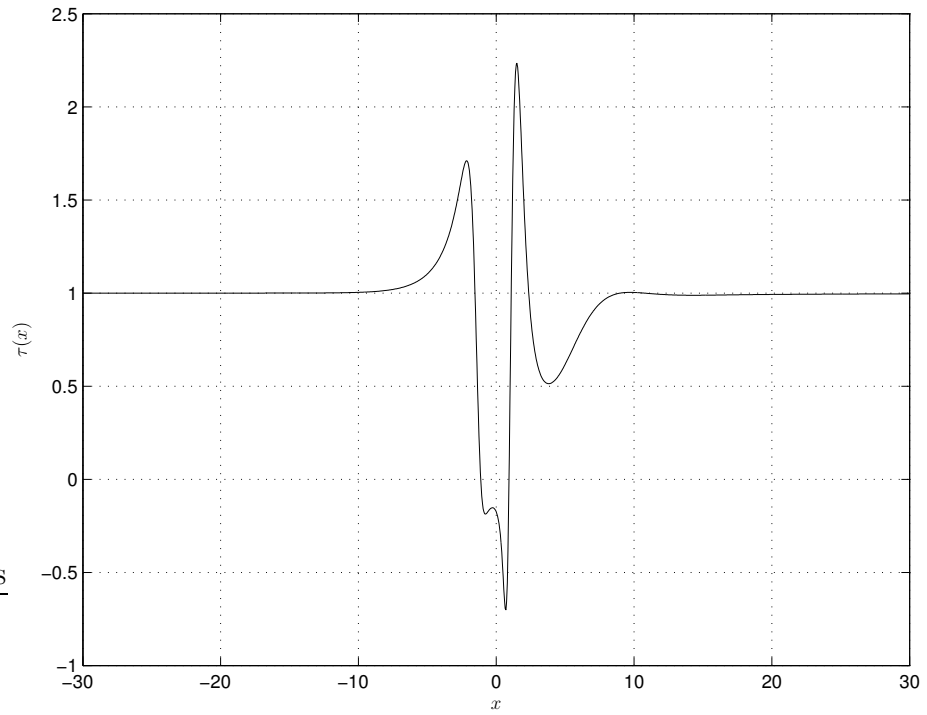
Figure 3.93: Skin friction distribution for $h = 7.0$ with $k = 1.0$, $\sigma = 0.5$.
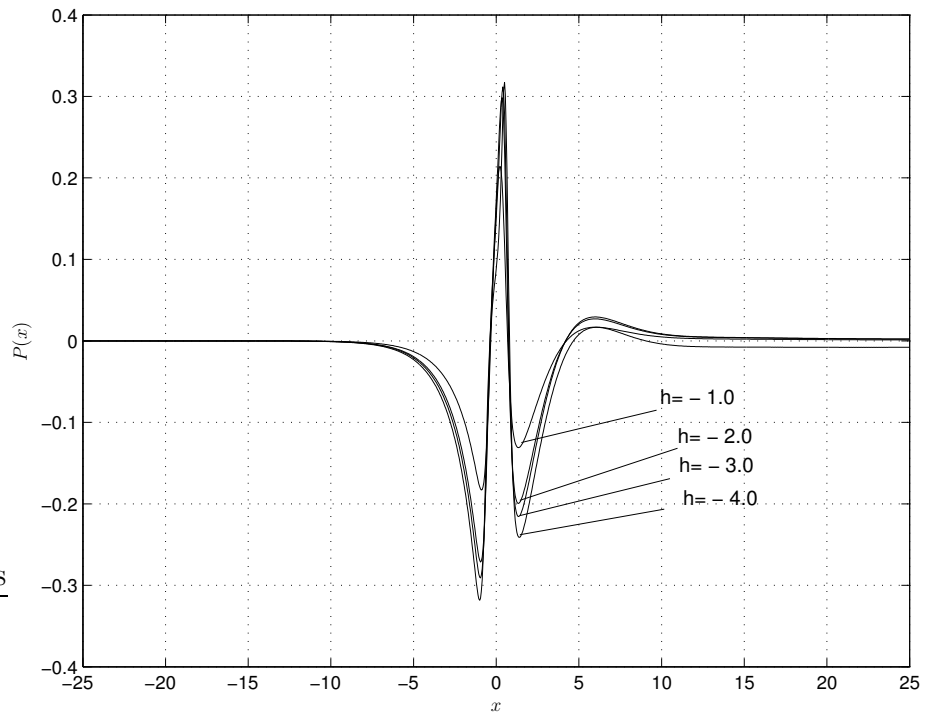
Figure 3.94: Pressure distributions for various values of h with $k = 2.0$, $\sigma = 0.5$.
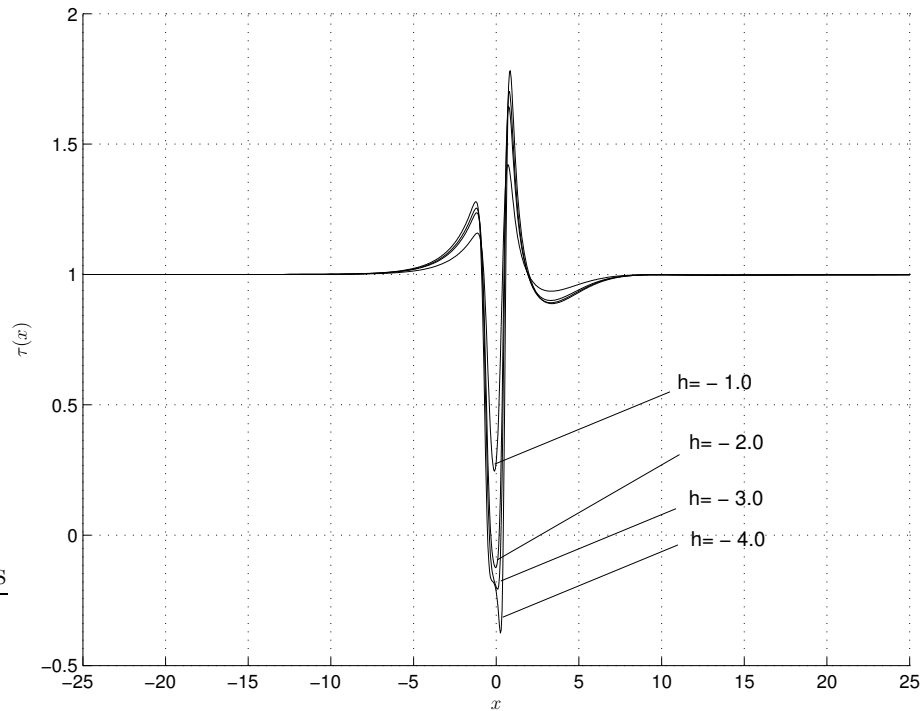
Figure 3.95: Skin friction distributions for various values of h with $k = 2.0$, $\sigma = 0.5$.

Results for $\sigma = 1.0$

For $k = 1.0$, the pressure decreases from its initial value ahead of the indent and increases in the vicinity of the centre of the indent as shown in Figure 3.96. The flow undergoes separation at $h = -2.2$ which can be observed by looking at the shear plot, see Figure 3.97. The shear stress increases from its initial value, decreases at the centre of the indent ($x = 0$), increases slightly behind the indent, decreases and finally increases to its initial value ($\tau = 1.0$). The separation region is centred around the indent.

For $k = 2.0$ the pressure and shear distributions are shown in Figures 3.98 and 3.99. The pressure decreases from its initial value and the exhibits a sharp increase at the centre of the indent ($x = 0$), decreases behind the indent, and finally increases before returning to its initial value. We observe that the flow separates at $h = -1.8$.

Comparing the pressure and skin friction distributions for $\sigma = 0.5$ and $\sigma = 1.0$ we observe that the pressure decreases to a much lower value than the initial value ahead of the indent for $\sigma = 1.0$ than for $\sigma = 0.5$. The increase in pressure in the

vicinity of the centre of the indent ($x = 0$) is greater for $\sigma = 1.0$. Finally the decrease in pressure is much lower for $\sigma = 1.0$ than $\sigma = 0.5$ behind the indent before returning to the initial value. The shear stress for $\sigma = 1.0$ shows a pattern of increase, decrease, increase and finally decrease before returning to the initial value behind the indent, whereas for $\sigma = 0.5$ the shear increases and then decreases before returning to the initial value behind the indent. One can observe that the separation occurs at lower values of $|h|$ for $\sigma = 1.0$ compared to $\sigma = 0.5$.

PSfrag replacements
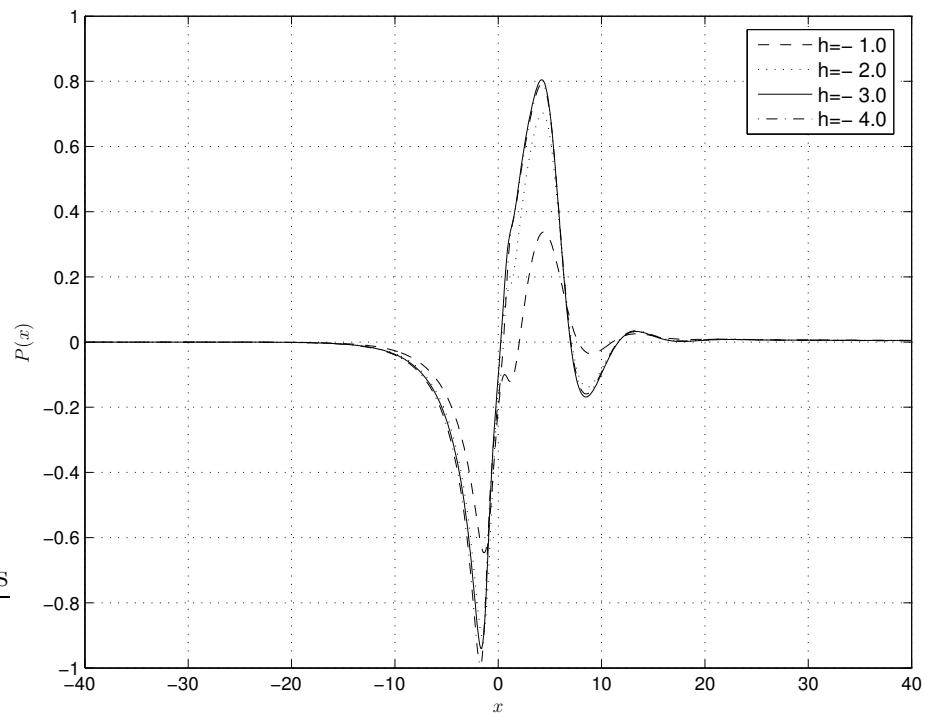
Figure 3.96: Pressure distributions for various values of h with $k = 1.0, \sigma = 1.0$.
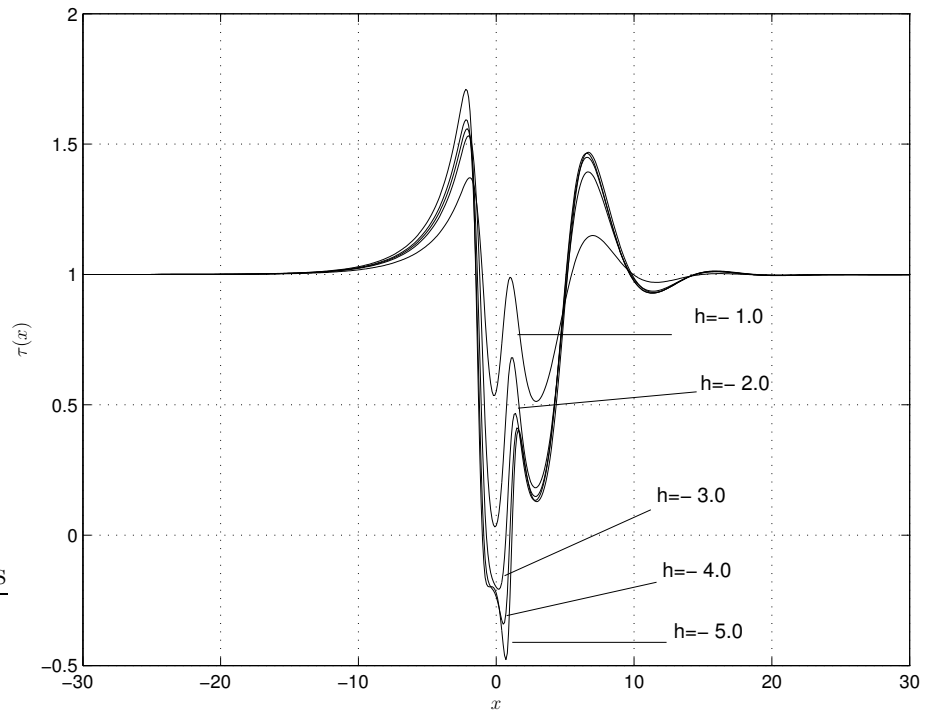
Figure 3.97: Skin friction distributions for various values of h with $k = 1.0$, $\sigma = 1.0$.
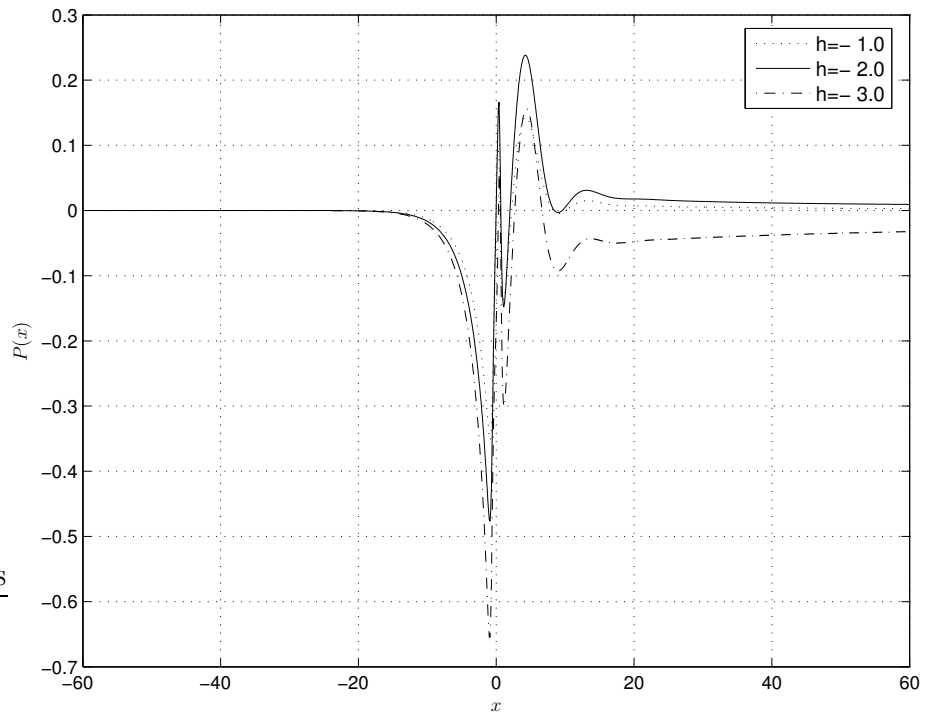
Figure 3.98: Pressure distributions for various values of h with $k = 2.0$, $\sigma = 1.0$.
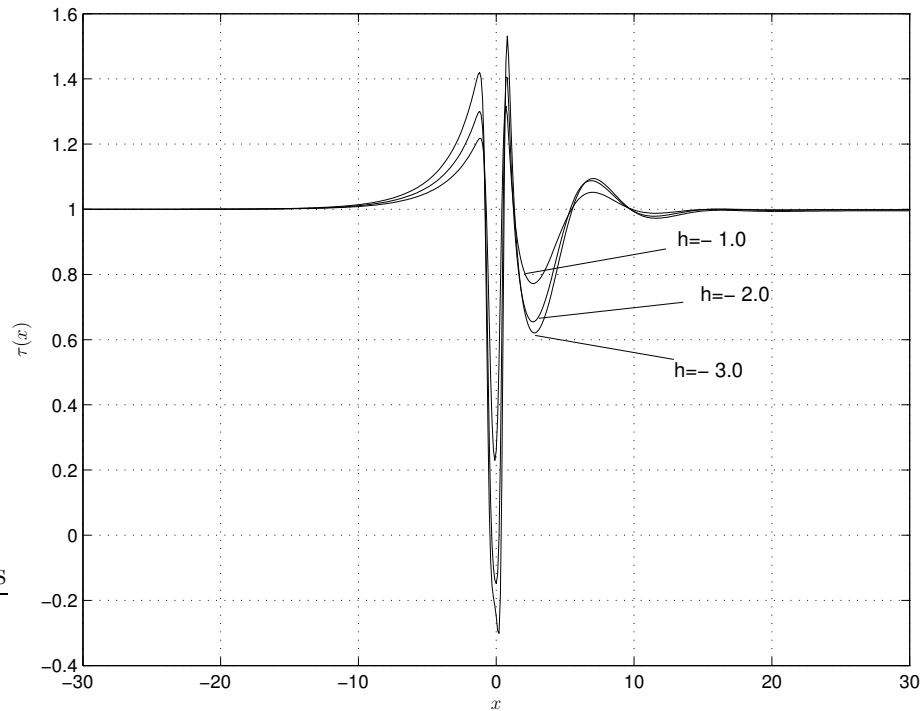
Figure 3.99: Skin friction distributions for various values of h with $k = 2.0$, $\sigma = 1.0$.

Results for $\sigma = 2.0$

For $k = 1.0$, the pressure and skin friction distributions are shown in Figures 3.100 and 3.101. The pressure decreases ahead of the indent and increases around the centre of the indent. The pressure decreases behind the indent and exhibits a oscillatory behaviour before returning to the initial value. The flow separation occurs at $h = -2.8$. The shear stress increases slightly from its initial value ahead of the indent, decreases at the centre of the indent $(x = 0)$ and finally increases whist exhibiting oscillatory behaviour downstream of the centre of the hump.

For $k = 2.0$, the pressure and skin friction distributions are shown in Figures 3.102 and 3.103. The pressure decreases ahead of the indent, increases sharply at the centre of the indent $(x = 0)$, shows a pattern of slight decrease and increase slightly behind the indent before decreasing to its initial value whist exhibiting oscillatory behaviour. The shear stress increases from its initial value very slightly ahead of the indent, decreasing sharply at the centre of the indent $(x = 0)$, increasing behind the

indent and returns to the initial value behind the indent whist exhibiting oscillatory behaviour. The flow separates at $h = -1.4$. As observed in the case of humps for higher values of σ, both pressure and shear stress exhibit oscillatory behaviour behind the indent. For even larger values of σ the oscillations grow.

PSfrag replacements
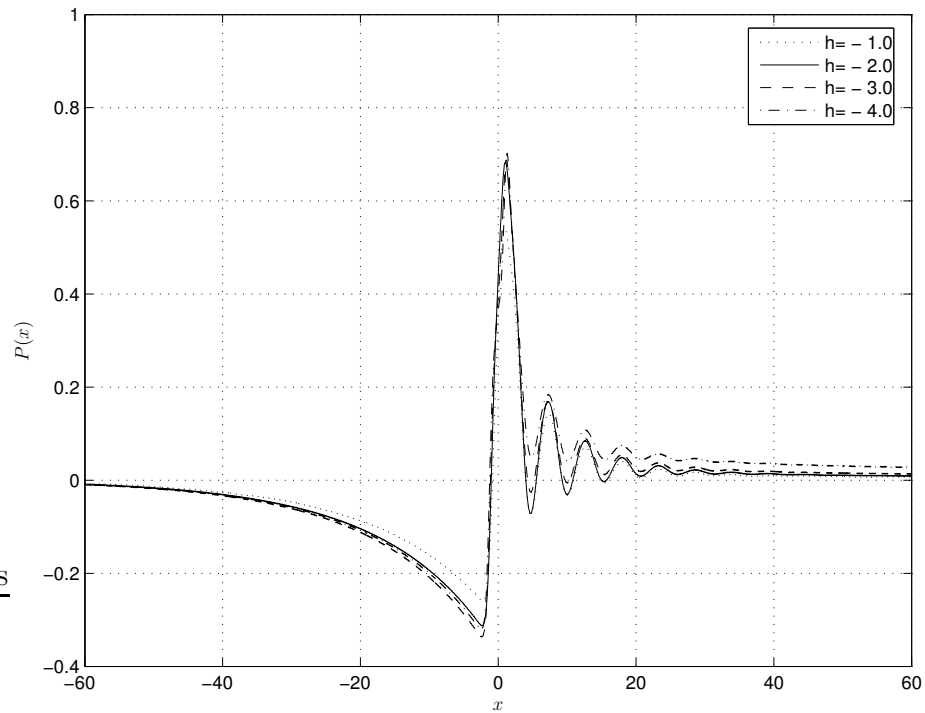
Figure 3.100: Pressure distributions for various values of h with $k = 1.0$, $\sigma = 2.0$.
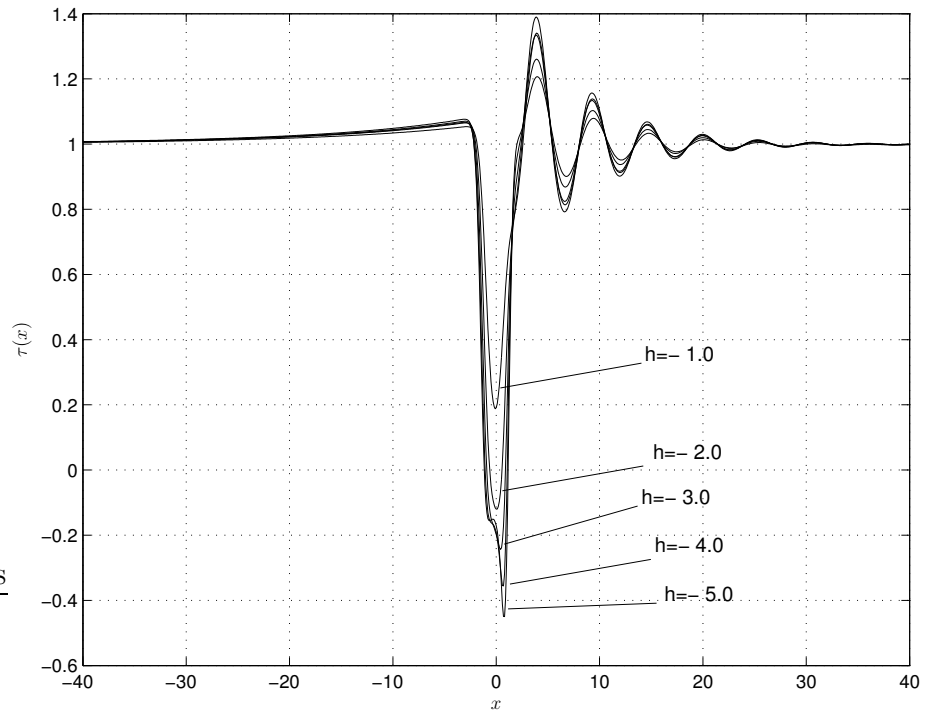
Figure 3.101: Skin friction distributions for various values of h with $k = 1.0$, $\sigma = 2.0$.
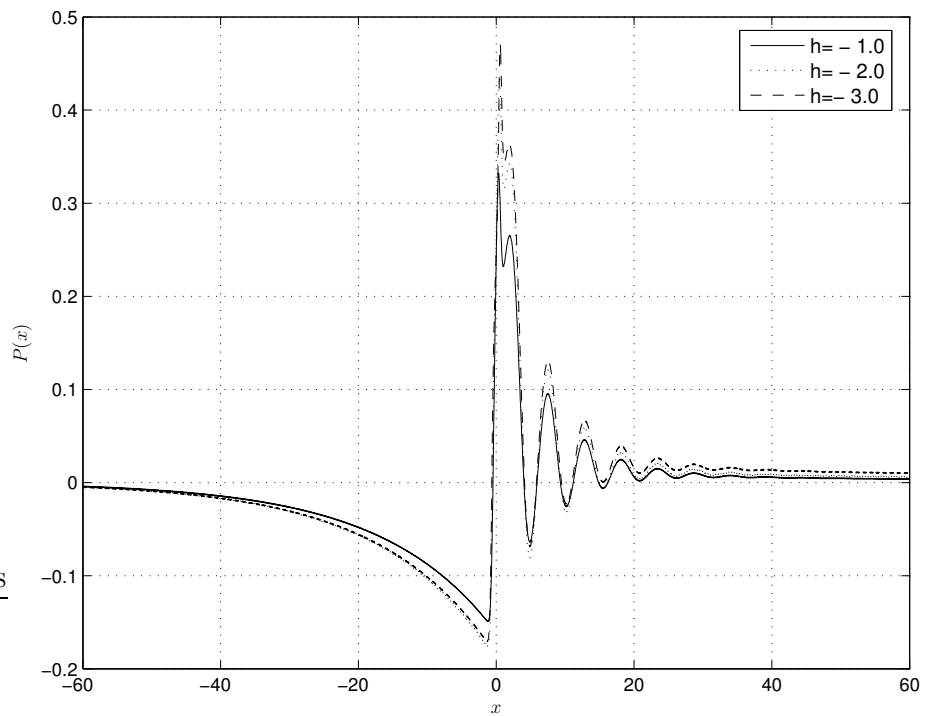
Figure 3.102: Pressure distributions for various values of h with $k = 2.0$, $\sigma = 2.0$.
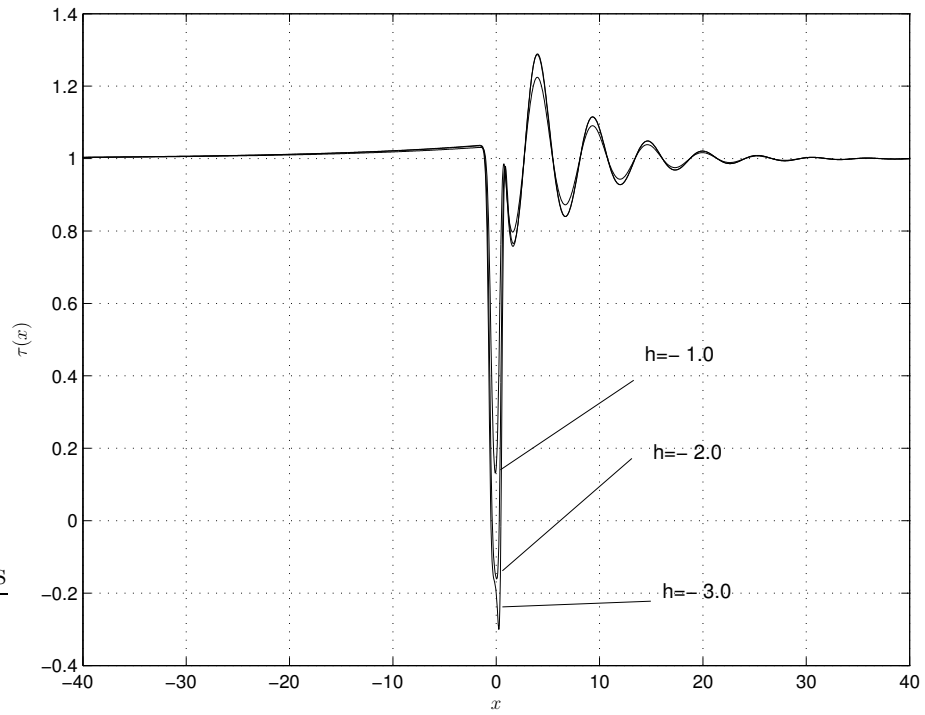
Figure 3.103: Skin friction distributions for various values of h with $k = 2.0$, $\sigma = 2.0$.
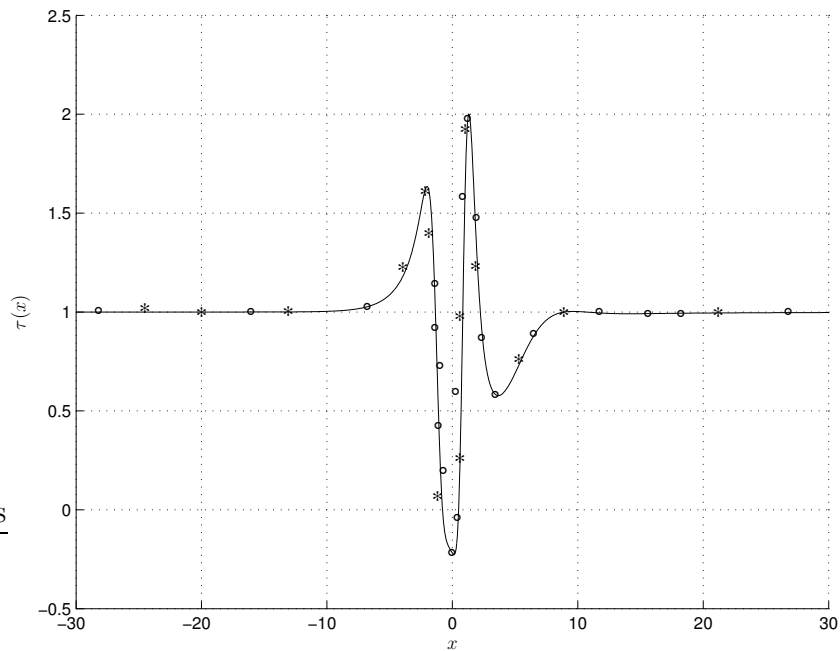
Figure 3.104: Skin friction for various grids with $\sigma = 0.5$, $k = 1.0$, $h = -3.0$: '-' (8001×64), 'o' (4001×70), '*' (6001×90).

PSfrag replacements
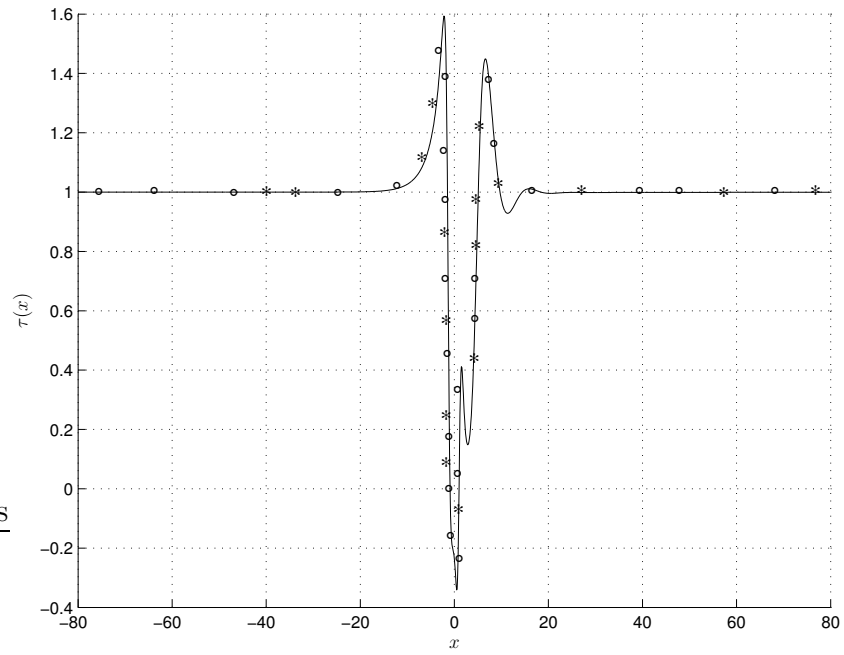
Figure 3.105: Skin friction for various grids with $\sigma = 1.0$, $k = 1.0$, $h = -4.0$: '-' (8001×64), 'o' (4001×70), '*' (6001×90).

PSfrag replacements
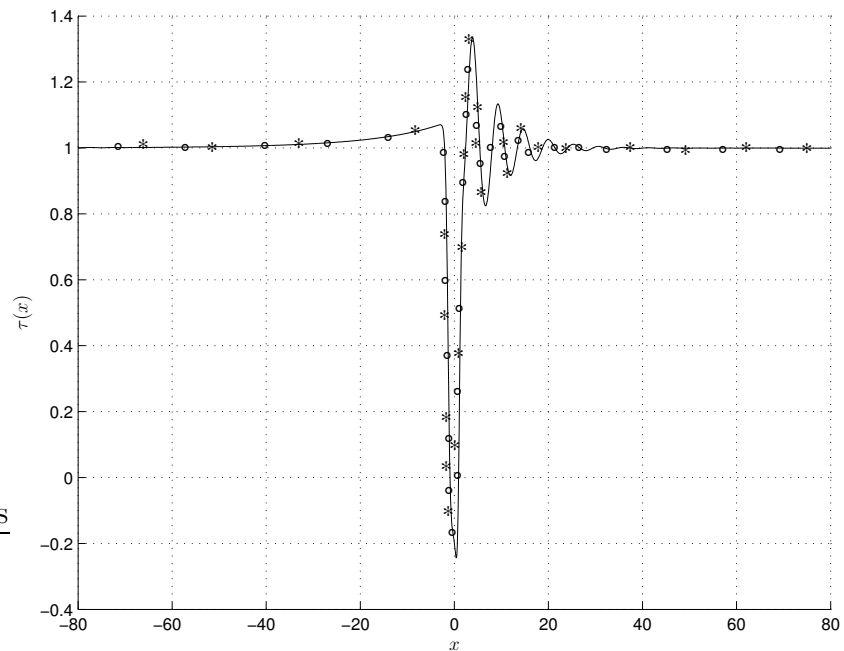
Figure 3.106: Skin friction for various grids with $\sigma = 2.0$, $k = 1.0$, $h = -3.0$: '-' (8001×64), 'o' (4001×70), '*' (6001×90).

Figures 3.105 and 3.106 refer to the skin friction distributions for $\sigma = 1.0$ and $\sigma = 2.0$ for various grids. The figures clearly suggest that for a sufficiently fine grid the numerical results are independent of the grid size.

3.6 Concluding remarks

In this section we provide concluding remarks for this chapter. A numerical method using a finite-difference approximation in the streamwise direction in combination with Chebychev collocation in the normal direction was used. The resulting equations are linearised using a Newton-Raphson technique and then solved using a direct method. This method has been successfully used for the compression ramp problem; see Korolev *et al.* (2002). We have extended this method to study jet-like boundary layers/thermal boundary layers encountering corners, humps and indents, liquid layer flows over convex corners, humps and indents. The results obtained were compared with the results of Merkin & Smith (1982), Merkin (1983), Gajjar (1987). For the corner flows, with a slight modification to the body shape (i.e. slightly smoothing the corner) one could achieve secondary separation for jet-like boundary layers/thermal boundary layers. New flow features were observed as the angle was increased. For the near-wall jets encountering humps and indentations, we observed flow separating ahead and behind the hump. In addition, we also observed a secondary separation region present within the primary separation region behind the hump. For the indentations, apart from the recirculation region centred on the indent, we could also see a secondary separation region. Convergence of our numerical method was possible for high values of h, typically convergence required 8-10 Newton iterations. We then applied our numerical technique to study liquid layer flows over convex corners, humps and indentations. The modelling was made easier by using a smooth body shape consistent with the lower deck scalings. Gajjar (1987) used three different numerical techniques, two based on shooting technique and the other based on global iteration. The implementation of the downstream boundary condition was difficult with the shooting technique, although this was overcome by the global iteration technique.

All three methods had problems with convergence as the value of α and "σ" were increased. The problems of implementing the downstream boundary condition and of convergence were overcome by our technique. We have shown that for $\sigma = 1.0$ even with $\alpha = -30$ there was no flow separation. For higher values of σ for liquid layer flows past a hump, free interaction takes place ahead of the hump with $p > 0$ as predicted in the paper by Gajjar (1987). For higher values of $\sigma \geq 2.0$ we found oscillatory behaviour in pressure and skin friction distributions for both humps and indentations which decays far downstream as seen in the papers by Gajjar (1987) and Bowles & Smith (1992). As the value of σ is increased the oscillations tend to grow.

Our method can also be extended to hypersonic self -induced separation (when the interaction law is $p = -A$). It can be easily further extended to incorporate unsteady terms, and for subsonic external flows.

Chapter 4

Supersonic flow past humps and indentations

In this chapter we consider supersonic flow over a flat plate past a hump or indent. Consider a flat plate on which a small hump is placed, situated at a length L downstream of the leading edge of the plate. If the length of the hump is an order $LRe^{-\frac{3}{8}}$ quantity and its height is of order $LRe^{-\frac{5}{8}}$, then the flow past the hump is governed by the equations of *triple-deck* theory. The problem was first studied by Hunt (1971) and Smith (1973). For certain short humps Hunt adopted a local short scale approach to study the flow response, whereas Smith suggested a more global long-scale treatment based on triple deck theory. Hunt used a method based on a two region structure well inside the boundary layer and assumed that the main stream has no first-order effect on the pressure within these regions. Only very small humps of dimensional length and height could be accommodated by Hunt's model. Smith extended Hunt's model to include much larger humps. The triple deck structure near the hump shows how the presence of the hump generates an interaction between the inviscid region just outside the layer and the viscous region near the hump. The pressure force dominant in the boundary layer and the connection of the local flow to the main stream develop together and are self perpetuating, and both are of primary significance for a wide range of hump sizes, even for humps buried well inside the boundary layer. Solutions have been obtained both analytically see Smith (1973) for the linearised weak

case $|h| \ll 1$, and numerically for $O(1)$ value of h by Sykes (1978), Napolitano *et al.* (1979), Ragab & Nayfeh (1980), Smith & Merkin (1982), Smith *et al.* (1981), Smith & Daniels (1981), Veldman & Dijkstra (1980). Most of the works mentioned deal with incompressible flows. Smith has obtained a linearised solution for flow past a supersonic hump. Napolitano *et al.* (1979) obtained the numerical solution for triple deck flows past both subsonic and supersonic humps, comparing their results with the linearised solution of Smith. Both Smith and Naploitano *et al* used a parabolic profile for the shape of the hump. This problem is of physical interest, especially with regard to the phenomenon of trip-wire transition. This theory provides a complete and consistent description of the flow characteristics for a wide variety of humps; ultimately an examination of, and criteria for, stability of the laminar flow would be desirable so that insight into more realistic problems may be gained.

4.1 Problem formulation
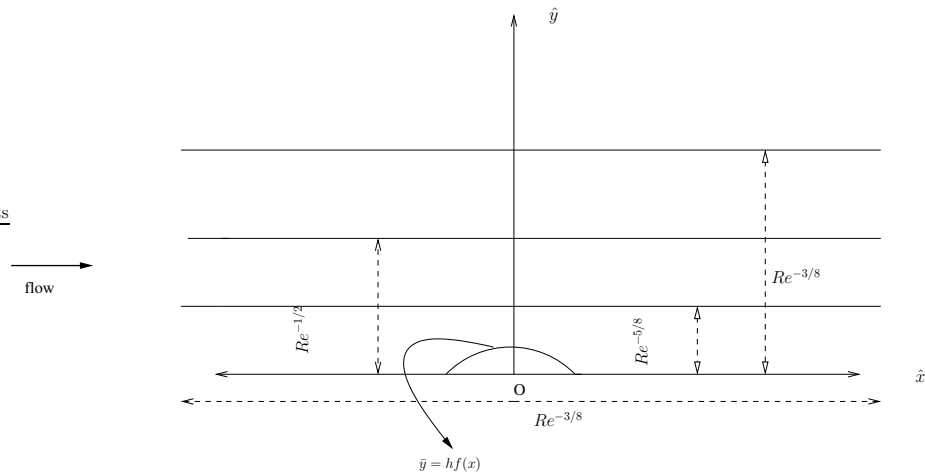
Figure 4.1: Flow past a supersonic hump

We consider fluid flow past a flat plate on which there is a small hump. The hump is 2D and in cross section has small dimensions compared with those of the boundary layer along the plate as shown in Figure 4.1. The fluid is compressible and viscous, and far upstream is moving with a uniform speed U_∞ parallel to the plate. The free stream density and pressure are given by ρ_∞ and p_∞. The fluid motion is assumed

to be laminar and two dimensional. We non-dimensionalize the problem as described in Chapter 1. The equations governing the motion in the viscous sublayer are given by (1.12)-(1.15) the pressure-displacement law is given by (1.16). We use the same numerical procedure as in the case of wall-jet flow past humps and indentations.

4.2 Numerical results

We use the same numerical method as described in Chapter 2. The form of the hump/indent is the same as considered in Chapter 3 given by (3.12). The $\frac{dp}{dx}$ term is approximated using the finite-difference (2.9). This leads to a matrix of the form (2.12) The elements of the matrix are given in Appendix C. Values of $x_{-\infty} = -40$ and $x_{\infty} = 40$ are used for the grid in the streamwise direction. A value of $y_{max} = 50$ was used to truncate the computational domain in the y direction. A uniform grid was used with 2001 points in the streamwise direction and 64 points in the y direction.

4.2.1 Flow past humps

Figures 4.2 - 4.3 show the pressure and skin friction distributions for $k = 0.5$ and different values of h. Far upstream of the hump the flow is unperturbed with $p = 0$ and the skin friction $\frac{\partial^2 \psi}{\partial y^2} = 1$. Downstream of the hump the flow has to return to its unperturbed state. For $k = 0.5$, the incipient separation first occurs ahead of the hump at $h = 6.15$. The flow separates behind the hump at $h = 8.15$. At higher values of h i. e, $h = 18$, the pressure and skin friction are shown in Figures 4.4 and 4.5. The pressure forms a "plateau" ahead of the hump, decreases sharply at $x = 0$ and then flattens out behind the hump within the separation region. Figures 4.6, 4.7 show the streamline pattern at $h = 10$ and $h = 18$ with separation bubbles both ahead and behind the hump. The flow separates at $x = -10$ and reattaches at $x = -1.2$ ahead of the hump. Behind the hump, the flow separates at $x = 1.0$ and reattaches at $x = 6.85$ for $h = 18.0$. In the present case we observe pressure plateauing ahead of the hump which is different to the wall-jets encountering a hump.For a wall-jet separation occurs first downstream of the hump at $k = 1.0$, where as for the supersonic flow separation

first occurs ahead of the hump at this value of k but this behaviour is reversed for higher values of k.

Next we increased the width of the hump to observe its effects. Calculations for $k = 1.0$ are given in Figure 4.8. We can see that the pressure increases from its initial value ahead of the hump and then decreases sharply at the centre of the hump $(x = 0)$. The pressure curves tend to flatten out in the separation region behind the hump as the value of h is increased. There is a sharp rise in pressure near the reattachment point before returning to its undisturbed condition. We first observe separation behind the hump at $h = 4.2$ and later ahead of the hump at $h = 5.15$ as evident from the skin friction distribution, see Figure 4.9. The streamline pattern in Figure 4.10, shows that the flow separates at $x = -4.8$ and reattaches at $x = 0.78$ ahead of the hump. Behind the hump the flow separates at $x = 0.5$ and reattaches at $x = 4.0$. One can observe that the recirculation region grows as k increases for the same value of h.

We further increased the width of the hump which corresponds to shrinking the hump in x-direction and performed calculations with $k = 2.0$, the pressure and skin friction distributions are shown in Figures 4.11 and 4.12. The pressure curves tend to flatten out in the separation region behind the hump before increasing sharply near the reattachment point as the value of h is increased. The separation behind the hump occurs at $h = 2.55$ and at $h = 5.0$ ahead of the hump as seen from the skin friction distribution. The streamline pattern shown in Figure 4.13 shows the two recirculation regions: One that separate at $x = -3.4$ and reattaches at $x = -0.5$ ahead of the hump and another that separates at $x = 0.2$ and reattaches at $x = 3.1$ behind the hump. The separation occurs at lower values of h as the value of k increases.

PSfrag replacements
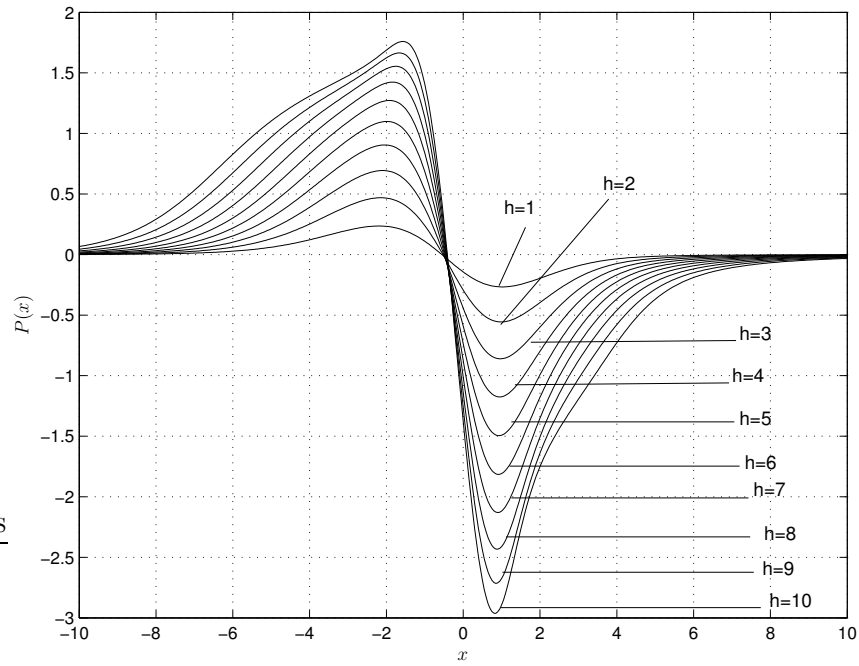
Figure 4.2: Pressure distributions for various values of h with $k = 0.5$.

PSfrag replacements
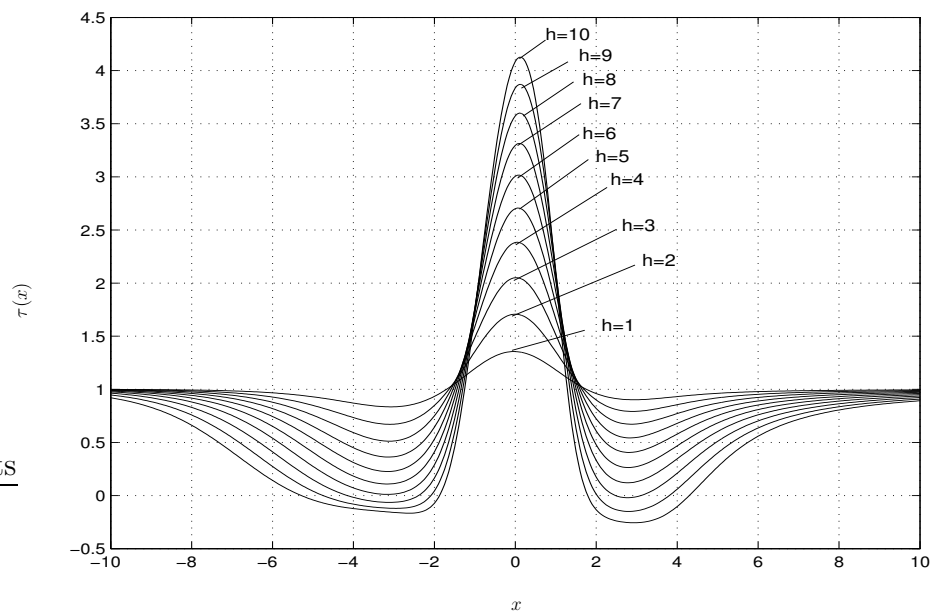
Figure 4.3: Skin friction distributions for various values of h with $k = 0.5$.
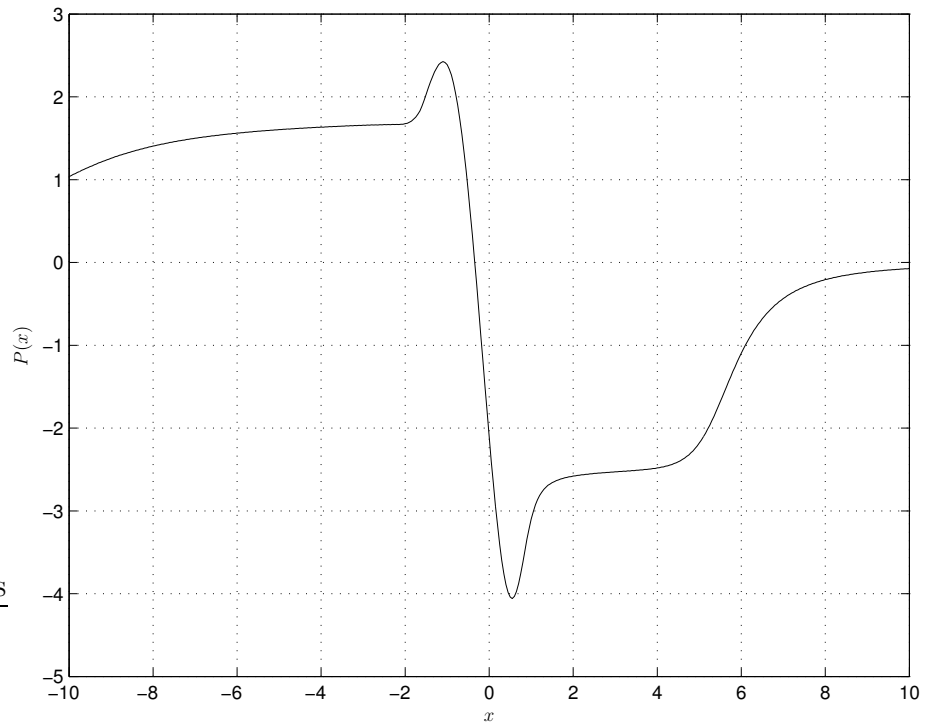
Figure 4.4: Pressure distribution for $h = 18$ with $k = 0.5$.
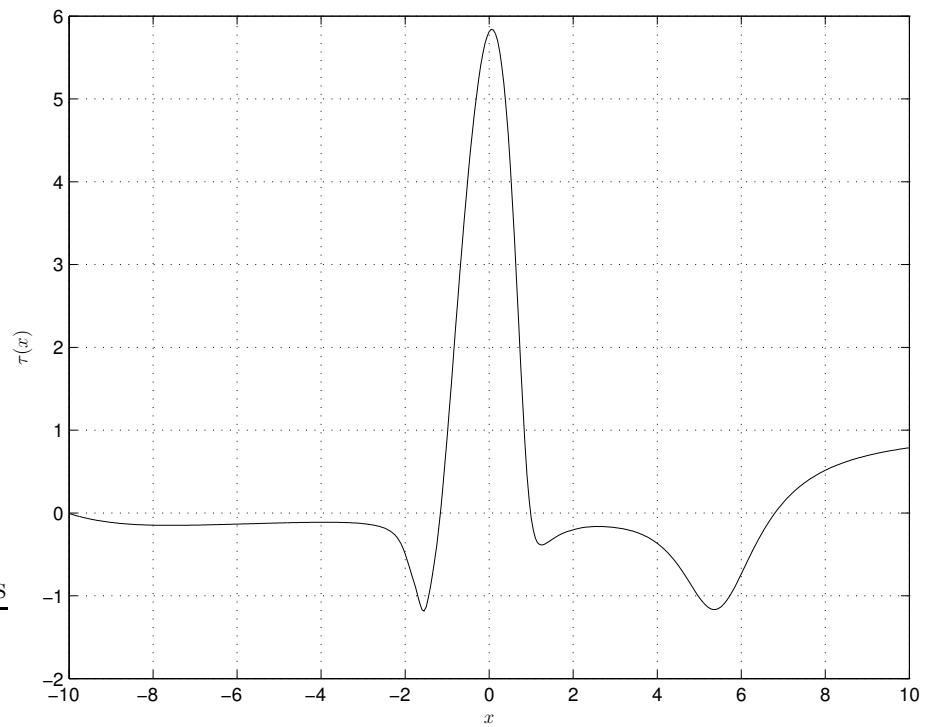
Figure 4.5: Skin friction distribution for $h = 18$ with $k = 0.5$.
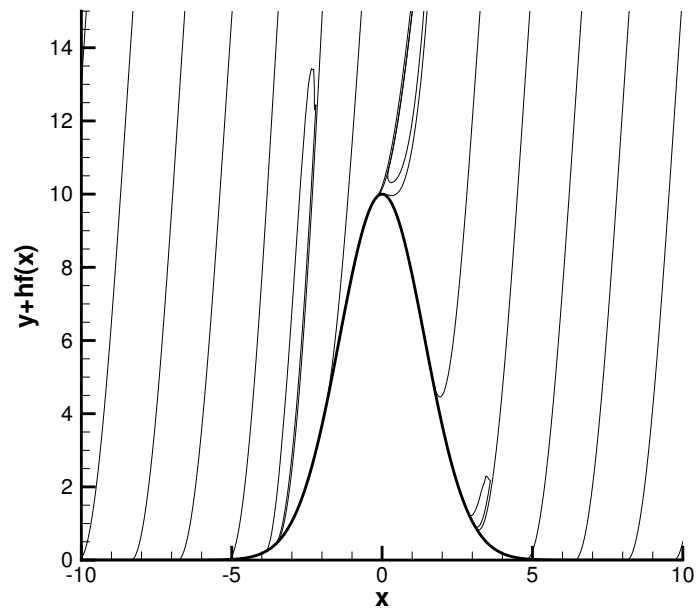
Figure 4.6: Streamline distribution for $h = 10$ with $k = 0.5$.
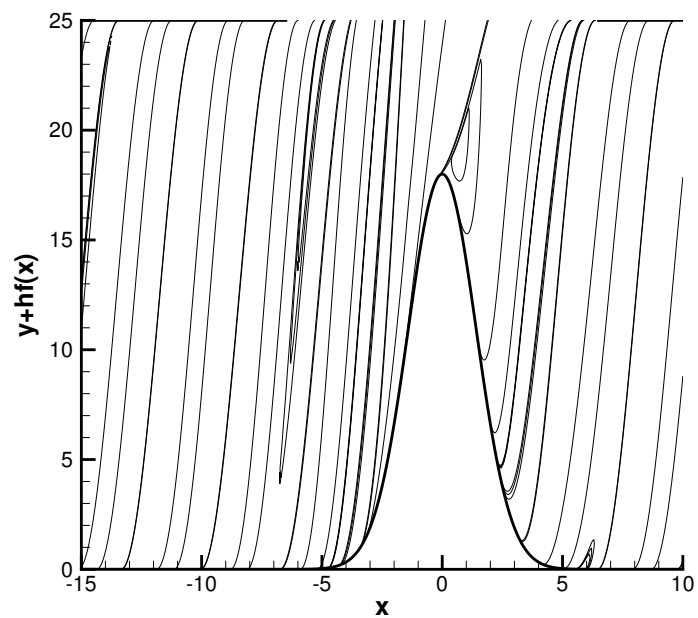
Figure 4.7: Streamline distribution for $h = 18$ with $k = 0.5$.
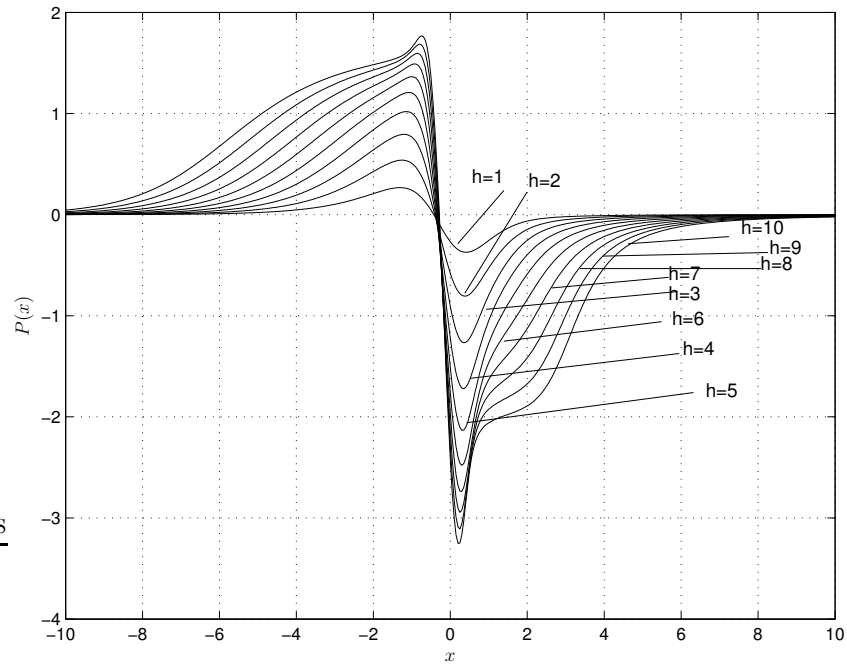
Figure 4.8: Pressure distributions for various values of h with $k = 1.0$.
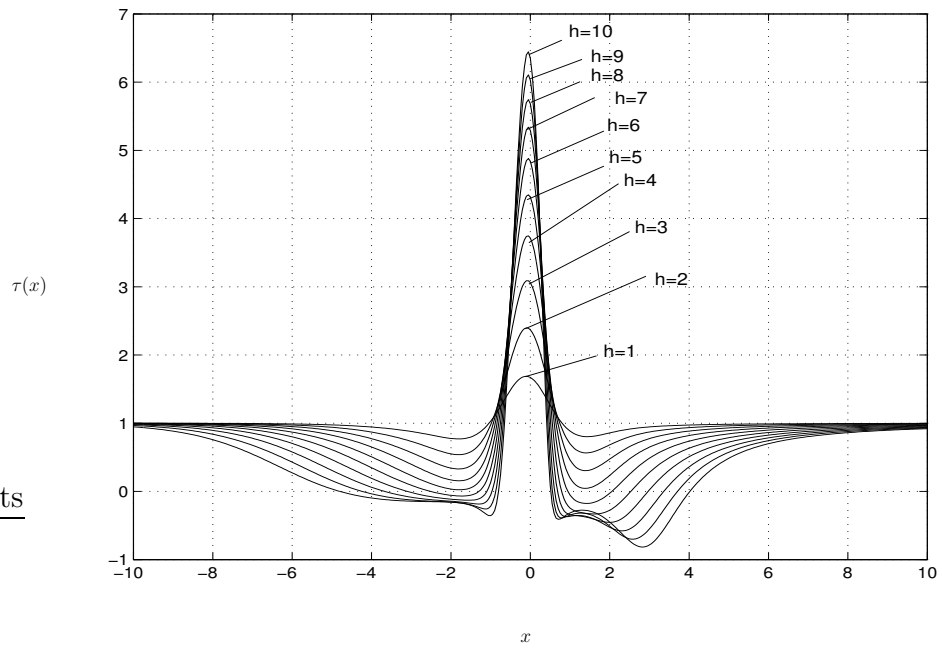
Figure 4.9: Skin friction distributions for various values of h with $k = 1.0$.
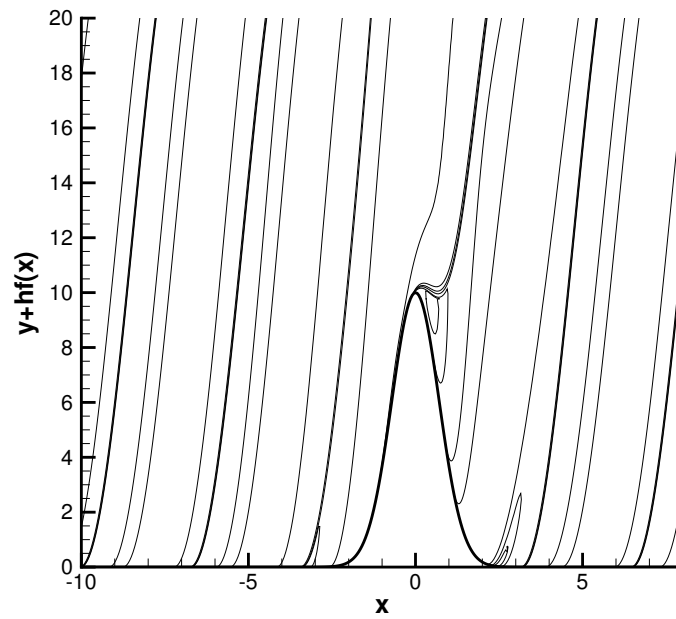
Figure 4.10: Streamline pattern for $h = 10$ with $k = 1.0$.

PSfrag replacements
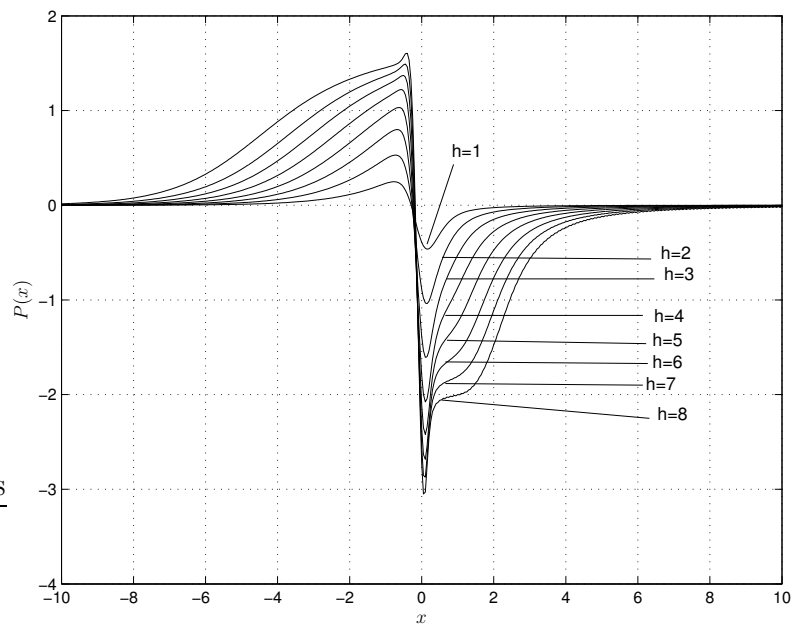
Figure 4.11: Pressure distributions for various values of h with $k = 2.0$.
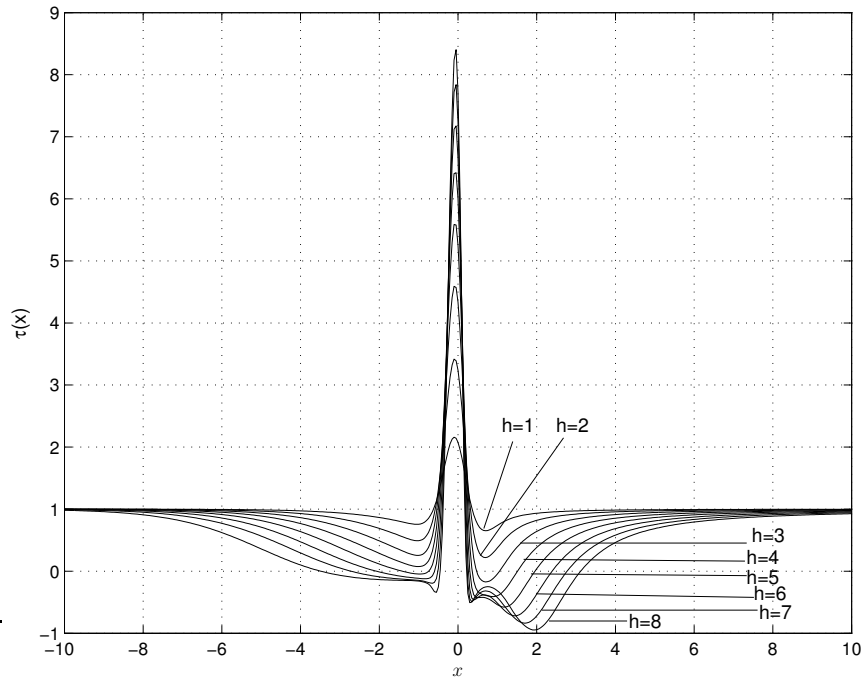
Figure 4.12: Skin friction distributions for various values of h with $k = 2.0$.
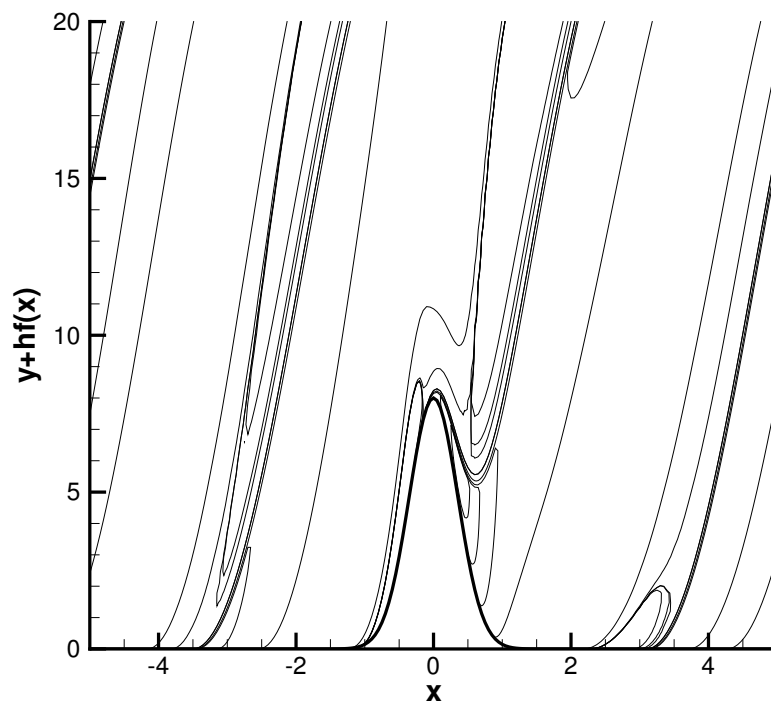
Figure 4.13: Streamline distribution for $h = 8$ with $k = 2.0$.

PSfrag replacements
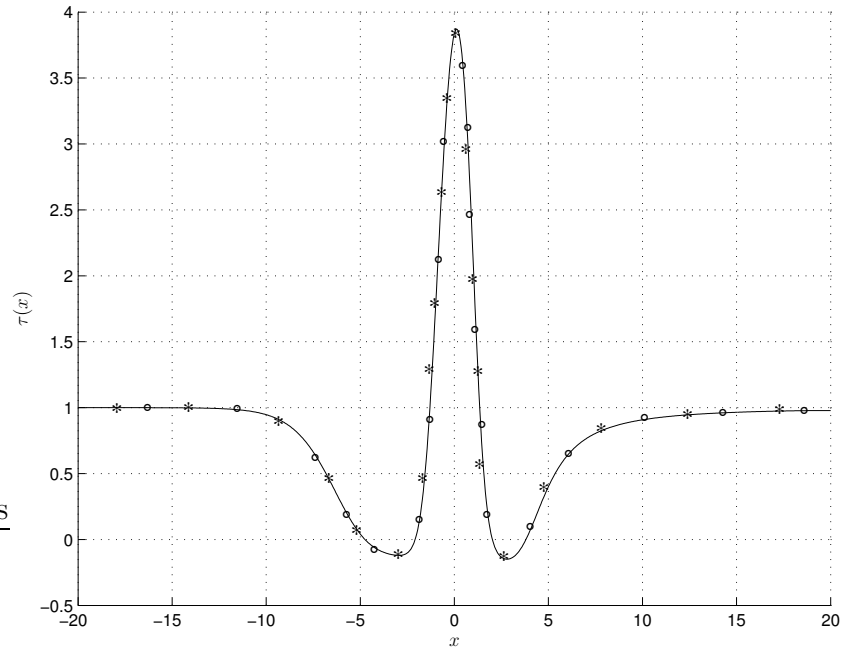
Figure 4.14: Skin friction distributions for various grids with $k = 0.5$, $h = 9.0$: '-' (8001×64), '∘' (4001×70), '∗' (6001×90).

PSfrag replacements
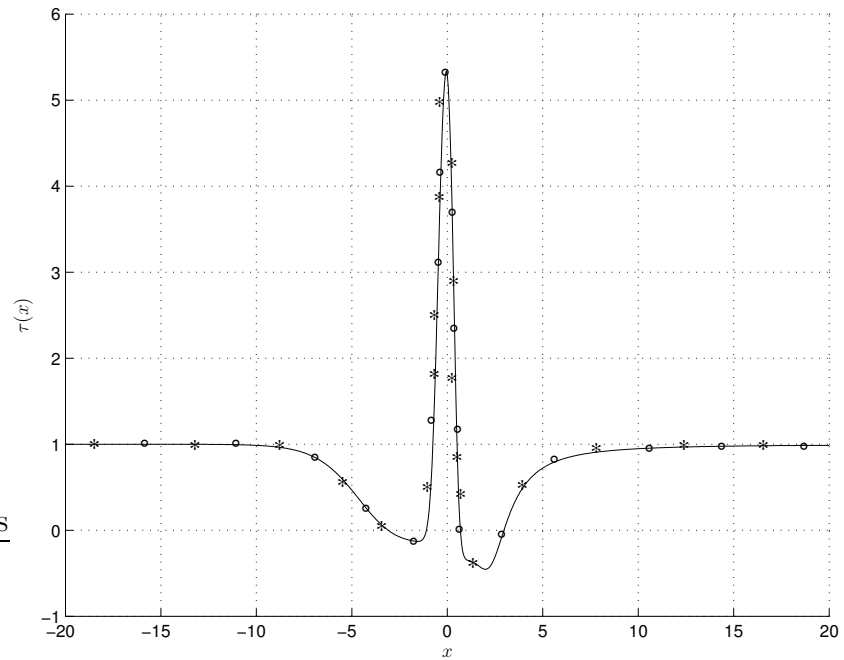
Figure 4.15: Skin friction distributions for various grids with $k = 1.0$, $h = 7.0$: '-' (8001×64), '∘' (4001×70), '∗' (6001×90).

PSfrag replacements
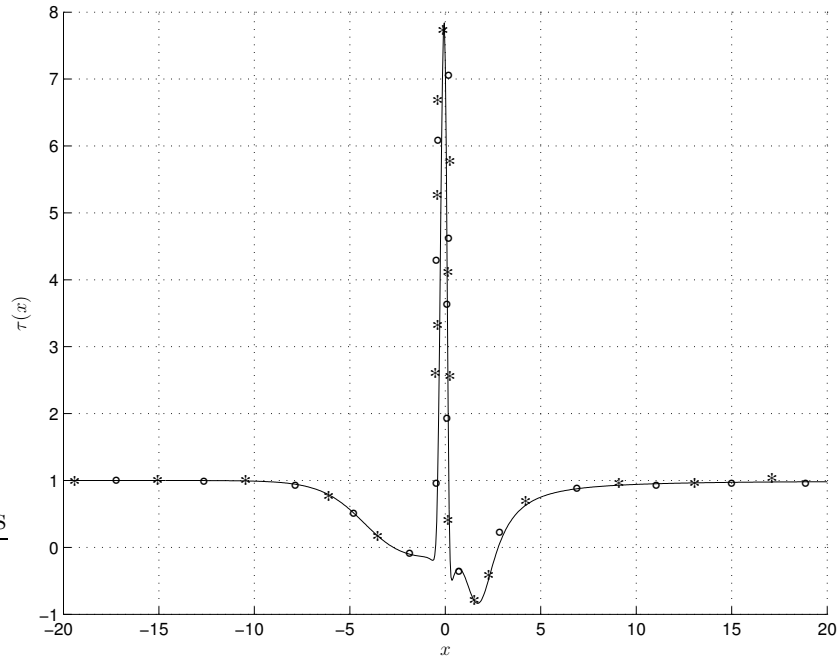
Figure 4.16: Skin friction for various grids at $k = 2.0$, $h = 7.0$: '-' (8001×64), 'o' (4001×70), '*' (6001×90).

Figures 4.14, 4.15, 4.16 show the behaviour of the skin friction for various grid sizes with different values of k. All the results are visually indistinguishable, suggesting that for a sufficiently fine grid the numerical results are independent of the grid size.

4.2.2   Flow past indentations

In this section we examine supersonic flow past an indentation. Figures 4.17 and 4.18 show the pressure and skin friction distributions with $k = 0.5$ for various values of h. The pressure decreases from its initial value ahead of the indent. One can observe a flattening out of the pressure profile in the vicinity of the centre of the indent ($x = 0$), with the pressure increasing behind the indent before returning to its initial value. We observe that separation occurs at $h = -3.23$. The pressure and skin friction distributions for $h = -15.45$ are shown in Figures 4.19 and 4.20. We can observe that the pressure forms a "plateau" around $x = 0$. Figure 4.21 shows the stream-line pattern at $h = -15.45$. We can observe that the primary separation region is

centred on the indentation. There is also a small secondary separation region within the primary recirculation region. The primary separation occurs at $x = -2.6$ and reattaches at $x = 2.4$. The separation region within this primary separation region extends from $x = 1.02$ to $x = 1.2$.

For $k = 1.0$, flow separation occurs at $h = -2.03$. One can observe that the pressure curves have a tendency to flatten out within the separation region as the value of h is increased. The flow separates at $x = -1.2$ and reattaches at $x = 1.1$ for $h = -6$. The separation region is centred on the indent.

For $k = 2.0$, flow separation occurs at $h = -1.0$. The pressure profile shows a hint of flattening in the separation region. The flow separates at $x = -1.1$ and reattaches at $x = 1.0$ for $h = -4$. One can observe from the streamline pattern that the recirculation region is centred on $x = 0$ for the indentations.

Figures 4.28, 4.29, 4.30 shows the behaviour of the skin friction for various grid sizes for different values of k. All the results are visually indistinguishable, suggesting that for a sufficiently fine grid the numerical results are again independent of the grid size.
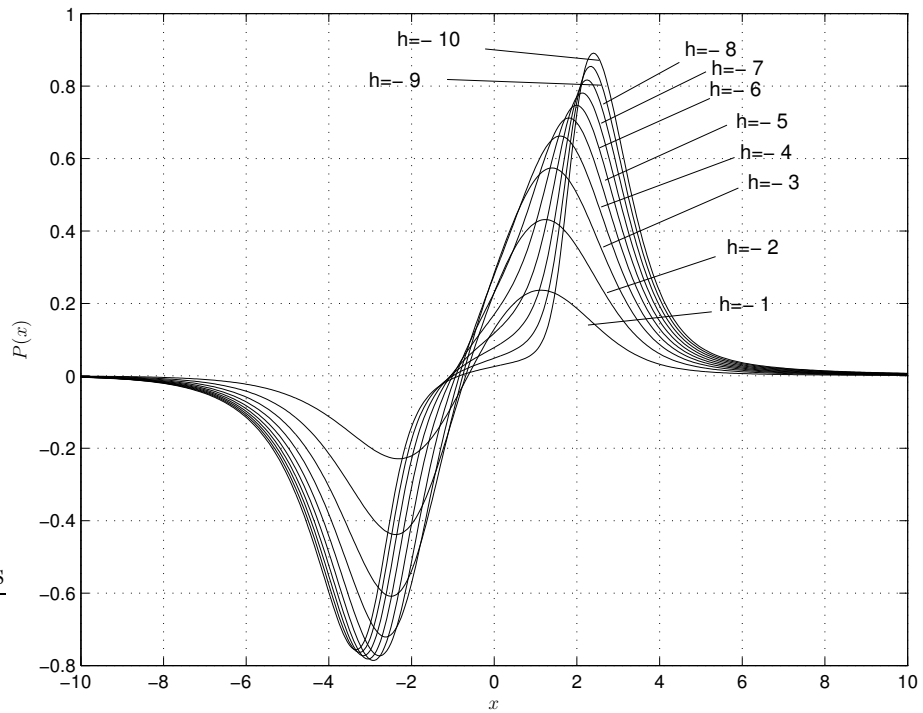
Figure 4.17: Pressure distributions for various values of h with $k = 0.5$.
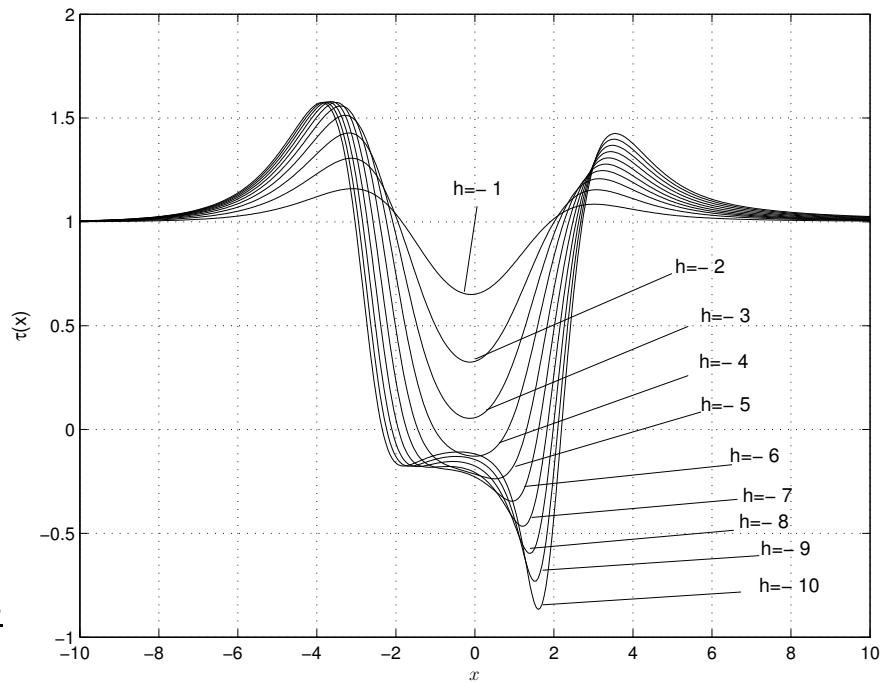
Figure 4.18: Skin friction distributions for various values of h with $k = 0.5$.
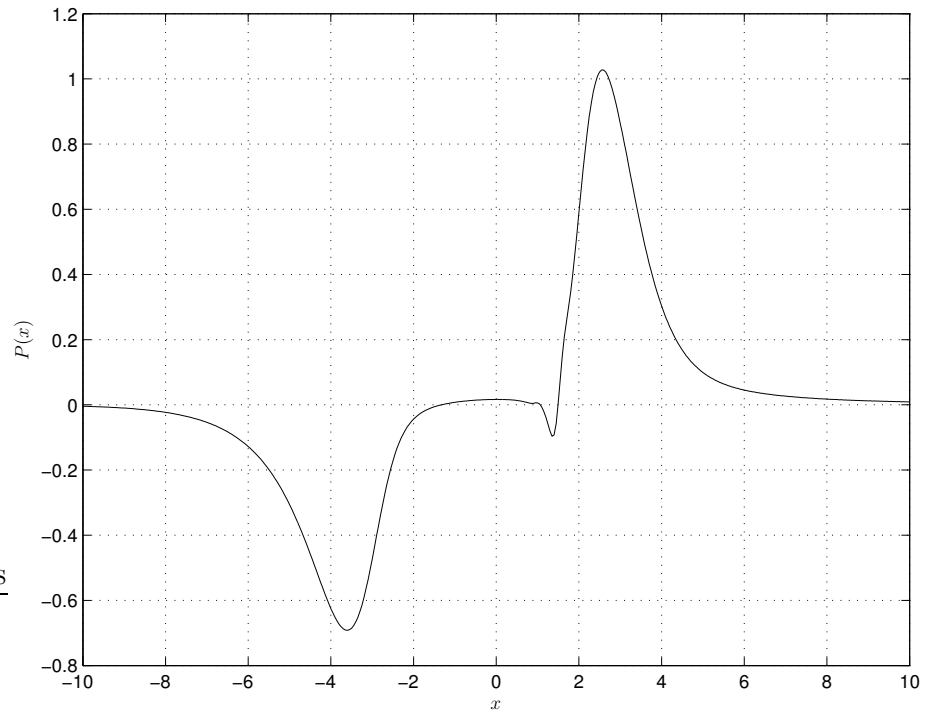
Figure 4.19: Pressure distribution for $h = -15.45$ with $k = 0.5$.
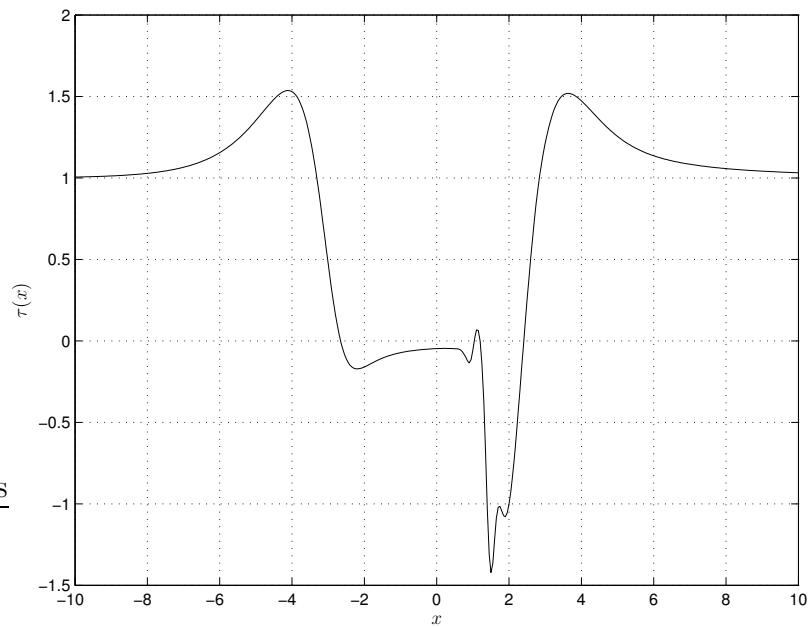
Figure 4.20: Skin friction distribution for $h = -15.45$ with $k = 0.5$.
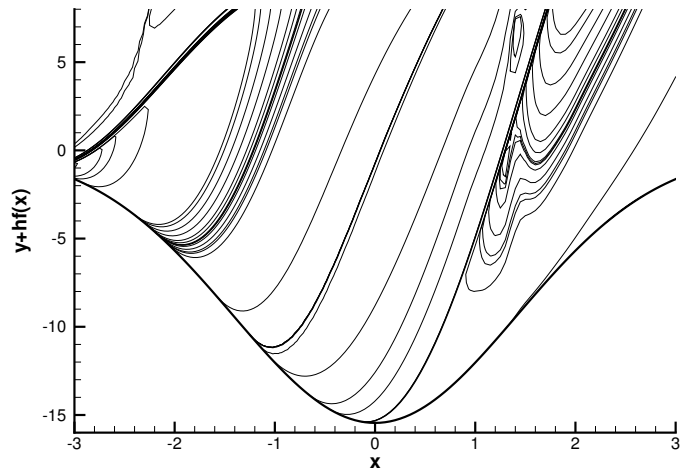
Figure 4.21: Streamline distribution for $h = -15.45$ with $k = 0.5$.

PSfrag replacements
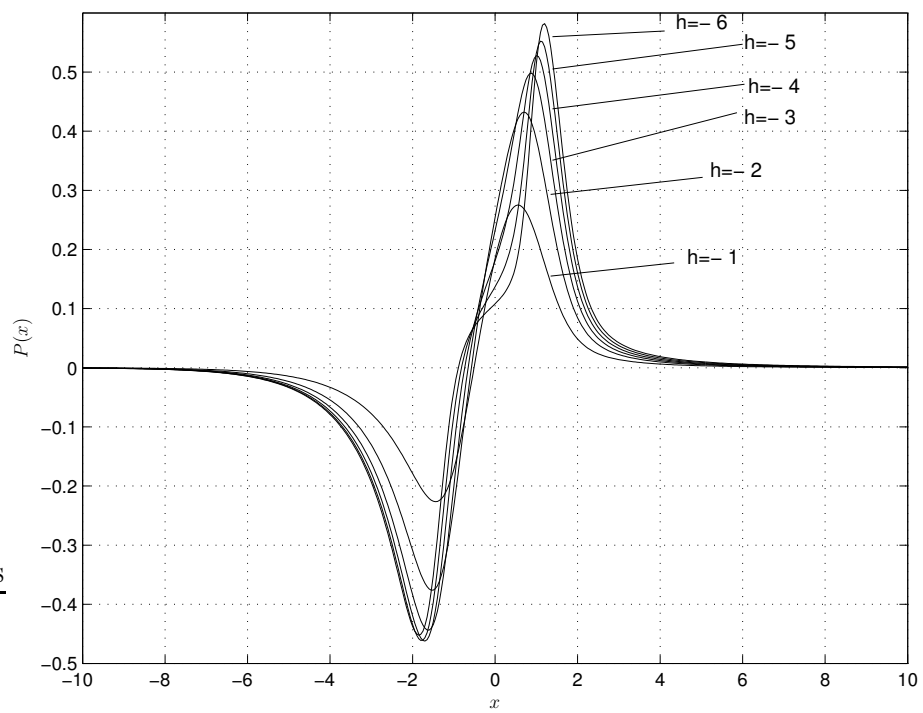
Figure 4.22: Pressure distributions for various values of h with $k = 1.0$.
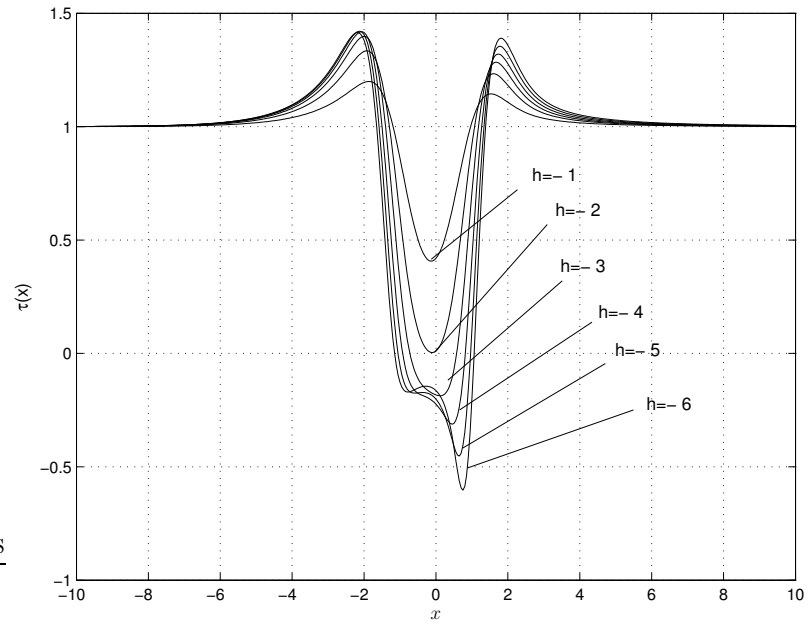
Figure 4.23: Skin friction distributions for various values of h with $k = 1.0$.
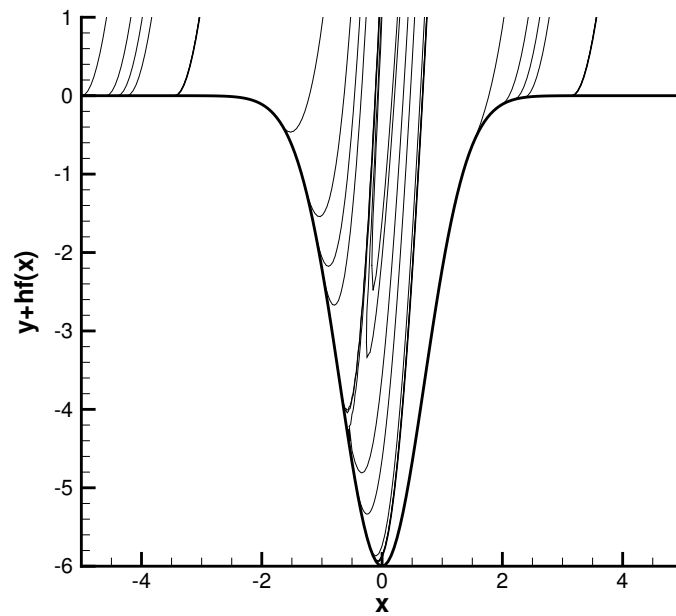
Figure 4.24: Streamline distribution for $h = -6$ with $k = 1.0$.
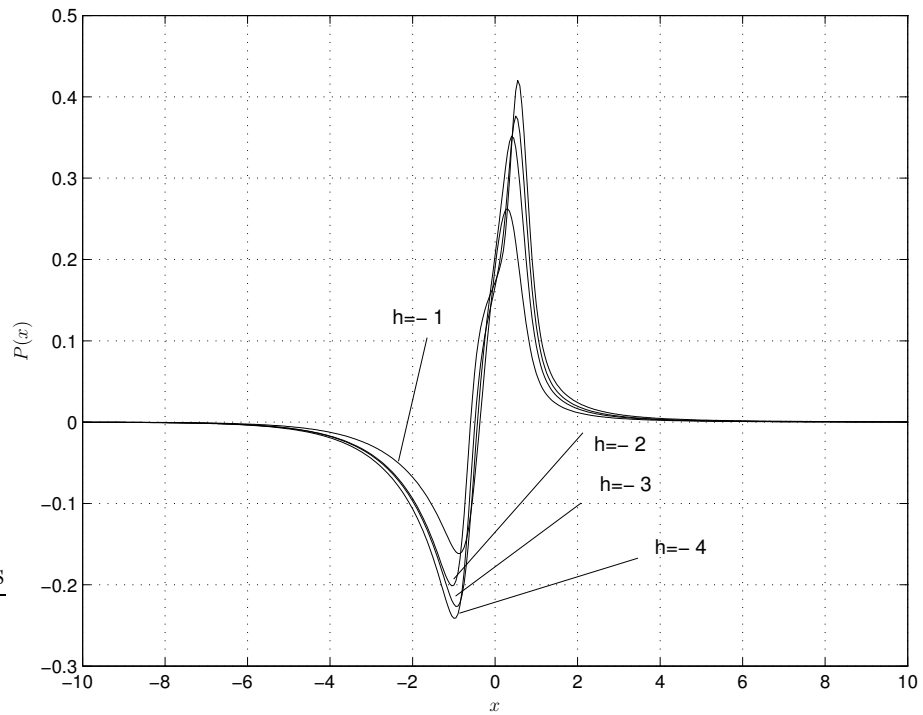
Figure 4.25: Pressure distributions for various values of h with $k = 2.0$.
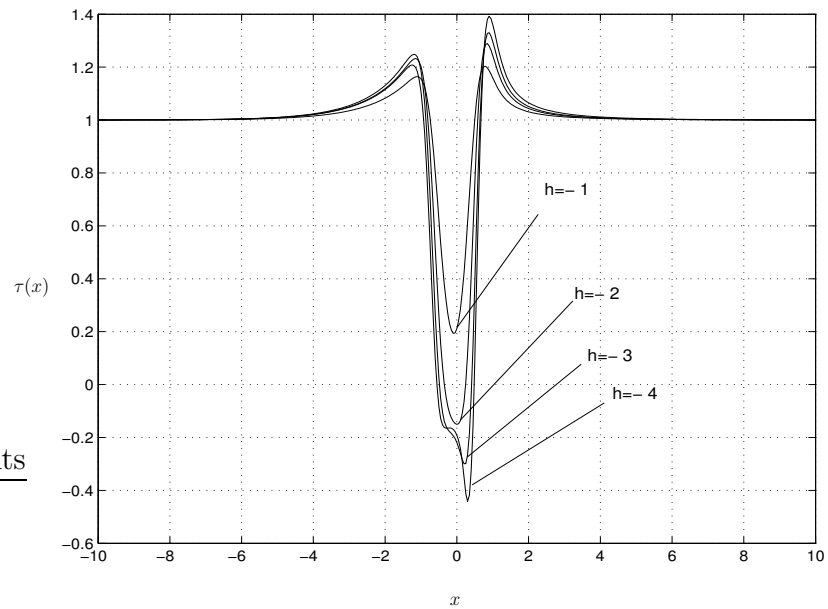
Figure 4.26: Skin friction distributions for various values of h with $k = 2.0$.
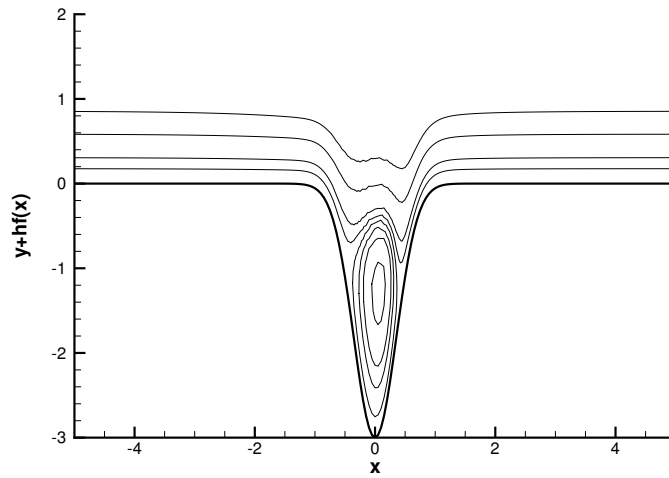
Figure 4.27: Streamline distribution for $h = -4$ with $k = 2.0$.

PSfrag replacements
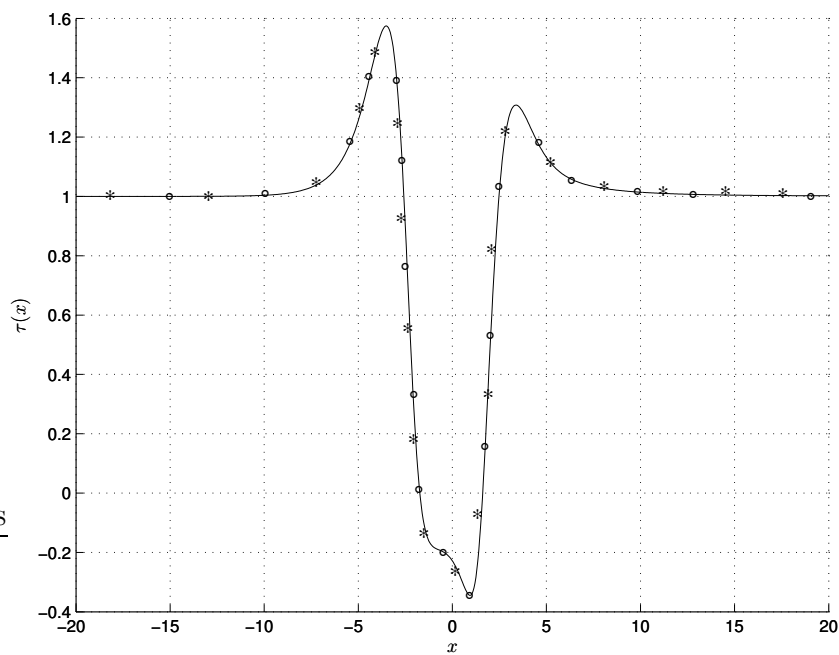
Figure 4.28: Skin friction distributions for various grids with $k = 0.5$, $h = -6.0$: '-' (8001×64), '$\circ$' (4001×70), '$*$' (6001×90).
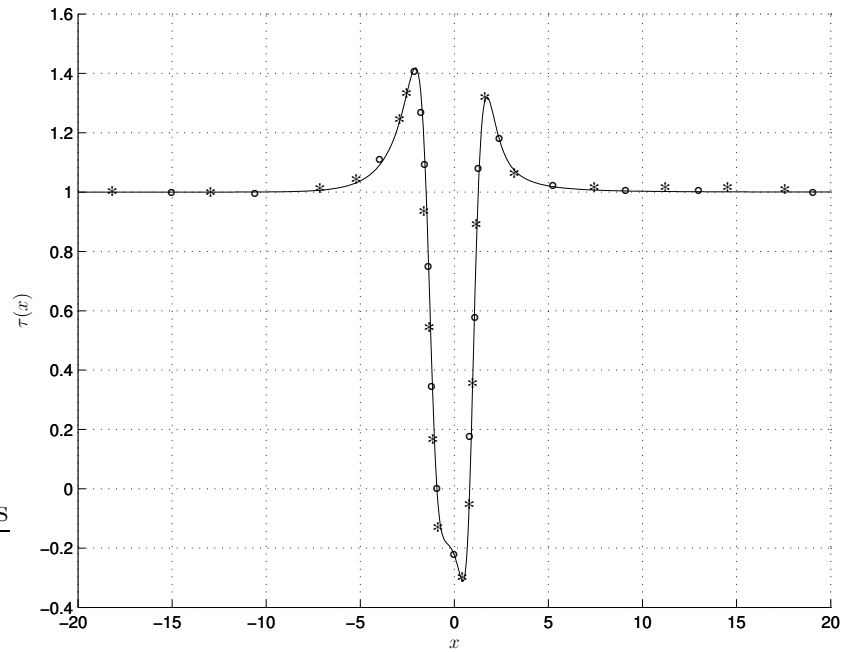
Figure 4.29: Skin friction distributions for various grids with $k = 1.0$, $h = -4.0$: '-' (8001×64), '∘' (4001×70), '∗' (6001×90).
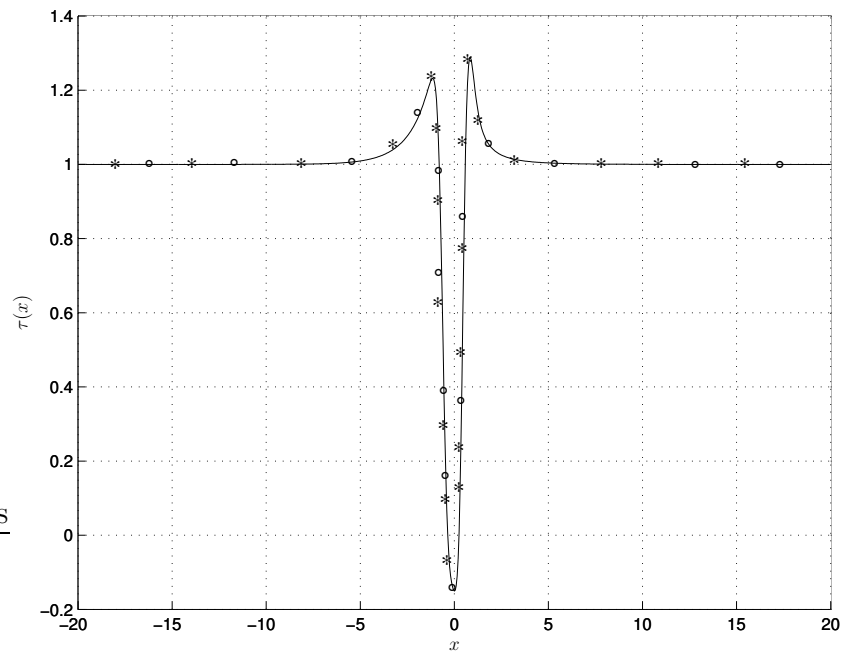
Figure 4.30: Skin friction distributions for various grids with $k = 2.0$, $h = -2.0$: '-' (8001×64), '∘' (4001×70), '∗' (6001×90).

4.3   Concluding remarks

In this section we provide concluding remarks for this chapter. We have extended our numerical technique explained in Chapter 2 for supersonic flow past humps and indents. Typically, our numerical method required 6-8 iterations for convergence. Smith (1973) provided the analytical solutions for the supersonic flow past humps considering a parabolic shape. Smith's results were confirmed numerically by Napolitano *et al.* (1979). Korolev (1987) studied the problem of supersonic flow past a hump and found regions of flow reversal ahead and behind of it. He considered the shape of the hump to be of the form $h(1 - x^2)^2$. In this study, we considered the shape of the hump/indent given by (3.12), which is of the same shape as that for wall-jets, liquid layers encountering humps/indents. In the case of humps, we find pressure plateauing in the separated regions both ahead behind the hump. We also observe regions of flow reversal ahead and behind the hump as observed by Korolev (1987). As the height of the hump increases, the size of the separation regions increases. In case of indents, the pressure curves tend to flatten in the separated region. In contrast to the case of humps, where there are regions of reversed flow, ahead of and behind the hump peak, here there is a single separated flow region located symmetrically with respect to indentation.

Chapter 5

Supersonic viscous-inviscid interaction with moving walls

5.1 Introduction

The study of steady flow over moving walls has been a fascinating topic for researchers for over 50 years. The point at which wall shear stress vanishes, which defines the separation point in steady flow over fixed walls (Prandtl (1904)), was found to be insufficient for separation in flows involving moving walls. The first explanation was given by Rott (1956), Sears (1956) and Moore (1958). These authors proposed another criterion for separation, different from that of Prandtl. The approach to the analysis was based upon an analogy between separation of an unsteady boundary layer and steady boundary layer separation from the surface of the moving body. For such flows numerical solutions were able to continue past the time at which reversed flow first occurs at the trailing edge, through times over which the separation point moved upstream with an accompanying increase in size of the reversed flow region, the so-called unsteady separation, up to a some finite time at which the solution appeared to break down at some definite point in the flow. In a generalization of the fixed wall case, that suggested, as indicated by the diagrams, that the solution breaks down at a stagnation point in the flow where there is also a vanisher shear. Rott (1956), Sears (1956) and Moore (1958) independently arrived at almost identical conclusions,

which are summarised in Figures 5.1 and 5.2. Their intent was to generalise the well-understood case of plane, steady flow at a fixed wall. As the sketches show, it was assumed that the boundary layer flow in both moving wall cases (downstream and upstream) would be bifurcated by the wake at some kind of stagnation point and that, in these steady flows, vanishing shear at a stationary point away from the wall would characterise the phenomenon. Thus, Moore, Rott and Sears (MRS) proposed

$$\frac{\partial u}{\partial y} = 0, \qquad u = 0, \tag{5.1}$$

as the criterion for separation.

The sketches in Figures 5.1, 5.2 and the separation criterion of (5.1) were convincingly verified by the experiments of Vidal (1959), Ludwig (1964) and Koromilas & Telionis (1980). The velocity profiles sketched in Figure 5.2, which correspond to the streamline sketches in Figure 5.1, are transformed to a wall fixed-frame by simply adding or subtracting appropriate constant velocities. This leads to the sketches in Figure 5.2.

Sears & Telionis (1975), Telionis *et al.* (1973) studied numerically the problem of steady separated flow over a downstream moving wall. In their papers, it was shown that a singularity appears at the MRS point instead of the point of zero skin friction. Sears & Telionis (1975) also suggested that a reversal of flow direction has no significance in boundary-layer flows other than the steady flow past a fixed wall and the singularity of boundary-layer equations identifies the location of a point of separation. Williams III (1977) transformed certain classes of semi-similar unsteady flows with separation into steady flows over a moving wall and verified the MRS criterion for separation was accompanied by a "singularity". Danberg & Fransler (1975) employed an integral method and calculated non-similar steady two-dimensional boundary-layer development over both upstream and downstream moving walls. Sychev (1979) studied the solution neighbourhood of the singular point and proved that the solution cannot be continued downstream of the MRS singularity, which is why this singularity is thought to represent boundary-layer separation. Van Dommelen & Shen (1982) demonstrated that the shedding of boundary-layer vorticity into the free stream at a

(a)

u_w

(b)

(c)

u_w
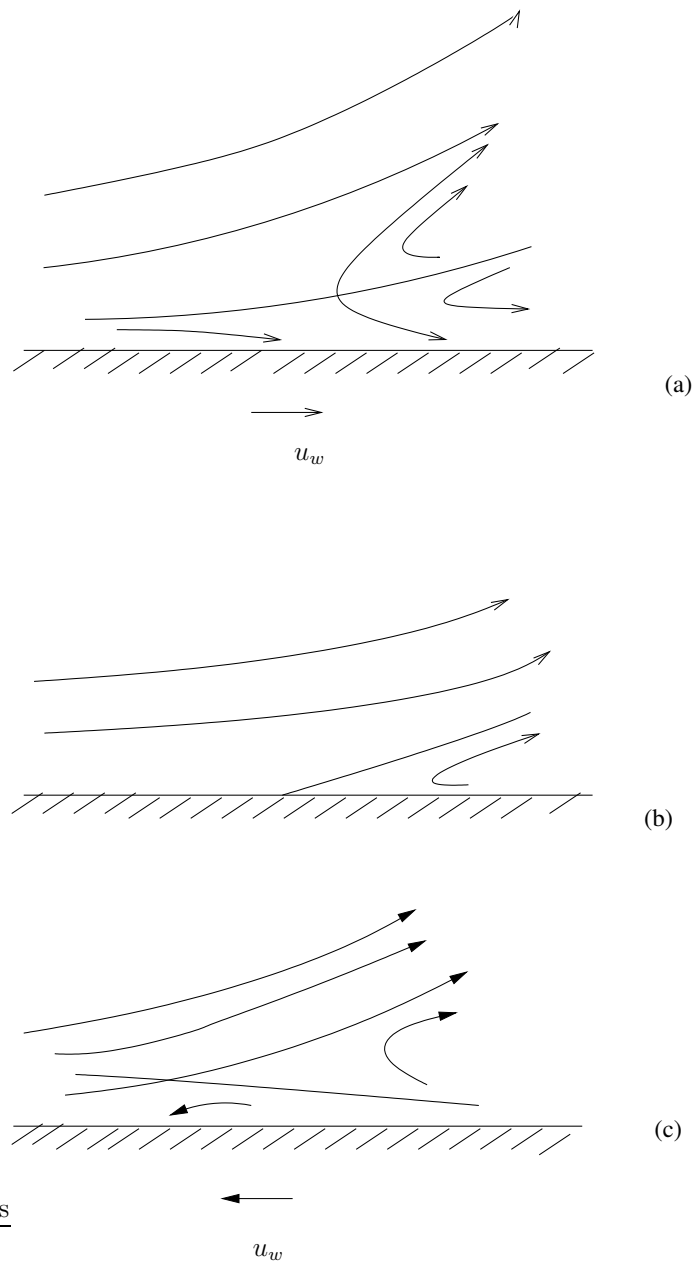
Figure 5.1: Stream line patterns proposed by Moore, Rott and Sears
(a) downstream moving wall (b) fixed wall (c) upstream moving wall (Proposed by
Sears & Telionis).
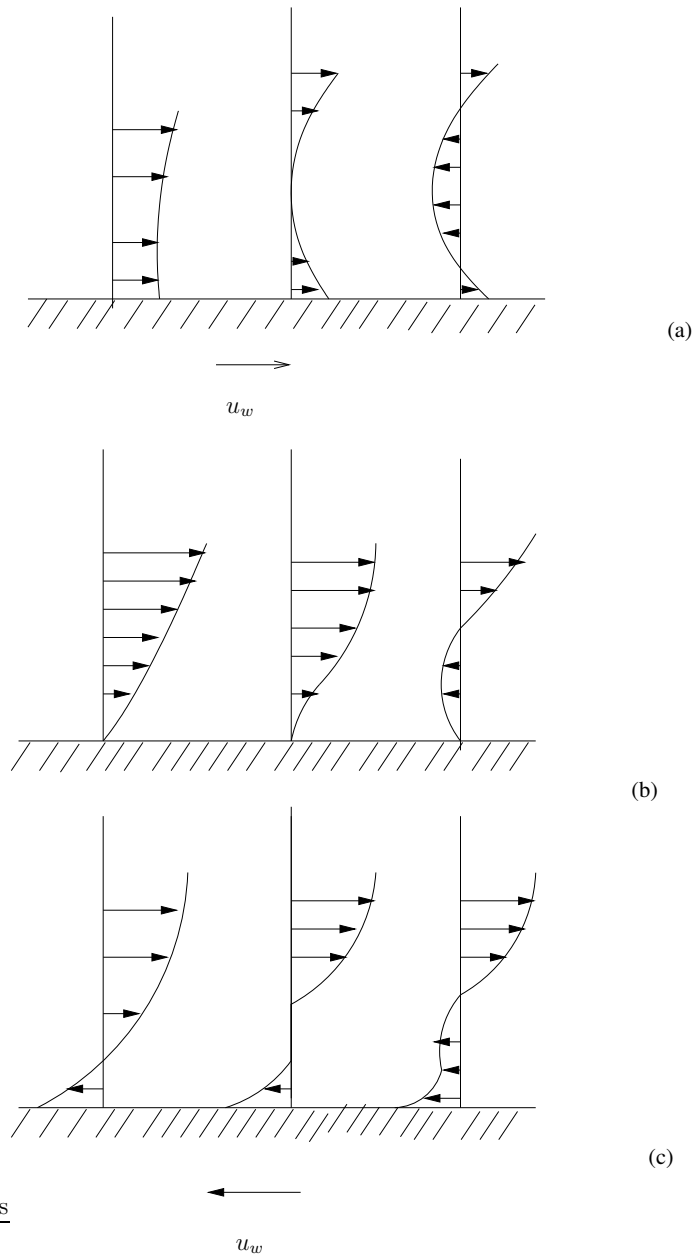
Figure 5.2: Velocity profiles as proposed by Moore, Rott and Sears
(a) downstream moving wall (b) fixed wall (c) upstream moving wall (Proposed by
Sears & Telionis).

singular point satisfied the MRS condition. Cebeci (1982), using a different technique, found his results agreed very well with Van Dommelen & Shen (1982) calculations and showed that in addition to the MRS singularity, a weaker non-removable singularity may arise. Tsahalis (1976) studied numerically the laminar boundary layer and separation for a steady outer inviscid flow over an upstream moving wall for the first time and concluded that for a steady flow over an upstream moving wall, the separation coincides with the boundary layer model with a Goldstein-type singularity. This paper also provided support for the theoretical model for the case of separation in unsteady flow over a downstream wall. Elliott *et al.* (1983) sought the form of the singularity near the MRS point using the assumption that the displacement function is inversely proportional to the N-th power of the distance from the separation point. For an adverse pressure gradient they obtained a displacement function that was inversely proportional to the 1/6-th power of the distance from the separation point, and with a favourable pressure gradient they found that the displacement function has a logarithmic form. Inoue (1981) obtained numerical results for the upstream moving wall and indicated that the recirculating region starts without the simultaneous vanishing of both longitudinal velocity and skin friction.

The concept of viscous-inviscid interaction in the classical scenario, has allowed us to remove the singularity for fixed walls and obtain small-scale separation. Early numerical solutions for the supersonic flow past concave corners based on triple-deck theory were provided by Rizzetta *et al.* (1978), Ruban (1978). They concluded that the solution near the separation point takes the form characteristic of separation with a semi-infinite eddy region forming as the scaled ramp angle becomes large and the size of the separation region increases. Smith & Khorrami (1991) studied this problem and their calculations revealed that a singularity develops in the solution at a finite value of scaled ramp angle which lead to the breakdown of solution. Recently this problem has been studied by Korolev *et al.* (2002) and their calculations did not confirm the concept of finite ramp angle singularity proposed by Smith & Khorrami (1991).

Araki (2006) studied the problem of boundary-layer separation on a moving wall

based on viscous-inviscid interaction and considered both the downstream and up-
stream cases. For a downstream moving wall, the interaction region had a four tier
structure and for sufficiently fast flows $1 \ll \hat{u}_w \ll Re^{1/8}$ the occurrence of separation
is delayed downstream by a distance

$$\Delta x = O\left[\frac{Re^{-5/8}}{\hat{u}_w^2}ln\frac{Re^{-3/4}}{\hat{u}_w^6}\right].$$

where $\epsilon = \frac{u_w^*}{u_\infty} = U_w = Re^{-\frac{1}{8}}\hat{u}_w = Re^{-\frac{1}{8}}\mu_0^{-1/4}\rho_0^{-1/2}\lambda^{1/4}\beta^{-1/4}u_w$ where

$x = u_w Re^{\frac{1}{8}}\mu_0^{-1/4}\rho_0^{-1/2}\lambda^{5/4}\beta^{3/4}x_{num}$ and $y = \frac{1}{u_w}Re^{-\frac{1}{8}}\mu_0^{1/4}\rho_0^{-1/2}\lambda^{-3/4}\beta^{-1/4}(y_{num} +$
$f(x))$. For the upstream moving wall case, he observed that there is a sharp pressure-
drop region in the vicinity of the point where the shock interacts with the boundary-
layer. The pressure increases rapidly after the pressure drop near the shock impinging
point. The width of the pressure drop region increases as $|u_w|$ increases.

In this chapter we consider steady supersonic flow past concave corners with
moving walls. A description of the flow is given by triple deck theory. We investigate
the quantitative properties of the fluid flow near the separation point when the wall
and separation point are in relative motion. We consider cases in which the wall is
moving in either the downstream or the upstream direction.

5.2   Problem Formulation
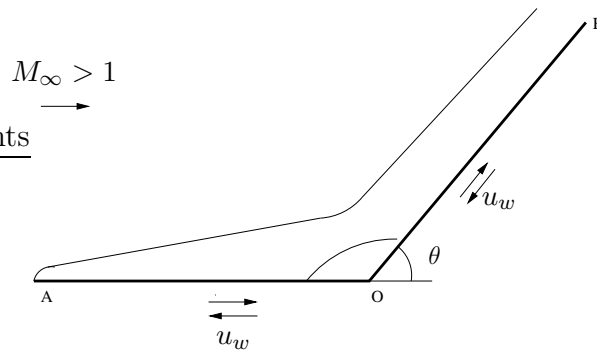
Figure 5.3: Diagram of the model.

Let us consider a supersonic flow past with constant velocity u_w of $O(Re^{-\frac{1}{8}})$ past a
compression ramp and parallel to the free-stream as shown in Figure 5.3.

The equations governing the flow are given by (1.12) and following conditions: On the body surface

$$u = u_w \qquad v = 0 \quad \text{at} \quad y = 0, \tag{5.2}$$

and in the middle layer

$$u = y + u_w \quad \text{at} \quad x \to -\infty, \tag{5.3}$$

and the boundary condition (1.15), where u_w is the scaled wall velocity. The interaction law is given by Ackeret's formula (1.16).

5.3   Numerical results

The $\frac{dp}{dx}$ term is approximated by a three point central difference formula incorporating the second derivative of $A''(x_j)$ given in (2.9) and this leads to a block pentadiagonal matrix of the form (2.12). The elements of the matrices are given in Appendix C. We use the numerical method described in Chapter 2 with an uniform grid. Values of $x_{-\infty} = -60$ and $x_{\infty} = 60$ were used to truncate the domain in the streamwise direction. A step size of $\Delta x = 0.01$ and 64 points in the y-direction were used. The shape $f(x)$ appears in the numerical algorithm as a second derivative with respect to x. The corner was rounded slightly so that $\frac{d^2 f}{dx^2}$ was a smooth function everywhere. In the present study the surface was defined by $f(x) = \frac{1}{2}\alpha\left[x + \sqrt{x^2 + r^2}\right]$, where α is the scaled ramp angle. Here r is called the rounding parameter, and as $r \to 0$ the surface collapses to a sharp plate. Our results are shown for $r = 0.5$. Calculations were performed using different values of y_{max} to determine the influence of the computational domain in the y direction. Korolev *et al.* (2002) reported that any value less than $y_{max} = 50$ provided unreliable results since over shooting of the minimum skin friction occurred. Thus we used a finite value of $y_{max} = 50$ in our calculations. $u_w = 0.0$

The results with $u_w = 0.0$ and various angles are shown in Figures 5.4 and 5.5. The case $p > 0$ leads to a pressure rise, and corresponding skin-friction fall (adverse pressure gradient), ultimately leading to a plateauing of the pressure and weakly

separated or reversed flow. The results show similar behaviour to the previous investigations of Rizzetta *et al.* (1978), Ruban (1978), Smith & Khorrami (1991) and Korolev *et al.* (2002). Our numerical technique produced oscillations for ramp angle $\alpha > 5.3$. It was shown in the paper by Korolev *et al.* (2002) that the solutions did not break down and there was no indication of a singularity developing at finite ramp angles.

PSfrag replacements
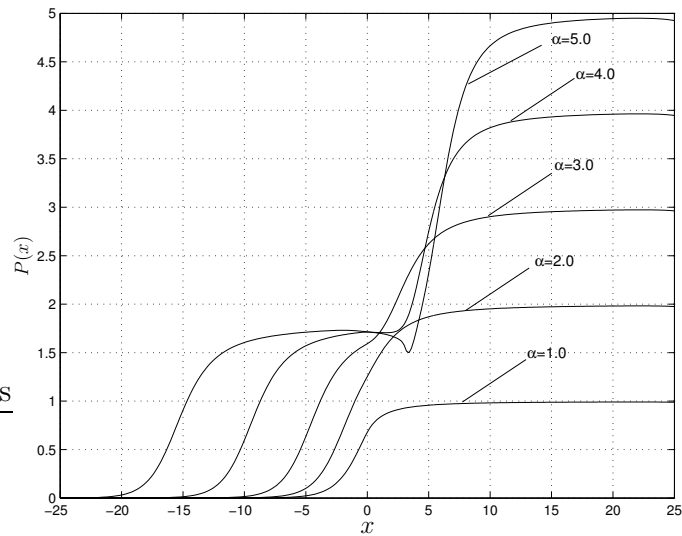
Figure 5.4: Pressure distributions for various α with $u_w = 0.0$.

PSfrag replacements
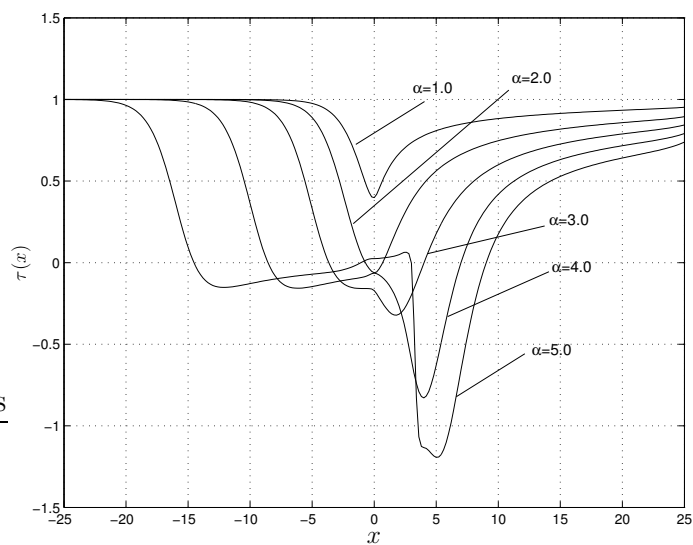
Figure 5.5: Skin friction distributions for various α with $u_w = 0.0$.

Before discussing the numerical results we need to describe what the skin friction graphs indicate. Figure 5.6 is a diagram showing the effect of skin friction. The skin friction having a negative sign no longer necessarily indicates if the flow is reversed, rather it indicates if the fluid in the boundary-layer is moving faster or slower than the wall.

positive U but negative τ

U

PSfrag replacements

u_w

y
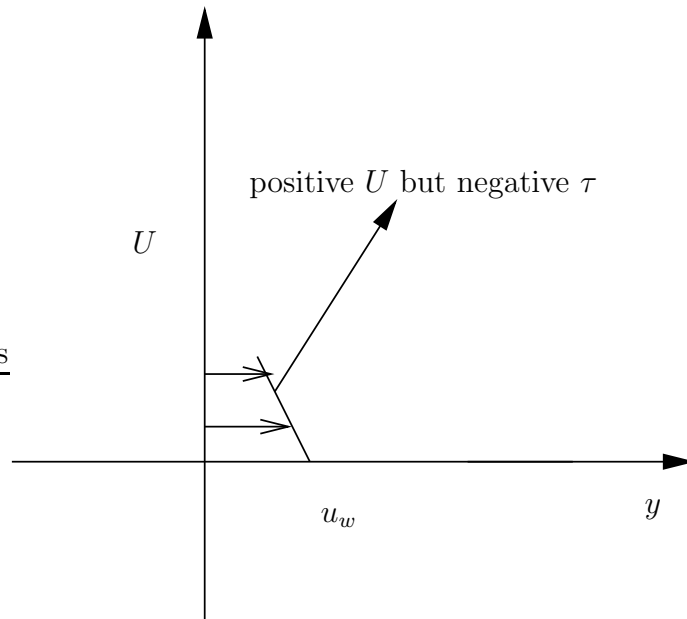
Figure 5.6: Diagram showing effect of skin friction.

5.3.1   Downstream moving wall

$u_w = 0.2$

The results for $u_w = 0.2$ are shown in Figures 5.7-5.11. The pressure distribution shown in Figure 5.7 increases from its initial value forming a "plateau" upstream of the corner. There is a hint of a second "plateau" region being formed, before finally the pressure increases corresponding to inviscid flow past the ramp. Figure 5.9 shows the streamline pattern. One can observe the formation of a saddle point upstream of the corner. The saddle point is formed approximately at $x = -15.2$, $y = 1.0$. There is a hint of another saddle point being formed approximately at $x = 8.0$ and $y = 0.4$ downstream of the corner. In addition a vortex centred on the corner can be seen. Downstream of the corner one can observe the formation

of another vortex. The velocity and vorticity profiles are shown in Figures 5.10 and 5.11. It is evident from the velocity profile that a point exists where $u = \frac{\partial u}{\partial y} = 0$. This is also clear from the vorticity distribution where there is a line of zero vorticity. We can conclude that the MRS criterion is satisfied for the downstream moving wall. All subsequent results are shown for $\alpha = 6.0$. We had problems with the convergence of our numerical technique as the angle was increased. Figure 5.12 shows velocity and vorticity contours indicating that two MRS points exist.

PSfrag replacements
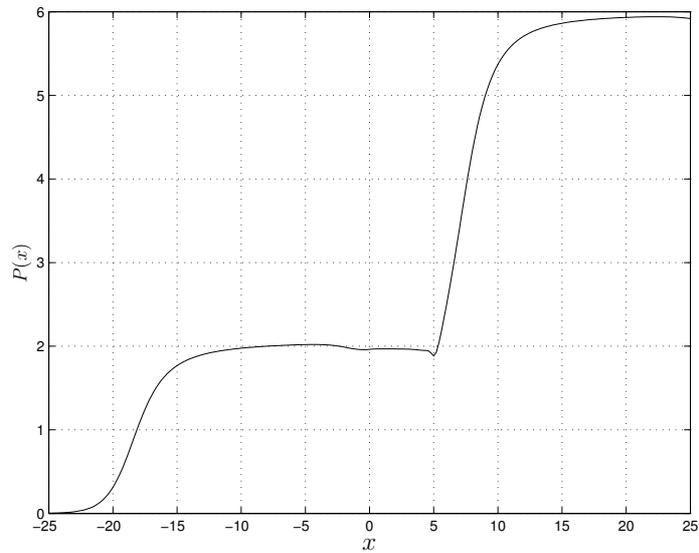
Figure 5.7: Pressure distribution for $u_w = 0.2$, $\alpha = 6.0$.
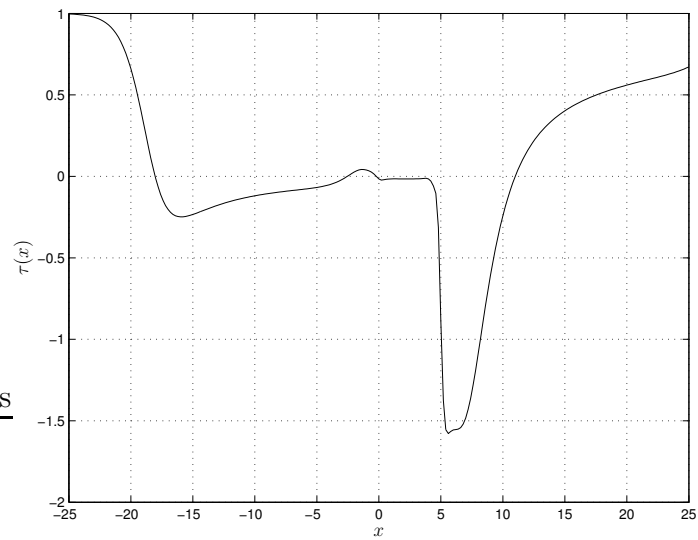
Figure 5.8: Skin friction for $u_w = 0.2$, $\alpha = 6.0$.
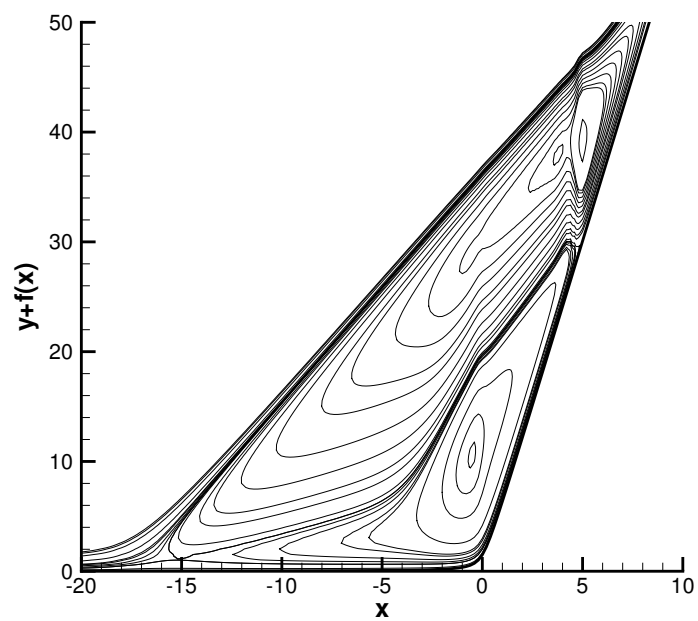
Figure 5.9: Streamline pattern for $u_w = 0.2$, $\alpha = 6.0$.
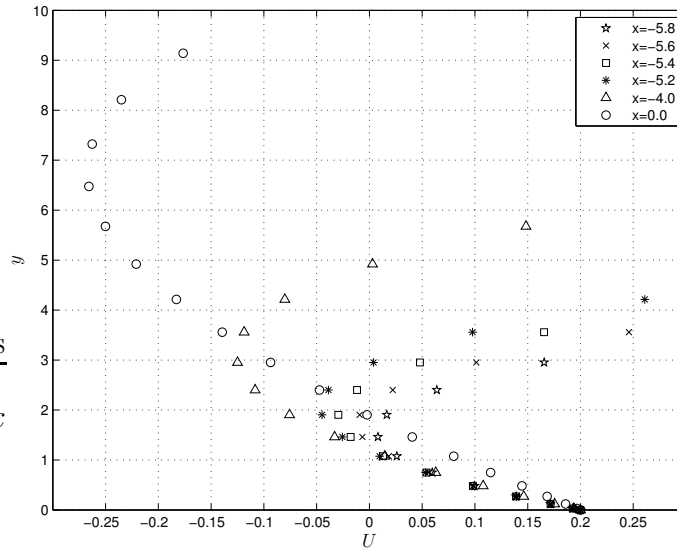
Figure 5.10: Velocity profile for $u_w = 0.2$, $\alpha = 6.0$.
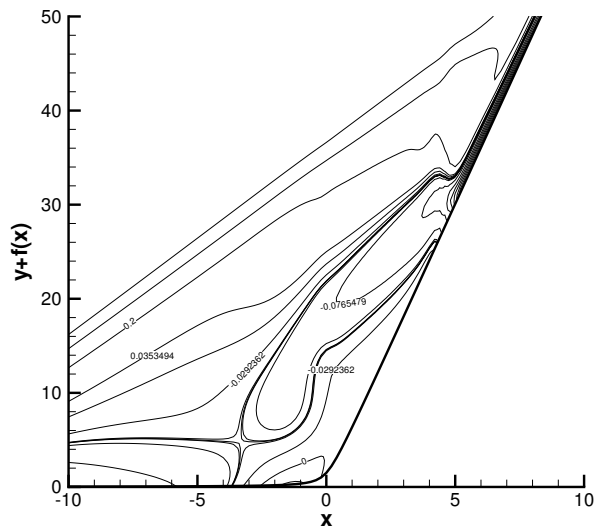
Figure 5.11: Vorticity for $u_w = 0.2$, $\alpha = 6.0$.

PSfrag replacements
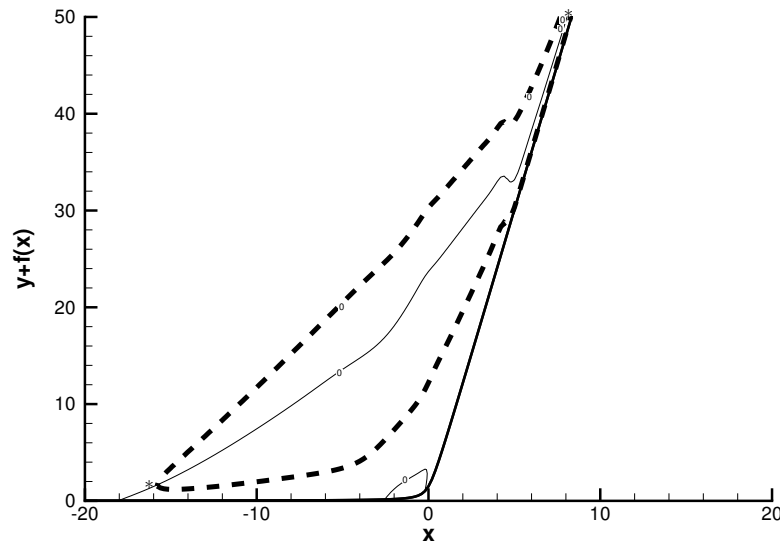
Figure 5.12: Velocity and vorticity contours indicating MRS points : $*$, '-':vorticity $\frac{\partial u}{\partial y} = 0$, '- -':velocity $u = 0$.

$u_w = 0.5$

The results for a wall moving downstream with velocity $u_w = 0.5$ and an angle $\alpha = 7.0$ are shown in Figures 5.13-5.15. The pressure forms a "plateau" far upstream of the corner. A second "plateau" region is formed downstream of the corner. One can see a saddle point is formed upstream of the corner approximately at $x = -16.8$, $y = 2.5$. Another saddle point is also formed downstream of the corner approximately at $x = 7.6$, $y = 0.5$. Vortices are formed one above the other and centred on the corner, another vortex is also formed downstream of the corner. Near the corner there is an intensive recirculating motion of fluid and upstream we observe a stationary (dead water) fluid region.
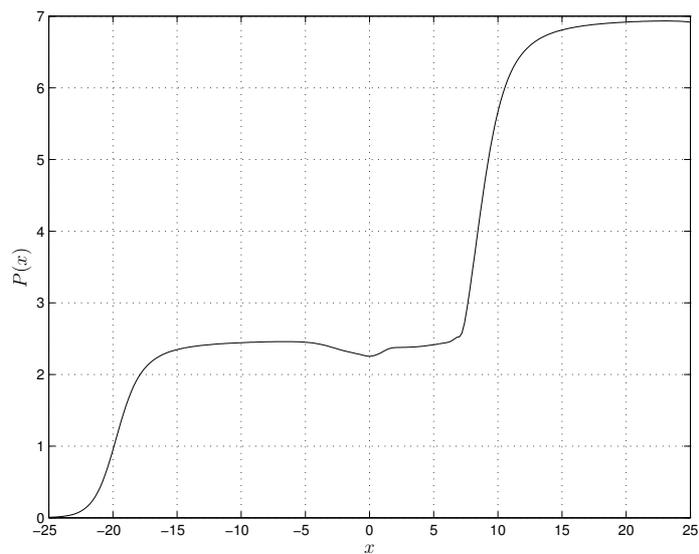
Figure 5.13: Pressure distribution for $u_w = 0.5$, $\alpha = 7.0$.
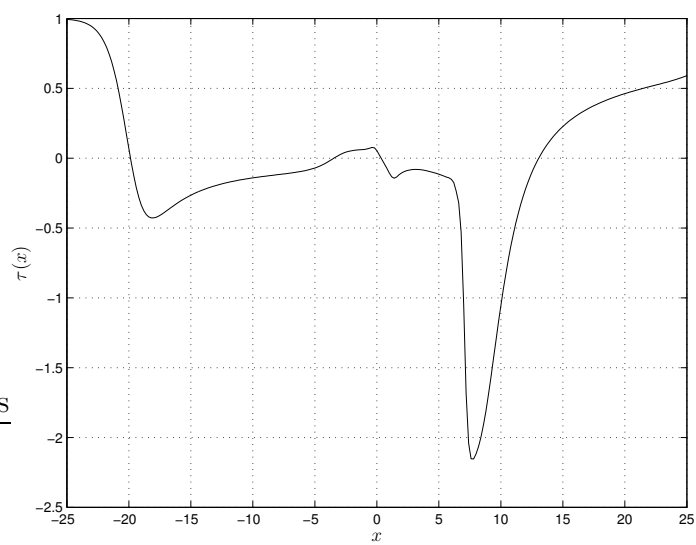
Figure 5.14: Skin friction for $u_w = 0.5$, $\alpha = 7.0$.
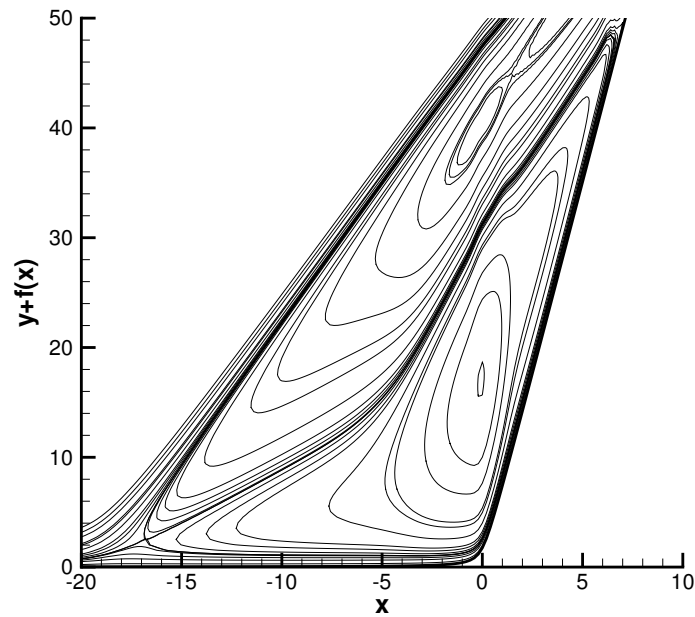
Figure 5.15: Stream line pattern for $u_w = 0.5$, $\alpha = 7.0$.

$u_w = 1.0$

The results for a wall moving downstream with velocity $u_w = 1.0$ and an angle $\alpha = 7.0$ are shown in the Figures 5.16-5.18. The pressure forms a "plateau" far upstream of the corner. Slightly upstream of the corner the pressure drops and then increases downstream of the corner and before finally increasing to $p = \alpha$ which corresponds to the inviscid flow past the ramp. The pressure drop near the corner is due to the intensive recirculating motion of the fluid, which also explains the behaviour of the skin friction seen in Figure 5.17. The streamline pattern shows the formation of a saddle point upstream of the corner approximately at $x = -16.8$, $y = 2.5$ and downstream of the corner approximately at $x = 7.6$, $y = 0.5$. One can observe the formation of vortices one above the other which are centred on the corner, another vortex is also formed downstream of the corner.

PSfrag replacements
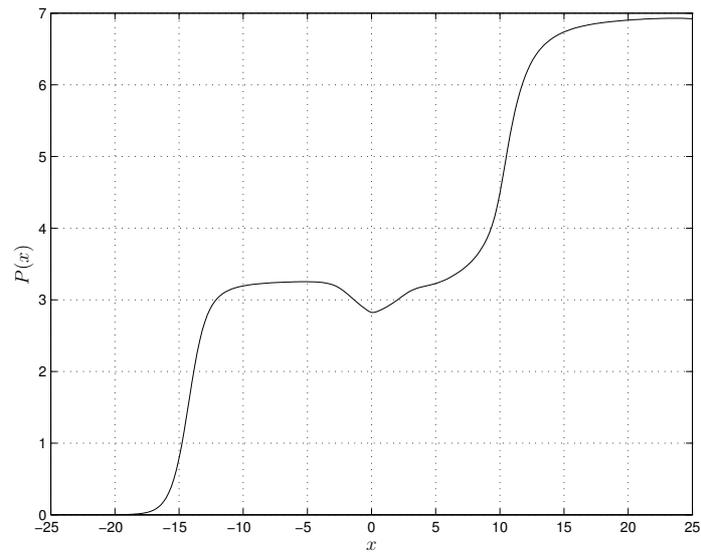
Figure 5.16: Pressure distribution for $u_w = 1.0$, $\alpha = 7.0$.

PSfrag replacements
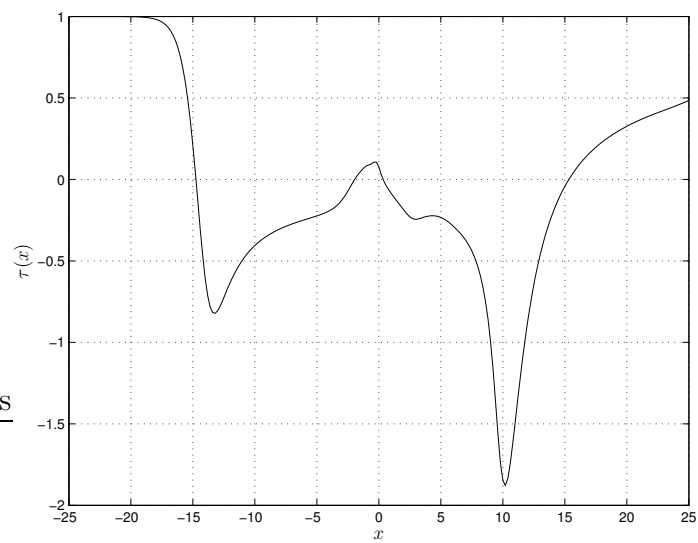
Figure 5.17: Skin friction for $u_w = 1.0$, $\alpha = 7.0$.
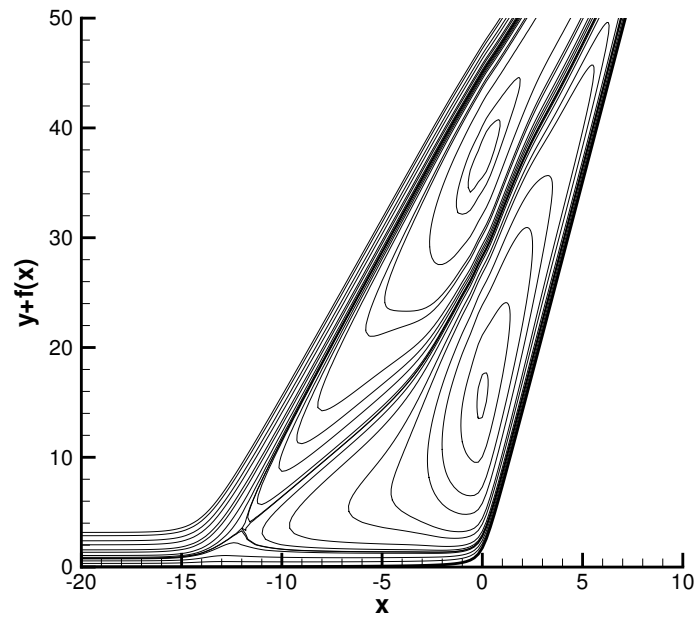
Figure 5.18: Stream line pattern for $u_w = 1.0$, $\alpha = 7.0$.

$u_w = 2.0$

The results for a wall moving with velocity $u_w = 2.0$ and an angle $\alpha = 9.0$ are shown in Figures 5.19-5.21. The pressure forms a "plateau" far upstream of the corner. The pressure drops significantly upstream of the corner and increases downstream of it before finally increasing to $p = \alpha$. The streamline pattern is shown in Figure 5.21. Upstream of the corner a saddle point is formed approximately at $x = -8.2$, $y = 4.2$, downstream of the corner another saddle point is formed approximately at $x = 11.4$, $y = 2.0$. Two vortices are formed one above the other and are centred on the corner. By comparing the pressure distributions for different wall speeds we see that size of the pressure drop increases upstream of the corner.

PSfrag replacements
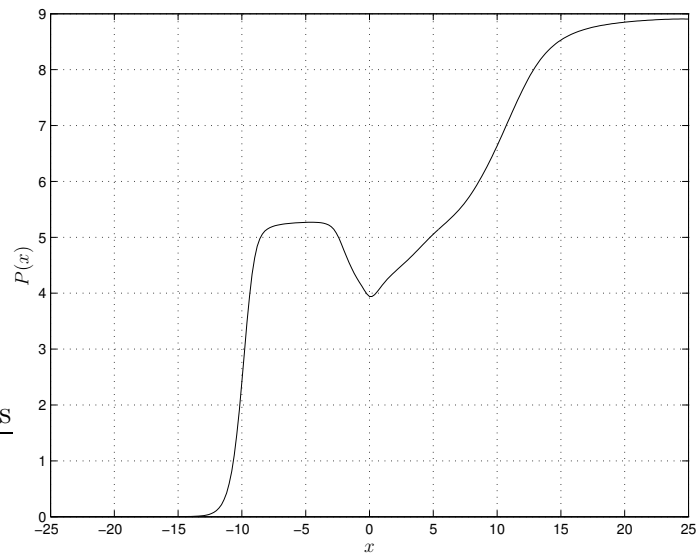
Figure 5.19: Pressure distribution for $u_w = 2.0$, $\alpha = 9.0$.

PSfrag replacements
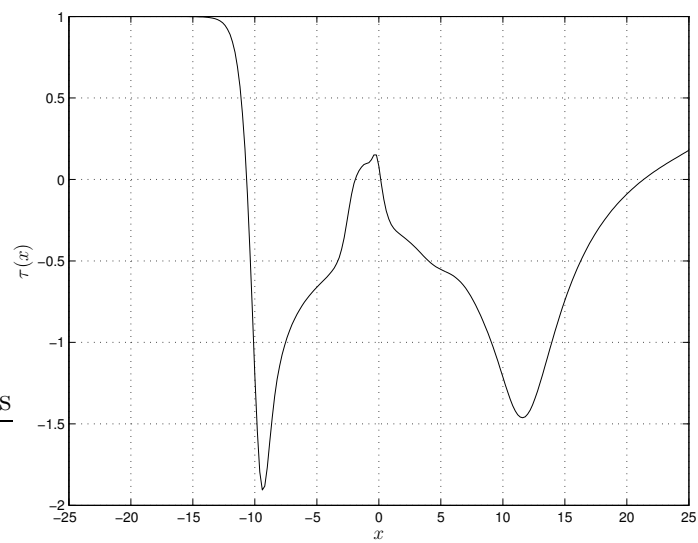
Figure 5.20: Skin friction for $u_w = 2.0$, $\alpha = 9.0$.
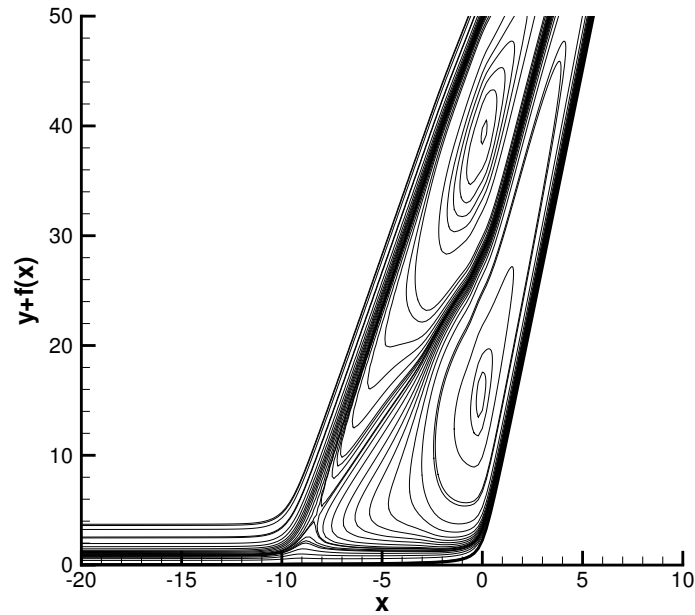
Figure 5.21: Streamline pattern for $u_w = 2.0$, $\alpha = 9.0$.

For $u_w = 2.0$ we compare the pressure distribution obtained numerically with that obtained using the analytical expression of Araki (2006), see Figure 5.22. The numerical solution shows good agreement with the analytical solution. The analytical solution for the pressure distribution at higher scaled wall speeds i.e $u_w \gg Re^{-\frac{1}{8}}$ but still $u_w \ll 1$ is given by

$$P = \frac{1}{2}\left[1 - \left(\frac{1 - e^x}{1 + e^x}\right)^2\right] \text{where} \quad x < 0 \tag{5.4}$$

which basically represents a soliton.

PSfrag replacements

x
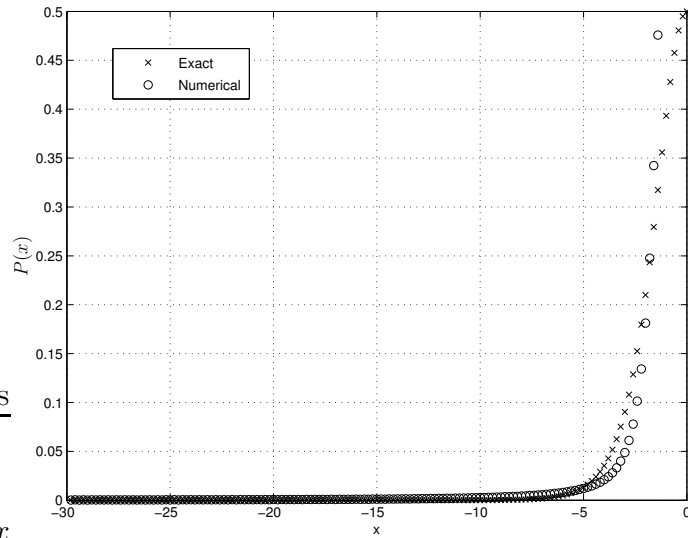
Figure 5.22: Analytical and numerical pressure distributions for $u_w = 2.0$.

This is related to steady-form of Smith & Burggraf (1985) Triple Deck analysis for large displacement in nonlinear stability theory. A review of solutions of soliton type can be found in Zhuk (2001). Analytical results for higher wall speeds have been obtained by E. J. Watson (private communication, J. W. Elliott) and Lipatov (1999). In order to show that downstream moving wall delays separation Figure 5.23 shows maximum value of α against u_w. A more detailed description about the relation between the analytical and numerical solutions are provided in Appendix A.
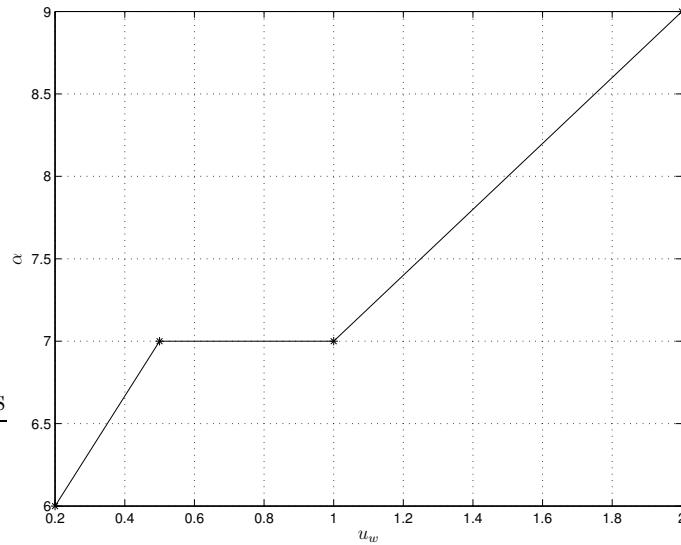
Figure 5.23: Figure showing the effect of the wall moving downstream.

5.3.2 Upstream moving wall

In this section we present numerical results for a wall moving upstream with different scaled wall velocities. Values of $x_{-\infty} = -100$ and $x_{\infty} = 100$ were used to truncate the domain in the x direction. A step size of $\Delta x = 0.05$ has been used in the streamwise direction and 64 points were sufficient in the y-direction. As before, we used a value of $y_{\infty} = 50$ to limit the computational domain in the y direction.

$u_w = -0.2$

Results for a wall moving upstream with velocity $u_w = -0.2$ and angle $\alpha = 3.25$ are shown in Figures 5.24-5.28. The pressure increases from its initial value and then decreases at the corner $(x = 0)$. The pressure forms a "plateau" upstream of the corner. We observe that the extent of the "plateau" is small compared to when the wall was moving downstream. The pressure increases downstream of the corner corresponding to $p = \alpha$. The drop in pressure around the corner explains the increase in skin friction around the corner which can be seen in the Figure 5.25. The corresponding streamline pattern in Figure 5.26 has a vortex centred on the corner

and a wedged shaped region. This wedged shaped region is the "pre-separation" region. The velocity profiles shown in Figure 5.27 do not show any evidence that $u = 0$, although Figure 5.28 has a zero vorticity line. Evidence that the MRS criterion is satisfied is inconclusive.

PSfrag replacements
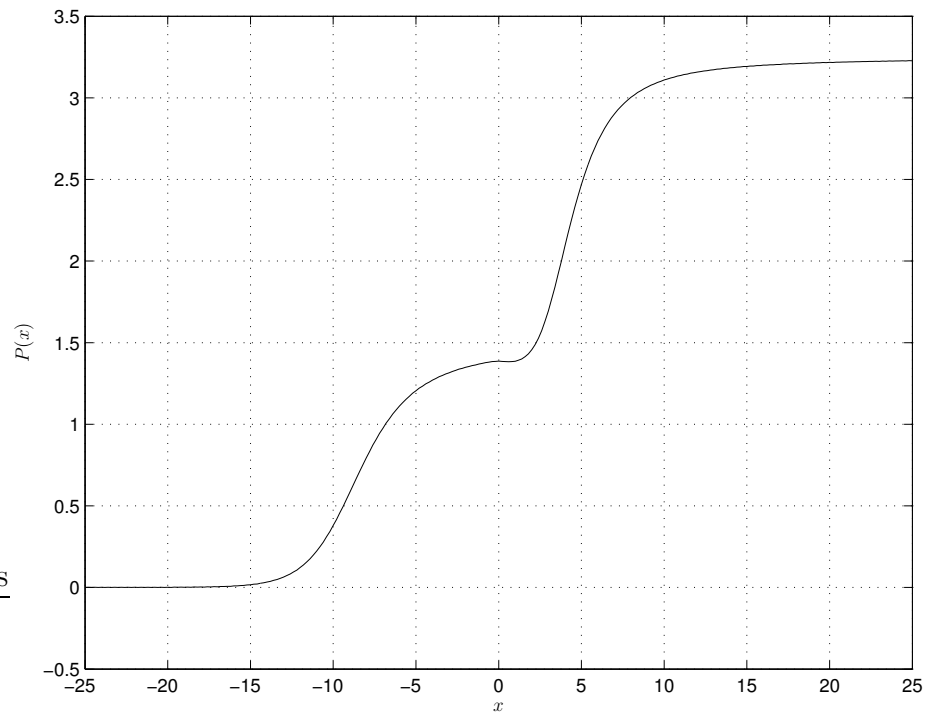
Figure 5.24: Pressure distribution for $u_w = -0.2$, $\alpha = 3.25$.
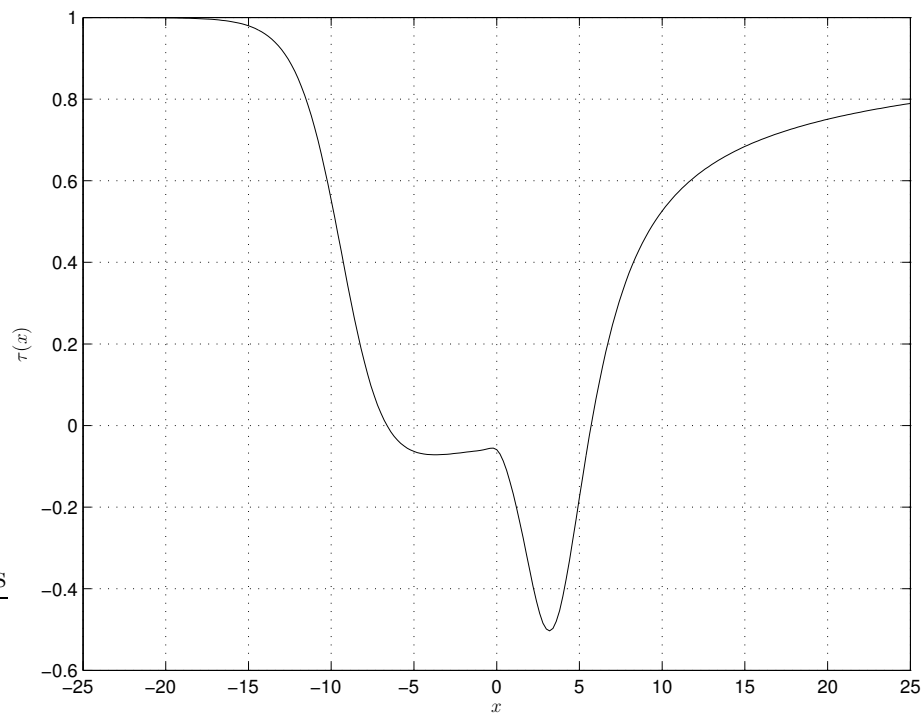
Figure 5.25: Skin friction for $u_w = -0.2$, $\alpha = 3.25$.
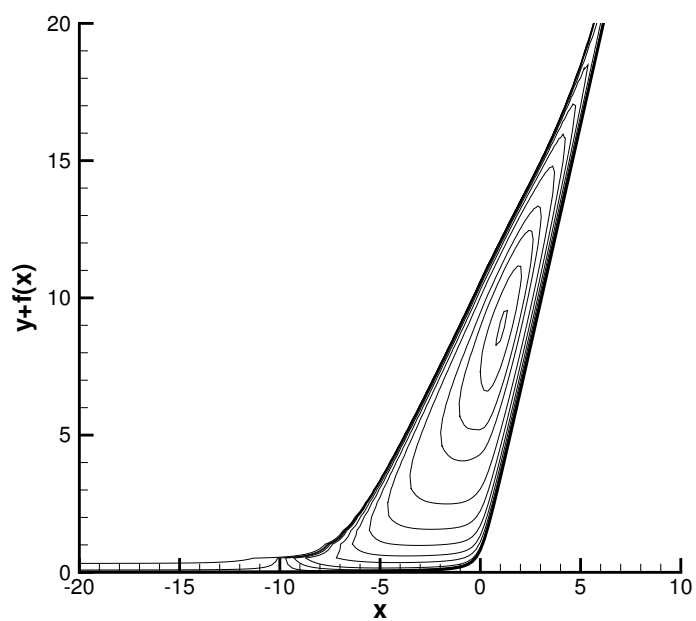
Figure 5.26: Stream line pattern for $u_w = -0.2$, $\alpha = 3.25$.

PSfrag replacements

U
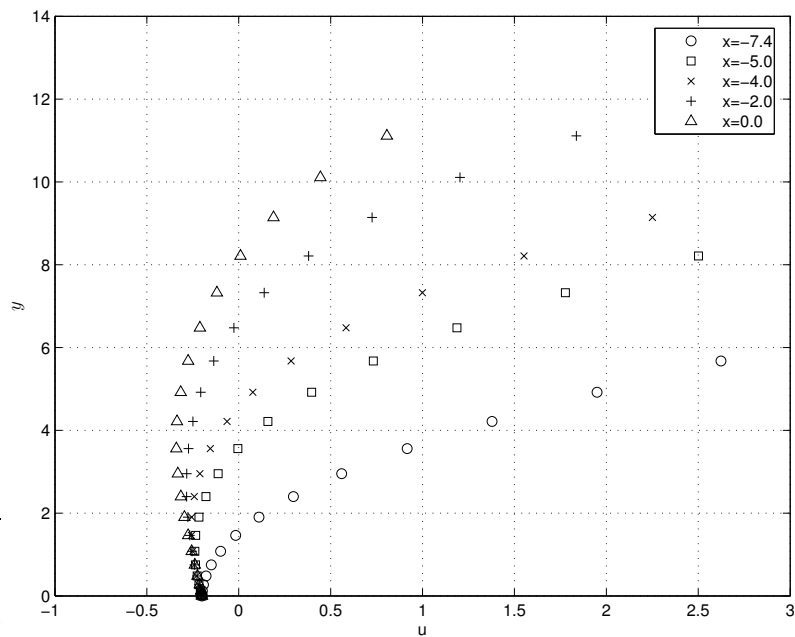
Figure 5.27: Velocity profiles for $u_w = -0.2$, $\alpha = 3.25$.
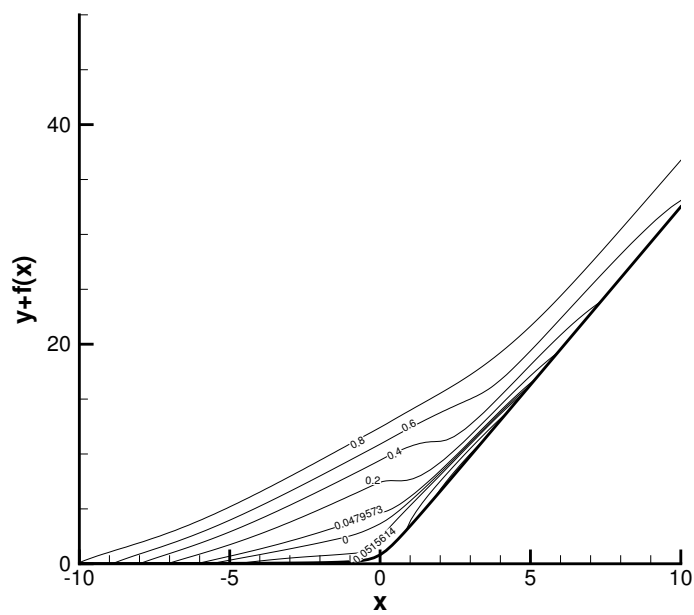
Figure 5.28: Vorticity distribution for $u_w = -0.2$, $\alpha = 3.25$.

$u_w = -0.5$

Figures 5.29-5.31 give the pressure and skin friction distributions and the streamline pattern for a wall moving with $u_w = -0.5$ and an angle $\alpha = 3.1$. The pressure behaves in a similar manner to the case when the velocity as $u_w = -0.2$ except that drop in pressure is more nearer the corner. The streamline pattern shows a vortex forms centred on the corner. The length of the "pre-separation" region has increased in comparison to the case $u_w = -0.2$.

PSfrag replacements
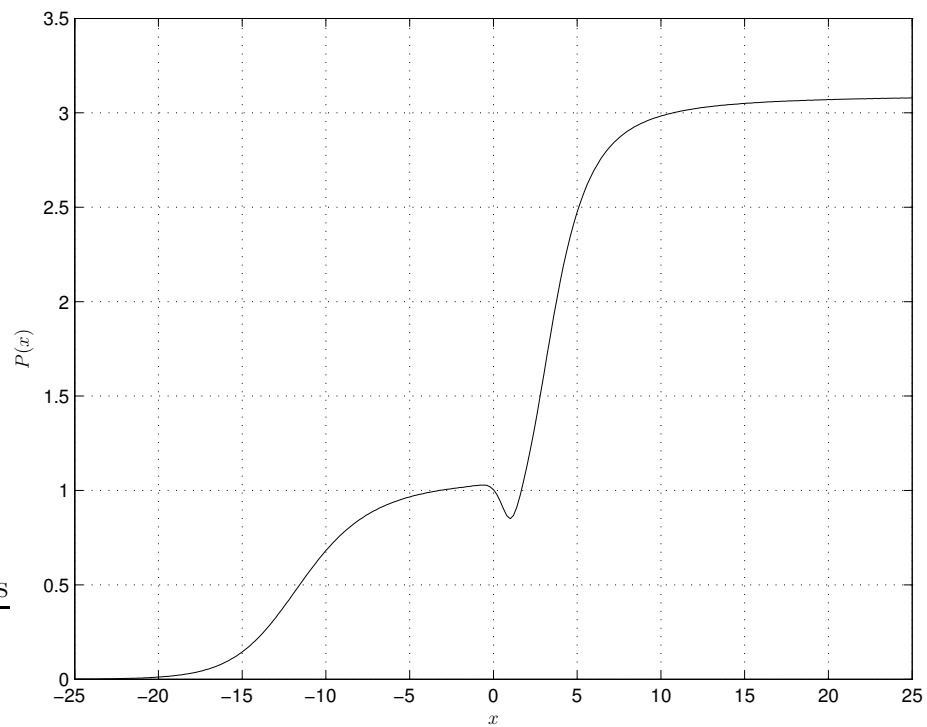
Figure 5.29: Pressure distribution for $u_w = -0.5$, $\alpha = 3.1$.

PSfrag replacements
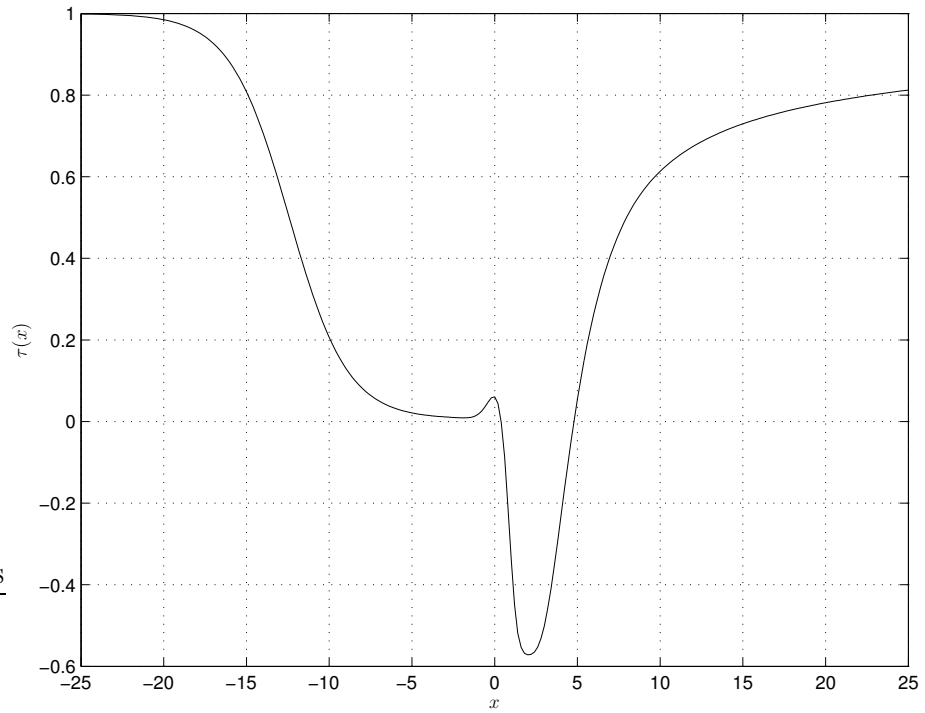
Figure 5.30: Skin friction for $u_w = -0.5$, $\alpha = 3.1$.
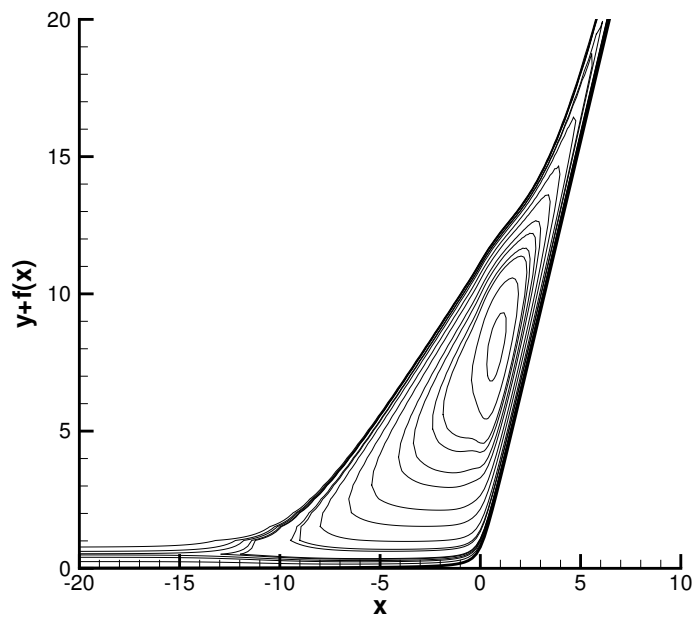
Figure 5.31: Stream line pattern for $u_w = -0.5$, $\alpha = 3.1$.

$u_w = -1.0$

The pressure and skin friction distributions and the streamline pattern are shown for a wall moving with $u_w = -1.0$ and an angle $\alpha = 2.25$ in Figures 5.29-5.31. The drop in pressure is more nearer the corner than when $u_w = -0.2, -0.5$. The rise in pressure from its initial value is slow compared to $u_w = -0.2, -0.5$. Again the streamline pattern shows a vortex forms centred on the corner.

PSfrag replacements
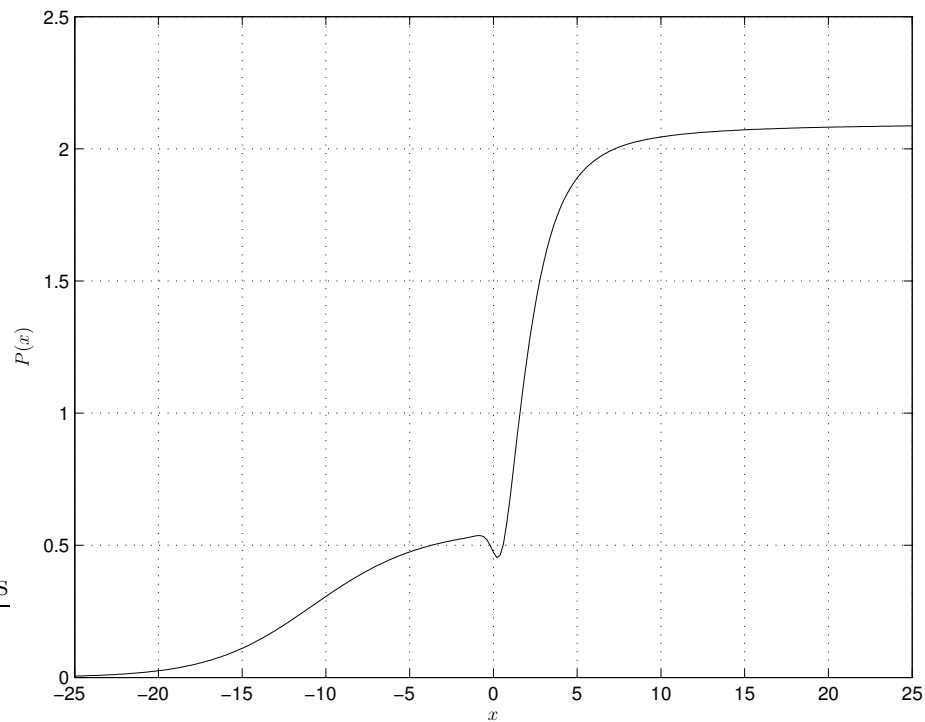
Figure 5.32: Pressure distribution for $u_w = -1.0$, $\alpha = 2.25$.
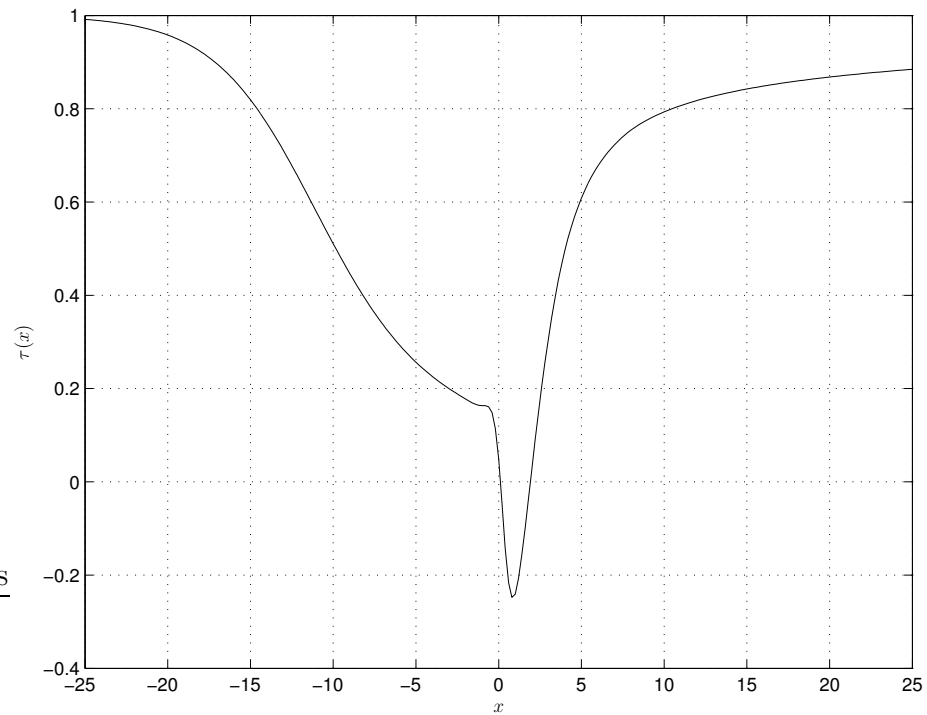
Figure 5.33: Skin friction for $u_w = -1.0$, $\alpha = 2.25$.
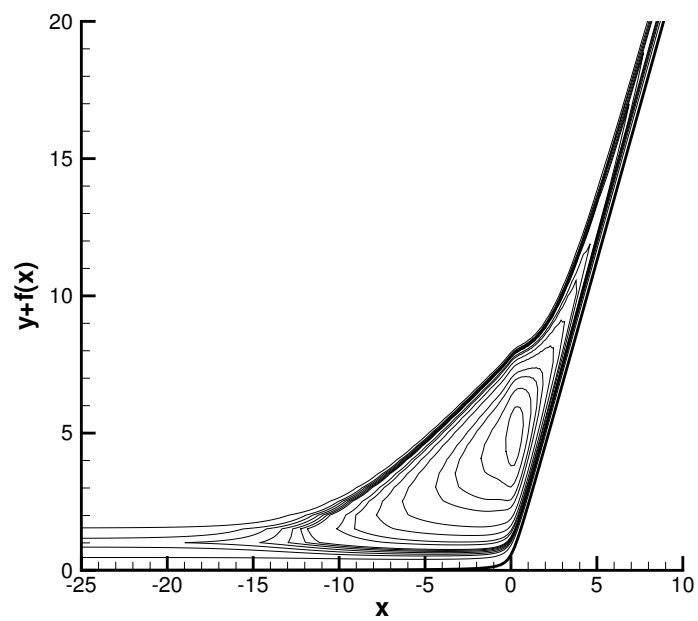
Figure 5.34: Stream line pattern for $u_w = -1.0$, $\alpha = 2.25$.

$u_w = -2.0$

The pressure and skin friction distributions and the streamline pattern for a wall moving with velocity $u_w = -2.0$ and an angle $\alpha = 2.0$ are shown in Figures 5.35-5.37. The pressure rise is very slow from its initial value. We believe that this behaviour happens for a turbulent boundary-layer prior to separation. The slow rise in pressure and then sharp decrease near the corner explains the behaviour in skin friction shown in Figure 5.36. The streamline pattern shows a vortex forms centred around the corner whose length increases as the wall velocity is lowered. As the wall velocity is lowered the length of the "pre-separation" region also increases.

PSfrag replacements
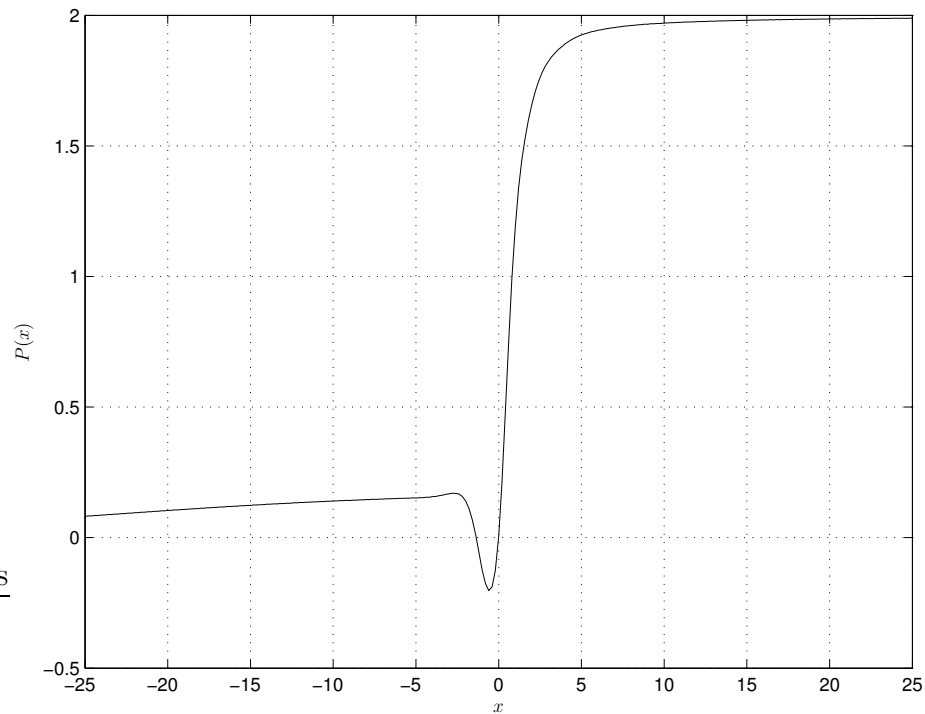
Figure 5.35: Pressure distribution for $u_w = -2.0$, $\alpha = 2.0$.
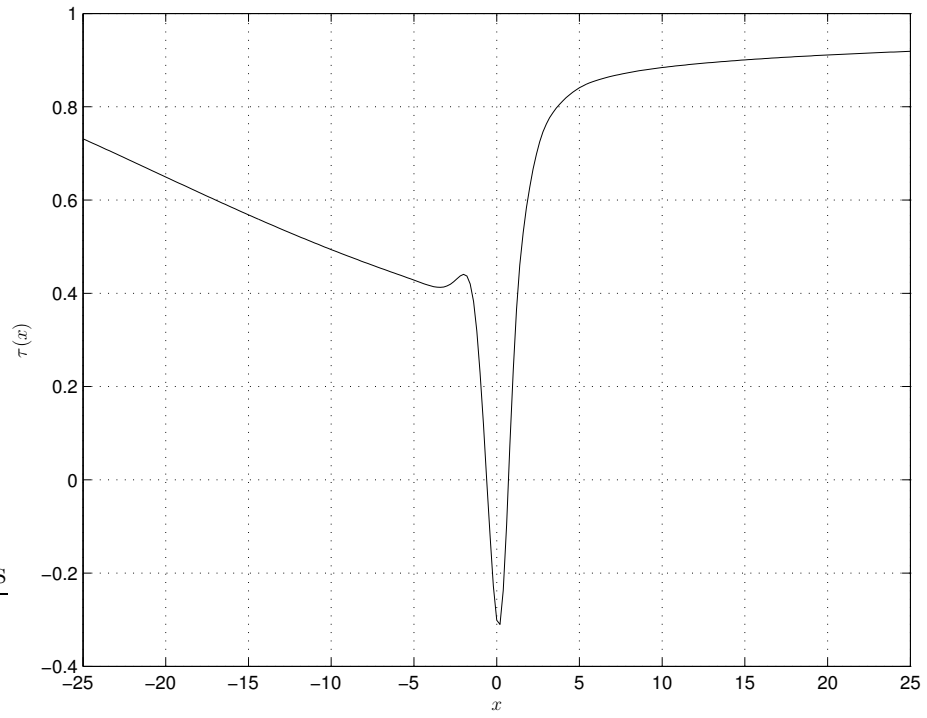
Figure 5.36: Skin friction for $u_w = -2.0$, $\alpha = 2.0$.

PSfrag replacements
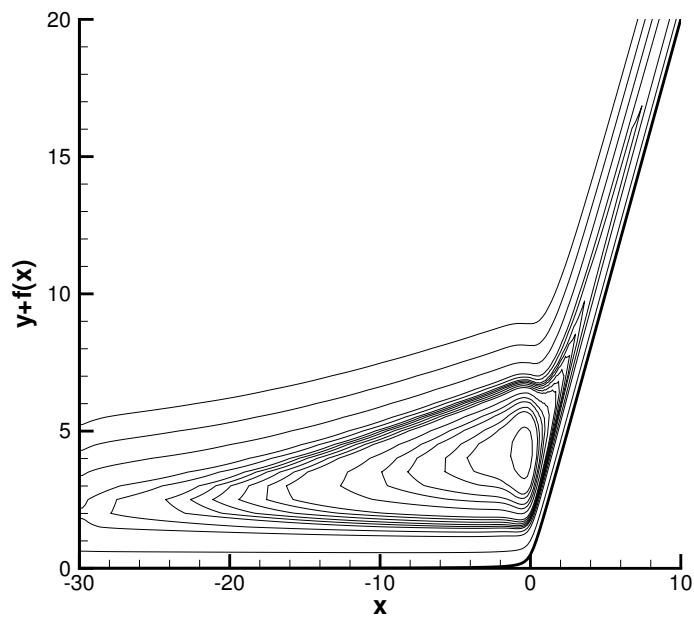
Figure 5.37: Streamline pattern for $u_w = -2.0$, $\alpha = 2.0$.
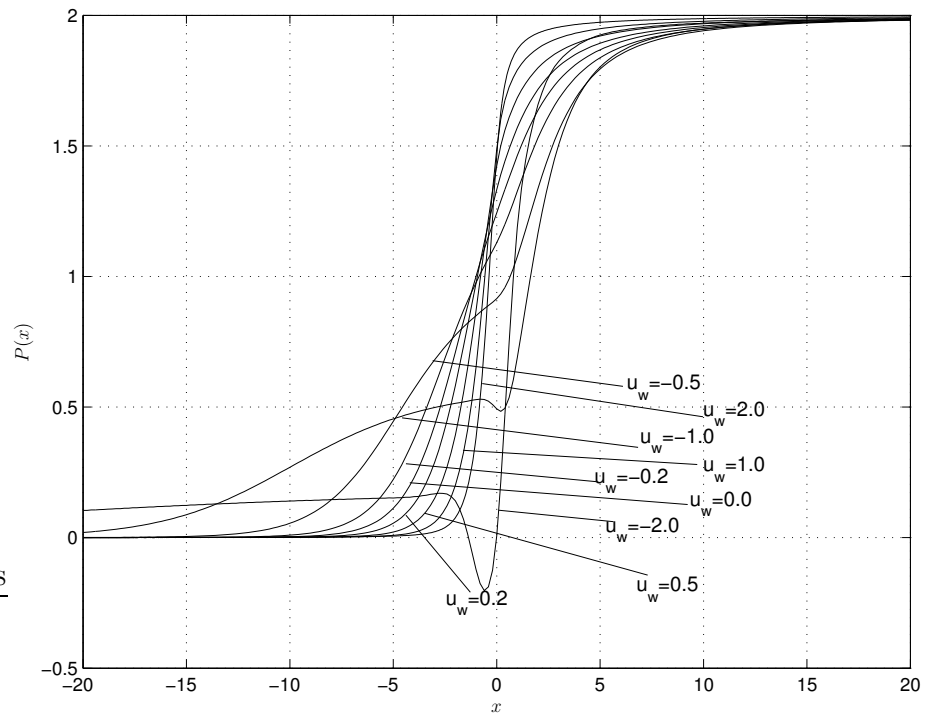
Figure 5.38: Pressure distribution for various values of u_w at $\alpha = 2.0$.

The effect of the velocity u_w on the pressure and skin friction distribution is shown in Figures 5.38 and 5.39. At negative wall velocities, the pressure rises very slowly from its initial value and then exhibits a sharp decrease near the corner. The skin friction also shows an increase near the corner for negative wall velocities.
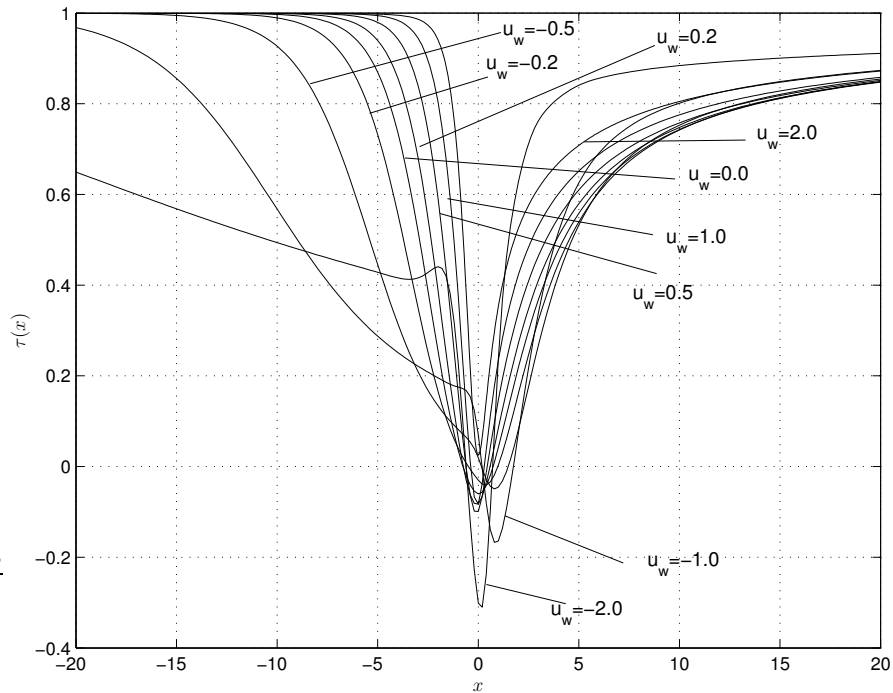
Figure 5.39: Skin friction for various values of u_w at $\alpha = 2.0$.

5.4 Concluding remarks

In this chapter we investigated boundary-layer separation over moving walls for a supersonic external flow. We have investigated cases where the wall is moving either in the downstream or in the upstream direction. We used the same numerical method as described in Chapter 2. Typically $8 - 10$ Newton iterations were sufficient for the method to converge. Results for various values of $|u_w|$ are shown for certain angles. We observe that beyond these scaled ramp angles our numerical method failed to converge. For the downstream moving wall, the pressure forms a "plateau" upstream of the corner. We observed that there exists a point where $u = \frac{\partial u}{\partial y} = 0$ satisfying the MRS criterion. This is evident from looking at the velocity and vorticity profiles and also from Figure 5.12 for the wall moving downstream with velocity $u_w = 0.2$. One can observe a saddle point being formed both upstream and downstream of the corner. At higher wall velocities, one can observe vortices being formed one above the other centred on the corner, and a further vortex is formed downstream of the corner.

For the upstream moving wall, the rise in pressure from its initial value is very slow at lower wall velocities which is evident from looking at the pressure distribution for $u_w = -2.0$. From the velocity and vorticity distribution it is not clear whether the MRS criterion is satisfied or not. We can say that the MRS criterion is not applicable for the upstream moving wall case. A recirculation region is formed that has a wedge shape. This region is described as a "pre-separation region". As the wall velocity is lowered the length of the "pre-separation" region increases. We believe that this sort of behaviour happens with turbulent boundary-layers prior to separation.

Thus we can say that the MRS criterion for separation is satisfied for the down-stream moving wall case but is not applicable to the upstream moving wall for the viscous-inviscid interaction problem considered in this chapter.

Chapter 6

Summary

Some fundamental fluid dynamics phenomena have been investigated in this thesis using an asymptotic analysis of the Navier-Stokes equation in the framework of *triple-deck* theory. The first problem is concerned with extending of numerical technique used in the paper of Korolev *et al.* (2002). This method uses a finite difference approximation in the x direction and Chebychev collocation in the y direction. We have applied this technique to study,

- Jet-like boundary layers encountering corners, humps and indents.

- Liquid layers encountering convex corner, humps and indents.

- Supersonic flow past humps, indents.

The interaction is represented by a double deck structure. For jet-like flow past corners, numerical results have been obtained and compared with the results of Merkin. The problem is formulated for a general body shape consistent with the lower deck scalings. We observed that separation occurs at $\alpha = 4.5$ contradicting Merkin & Smith (1982) results. An angle $\alpha = 14.0$ is sufficient to cause secondary separation. New flow features at higher angles have been observed which show the presence of a secondary separation region within the primary separation bubble. In the calculations of Merkin & Smith (1982), the computational domain in the y direction was restricted to $y_\infty = 14$. In our calculations we used a value of $y_\infty = 50$ that was

determined by trying with different values of y_∞ and assessing their impact on the computed solution. We observed that by restricting the domain in the y direction to too low a value of y_∞ as done by Merkin & Smith (1982), "overshooting " of the minimum skin friction occurs and under these circumstances no reliable results can be obtained. For a wall-jet flow past humps and indents, the shape of the hump/indent was given by $\bar{y} = h\exp(-k^2 x^2)$ depending upon the sign of h. We observed that separation occurs at much lower values of $|h|$ for various values of k compared to Merkin (1983) results. In case of humps, one can observe separation both ahead and behind the hump. Additionally, one can also observe a small recirculation region behind the hump within the large separation region. In case of indents, one can observe a separation region centred on $x = 0$. In addition to this we have also observed a small region of recirculation just behind the indent within the primary separation region for very low values of h.

We have also obtained numerical results for fully developed liquid layer flows over convex corners, humps and indents. For flow over convex corners, the numerical modelling is made simpler by using a smooth body shape. We saw that separation occurs at $\alpha = -13.4$ for $\sigma = 0.1$. We have observed from the numerical calculations that at $\sigma = 1$, there was no separation although Gajjar (1987) mentions that separation might occur at $\alpha = -15$. Separation was not observed even when the angle was decreased as far as $\alpha = -30$. Our numerical technique did not encounter any problems with convergence nor with the implementation of downstream boundary condition as faced by Gajjar. For the flow past humps and indentations, the shape was chosen to be the same as that used for near-wall jets. For the flow past humps, we observed that separation occurs both ahead and behind the hump. In the case of indents the separation region is centred at $x = 0$. For both humps and indents, at $\sigma = 2.0$ we observed short-scale waves decaying downstream. This sort of behaviour was observed by Gajjar (1987) and Bowles & Smith (1992).

We also extended our numerical technique to study supersonic flow past humps and indents. For the flow past humps we observed separation both ahead and behind the hump, and in the case of flow past indents the separation region is centred at

$x = 0$. Only 6-10 Newton iterations were typically required for convergence of our method. As a result of these efforts, we have demonstrated the versatility of our method.

In the second problem, we investigated boundary-layer separation over moving walls in supersonic flow. We have investigated the validity of the MRS criterion for separation over moving walls. In order to investigate the problem, a compression ramp moving with a finite wall velocity was considered. The velocity of the wall was assumed to be of order $Re^{-\frac{1}{8}}$. Wall velocities with $|u_w| = 0.2, 0.5, 1.0, 2.0$ for both downstream and upstream moving walls was investigated. For the downstream moving wall, the pressure forms a "plateau" upstream of the corner. The velocity and vorticity distributions for $u_w = 0.2$ clearly suggest that the MRS criterion is satisfied for the downstream moving wall. We observed the formation of a saddle point upstream and downstream of the corner. The streamline pattern shows that vortices are formed one above the other which are centred on the corner. We have also observed a vortex being formed downstream of the corner. At higher wall speeds i.e $u_w \gg Re^{-\frac{1}{8}}$ but still at $u_w \ll 1$, the pressure calculated numerically agrees with the analytical solution. For the upstream moving wall, at lower values of u_w, we observed that the pressure rise from its initial value is very slow. The streamline pattern shows a wedge-shaped structure with a vortex centred on the corner. We believe that this sort of behaviour happens with turbulent boundary-layers prior to separation and is known as "pre-separation region". As the wall speed is lowered, the length of the pre-separation region increases. The velocity profiles and vorticity distribution do not indicate that the MRS criterion is satisfied. We can say that the MRS criterion is satisfied for the downstream moving wall, but that it may not be applicable for the upstream moving wall.

Bibliography

ACKERET, J., FELDMANN, F. & ROTT, N. 1947 Investigations of compression shocks and boundary layers in gases moving at high speed. *Tech. Rep.* 1113.

ADAMSON, T. C. & MESSITER, A. F. 1980 Analysis of two-dimensional interactions between shock waves and boundary layers. *Ann. Rev. Fluid Mech.* **12**, 103–138.

ARAKI, D. 2006 Boundary-layer separation on moving surface in supersonic flow. PhD thesis, University of Manchester.

BLASIUS, H. 1908 Grenzschichten in flüssigkeiten mit kleiner reibung. *Tech. Rep.* 56. Engl. transl. NACA TM 1256.

BOWLES, R. I. & SMITH, F. T. 1992 The standing hydraulic jump: theory, computations and comparisons with experiment. *J. Fluid Mech* **242**, 145–198.

BROWN, S. N., STEWARTSON, K. & WILLIAM, P. G. 1975 On hypersonic self induced separation. *Phys. Fluids* **18** (6), 633–639.

CANUTO, C., HUSSAINI, M. Y., QUATTERONI, A. & ZANG, T. 1988 *Spectral methods in Fluid dynamics*. Springer Verlag.

CATHERALL, D. & MANGLER, K. W. 1966 The integration of the two-dimensional laminar boundary-layer equations past the point of vanishing skin friction. *J. Fluid. Mech* **26** (1), 163–182.

CEBECI, T. 1982 Unsteady separation. In *Numerical and Physical Aspects of Aerodynamic Flows* (ed. T. Cebeci), pp. 265–267. Springer.

CHAPMAN, D. R., KUEHN, D. M. & LARSON, H. K. 1958 Investigation of separated flows in supersonic and subsonic streams with emphasis on the effect of transition. *NACA Rep.* 1356.

CROCCO, L. & LEES, L. 1952 A mixing theory for the interaction between dissipative flows and nearly isentropic streams. *J. Aero. Sci* **19**, 649–676.

DANBERG, J. E. & FRANSLER, K. S. 1975 Separation like similarity solutions of two dimensional moving walls. *AIAA J* **13**, 110–112.

ELLIOTT, J. W., SMITH, F. T. & COWLEY, S. J. 1983 Breakdown of boundary layers (i) on moving surfaces; (ii) in semi-similar flows; (iii) in fully unsteady flow. *Geo. Astrophys. Fluid Dyn* **25**, 77–138.

GAJJAR, J. & SMITH, F. T. 1983 On hypersonic self-induced separation, hydraulic jumps and boundar layers with algebraic growth. *Mathematika* **30**, 77–93.

GAJJAR, J. S. B. 1987 Fully developed free surface flows- liquid layer flow over a convex corner. *Computers and Fluids* **15** (4), 337–360.

GOLDSTEIN, S. 1948 On laminar boundary-layer flow near a position of separation. *Q. J. Mech. Appl. Math* **1** (1), 43–69.

HAKKINEN, R. J., GREBER, I., TRILLING, L. & ABARBANEL, S. S. 1959 The interaction of an oblique shock wave with a laminar boundary layer. *NACA memo.* 2-18-59W.

HOWARTH, L. 1948 The propogation of small disturbances in a supersonic stream bounded on one side by a parallel subsonic stream. *Proc. Cambridge Phil. Soc* **44**, 380–390.

HUNT, J. C. R. 1971 A theory for the laminar wake of a two-dimensional body in a boundary-layer. *J. Fluid. Mech.* **49**, 159–178.

INOUE, O. 1981 A numerical investigation of flow separation over moving walls. *J. Phys. Soc. Japan* **50** (3), 1002–1008.

KIRCHOFF, G. 1869 Zur theorie freier flüssigkeitsstrahlen. *J. Reine Angew. Math.* **70** (4), 289–298.

KOROLEV, G., GAJJAR, J. S. B. & RUBAN, A. I. 2002 Once again on the super-sonic flow separation near a corner. *J. Fluid. Mech.* **463**, 173–199.

KOROLEV, G. L. 1987 A method of solving solving problems of the asymptotic theory of interaction between a boundary layer and the external flow. *USSR Comput. Math. and Math. Phys* **27** (4), 534–537.

KOROMILAS, C. A. & TELIONIS, D. P. 1980 Unsteady laminar: an experimental study. *J. Fluid Mech.* **97** (2), 347–384.

LANDAU, L. D. & LIFSHITZ, E. M. 1944 *Mechanics of continous media*. Moscow: Gostekhizdat.

LIEPMANN, H. W. 1946 The interaction between boundary layers and shock waves in transonic flow. *J. Aero. Sci* **13** (12), 623–637.

LIGHTHILL, M. J. 1950 Reflection at a laminar boundary layer of a weak steady disturbance to a supersonic stream, neglecting viscosity and heat conduction. *Quart. J. Mech. Appl. Math* **3**, 303–325.

LIGHTHILL, M. J. 1953 On boundary layers and upstream influence. II. Supersonic flows without separation. *Proc. R. Soc. Lond. A* **217**, 478–507.

LIPATOV, I. I. 1999 Problems with discontinous boundary conditions describing flows at high reynolds number. *J. Appl. Maths. Mechs* **63**, 31–39.

LUDWIG, G. R. 1964 An experimental investigation of laminar separtion from a moving wall. In *AIAA paper 64-6*. AIAA Aerosp. sci. meeting, New York.

MERKIN, J. H. 1983 Free convection boundary layers over humps and indentaions. *Q. J.Mech. appl. Math* **36**, 71–85.

MERKIN, J. H. & SMITH, F. T. 1982 Free convection boundary layers near corners and sharp trailing edge. *J. Appl. Maths and Phys(ZAMP)* **33**, 35–82.

MESSITER, A. F. 1979 Boundary-layer separation. In *Proc. 8th US Natl Congr. Appl. Mech.*, pp. 157–159. Western Periodicals, North Hollywood, California.

MESSITER, A. F. 1983 Boundary-layer interaction theory. *Trans. ASME J. Appl. Mech.* **50** (4b), 1104–1113.

MOORE, F. K. 1958 On the separation of the unsteady laminar boundary layer. In *Boundary Layer research* (ed. H. Görtler), pp. 431–432. Berlin: Springer.

NAPOLITANO, M., WERLE, M. J. & DAVIES, R. T. 1979 Numerical technique for the triple deck problem. *AIAA Journal.* **17** (7), 699–705.

NEILAND, V. YA. 1969 Theory of laminar boundary-layer separation in supersonic flow. *Izv. Akad. Nauk SSSR, Mekh. Zhid. Gaza* (4), 53–57, in Russian. English transl. *Fluid Dyn.* **4** (4), 33–35.

NEILAND, V. YA. 1971b On the asymptotic theory of the interaction of supersonic flow with the boundary layer. *Izv. Akad. Nauk SSSR, Mekh. Zhid. Gaza* (4), 41–47.

NEILAND, V. YA. 1974 Asymptotic problems in the theory of viscous supersonic flows. *Tr. TsAGI* 1529, in Russian.

NEILAND, V. YA. 1981 Asymptotic theory of boundary-layer separation and interaction with supersonic gas flow. *Usp. Mekh.* **4** (2), 3–62, in Russian.

PRANDTL, L. 1904 Über Flüssigkeitsbewegung bei sehr kleiner Reibung. In *Verh. III Intl. Math. Kongr., Heidelberg*, pp. 484–491. Teubner, Leipzig, 1905, English transl. *NACA Tech. Memo.* 452.

RAGAB, S. A. & NAYFEH, A. H. 1980 A comparison of the second order triple deck theory and interacting boundary layers for incompressible flows past humps. AIAA 18th Aerosp. Sci. Meeting, Pasadena , California, USA.

RIZZETTA, D. P., BURGGRAF, O. R. & JENSON, R. 1978 Triple-deck solutions for viscous supersonic and hypersonic flow past corners. *J. Fluid Mech.* **89** (3), 535–552.

ROTT, N. 1956 Unsteady viscous flow in the vicinity of a stagnation point. *Q. Jour. Appl. Maths* **13**, 444–451.

RUBAN, A. I. 1978 Numerical solution of the local asymptotic problem of the unsteady separation of a laminar boundary layer in supersonic flow. *Zh. Vych. Mat. Mat. Fiz.* **18** (5), 1253–1265, in Russian. English transl. *USSR Comput. Math. and Math. Phys.* **18** (5), 175–187.

SEARS, W. R. 1956 Some recent developments in airfoil theory. *J. Aeronaut. Sci* **23**, 490–499.

SEARS, W. R. & TELIONIS, D. P. 1975 Boundary-layer separation in unsteady flow. *SIAM Journal of Applied Mathematics* **28** (1), 215–235.

SMITH, F. T. 1973 Laminar flow past a small hump on a flat plate. *J. Fluid Mech.* **57** (4), 803–824.

SMITH, F. T. 1982 On the high Reynolds number theory of laminar flows. *IMA J. Appl. Math.* **28** (3), 207–281.

SMITH, F. T., BRIGHTON, P. W. M., JACKSON, P. S. & HUNT, J. C. R. 1981 On boundary-layer flow past two-dimensional obstacles. *J. Fluid Mech* **113**, 123–152.

SMITH, F. T. & BURGGRAF, O. R. 1985 On dvelopment of large-sized short-scaled disturbances in boundary layers. *Proc. R. Soc. Lond. A* **399** (1816), 25–55.

SMITH, F. T. & DANIELS, P. G. 1981 Removal of goldstein singularity at separation, in flow past obstacles in wall layers. *J. Fluid Mech* **110**, 1–37.

SMITH, F. T. & DUCK, P. W. 1977 Separation of jets or thermal boundary-layers from a wall. *Q. J. Mech. Appl. Maths* **30**, 143–156.

SMITH, F. T. & KHORRAMI, A. F. 1991 The interactive breakdown in supersonic ramp flow. *J. Fluid Mech* **224**, 197–215.

SMITH, F. T. & MERKIN, J. H. 1982 Triple deck solutions for subsonic flow past humps, steps, concave or convex corners and wedged trailing edges. *Computers. Fluids.* **10**, 7–25.

SOBEY, I. 2000 *Introduction to interactive boundary layer theory*. Oxford University Press.

STEWARTSON, K. 1951 On the interaction between shock-waves and boundary layers. *Proc. Cambridge. Phil. Soc.* **46**, 182–198.

STEWARTSON, K. 1974 Multistructured boundary layers on flat plates and related bodies. *Adv. Appl. Mech.* **14**, 145–239.

STEWARTSON, K. 1981 D'Alembert's paradox. *SIAM Rev.* **23** (3), 308–343.

STEWARTSON, K. & WILLIAMS, P. G. 1969 Self-induced separation. *Proc. R. Soc. Lond. A* **312**, 181–206.

SYCHEV, V. V. 1979 Asymptotic theory of non-stationary separation. *Izv. Akad. Nauk SSSR, Mekh. Zidk. Gaza* **6**, 21–32, in Russian. English transl. *Fluid Dynamics* (1980) **14** , 829–838.

SYCHEV, V. V., RUBAN, A. I., SYCHEV, VIC. V. & KOROLEV, G. L. 1998 *Asymptotic Theory of Separated Flows*. Cambridge University Press.

SYKES, R. I. 1978 Stratification effects in boundary layer flows over hills. *Proc. R. Soc.* **A361**, 225–243.

TELIONIS, D. P., TSAHALIS, D. T. & WERLÉ, M. J. 1973 Numerical investigation of unsteady boundary-layer separation. *Phys Fluids* **16** (8), 968–973.

TREFETHEN, L. N. 2000 *Spectral methods in Matlab*. SIAM.

TSAHALIS, D. T. 1976 Laminar boundary-layer separation from an upstream moving wall. In *AIAA 9th Fluid and Plasma Dynamics Conference*. San deigo, California.

Van Dommelen, L. L. & Shen, S. F. 1982 A bifurcation-free interaction solution for steady separation from a downstream moving wall. In *AIAA Aero. Sci. meeting*. Orlando, Florida, USA.

Veldman, A. E. P. & Dijkstra, D. 1980 A fast method to solve incompressible interaction problems. In *Proc . 7th Int. Conf. Num. meth. Fluid Dyn*. Stanford, USA.

Vidal, R. J. 1959 Research on rotating stallin axial flow compressor; part III-experiments on laminar separation from a moving wall. *Tech. Rep.* 59-75. Wright Air Dev. Cent.

Werle, M. J. & Vatsa, V. N. 1974 New method for supersonic boundary-layer separation. *AIAA J.* **12** (11), 1491–1497.

Williams, P. G. 1975 A reverse flow computation in the theory of self-induced separation. In *lecture notes in Phys*, pp. 445–451.

Williams III, J. C. 1977 Incompressible boundary-layer separation. *Ann. Rev. Fluid. Mech* **9**, 113–144.

Zhuk, V. I. 2001 *Tollmien-Schlichting wave and solitons*. Nauka, Moscow.

Appendix A

Relation between analytical and numerical scalings

From Araki (2006) we have

$$p = \epsilon^2 P_{th} \tag{A.1}$$

where $\epsilon = \frac{U_w^{th}}{U_\infty} \ll 1$ and

$$p = Re^{-\frac{1}{4}} P_{num} \tag{A.2}$$

P_{th} can be expressed as

$$P_{th} = \frac{Re^{-\frac{1}{4}} P_{num}}{\epsilon^2} \tag{A.3}$$

$$= \frac{Re^{-\frac{1}{4}} P_{num}}{(U_w^{th})^2} \tag{A.4}$$

We have

$$U_w^{th} = Re^{-\frac{1}{8}} U_w \tag{A.5}$$

Substituting (A.5) into (A.4) we get,

$$P_{th} = \frac{Re^{-\frac{1}{4}}}{(Re^{-\frac{1}{8}} U_w)^2} P_{num} \tag{A.6}$$

$$= \frac{P_{num}}{(U_w^2)} \tag{A.7}$$

Similarly

$$x = \frac{Re^{-\frac{1}{2}}}{\epsilon} X_{th} \tag{A.8}$$

$$x = Re^{-\frac{1}{8}} X_{num} \tag{A.9}$$

X_{th} is given by

$$
\begin{aligned}
X_{th} &= \frac{Re^{-\frac{1}{8}}}{Re^{-\frac{1}{2}}}\epsilon X_{num} & \text{(A.10)} \\
&= Re^{\frac{1}{8}}\epsilon X_{num} & \text{(A.11)} \\
&= Re^{\frac{1}{8}}U_w^{th} X_{num} & \text{(A.12)}
\end{aligned}
$$

Substituting (A.5) into (A.12) we obtain

$$
X_{th} = U_w X_{num} \tag{A.13}
$$

Appendix B

Elements of Matrix- Double deck structure

$$\mathbf{F_p} = \frac{1}{2\Delta x} \begin{pmatrix} & & \frac{1}{\Delta x^3} \\ & (\mathbf{F_l})_{N+1 \times N+1} & \vdots \\ & & \\ 0 & \cdots & \end{pmatrix}$$

where $\mathbf{F_l}$ is given by

$$\mathbf{F_l} = \begin{pmatrix} \epsilon_0 D\bar{\psi}_{j,0} & 0 & \cdots \\ 0 & \ddots & 0 \\ \vdots & 0 & \epsilon_N D\bar{\psi}_{j,N} \end{pmatrix} D_1 - \begin{pmatrix} D\bar{\psi}_{j,0} & 0 & \cdots \\ 0 & \ddots & 0 \\ \vdots & 0 & D\bar{\psi}_{j,N} \end{pmatrix}$$

The elements of the matrix $\mathbf{A_p}$ are given by

$$\mathbf{A_p} = \begin{pmatrix} & & -\frac{3}{\Delta x^3} - \frac{\sigma}{\Delta x^2} \\ & (\mathbf{A_l})_{N+1 \times N+1} & \vdots \\ & & \\ 0 & \cdots & \end{pmatrix}$$

where,

$$\mathbf{A_l} = -\frac{2}{\Delta x} \begin{pmatrix} \epsilon_0 D\bar{\psi}_{j,0} & 0 & \dots \\ 0 & \ddots & 0 \\ \vdots & 0 & \epsilon_N D\bar{\psi}_{j,N} \end{pmatrix} D_1 + \frac{2}{\Delta x} \begin{pmatrix} D\bar{\psi}_{j,0} & 0 & \dots \\ 0 & \ddots & 0 \\ \vdots & 0 & D\bar{\psi}_{j,N} \end{pmatrix}$$

The elements of the matrix $\mathbf{B_p}$ are written in the following structure

$$\mathbf{B_p} = \begin{pmatrix} & & \frac{3}{\Delta x^3} + 2\frac{\sigma}{\Delta x^2} \\ (\mathbf{B_l})_{N+1 \times N+1} & \vdots \\ \\ 0 & \dots \end{pmatrix}$$

where,

$$\mathbf{B_l} = \frac{3}{\Delta x} \begin{pmatrix} \epsilon_0 D\bar{\psi}_{j,0} & 0 & \dots \\ 0 & \ddots & 0 \\ \vdots & 0 & \epsilon_N D\bar{\psi}_{j,N} \end{pmatrix} D_1 - \frac{3}{2\Delta x} \begin{pmatrix} (1-\epsilon_0)D\bar{\psi}_{j,0} & 0 & \dots \\ 0 & \ddots & 0 \\ \vdots & 0 & (1-\epsilon_N)D\bar{\psi}_{j,N} \end{pmatrix} D_1$$

$$+\frac{1}{2\Delta x} \begin{pmatrix} \epsilon_0(D\bar{\psi}_{j-2,0} - 4D\bar{\psi}_{j-1,0} + 3D\bar{\psi}_{j,0}) & 0 & \dots \\ 0 & \ddots & 0 \\ \vdots & 0 & \epsilon_N(D\bar{\psi}_{j-2,N} - 4D\bar{\psi}_{j-1,N0} + 3D\bar{\psi}_{j,N}) \end{pmatrix} D_1$$

$$-\frac{1}{2\Delta x} \begin{pmatrix} (1-\epsilon_0)S_0 & & \\ 0 & \ddots & 0 \\ \vdots & 0 & (1-\epsilon_N)S_N \end{pmatrix}$$

$$-\frac{1}{2\Delta x} \begin{pmatrix} (\bar{\psi}_{j-2,0} - 4\bar{\psi}_{j-1,0} + 3\bar{\psi}_{j,0}) & 0 & \dots \\ 0 & \ddots & 0 \\ \vdots & 0 & (\bar{\psi}_{j-2,N} - 4\bar{\psi}_{j-1,N0} + 3\bar{\psi}_{j,N}) \end{pmatrix} D_2$$

$$-\frac{3}{2\Delta x} \begin{pmatrix} D^2\bar{\psi}_{j,0} & 0 & \dots \\ 0 & \ddots & 0 \\ \vdots & 0 & D^2\bar{\psi}_{j,N} \end{pmatrix} - D_3$$

where

$$
\begin{aligned}
S_0 &= D\bar{\psi}_{j+2,0} - 4D\bar{\psi}_{j+1,0} + 3D\bar{\psi}_{j,0}) \\
S_N &= D\bar{\psi}_{j+2,N} - 4D\bar{\psi}_{j+1,N0} + 3D\bar{\psi}_{j,N})
\end{aligned}
$$

The elements of the matrix $\mathbf{C_p}$ are given by

$$
\mathbf{C_p} = \begin{pmatrix} & & & -\frac{1}{\Delta x^3} - \frac{\sigma}{\Delta^2} \\ & (\mathbf{C_l})_{N+1 \times N+1} & & \vdots \\ & & & \\ 0 & & \cdots & \end{pmatrix}
$$

where $\mathbf{C_l}$ is given by

$$
\mathbf{C_l} = \frac{2}{\Delta x} \begin{pmatrix} (1-\epsilon_0)D\bar{\psi}_{j,0} & 0 & & \cdots \\ 0 & \ddots & & 0 \\ \vdots & & 0 & (1-\epsilon_N)D\bar{\psi}_{j,N} \end{pmatrix}
$$

The elements of the matrix $\mathbf{E_p}$ are given by

$$
\mathbf{E_p} = \begin{pmatrix} & & & 0 \\ & (\mathbf{E_l})_{N+1 \times N+1} & & \vdots \\ & & & \\ 0 & & \cdots & \end{pmatrix}
$$

where,

$$\mathbf{E_l} = -\frac{1}{2\Delta x} \begin{pmatrix} (1-\epsilon_0)D\bar{\psi}_{j,0} & 0 & \cdots \\ 0 & \ddots & 0 \\ \vdots & 0 & (1-\epsilon_N)D\bar{\psi}_{j,N} \end{pmatrix} D_1$$

Appendix C

External Supersonic flow-Matrix Structure

$$\mathbf{F_p} = \frac{1}{2\Delta x} \begin{pmatrix} & & & 0 \\ & (\mathbf{F_l})_{N+1\times N+1} & & \vdots \\ & & & \\ 0 & & \dots & \end{pmatrix}$$

where $\mathbf{F_l}$ is given by

$$\mathbf{F_l} = \begin{pmatrix} \epsilon_0 D\bar{\psi}_{j,0} & 0 & \dots \\ 0 & \ddots & 0 \\ \vdots & 0 & \epsilon_N D\bar{\psi}_{j,N} \end{pmatrix} D_1 - \begin{pmatrix} D\bar{\psi}_{j,0} & 0 & \dots \\ 0 & \ddots & 0 \\ \vdots & 0 & D\bar{\psi}_{j,N} \end{pmatrix}$$

The elements of the matrix $\mathbf{A_p}$ are given by

$$\mathbf{A_p} = \begin{pmatrix} & & & -\frac{1}{\Delta x^2} \\ & (\mathbf{A_l})_{N+1\times N+1} & & \vdots \\ & & & \\ 0 & & \dots & \end{pmatrix}$$

where,

$$
\mathbf{A_l} = -\frac{2}{\Delta x}
\begin{pmatrix}
\epsilon_0 D\bar{\psi}_{j,0} & 0 & \dots \\
0 & \ddots & 0 \\
\vdots & 0 & \epsilon_N D\bar{\psi}_{j,N}
\end{pmatrix}
D_1 + \frac{2}{\Delta x}
\begin{pmatrix}
D\bar{\psi}_{j,0} & 0 & \dots \\
0 & \ddots & 0 \\
\vdots & 0 & D\bar{\psi}_{j,N}
\end{pmatrix}
$$

The elements of the matrix $\mathbf{B_p}$ are written in the following structure

$$
\mathbf{B_p} =
\begin{pmatrix}
& & \frac{2}{\Delta x^2} \\
(\mathbf{B_l})_{N+1 \times N+1} & \vdots \\
& \\
0 & \dots
\end{pmatrix}
$$

where,

$$
\mathbf{B_l} = \frac{3}{\Delta x}
\begin{pmatrix}
\epsilon_0 D\bar{\psi}_{j,0} & 0 & \dots \\
0 & \ddots & 0 \\
\vdots & 0 & \epsilon_N D\bar{\psi}_{j,N}
\end{pmatrix}
D_1 - \frac{3}{2\Delta x}
\begin{pmatrix}
(1-\epsilon_0)D\bar{\psi}_{j,0} & 0 & \dots \\
0 & \ddots & 0 \\
\vdots & 0 & (1-\epsilon_N)D\bar{\psi}_{j,N}
\end{pmatrix}
D_1
$$

$$
+ \frac{1}{2\Delta x}
\begin{pmatrix}
\epsilon_0(D\bar{\psi}_{j-2,0} - 4D\bar{\psi}_{j-1,0} + 3D\bar{\psi}_{j,0}) & 0 & \dots \\
0 & \ddots & 0 \\
\vdots & 0 & \epsilon_N(D\bar{\psi}_{j-2,N} - 4D\bar{\psi}_{j-1,N0} + 3D\bar{\psi}_{j,N})
\end{pmatrix}
D_1
$$

$$
- \frac{1}{2\Delta x}
\begin{pmatrix}
(1-\epsilon_0)S_0 & & \\
0 & \ddots & 0 \\
\vdots & 0 & (1-\epsilon_N)S_N
\end{pmatrix}
$$

$$
- \frac{1}{2\Delta x}
\begin{pmatrix}
(\bar{\psi}_{j-2,0} - 4\bar{\psi}_{j-1,0} + 3\bar{\psi}_{j,0}) & 0 & \dots \\
0 & \ddots & 0 \\
\vdots & 0 & (\bar{\psi}_{j-2,N} - 4\bar{\psi}_{j-1,N0} + 3\bar{\psi}_{j,N})
\end{pmatrix}
D_2
$$

$$
- \frac{3}{2\Delta x}
\begin{pmatrix}
D^2\bar{\psi}_{j,0} & 0 & \dots \\
0 & \ddots & 0 \\
\vdots & 0 & D^2\bar{\psi}_{j,N}
\end{pmatrix}
- D_3
$$

where

$$S_0 = D\bar{\psi}_{j+2,0} - 4D\bar{\psi}_{j+1,0} + 3D\bar{\psi}_{j,0})$$

$$S_N = D\bar{\psi}_{j+2,N} - 4D\bar{\psi}_{j+1,N0} + 3D\bar{\psi}_{j,N})$$

The elements of the matrix $\mathbf{C_p}$ are given by

$$\mathbf{C_p} = \begin{pmatrix} & & & -\frac{1}{\Delta x^2} \\ & (\mathbf{C_l})_{N+1 \times N+1} & & \vdots \\ & & & \\ 0 & & \cdots & \end{pmatrix}$$

where $\mathbf{C_l}$ is given by

$$\mathbf{C_l} = \frac{2}{\Delta x} \begin{pmatrix} (1-\epsilon_0)D\bar{\psi}_{j,0} & 0 & & \cdots \\ 0 & \ddots & & 0 \\ \vdots & & 0 & (1-\epsilon_N)D\bar{\psi}_{j,N} \end{pmatrix}$$

The elements of the matrix $\mathbf{E_p}$ are given by

$$\mathbf{E_p} = \begin{pmatrix} & & & 0 \\ & (\mathbf{E_l})_{N+1 \times N+1} & & \vdots \\ & & & \\ 0 & & \cdots & \end{pmatrix}$$

where,

$$\mathbf{E_l} = -\frac{1}{2\Delta x} \begin{pmatrix} (1-\epsilon_0)D\bar{\psi}_{j,0} & 0 & & \cdots \\ 0 & \ddots & & 0 \\ \vdots & & 0 & (1-\epsilon_N)D\bar{\psi}_{j,N} \end{pmatrix} D_1$$